MICROFABRICATED CIRCUITS FOR TERAHERTZ WAVE AMPLIFICATION AND TERAHERTZ BIOSENSORS

by

Olutosin Charles Fawole

A dissertation submitted to the faculty of
The University of Utah
in partial fulfillment of the requirements for the degree of

Doctor of Philosophy

Department of Electrical and Computing Engineering

The University of Utah

December 2016

The University of Utah Graduate School

STATEMENT OF DISSERTATION APPROVAL

The dissertation of **Olutosin Charles Fawole**

has been approved by the following supervisory committee members:

Massood Tabib-Azar	, Chair	**9/23/2016** Date Approved
Bruce Kent Gale	, Member	**8/4/2016** Date Approved
David Alan Schurig	, Member	**8/3/2016** Date Approved
Om P Gandhi	, Member	Date Approved
Carlos H Mastrangelo	, Member	**8/3/2016** Date Approved

and by **Gianluca Lazzi** , Chair/Dean of

the Department/College/School of **Electrical and Computer Engineering**

and by David B. Kieda, Dean of The Graduate School.

ABSTRACT

The terahertz frequency band extends from deep infrared (100 THz) down to millimeter waves (0.4 THz), and this band was mostly inaccessible due to the lack of appropriate sources and detectors. Those with access to this band had to endure the small-intensity pulsed signals (nanowatts to microwatts) that the terahertz sources of those times could provide. In recent years, however, sufficient development has led to the availability of terahertz sources with sufficient power (1-100 μW) and the ease of use these sources has in turn enabled researchers to develop newer sources, detectors, and application areas.

The terahertz regime is interesting because a) many molecules have vibrational, rotation and transition absorption bands in this regime, b) the terahertz electromagnetic wavelength is sufficiently small to resolve centimeter to millimeter scale objects, and c) scattering and absorption in metals in the terahertz regime make it very challenging to devise terahertz signal processing circuits. Thus, performing terahertz reflection/transmission measurements may enable precise identification of chemicals in a sample. Furthermore, small wavelengths and strong scattering by metallic objects make imaging with terahertz waves quite attractive. Finally, the ability to devise terahertz communication circuits and links will provide access to a frequency domain that is restricted and not available to others.

One of the main objectives of this work is to develop 0.75 - 1.1 terahertz (free

space wavelength 272 μm – 400 μm) amplifiers. Another objective of this work is to explore the suitability of terahertz waves in biological imaging and sensing.

The terahertz amplifiers developed in this work consisted of distributed components such as rectangular waveguides and cylindrical dielectric resonators. In contrast to discrete amplifiers, which are based on solid-state devices, distributed traveling wave amplifiers can potentially handle and produce larger powers. Three different distributed terahertz amplifier circuits were considered in this work. These were based on a) coupled dielectric resonators, b) dielectric waveguides with periodic slots, and c) metallic meandering waveguides. The result of the hot test of the last circuit on interaction with an electron beam energy source yielded an amplification of 12 dB of a -55 dBm, 0.9 terahertz signal over ~1 gigahertz bandwidth. The electron beam acceleration voltage was 4.8 kV and its current was approximately 20 microamps. The terahertz biosensing system developed in this work was used to study the unique interaction of terahertz waves with the chemical and physical components of biological tissues, and the products of biochemical reactions. A terahertz near-field imaging system was also developed to image mouse brain slices, plants, and bug wings. In addition, this work also demonstrated the capabilities and limitations of terahertz waves for the real-time noninvasive monitoring of bioethanol production by yeast cells.

To my family of present, and future…

TABLE OF CONTENTS

LIST OF TABLES

ACKNOWLEDGEMENTS

I believe the noblest of all pursuits in life is the pursuit of perfection in one's endeavors, and a path one can follow to achieve perfection is by opening one's mind to imbibe new ideas and by ruminating on already acquired ideas for a more profound perspective. Over the past four years, in my journey towards perfection, I was fortunate to have a giant on whose shoulders I could stand, and this giant has helped me to make giant strides towards my life goal. The giant shoulder I stood on was that of my PhD advisor, Professor Massood Tabib-Azar, to whom I express my utmost gratitude. 'Professor' gave me a great opportunity, without any reservations, to work under his expert tutelage at the Advanced Metrology and Nano Device Laboratory (AMANDA) at the University of Utah, and for this I am very grateful. I also thank him for being very patient with me by putting up with my imperfections, and for being the mentor who guided me over countless miles on my journey towards perfection. I am very grateful to him for giving me the wonderful opportunity to work on cutting-edge research projects in a state-of-the-art laboratory, for providing me with the exposures that were necessary to be a cosmopolitan researcher, for implanting in me numerous scientific ideas, technical skills, and aptitude for critical thinking. This knowledge, experiences, and skills have not only helped me in my academics, but also in other endeavors in my life. Without any doubt in my mind, I can say Prof. Tabib-Azar's guidance has propelled me closer to my ultimate life goal.

Furthermore, I thank the members of my supervisory committee for their invaluable contributions to my research and for their time in evaluating this work. In particular, I thank Prof. Carlos Mastrangelo in whose research group I collaborated to microfabricate some of my experimental devices.

Moreover, I thank the other student researchers with whom I collaborated over the course of my research work in AMANDA: Pradeep Pai (I further thank Pradeep for being an exemplary senior PhD student to me), Shashank S. Pandey, Rugved Likhite, Kushagra Sinha, and Mitchell Terry.

In addition, I thank the colleagues who have helped me be proficient with some technical tools which helped me with my research: Lingyao Chen and Tien-Vinh Dang-Tran (with LabVIEW), Hoorad Pourzand and Zhe Yang (with SolidWorks and AutoCAD).

Finally, I am indebted to Chandra Martz and her family for their invaluable support.

This work is supported in part by research funding from the Defense Advanced Research Projects Agency (DARPA).

CHAPTER 1

INTRODUCTION

1.1 Introduction to terahertz waves research

The main goal of this work is to develop circuits for amplifying terahertz waves. As shown in Fig. 1.1 [1], terahertz waves (also known as submillimeter waves or far infrared waves) lie in a frequency range that is between optical frequencies and microwave (millimeter waves) frequencies, and this is between 0.4 x 10^{12} Hz and 100 x 10^{12} Hz [2]. Compared to the flanking microwave and optical frequency bands, not a lot of circuits and niche applications have existed for terahertz waves. Hence, the terahertz band was referred to as the terahertz gap. It has also been referred to as the 'last frontier' of the electromagnetic spectrum [3,4] because researchers have extensively studied all other bands in the electromagnetic spectrum except for the terahertz band.

Although terahertz waves have been used for research work in astronomy and spectroscopy since the 1960s [5], it was not until the early 2000s that advancement in terahertz generation and detection technology made the terahertz band more accessible to the researcher. This advancement increased research interest in terahertz waves.

Consequently, researchers have demonstrated new and exciting applications of terahertz waves. The timeline of terahertz research activity from the 1960s is given in Fig. 1.2. This activity is measured by the number of publications with the word 'terahertz' or 'far infrared' in their titles, and the number of citations to works with those

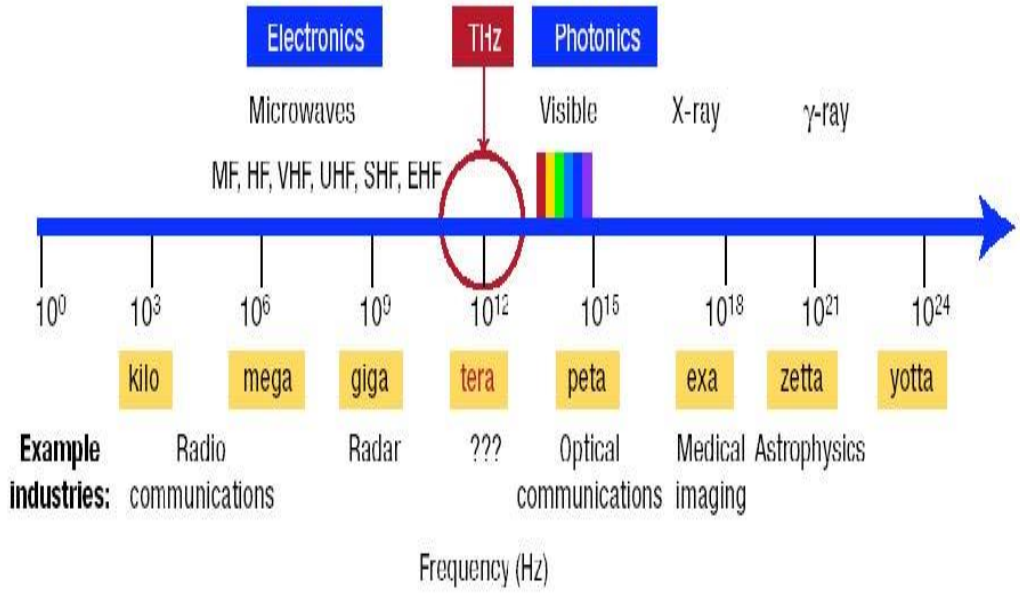

Fig. 1.1. The location of the terahertz gap in the electromagnetic spectrum.

keywords [6].

The free space propagation properties of terahertz waves, like all electromagnetic waves, are governed by the Maxwell's equations. However, what differentiates terahertz waves from other types of waves is the peculiar way terahertz waves interact with matter [5]. The permittivity and permeability of materials (the macroscopic quantities that govern electromagnetic wave propagation/interaction in/with a material) at terahertz frequency differ considerably from the permittivity and permeability at other frequencies.

Furthermore, many materials show strong resonant absorption (due to molecular and vibrational resonances) at certain well-defined frequencies in the terahertz band. For example, the resonant absorption lines of water vapor and carbon monoxide are shown in Fig. 1.3 [7]. This means terahertz waves can be used to detect the presence of small amounts of such resonant materials in an unknown sample.

Furthermore, if an electromagnetic wave is used to image an object, the spatial

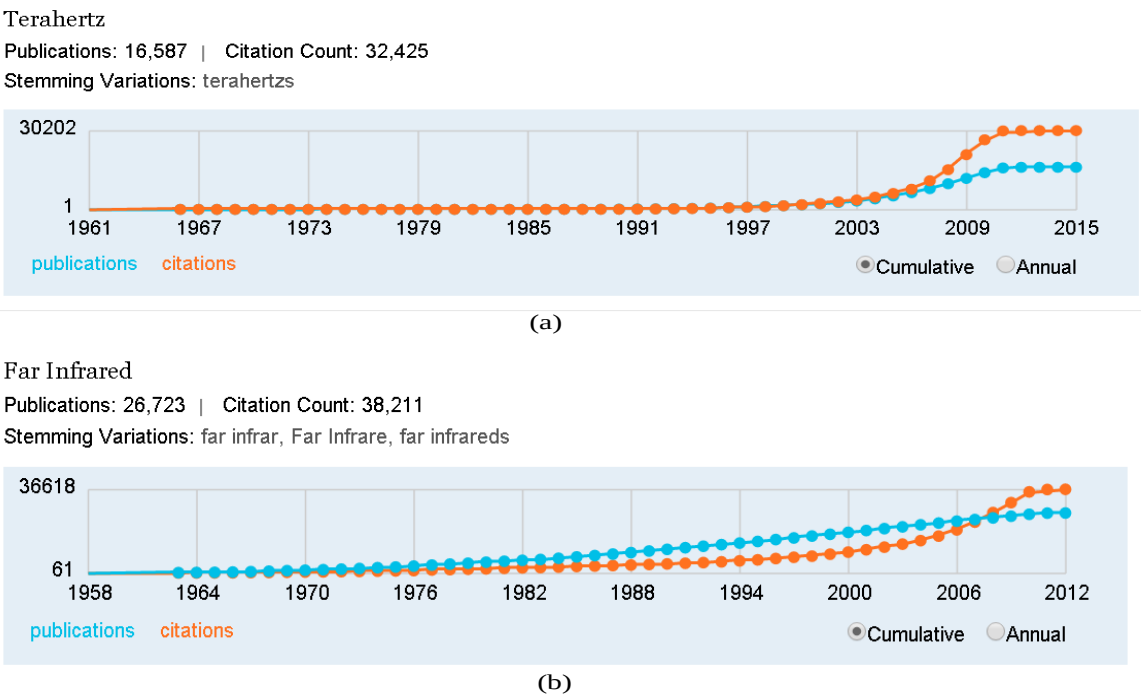

Fig. 1.2. Publication and citation trends in terahertz research. (a) Publications and citations relating the word 'terahertz' (b) Publications and citations relating the word 'far infrared' (synonymous with 'terahertz'). Graph retrieved from Microsoft Academic.

resolution of image produced by the wave is proportional to the wavelength of the probing wave. Hence, terahertz waves are better suited for high spatial resolution imaging compared to longer wavelength millimeter waves and microwaves.

In addition, since the frequency of the carrier wave in a communication system determines the data carrying capacity of the system, terahertz waves are potentially suitable for high-speed (data rates of up to 100 Gb/S) communication. The properties of the terahertz waves, its possible applications, and its demonstrated applications are summarized in two classic review papers on terahertz technology [8,9].

However, some researchers have expressed some caution over the overly optimistic attitude towards terahertz technology. In [10], the author cautioned that the many purported attractive applications of terahertz waves (e.g., standoff spectroscopy)

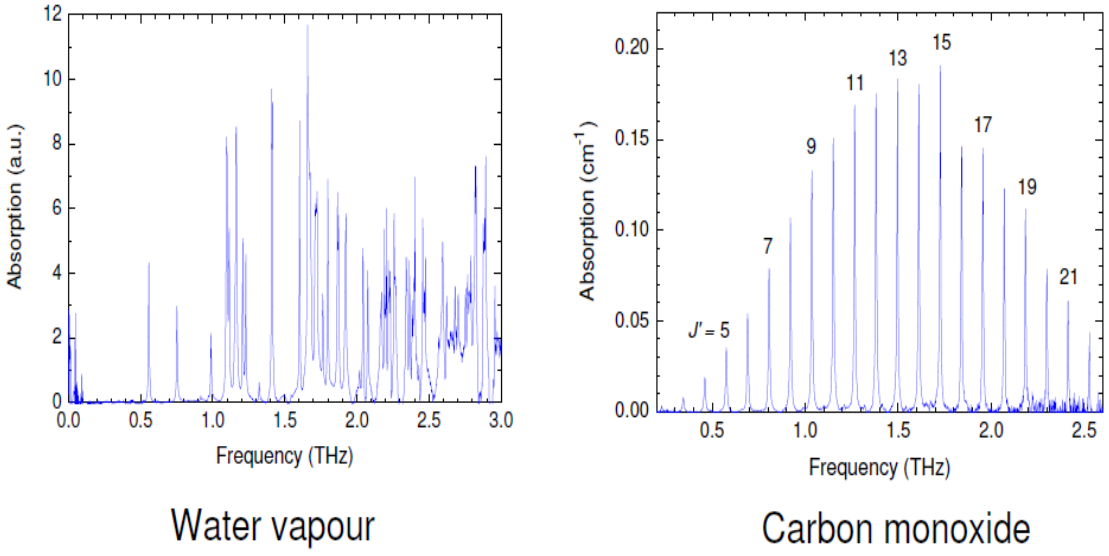

Fig. 1.3. Terahertz signature of water vapor (left) and carbon monoxide (right).

that are easily demonstrated in a controlled laboratory environment would be difficult to reproduce in the real world because the small wavelength of terahertz waves would make terahertz waves be easily scattered (diffracted) by small objects. Furthermore, the author argued that wireless communication with terahertz waves would be difficult to achieve because terahertz waves are strongly absorbed by water, which is present as vapor in the atmosphere, and also because terahertz waves are strongly absorbed by concrete walls.

In [11], the authors presented an overview of the capability of terahertz waves by comparing the suitability of terahertz waves with other waves for specific applications.

In Table 1.1, some common applications of electromagnetic waves, in general, are presented and the suitability of terahertz waves for each application, in particular, is examined. However, this table is not final because as research in terahertz science and technology progresses further, it is hoped that researchers will discover more niche applications for terahertz waves.

Without doubt, the discovery of more applications for terahertz waves will be

Table 1.1. Terahertz waves applications: capabilities and limitations

Application	**Are terahertz waves most suitable?**	**Comment(s)**
Wireless communication	Depends	Except for short range communication or with low-frequency terahertz waves (because terahertz waves are strongly absorbed by atmospheric water vapor and walls).
Wired communication	No	Nondispersive materials/schemes that can transmit terahertz waves over long distances, like optical fibers for light waves, are yet to be proven feasible.
Spectroscopy	Yes	Many chemicals respond with unique signatures on excitation with terahertz waves.
Detection of trace amount of water	Yes	A small amount of water is strongly absorbed by terahertz waves.
Security applications (e.g., body scanner)	Yes	Millimeter-waves technology is a more mature technology for this application.
Near-field imaging	Depends	Though imaging resolution is not frequency dependent in near-field imaging, samples with components that interact with terahertz waves in a unique manner can be imaged in high resolution with near-field terahertz imaging [12].
Space communication	Yes	The emptiness of space makes terahertz waves suitable for high-speed space communication.
Astronomy	Yes	A lot of radiation emitted at the beginning of the universe lies in the terahertz frequency range.

Table 1.1. continued.

Application	Are terahertz waves most suitable?	Comment(s)
Applications require nonionizing radiation	Yes	However, other electromagnetic radiations below ultraviolent radiation frequency are also nonionizing.

accelerated by the wider availability of brighter terahertz sources (and more sensitive terahertz detectors). Hence, one of the main goals of this research is to develop an amplifier for terahertz waves. Such an amplifier will provide a brighter source for terahertz waves. Another main goal of this research is to find new niche applications for terahertz waves in biological imaging and sensing. This exploration will further advance the technological relevance of terahertz waves.

1.2 Literature review on terahertz wave amplifiers

Terahertz wave amplifiers may consist of either discrete components or distributed components. Discrete component amplifiers use solid-state components for amplification. Contrarily, distributed component amplifiers use the interaction between a wave propagating in waveguide-based structures/resonators and a plasma (electron or quasineutral) beam to produce wave amplification. Historically, discrete component amplifiers have low power handling capability, whereas distributed-component amplifiers can handle higher power. More importantly, these distributed component devices can be easily scaled to a different operating frequency regime by simply scaling their characteristic dimensions. An illustration of the ease of scaling a distributed amplifier is from the distributed amplifier research work at Northrop Grumman Electronic Systems (NGES). NGES demonstrated a waveguide-based amplifier first at 0.22 THz, and then rapidly demonstrated a scaled version of this amplifier at 0.85 THz [13-17].

Distributed-component amplifiers are generally referred to as electron tube amplifiers. Two common forms of the electron tube are the klystron and the traveling-wave-tube (TWT) amplifier. In these electron tubes, the synchronous transfer of energy

from an electron beam to the wave in a TWT results in the amplification of the wave.

Furthermore, with an appropriate feedback mechanism, an electron-tube amplifier circuit can be modified to work as an oscillator. This type of amplifier/oscillator has been around since the 1940s, and it is reputed for long lifetime and high power handling capabilities [18].

In addition to the electron-tube amplifier research efforts at NGES mentioned earlier, other research groups elsewhere have worked or are working on developing electron-tube (traveling-wave tube) amplifiers/oscillators for terahertz waves. Table 1.2 summarizes the efforts of prominent research groups in this area. This table also includes an earlier research effort at the University of Utah that led to the development of a terahertz TWT oscillator. This table presents only experimental results (although most of the listed research groups have also developed simulation models for their designs).

The goal of this work is to develop a distributed amplifier at ~1 THz. In addition to an electron beam energy source for use in this amplifier, this work will also explore the use of plasma as an energy source in distributed amplifiers. Plasma is a complex and nonlinear media that can support a wide array of waves and instabilities. Nonlinearity and instabilities in plasma can make plasma act as a source or sink of electromagnetic waves. [40,41].

1.3 Research goals and contributions

One main goal of this work is to develop an amplifier circuit for terahertz waves. This amplifier circuit will amplify traveling terahertz waves through the synchronous interaction between the waves in the amplifier circuit (energy sink) and a beam of electron or plasma (energy source). This work started on the path towards this goal b

Table 1.2. Summary of the effort of major research groups towards the development TWT-based amplifiers and oscillators

Research group [references]	**Circuit - type**	**Operating frequency**	**Microfabrication method**	**Circuit loss**	**Gain/output power**	**Contribution to terahertz source/amplifier technology**
Northrop Grumman Electronic Systems [13-17]	Folded Waveguide	0.22 (0.65, 0.67, 0.85) THz	DRIE	< -3 dB	~ 30 dB	(1) High power THz amplifier (2) Multibeam multiSWS TWT
UC Davis –led consortium [19-31]	TE-mode, staggered, double grating circuit	0.22 THz	UV LIGA, DRIE NanoCNC Mill	~ -5 dB	No hot tests	(1) NanoCNC fabrication of TWT (2) Elliptical sheet beam electron source design
European community OPTHER project [32-35]	Corrugated Rectangular waveguide (single and double)	1 THz	Deep X-ray LIGA	No cold tests	No hot tests	(1) Cascaded backward wave terahertz amplifier
University of Wisconsin-led consortium[36,37]	Folded waveguide	0.4 THz	LIGA, DRIE	No cold tests	No hot testing at THz. (30 dB gain in a 50 GHz) prototype	(1) Development of Particle-In-Cell simulation benchmarks for TWT design
Previous work at the University of Utah[38, 39]	Free Interdigital Line	1.25 THz	DRIE	Not applicable	1μW Oscillation power	(1) Very high interaction impedance device (2) beam focusing magnet-free design

designing experiments to understand the characteristics of plasma (sourced from a DC gas discharge), the behavior of plasma under static electric and magnetic fields, the behavior of plasma under slowly varying fields, and the interaction of plasma with matter (such as dielectrics).

In addition, this work presented the design and characterization of an electron beam source. Later on, this work proceeded to develop an electromagnetic circuit at GHz frequency whose electromagnetic fields can interact with the particles in a plasma beam. This circuit was then proposed for use in the design in gigahertz frequency and terahertz frequency electron tube klystrons. More importantly, a terahertz meandering traveling wave amplifier circuit was demonstrated in this work.

Another goal of this work is to develop new techniques and circuits for terahertz biosensing applications. Hence, in this work, a near-field imaging system for biological samples and a terahertz system for the real-time monitoring of yeast fermentation were presented.

In this research work, the studies towards the development of a terahertz amplifier led to develop a number of new microplasma, microwave, and terahertz circuits. Some of these circuits are presented in this work, and some are presented elsewhere [42,43]. Figure 1.4 illustrates the interrelationships of the studies performed in this work, and the new circuits and applications that resulted from these studies. An overview of the circuits developed and the applications demonstrated in this work are enumerated below.

1.3.1 A 3D-printed electrohydrodynamic pump

An electrohydrodynamic (EHD) pump that used the collision of the drifting ions and electrons in a corona discharge with air molecules to actuate the sustained flow of air

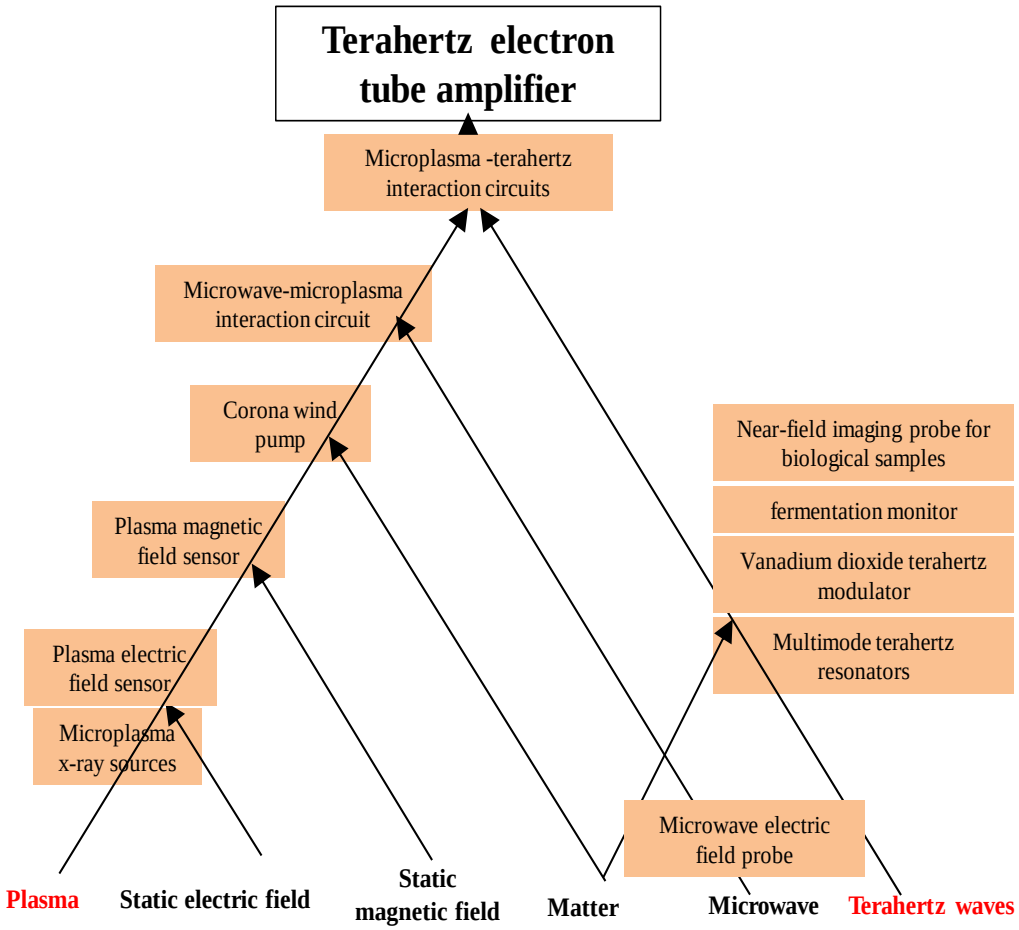

Fig. 1.4. The relationship between the different studies in this work, the resulting novel applications and circuits, and how these studies led to the ultimate goal of realizing a terahertz amplifier.

was demonstrated. EHD pumps actuate the flow of air without the use of moving parts that characterized conventional pumps. The contribution of this work is the first time use of a 3D printer to rapidly fabricate EHD pumps. Fabricated pumps actuated air flow at the rate of ~ 2 m/s with an efficiency of ~ 0.1%.

1.3.2 A microplasma magnetic field sensor

This is a first-time demonstration of plasma for magnetic field sensing. In the plasma magnetic field sensor device, an atmospheric-pressure glow discharge (plasma beam) in the device rotated (due to Lorentz force) on application of an external magnetic field to the device. The rate of rotation of the plasma beam is proportional to the applied magnetic field. Therefore, the rate of rotation of the plasma beam is a measure of the strength of the applied magnetic field. The magnetic field sensor could measure a minimum magnetic field strength of 40 mT (the minimum magnetic field needed to make the plasma beam rotate) with a sensitivity of 10 Hz/mT.

1.3.3 A microplasma electric field sensor

This sensor is a Lorentz force-based sensor similar to the magnetic field sensor. However, because the glow discharge (plasma) in this device is mostly neutral, large electric fields were necessary to actuate the quasineutral beam (except at the nonneutral regions that are close to the plasma cathode and anode).

1.3.4 Plasma soft x-ray source

This dissertation quantified for the first time the x-ray emission from atmospheric pressure plasma. Soft x-rays with energy form 0 keV to 10 keV were measured from a 6 kV atmospheric pressure plasma.

1.3.5 A dielectric microwave-microplasma interaction circuit

This work demonstrated a ~10 % change in transmission between two coupled cylindrical dielectric resonators when a nitrogen microplasma beam with a voltage of 1.1 kV, current of 9 mA, at a pressure of 50 Torr was introduced in the coupling gap of the two cylindrical resonators.

1.3.6 A dielectric near-field probe

This work developed a novel probe whose main volume consisted of a dielectric material for application in imaging electromagnetic field patterns. This probe was used as a diagnostic tool to map the microwave electric field patterns in the cylindrical dielectric resonators. This probe can be extended for use as a diagnostic tool in electromagnetic interference and compatibility applications.

1.3.7 Terahertz sensing for noninvasive real time monitoring of yeast fermentation

This work presented a system that used terahertz waves to quantify minute quantity of sugar (1.5 % by weight) and ethanol (0.3 % by weight) in water. This system was then extended to monitor the conversion of aqueous sugar into ethanol by yeast cells. This is a first time demonstration of terahertz waves for fermentation monitoring.

1.3.8 Near-fields probes for terahertz imaging of biological samples

This work developed three different near field probes for imaging biological samples. These near-field probes were designed such that the probes could confine terahertz fields at their tips. These strong fields effectively interact with samples in such a way that the probe response will be modified by the samples. The image of a sample was

then constructed by measuring the response at different position over the sample. With these near field probes, a mouse brain slice, a section of a plant leaflet, and a section of a bug wing were imaged at terahertz frequency.

1.3.9 MEMS-fabricated waveguides and resonators

With MEMS (Microelectromechanical system) fabrication processes (mainly Deep Reactive Ion Etching), rectangular waveguides in the WR 1.0 frequency range (0.75 THz to 1.1 THz) were fabricated. The characteristic dimension of these rectangular waveguide was 125 µm x 250 µm. The attenuation in these waveguides was ~ 1 dB/ mm. Waveguide-integrated rectangular cavity multimode resonators (resonators with multiple resonant frequencies and field patterns between 0.75 – 1.1 THz) were also fabricated. The characteristic dimensions of these resonators were 125 µm x 250 µm x 250 µm, and 250 µm x 250 µm x 250 µm.

1.3.10 A vanadium dioxide-integrated terahertz Fabry-Perot modulator

In this work, a new type of vanadium-dioxide based terahertz modulator was developed. In this modulator, vanadium dioxide was integrated in one of the two plates of a terahertz Fabry-Perot resonator. Vanadium dioxide is a Mott metal that can switch rapidly from an insulating state to a metallic state on the application of an external stimulus such as voltage, current, temperature, etc. In the developed modulator, current was injected into the vanadium dioxide in the resonator plate to change the terahertz reflection properties of the plate, and thus modulate the amplitude of the terahertz standing waves in the Fabry-Pérot modulator.

1.3.11 Terahertz-plasma interaction circuit

A number of plasma-terahertz interaction circuits were developed in this work. Different materials that could be easy machined, and would withstand the high temperature of the plasma beam while at the same time providing a good guidance for terahertz waves were studied. In addition, different geometry for these devices was studied. Candidate materials (geometry) for these circuits are Teflon (tube), quartz (slab), fused silica (rod), and fused silica (tube). These interaction devices also produced terahertz wave amplification.

1.3.12 Microfabricated terahertz traveling-wave-tube amplifier

This work presented a meandering terahertz waveguide that acted as an interaction circuit between the terahertz waves in the waveguide and an electron beam. The meandering waveguide was designed with theoretical equations and with computer simulations. Particle-in-cell simulation was used to determine the optimal parameters of an electron beam that can effectively interact with the terahertz wave and eventually amplify the wave. The meandering waveguides were microfabricated with MEMS fabrication processes. The measured amplification of this device was 12 dB at ~ 0.9 THz.

1.4 Research outline

Chapter 1 is an introduction to this work. It discusses the goal of this work: the development of terahertz amplifier circuits. This chapter gives the background literature on terahertz amplifier design. It also gives the interrelation between the main goal of this dissertation and the diversions that will occur later in this work. Chapter 2 gives the

background information about gas discharge, plasma, and electron beams. This background will be useful later in this work. Chapter 2 continues to present novel plasma circuits and applications of plasmas. Chapter 3 details the development of a dielectric klystron. This chapter first presents the design of dielectric resonator at gigahertz frequency then shows that dielectric resonators can be used as an efficient interaction circuit between gigahertz electromagnetic waves and plasma. This chapter proposed these resonators for use in terahertz dielectric klystron amplifiers. Chapter 4 is an introduction to the terahertz frequency band. After an overview of the peculiarities of the frequency band, this chapter demonstrates some new application of this frequency band in biosensing. Chapter 5 presents the design of a meandering waveguide slow wave structure for use as an interaction circuit between terahertz waves and an electron beam. This chapter presents the numerical simulation results for the design (cold and hot test simulation results) of these devices, the MEMS processes for fabricating these devices, and the characterization of these devices. Chapter 6 concludes this work.

1.5 References

[1] Lawrence Berkeley National Laboratory. [Online]. Available: *http://circe.lbl.gov/THzGap.html*

[2] Y. Lee, *Principles of terahertz science and technology*, vol. 170, New York, NY: Springer Science & Business Media, 2009.

[3] C. Sirtori, "Applied physics: Bridge for the terahertz gap," *Nature*, vol. 417, no. 6885, pp. 132-133, 2002.

[4] T. H. Lee, "Terahertz electronics: The last frontier," in *Proc. 44th European Solid State Device Research Conference (ESSDERC)*, 2014, pp. 30-34.

[5] D. Mittleman, *Sensing with terahertz radiation*, vol. 85, New York, NY: Springer, 2013.

[6] Microsoft academic graph. [Online]. Available: *http://research.microsoft.com/en-us/projects/mag/*

[7] National Physical Laboratory. [Online]. Available: *http://www.npl.co.uk/upload/pdf/091217_terahertz_naftaly.pdf*

[8] M. Tonouchi, "Cutting-edge terahertz technology," *Nature Photonics,* vol. 1, no. 2, pp. 97-105, 2007.

[9] P. H. Siegel, "Terahertz technology," *IEEE Transactions on Microwave Theory and Techniques,* vol. 50, no. 3, pp. 910-928, 2002.

[10] C. Armstrong, "The truth about terahertz," *IEEE Spectrum,* vol. 9, no. 49, pp. 36-41, 2012.

[11] A. Redo-Sanchez and X. Zhang, "Terahertz science and technology trends," *Selected Topics in Quantum Electronics, IEEE Journal of,* vol. 14, no. 2 pp. 260-269, 2008.

[12] A. J. Huber, F. Keilmann, J. Wittborn, J. Aizpurua, and R. Hillenbrand, "Terahertz near-field nanoscopy of mobile carriers in single semiconductor nanodevices," *Nano Letters,* vol. 8, no. 11, pp. 3766-3770, 2008.

[13] K. E. Kreischer, J. C. Tucek, M. A. Basten, and D. A. Gallagher, "Integrated 220 GHz Source Development HiFIVE Final Report," Northrop Grumman Corp., Baltimore, MD, 2014.

[14] K. E. Kreischer, J. C. Tucek, M. A. Basten, and D. A. Gallagher, "220 GHz power amplifier testing at Northrop Grumman," in *Vacuum Electronics Conference (IVEC), 2013 IEEE 14th International,* 2013, pp. 1-4.

[15] J. C. Tucek, M. A. Basten, D. A. Gallagher, K. E. Kreischer, R. Lai, V. Radisic, K. Leong, and R. Mihailovich, "A 100 mW, 0.670 THz power module," in *Vacuum Electronics Conference (IVEC), 2012 IEEE 13th International*, 2012, pp. 31-32.

[16] J. C. Tucek, M. A. Basten, D. A. Gallagher, and K. E. Kreischer, "Testing of a 0.850 THz vacuum electronic power amplifier," in *Vacuum Electronics Conference (IVEC), 2013 IEEE 14th International*, 2013, pp. 1-2.

[17] J. C. Tucek, D. Gallagher, K. Kreischer, and R. Mihailovich, "A compact, high power, 0.65 THz source," in *Vacuum Electronics Conference (IVEC), 2008 IEEE 9th International*, 2008, pp. 16-17.

[18] A. S. Gilmour, *Klystrons, traveling wave tubes, magnetrons, crossed-field amplifiers, and gyrotrons*, Norwood, MA: Artech House, 2011.

[19] Y. Shin, L. R. Barnett, and N. C. Luhmann Jr., "Strongly confined plasmonic wave propagation through an ultrawideband staggered double grating waveguide," *Applied Physics Letters*, vol. 93, no. 22, p. 221504, 2008.

[20] Y. Shin, A. Baig, L. R. Barnett, N. C. Luhmann Jr., J. Pasour, and P. Larsen, "Modeling investigation of an ultrawideband terahertz sheet beam traveling-wave tube amplifier circuit," *Electron Devices, IEEE Transactions on*, vol. 58, no. 9, pp. 3213-3218, 2011.

[21] Y. Shin, L. R. Barnett, D. Gamzina, N. C. Luhmann Jr., M. Field, and R. Borwick, "Terahertz vacuum electronic circuits fabricated by UV lithographic molding and deep reactive ion etching," *Applied Physics Letters*, vol. 95, no. 18, p. 181505, 2009.

[22] Y. Shin, A. Baig, L. R. Barnett, W. Tsai, and N. C. Luhmann Jr., "System design analysis of a 0.22-THz sheet-beam traveling-wave tube amplifier," *Electron Devices, IEEE Transactions on*, vol. 59, no. 1, pp. 234-240, 2012.

[23] A. Baig, D. Gamzina, R. Barchfeld, C. Domier, L. R. Barnett, and N. C. Luhmann Jr., "0.22 THz wideband sheet electron beam traveling wave tube amplifier: Cold test measurements and beam wave interaction analysis," *Physics of Plasmas (1994-present)*, vol. 19, no. 9, p. 093110, 2012.

[24] Y. Shin, A. Baig, R. Barchfeld, D. Gamzina, L. R. Barnett, and N. C. Luhmann Jr., "Experimental study of multichromatic terahertz wave propagation through planar micro-channels," *Applied Physics Letters*, vol. 100, no. 15, p. 154103, 2012.

[25] Y. Shin, J. Zhao, L. R. Barnett, and N. C. Luhmann Jr., "Investigation of terahertz sheet beam traveling wave tube amplifier with nanocomposite cathode," *Physics of Plasmas (1994-present)*, vol. 17, no. 12, p. 123105, 2010.

[26] A. Baig, D. Gamzina, M. Johnson, C. W. Domier, A. Spear, L. R. Barnett, N. C. Luhmann Jr., and Y. Shin, "Experimental characterization of LIGA fabricated 0.22 THz TWT circuits," in *Vacuum Electronics Conference (IVEC), 2011 IEEE 12th International*, 2011, pp. 275-276.

[27] D. Gamzina, R. Barchfeld, L. R. Barnett, N. C. Luhmann Jr., and Y. Shin, "Nano CNC milling technology for terahertz vacuum electronic devices," in *Vacuum Electronics Conference (IVEC), 2011 IEEE 12th International*, 2011, pp. 345-346.

[28] A. Baig, D. Gamzina, R. Barchfeld, J. Zhao, I. Domier, A. Spear, L. R. Barnett, and N. C. Luhmann Jr., "220 GHz ultra wide band TWTA: Nano CNC fabrication and RF testing," in *Vacuum Electronics Conference (IVEC), 2013 IEEE 14th International*, 2013, pp. 1-2.

[29] Y. Shin, L. R. Barnett, and N. C. Luhmann Jr., "Phase-shifted traveling-wave-tube

circuit for ultrawideband high-power submillimeter-wave generation," *Electron Devices, IEEE Transactions on*, vol. 56, no. 5, pp. 706-712, 2009.

[30] Y. Shin, L. R. Barnett, A. Baig, N. C. Luhmann Jr., J. Pasour, and P. Larsen, "Numerical modeling analysis of 0.22 THz sheet beam TWT circuit," in *Vacuum Electronics Conference (IVEC), 2011 IEEE 12th International*, 2011, pp. 139-140.

[31] R. Barchfeld, D. Gamzina, A. Baig, L. R. Barnett, and N. C. Luhmann Jr., "Nano CNC milling of two different designs of 0.22 THz TWT circuits," in *Vacuum Electronics Conference (IVEC), 2012 IEEE 13th International*, 2012, pp. 549-550.

[32] C. Paoloni, A. Carlo, F. Bouamrane, T. Bouvet, A. J. Durand, M. Kotiranta, V. Krozer, S. Megtert, M. Mineo, and V. Zhurbenko, "Design and realization aspects of 1-THz cascade backward wave amplifier based on double corrugated waveguide," *Electron Devices, IEEE Transactions on*, vol. 60, no. 3, pp. 1236-1243, 2013.

[33] C. Paoloni, M. Mineo, A. Carlo, A. J. Durand, V. Krozer, M. Kotiranta, F. Bouamrane, T. Bouvet, and S. Megtert, "1-THz cascade backward wave amplifier," in *Vacuum Electronics Conference (IVEC), 2012 IEEE 13th International*, 2012, pp. 237-238.

[34] C. Paoloni, A. Carlo, F. Brunetti, M. Mineo, G. Ulisse, A. Durand, V. Krozer, M. Kotiranta, A. de Rossi, D. Dolfi, and P. Legagneux, "A European project on vacuum tube amplifiers for THz amplification," in *The 5th UK/Europe-China Workshop on Millimeter Waves and Terahertz Technologies*, 2012.

[35] M. Mineo and C. Paoloni, "Improved corrugation cross-sectional shape in terahertz double corrugated waveguide," *Electron Devices, IEEE Transactions on*, vol. 59, no. 11, pp. 3116-3119, 2012.

[36] S. Bhattacharjee, J. H. Booske, C. L. Kory, D. W. Van der Weide, S. Limbach, S. Gallagher, J. D. Welter, M. R. Lopez, R. M. Gilgenbach, R. L. Ives, M. E. Read, "Folded waveguide traveling-wave tube sources for terahertz radiation," *Plasma Science, IEEE Transactions on*, vol. 32, no. 3, pp. 1002-1014, 2004.

[37] J. H. Booske, R. J. Dobbs, C. D. Joye, C. L. Kory, G. R. Neil, G. Park, J. Park, and R. J. Temkin, "Vacuum electronic high power terahertz sources," *Terahertz Science and Technology, IEEE Transactions on*, vol. 1, no. 1, pp. 54-75, 2011.

[38] G. O. Vela, "Terahertz backward wave oscillator circuits," PhD dissertation, Dept. Elect. & Comp. Eng., The University of Utah, Salt Lake City, UT, 2010.

[39] G. O. Vela, M. S. Miller, R. W. Grow, and J. M. Baird, "Terahertz backward-wave oscillators with photonic crystal waveguides," in *Vacuum Electronics Conference, 2006 Held Jointly with 2006 IEEE International Vacuum Electron Sources., IEEE*

International, 2006, pp. 425-426.

[40] A. W. Trivelpiece and R. W. Gould, "Space charge waves in cylindrical plasma columns," *Journal of Applied Physics*, vol. 30, no. 11, pp. 1784-1793, 1959.

[41] R. P. H. Chang and M. Porkolab, "Experimental observation of nonlinear Landau damping of plasma waves in a magnetic field," *Physical Review Letters*, vol. 25, no. 18, p. 1262, 1970.

[42] O. Fawole and M. Tabib-Azar, "A terahertz Fabry-Perot modulator using charge injection-induced insulator-metal transition in vanadium dioxide," in *Wireless Symposium (IWS), 2016 IEEE MTT-S International*, 2016, pp. 1-4.

[43] O. Fawole and M. Tabib-Azar, "Multimode rectangular cavity terahertz resonators," in *Wireless Symposium (IWS), 2016 IEEE MTT-S International*, 2016, pp. 1-4.

CHAPTER 2

PLASMA AND ELECTRON BEAMS: SOURCES AND CIRCUITS

2.1 Introduction

One of the main goals of this work is to develop an electromagnetic amplifier circuit that converts the energy of plasma (electrons and ions) or electrons into electromagnetic energy. Therefore, this chapter will present the results on some fundamental studies on plasma and electrons. First, this chapter will present a study of plasma sources and circuits. The plasmas used in these experiments were derived from gas discharges. A gas discharge occurs when a high voltage is applied between two electrodes in a gas environment at some gas pressure. The applied high voltage initiates and sustains the breakdown of the gas into electron and ions. Hence, the plasma studied in this chapter consisted of electrons, ions, and some seed gas molecules. This chapter investigates the interaction of this type of plasma with static, slowly varying fields, and with dielectric materials. Moreover, the knowledge gained from this interaction study would be used to develop some new plasma-based switches, actuators, and sensors. In addition, this chapter presented the design of an electron gun that employed a thermionic emitter (heated tungsten filament) to generate an electron beam.

The understanding of charged particles gained in the section will be used in developing wave-particle interactions circuits (electromagnetic wave amplifier) that will be presented later in this dissertation.

2.2 DC plasma properties

Plasma is defined as a quasineutral mix of ions and electrons (and some gas molecules) that exhibit collective behavior [1]. A DC gas discharge, formed by breaking down a gas into electrons and ions with a high voltage applied between two electrodes, is a common source of plasma. The general schematic of a setup for creating a DC gas discharge plasma is shown in Fig. 2.1.

The breakdown of a gas into charged particles occurs when seed electrons (background electrons from cosmic ray ionization or electrons that are extracted from the metallic electrodes via field emissions) are accelerated by electric field in the interelectrode gap to energies sufficient to cause ionization of the gas atoms/molecules into electrons [2]. The gas breakdown process is an avalanche process in which the initial seed electrons ionize the gas to create more seed electrons that later produce more gas ionization, and so on.

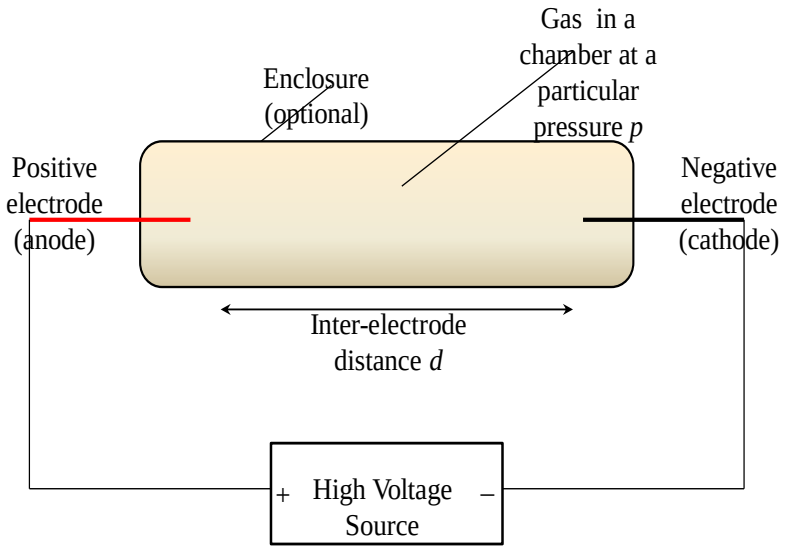

Fig. 2.1. General schematic of setup for creating a DC gas discharge plasma.

The discharge current in a gas discharge is given by the relation [2]:

$$i = i_0 \frac{e^{\alpha d}}{1 - \gamma[e^{\alpha d} - 1]} \tag{2.1}$$

where i_0 is the initial current flowing in the interelectrode gap, α is the ionization coefficient (the number of ionization events performed by an electron over a 1 cm path along the field), d is the interelectrode gap distance, and γ is the effective secondary emission of the cathode.

For positive values of the denominator in (2.1), the discharge current is not self-sustaining because an initial current i_0 is needed to obtain a discharge current i. If the interelectrode voltage V is increased such that the denominator equals 0 (because α generally increases with V), then a nonsustaining discharge occurs. A denominator value of zero means that a finite value of i_0 is not necessary to obtain a discharge current i. It is worthy to note that a negative value of the denominator is nonphysical as it is equivalent to a nonstable gas discharge.

The voltage at which the discharge becomes self-sustaining is referred to as the ignition potential, V_t. V_t is a function of the gas pressure p and the interelectrode gap distance d. In gaseous electronics, the plots that present V_t as a function of the product pd are called Paschen curves. The general form of the Paschen curve is given in Fig. 2.2. This curve shows that a high voltage is required to break down a gas at high pd values. The traditional Paschen curve also shows that decreasing the pd values leads to a lower breakdown voltage V_t until a V_t minimum is reached after which decreasing pd leads to an increase in V_t. However, it has recently been shown that at very small interelectrode distances, deviation from the traditional Paschen curves occurs [3], where the gas

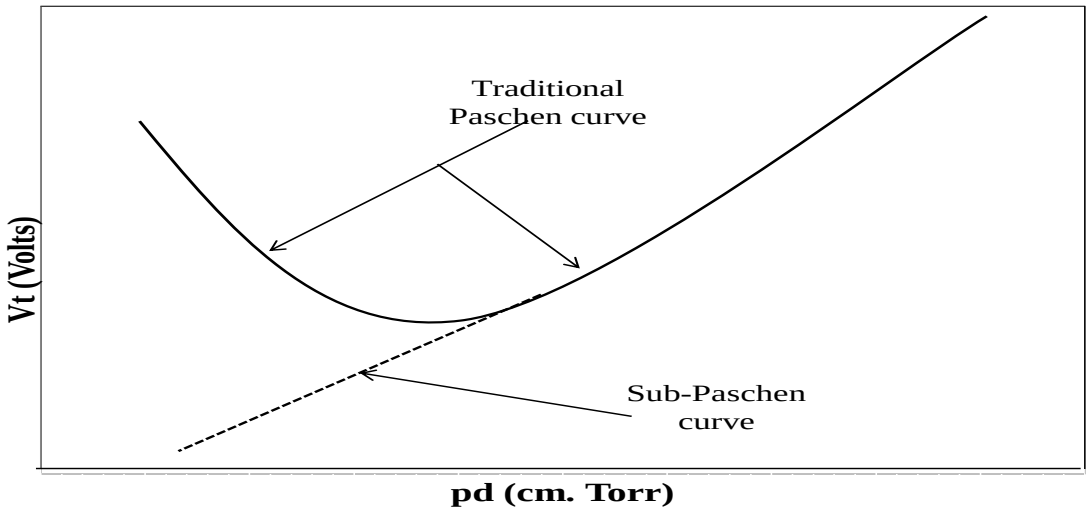

Fig. 2.2. A general Paschen curve that shows the variation in the breakdown voltage (V_t) as a function of interelectrode distance-pressure product.

discharge process operates in sub-Paschen regime annotated in Fig. 2.2.

The general voltage-current (*v-i*) characteristic of a gas discharge is shown in Fig. 2.3. Depending on the operating regime of the curve, different types of discharges occur between the electrodes. The position where a load-line (due to an external resistance in discharge circuit) intercepts the *v-i* curve of the discharge determines the type of discharge that will result.

The type of discharge that was used in this work was the stable DC glow discharge. The DC glow discharge is inhomogeneous along its length, with different regions having different electron and ion density, electron and ion current, potentials, and electric fields. The distribution of these parameters at different position in a generic glow discharge is given in Fig. 2.4 [2]. In this figure, it is seen that the positive column of the glow discharge has equal electron and ion density. This region is the plasma region in the glow discharge. DC glow discharge can occur from low gas pressures to above

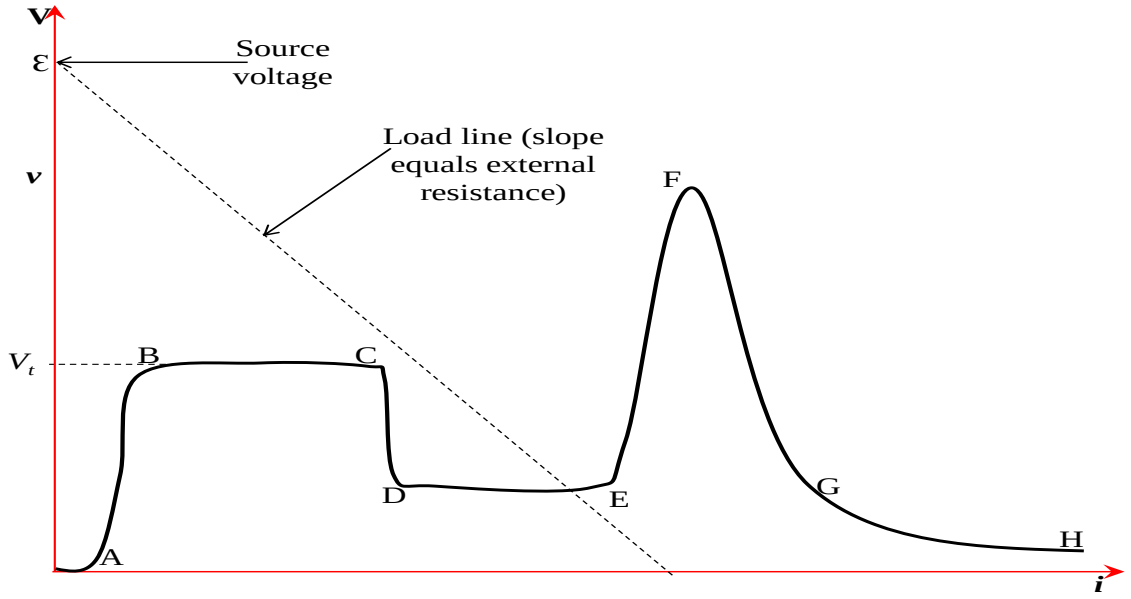

Fig. 2.3. *v-i* curve of a gas discharge showing the different possible types of discharge modes (A) region of non-self-sustaining discharge (BC) Townsend dark discharge (DE) normal glow discharge (EF) abnormal glow discharge (FG) transition to arcing (GH) arc.

atmospheric gas pressure [3,4].

In the following sections, we will explore the spatially inhomogeneous electronic and ionic properties of plasma (henceforth, we shall refer to the gas discharge as plasma beam) to develop new circuits that use the static and the slowly varying fields to control the behavior of plasma beams. The knowledge gained from this circuit design will be used later in this work to design high frequency wave-plasma interaction circuits.

2.3 Interaction of DC plasma beam with static electric fields

As shown in Fig. 2.4, the cathode of the plasma beam has a high ion charge density while the anode has a high electron charge density. This localized space charge density contrasts the quasineutral state of the middle region of the plasma. Therefore, a relatively small electric field can be applied at the space charge regions close to either of the two plasma electrodes to create a large effect (actuation).

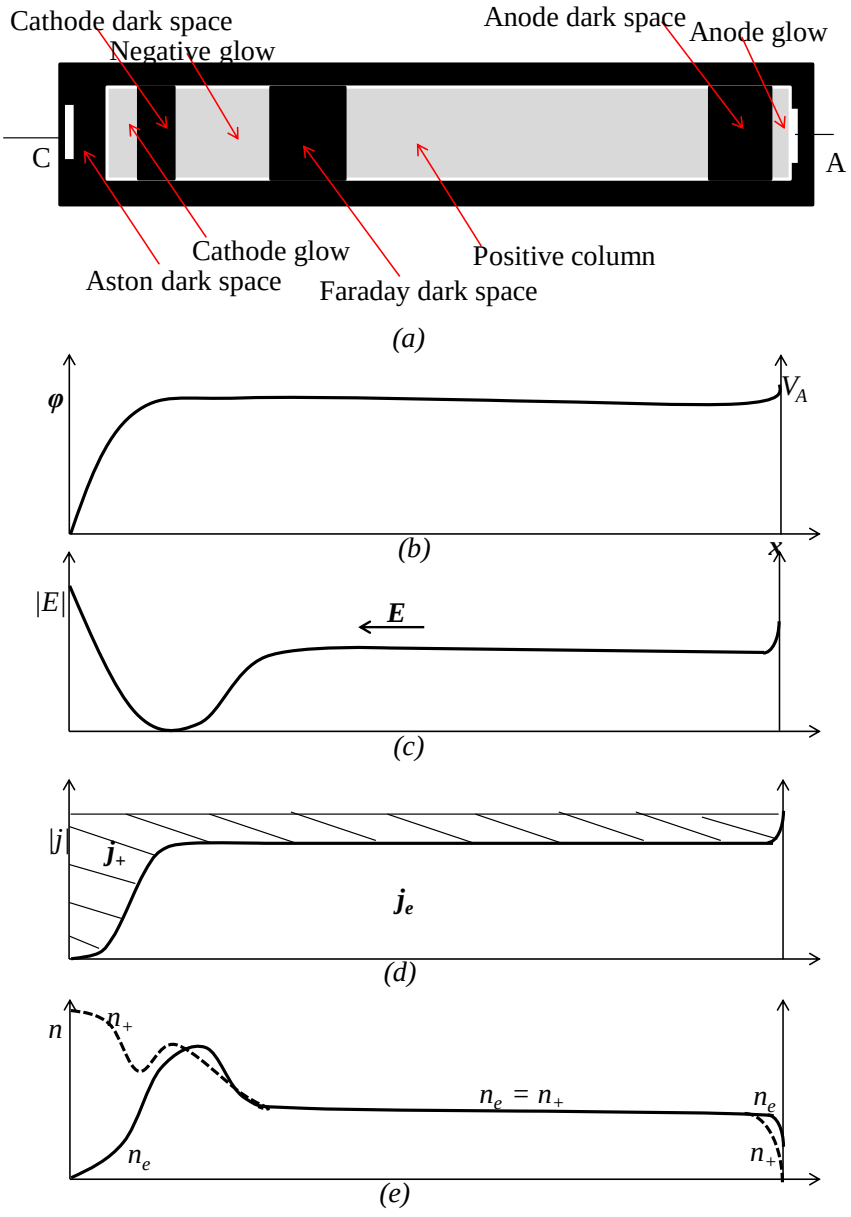

Fig. 2.4. Regions of a glow discharge. (a) A spatially inhomogeneous normal glow discharge and the distribution of its (b) potential φ (c) electric field E (d) electronic j_e and ionic j_+ current densities (e) electronic and ionic charge densities n_e and n_+.

In addition, an electric field can be used to actuate the plasma beam at other plasma locations, as long as a space charge exists at that location. However, theoretically, a smaller electric field will be required to modify the plasma if the electric field is applied closer to the electrodes.

In the experimental setup shown in Fig. 2.5, the shape of a longitudinal plasma jet was modified locally by applying a transverse electric field at a position along the jet. This actuation electric field interacted with the space charges in the plasma jet to produce a macroscopic change in the beam. The plasma jet was created in open air between two electrodes separated by 7 cm. Helium gas with a flow velocity of ~1.2 m/s was flowed from one of the electrodes and a voltage of 7 kV was applied between the two electrodes. The plasma current on gas discharge was about 1 mA. The electrodes for modifying the plasma were placed transverse to the length of the plasma jet as shown in Fig. 2.5. The interelectrode gap between these actuation electrodes was ~ 1 cm. This experimental setup was designed such that the polarity of the plasma electrodes could be easily reversed. This would ease the study the interaction between the beam and the actuation electric field for the case when the gas flow was from the anode, and when the gas flow was from the cathode. Figure. 2.6a shows the plasma-field interaction in a configuration in which the helium gas flowed out from the cathode for the cases of different polarities of an actuation voltage of 600 V. The figure also shows the case of no applied actuation. Figure. 2.6b shows the configuration in which the helium gas flowed out from the anode, for the three cases of a 700 V actuation voltage as for the previous configuration. The insets in the middle of these figures are zoom-ins on the actuation region. These zoom-in figures clearly show that the plasma locally deflects away from the negative actuation

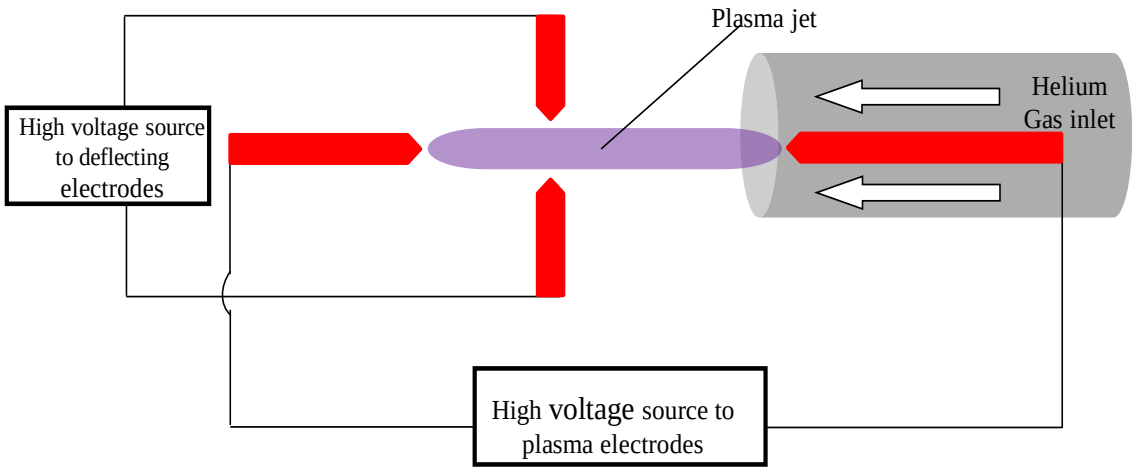

Fig. 2.5. Schematic of setup to create an atmospheric pressure plasma jet and to demonstrate the interaction of an electric field with the plasma jet. In this setup, the polarities of the plasma electrodes can be easily reversed so that the plasma jet can flow from the anode or the cathode. In addition, the polarity of the actuation electrodes can be easily reversed.

electrode to produce a notch around the actuation region.

Interestingly, it can be observed from the zoomed-in figure that the location of the local maximum deflection of the plasma does not coincide with the location of maximum applied transverse field. This is because the resultant field acting on the plasma is the combination of the transverse actuation field and the longitudinal plasma fields. Furthermore, the plasma notches bent in a direction that indicates that the local deflection of the plasma is due to the effect of the resultant electric field on the plasma electrons. The deflection is always towards the positive electrode. This means the negative electrons in the plasma move towards the positive electrodes, and these electrons drag along the reluctant ions. Hence, the applied electric field interacted directly with the plasma electrons.

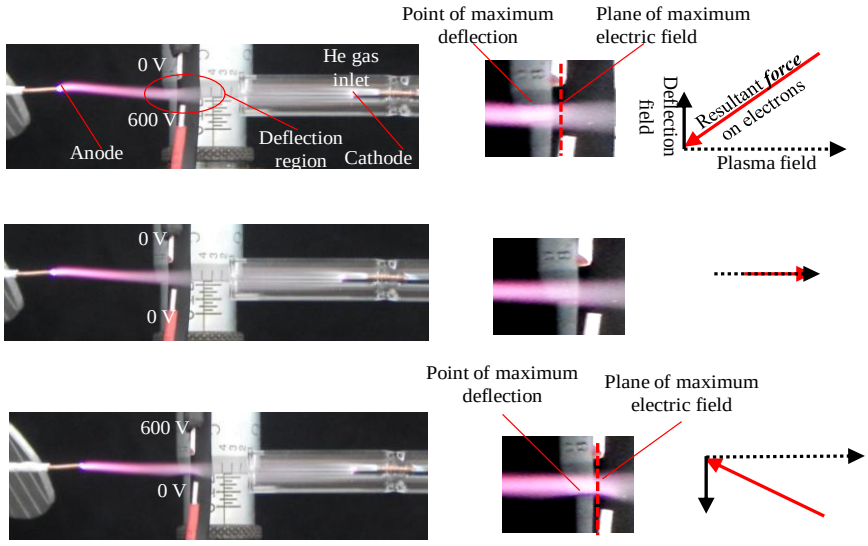

(a)

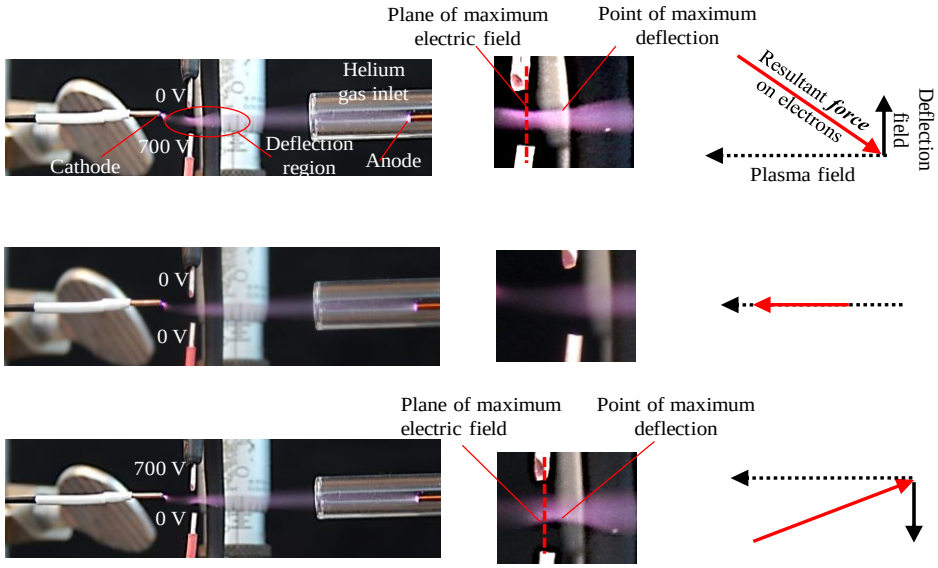

(b)

Fig. 2.6. Study of interaction between an atmospheric plasma jet and static electric field of different polarities (including the unpolarized case). The degree of local deflection depended on the amount of space charge present in the region between the deflection electrodes and the deflection field. The middle figures are zoomed to the deflection region. The vector figures illustrate how observed deflection of the plasma jet is due to the interaction between plasma fields (internal and external) and the plasma electron space charge. (a) configuration with gas flow from the cathode. (b) configuration with gas flow from anode.

2.4 A plasma-beam electric switch

The insight gained from the experiment of the last section, and from some other related experiments, was used to design a plasma electric switch. The switch was designed to have its actuation electrodes close to the plasma beam electrodes. As illustrated in Fig. 2.4e, there is a relatively high space charge density at the plasma electrodes. Since the actuation electrodes are close to the plasma electrodes (essentially at a plasma source), it is reasonable to expect that the effect of the actuation electric field would propagate down the whole length of the plasma beam.

In Fig. 2.7, the plasma beam electric switch is shown in Fig. 2.7a. This device has one cathode and two anodes. This device operated in helium gas at atmospheric pressure. Two actuation electrodes were placed at the plasma cathode, as shown in Fig. 2.7a. The closeness of this electrode to the cathode means that actuation field of this electrode can interact with the space charge at the plasma cathode. With no actuation voltage, the plasma current in this device was split between the two anodes. With a relatively positive voltage on the left actuation electrode, the plasma deflected towards anode 1 and this increased the current flowing between the cathode and anode 1. On the other hand, application of a positive actuation voltage to the deflection electrode 2 increased the current flowing between the cathode and anode 2.

In this switch, the two anodes had a common terminal and the interelectrode distance between the anodes and the cathode was 5 mm. The voltage applied between the anodes and the cathode terminals was ~4 kV. The plasma current was ~0.5 mA. The distance between the actuation electrodes was 4 mm. Figure 2.7b shows the case when 3.7 kV was applied to deflection electrode 1 relative to deflection electrode 2.

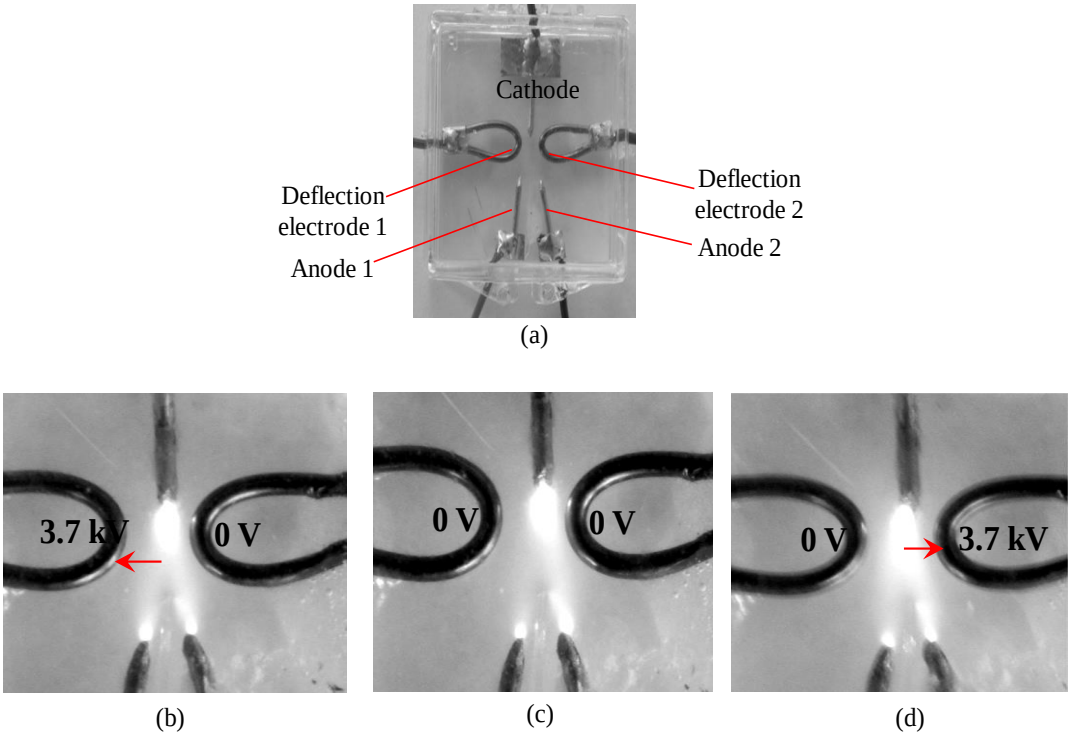

Fig. 2.7. A plasma electric switch that exploits the high space charge at the plasma cathode to electrically switch the plasma current between two anodes. The plasma brightness close to the positive deflection electrodes increases as a result of the interaction between the external field and the electron components of the plasma.

As seen from the intensity of the plasma beam glow, the leg of the plasma close to the positive deflection electrode increased in brightness. Figure 2.7c shows the case in which no deflection voltage was applied. Fig. 2.7d shows the situation in which the deflection electrode 2 is positive relative to the deflection electrode 1 and thus the leg of the plasma close to the deflection electrode 2 increased in brightness.

It can be seen from Fig. 2.7c that the actuation fields of the switch interacted directly with the plasma electrons as in the experimental setup of the previous section. Furthermore, it can be seen that this relay switch is nonsymmetric. The intensity of the plasma is uneven in the two legs of the unexcited device. This is due to fabrication errors. This limited the current switching capability of this device.

Furthermore, by comparing Figs. 2.7b and 2.7d, it can be seen this switch has a large leakage current suggesting that the effect of the actuation electrode is more localized than desired. However, if this device is designed with a more precise fabrication technique, their switching performance might be improved and it could be adapted for switching high currents.

2.5 Interaction of DC plasma with low frequency electric fields

In the experiment illustrated in Fig. 2.8, the interaction of a plasma beam with low-frequency electromagnetic pulses was studied with the aim of finding how fast a plasma beam could respond to rapidly varying longitudinal fields. Another goal of the illustrated experiment was to find the mean free path of plasma particles (a Shockley-Hayes experiment for plasma [5]). In this experiment, helium gas was continuously flowed into a glass tube chamber, while at the same time a rotary pump was used to evacuate the glass tube such that the helium pressure in the tube was maintained at ~100 Torr. A metallic double mesh was inserted inside the tube between the plasma electrodes of this setup. The mesh served to diffuse the helium gas flow so that the flow would not perturb the deflection of the plasma by the actuator electrodes. A copper ring was then placed at a location around the glass tube. An actuation signal was applied between this ring electrode and the mesh inside to compress the plasma longitudinally. This longitudinal actuation contrasts the transverse actuations employed in the last two experiments. At another location on the glass tube, a pair of copper ring electrodes were placed. These electrodes, which would be connected to an oscilloscope, were used to detect the response of the plasma on longitudinal actuation. The separation between the actuator electrodes and the response electrodes was 4 cm.

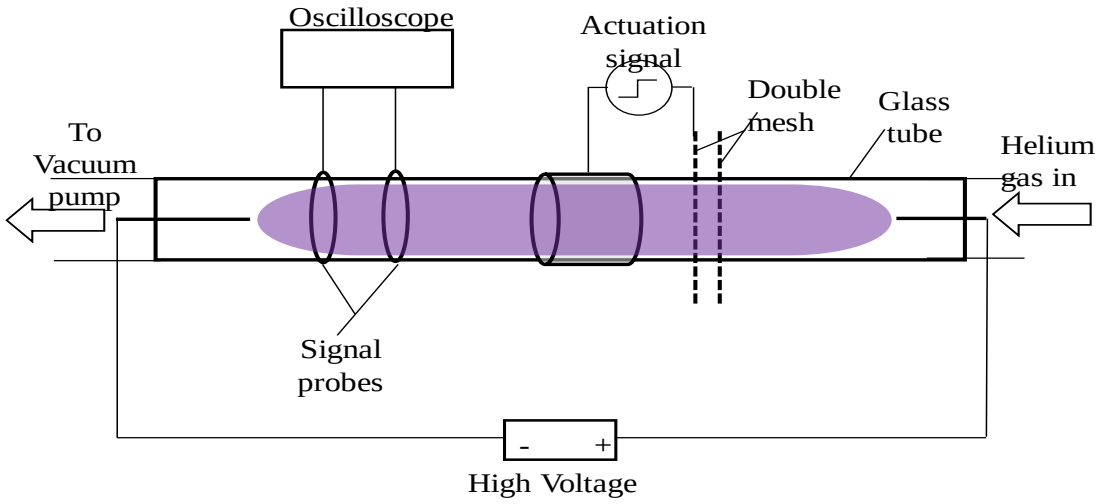

Fig. 2.8. Schematic of experimental setup to measure the response of plasma to electric pulse excitation.

Figure 2.9a shows the experimental setup, and Figs. 2.9b and 2.9c show the plasma before and under a DC actuation. The actuation electrodes produced a longitudinal electric field on the plasma beam. The effect is seen in Fig. 2.9c where the striations in the plasma have been compressed longitudinally. Striations are strata of alternating light and dark areas that occur in the DC discharge due to high frequency ionization oscillations in the plasma [2, 6]. In this experiment, the plasma voltage was 4 kV and the amplitude of the actuator voltage was 2.5 kV.

In addition to the macroscopic manifestation of the longitudinal plasma actuation of Fig. 2.9b, the effect of the actuation downstream of the plasma beam could be detected with the sensing electrodes. Fig. 2.10 shows the signals recorded by the oscilloscope connected to the sensing electrodes for different actuation pulse repetition rates. From these figures, it could be observed that beyond an actuation pulse repetition rate of 40 Hz, the plasma did not respond appreciable to the excitation pulses. This irresponsiveness of the plasma was due to the bulk inertial of the plasma beam.

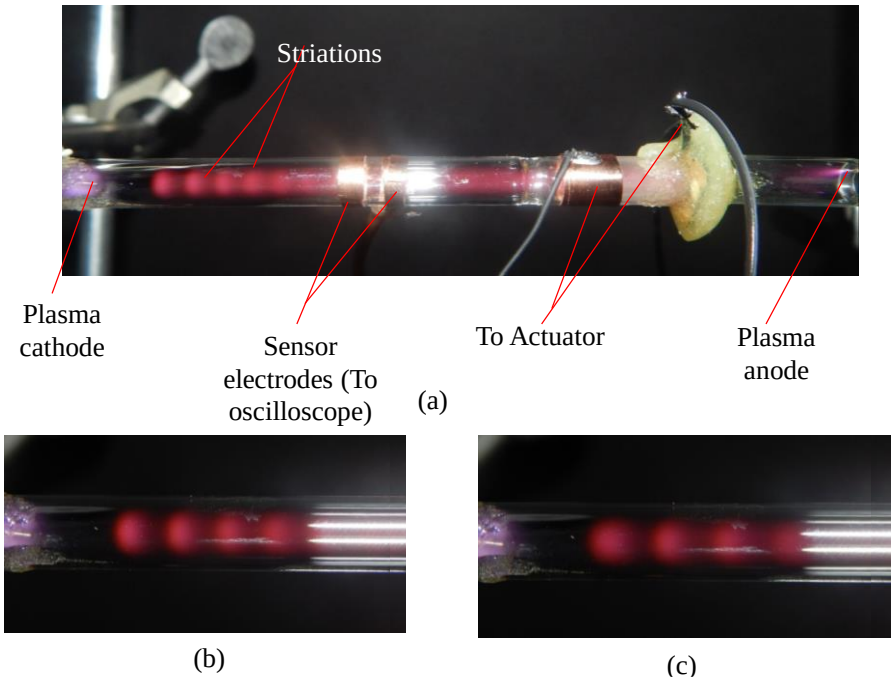

Fig. 2.9. Plasma actuation by electric pulses. (a) Experimental setup to observe plasma response to longitudinal electric pulses. (b) with no excitation, the striations are compact (c) with a constant DC voltage at the actuator electrodes, the striation expands.

Furthermore, it was difficult to extract the mean free path of the plasma beam by comparing the rise times of the excitation and response signals because of the noise introduced in the response signals by the plasma power supply.

2.6 Interaction of DC plasma with magnetic fields

Next, a device was designed to study the interaction between DC plasma and static magnetic field. The schematic for this device, with its experimental setup is shown in Fig. 2.11. The planar device consisted of a ring plasma anode and a pin plasma cathode. Plasma was created in atmospheric air by applying a high voltage between the anode and the cathode. The device was placed over a permanent magnet of magnetic flux density of 0.5 T. Figure 2.12 shows the deflection of the plasma for different polarities of the magnetic field. The inset to the right of the figure shows the magnetic field direction,

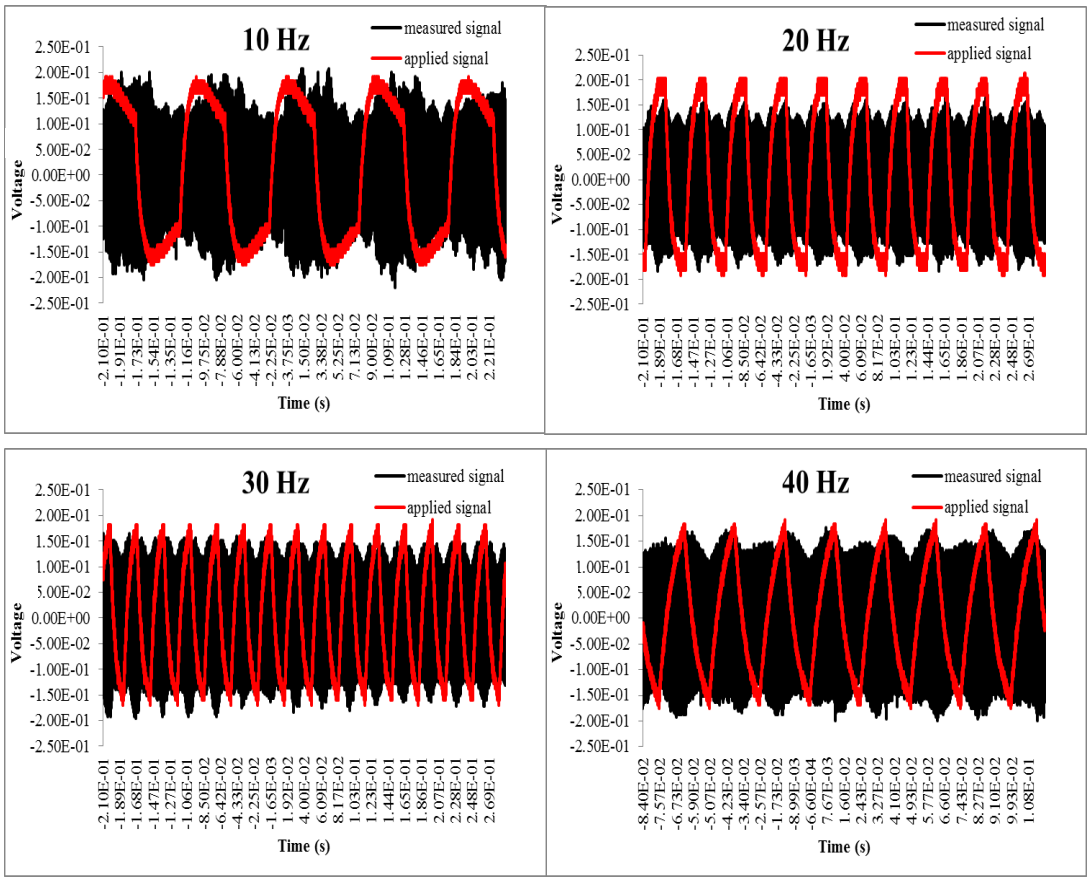

Fig. 2.10. Plasma actuation pulses and plasma response signals for different actuation pulse repetition rates. Beyond an actuation pulse rate of 40 Hz, the plasma did not show appreciable response to the excitation. The scale for the voltage axis is arbitrary.

the direction of electron and ion drift in the plasma, and the direction of the magnetic force that deflects the plasma beam. The observed deflection of the plasma beam obeys the Lorentz force law. The inset shows that electrons in the plasma drift from the cathode to the anode with velocity u_e, crossing the applied longitudinal magnetic field B lines. The electrons experience an angular force that depends on the direction of their drift, their charge and the direction of the magnetic field lines. The drifting ions also experienced similar forces and the sense of the force experienced by the ions will be the same for electrons since the drift velocity u_i of ions is oppositely directed to that of the

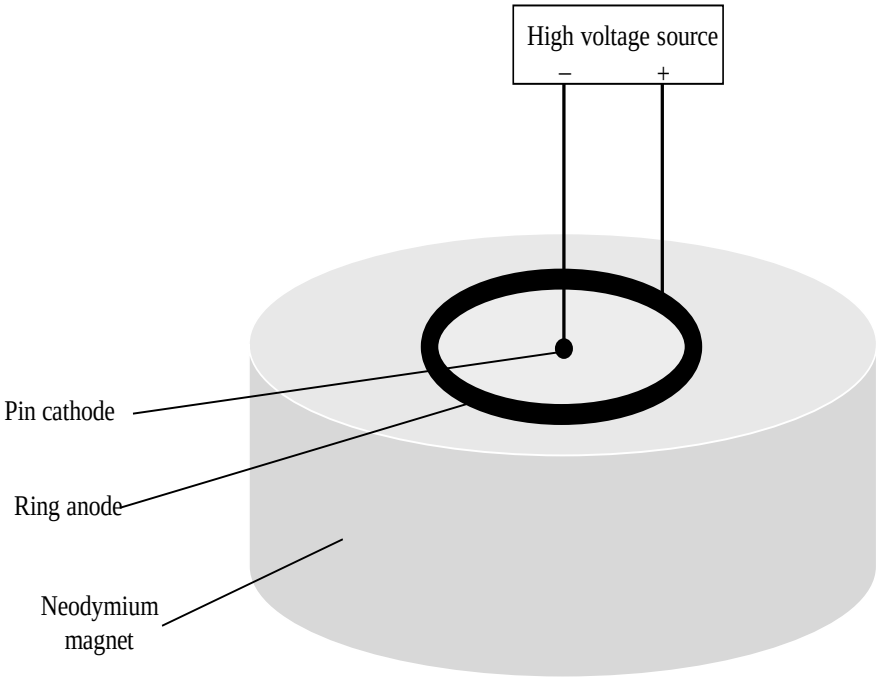

Fig. 2.11. Schematic of device and setup to demonstrate interaction of static magnetic fields with plasma.

electrons. The superposition of these forces deflects the plasma beam. The observed steady state deflection of the plasma beam for a constant magnetic field of 0.5 Tesla was about 50 degrees for both clockwise and counterclockwise deflection.

The deflection of the plasma beam is limited by the imperfection of the device (nonsymmetry, edges of imperfect smoothness), by frictional forces on the plasma beam due to gas pressure, and imperfection of the plasma beam (the plasma beam is more of a spark in air than it is a stable glow discharge).

Therefore, to strongly make plasma interact with a magnetic field, this device was fabricated with more precision with microfabrication techniques. The microfabricated device will be presented in the next section.

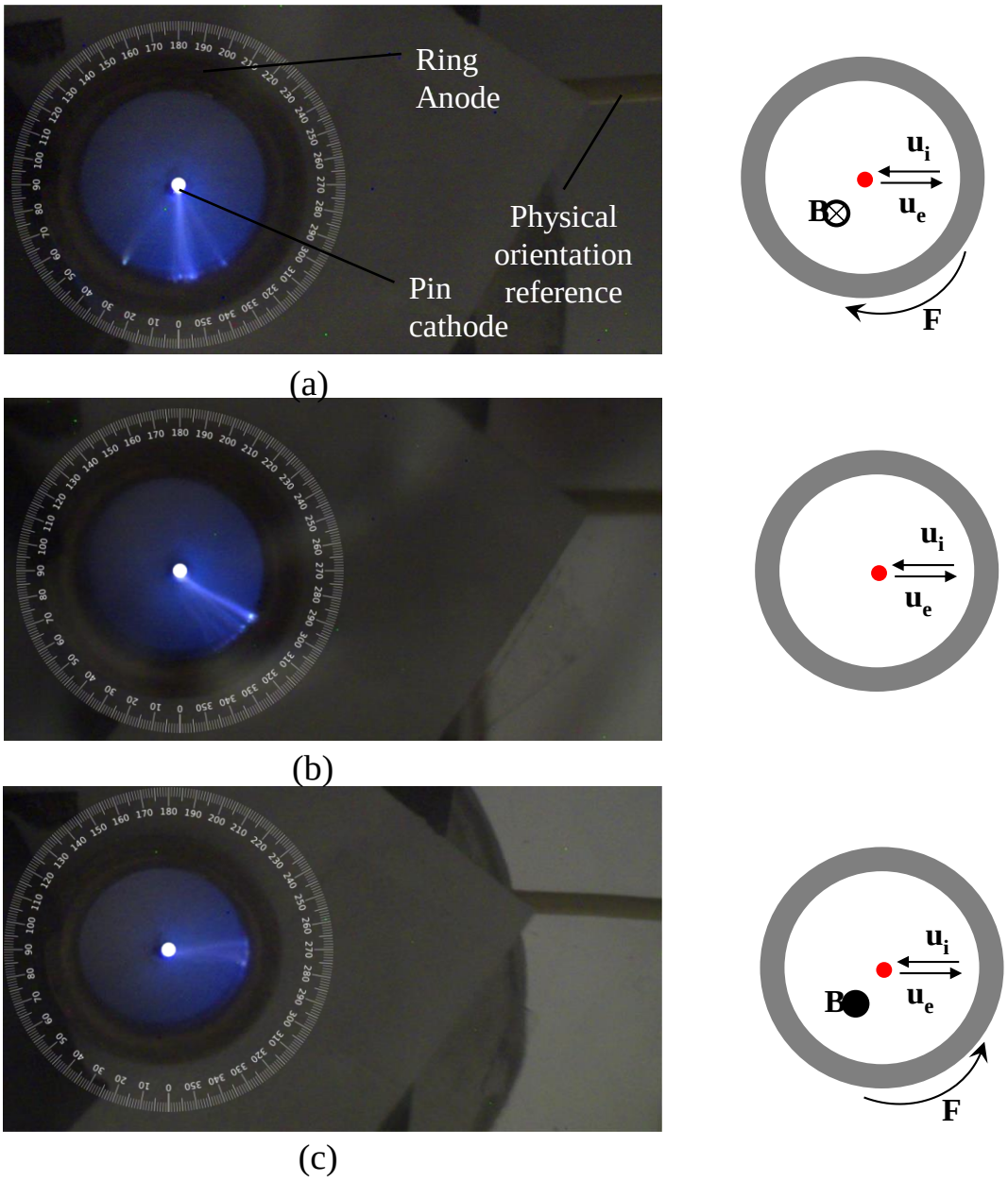

Fig. 2.12. Top view of device and experimental setup of Fig. 2.11. The pin cathode ring anode device is placed on a 0.5 T magnet. The wire in the background in each figure serves as a physical orientation reference. The overlaid compass gives a measure of the angular deflection of the plasma by the magnetic field in degrees. The schematic to the right of the figure illustrates the direction of electron (u_e) and ion drift (u_i), the direction of the magnetic field (B), and the sense of the resulting Lorentz force on the plasma beam (F). (a) magnetic field lines into the page (b) no magnetic field (c) magnetic field lines out of the page.

2.7 A circular microplasma magnetic field sensor

As mentioned in the previous section, lack of symmetry, imperfect metallic edges, and imperfection of the plasma are some of the factors that weakened the response of the plasma in the device presented in the previous section to an external magnetic field. Therefore, with precision microfabrication techniques, a smoother and more symmetric version of the device in Fig. 2.12 was microfabricated. The device with its experimental setup is shown Fig. 2.13. This device consisted of a 2 mm diameter center pin electrode that serves as the anode and a 6 mm outer diameter ring electrode that serves as the cathode. The device electrodes were defined by electrochemically depositing 60 μm-thick copper on a glass substrate. A thin 50 μm diameter copper wire was wire bonded from the center of the pad to a copper strip electrical terminal. The ring electrode was also wire bonded to a terminal. To record the angular frequency of the beam when it moves along the rim of the cathode under the influence of a magnetic field, a capacitive sensor was integrated on the outer ring cathode by first placing a layer of Polyvinyl Chloride (PVC) dielectric on a section of the ring, and then placing a layer of copper strip on the PVC. This copper strip will be connected to an oscilloscope to record the angular frequency of the beam. The device was then placed inside a chamber that allowed for the supply of different gases needed to create the discharge that produces the plasma beam [7]. Fig. 2.14 shows snapshots of the rotating plasma for three different inert gases. Fig. 2.15 shows the angular rotation frequency of the helium micro plasma magnetic field sensor.

2.8 A physical model for the rotating glow discharge

The following is a derivation of the equations to model a rotating glow discharge. Within the length of a glow discharge, electrons drift towards the anode, and ions drift

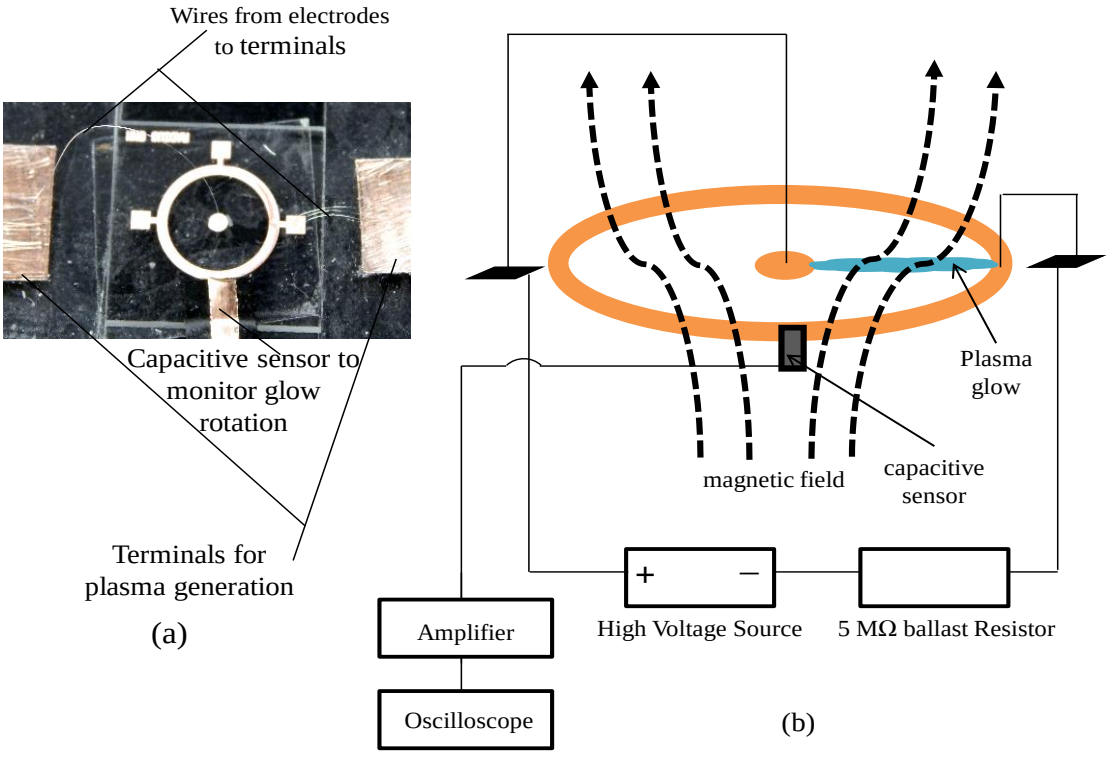

Fig. 2.13. A microplasma magnetic field sensor. (a) The microfabricated circular microplasma magnetic sensor device. (b) Schematic of the experimental setup for this device. The ballast resistor biases the gas discharge to burn as a glow discharge (see Fig. 2.3). The oscilloscope records a pulse when a glow passes by the capacitive sensor.

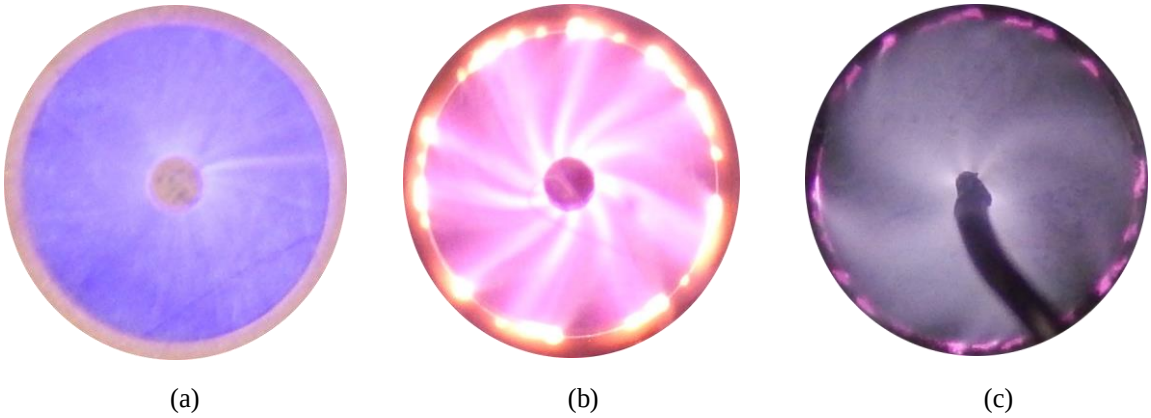

Fig. 2.14. Rotating glow discharges at atmospheric pressure for (a) Helium (b) Neon (c) Argon. The rotations of Neon and Argon glow have some interesting spatial features as seen from the ‘spokes’ in their rotations.

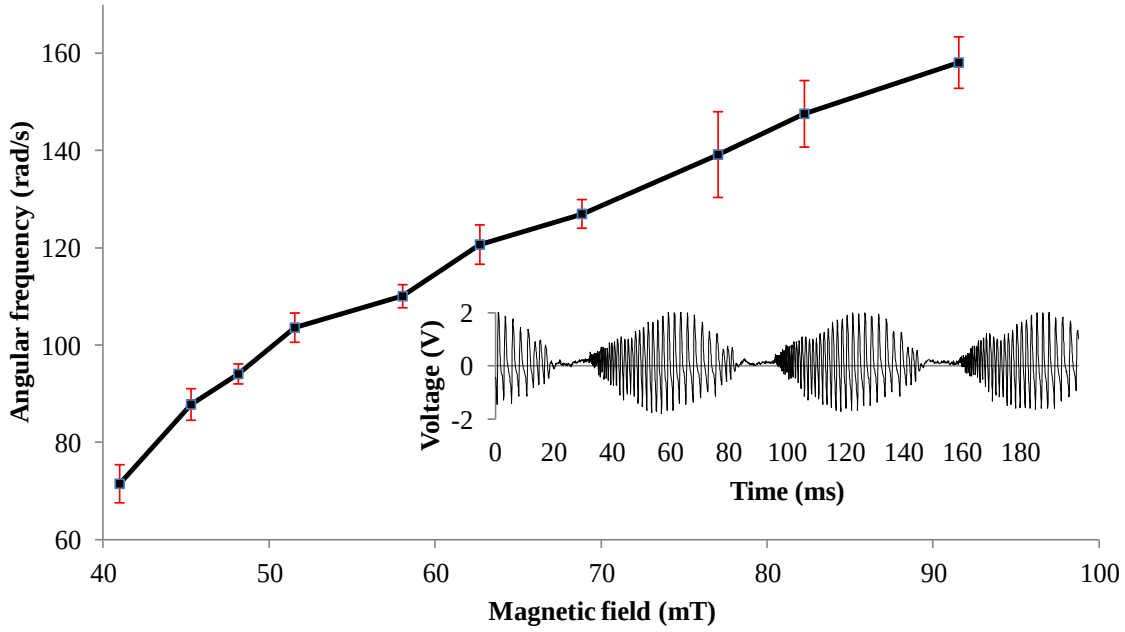

Fig. 2.15. Angular rotation frequency of the helium glow discharge as a function of the applied magnetic field. The error bars show the data spread over six consecutive measurements. Inset shows a typical waveform from the capacitive sensor for a rotating helium glow discharge. The angular frequency in this case is 104 rad/s (magnetic field of 50 mT).

towards the cathode. The mobility (μ) and drift velocity (v_d) in a weak field is given by [2]:

$$\mu_{e,i} = \frac{q_{e,i}}{m_{e,i}\upsilon_{m_{e,i}}} \tag{2.2}$$

where

$$v_{d_{e,i}} = \pm \frac{q_{e,i}E}{m_{e,i}\nu_{m_{e,i}}}, v_{d_{e,i}} = \mu_{e,i}E \tag{2.3}$$

where $q_{e,i}$ is the charge of the electron/ion, E is the electric force, $m_{e,i}$ is the mass of the electron/ion, and $\nu_{me,i}$ is the effective collision frequency for momentum transfer for

electrons/ions. When a circular magnetic sensor device is placed in a magnetic field (B_z) perpendicular to the plane of device, the electrons and ions drifting in this magnetic field experience a Lorentz force (F_θ) given in cylindrical coordinates as:

$$F_\theta = q_e v_{d_e} B_z + q_i v_{d_i} B_z \tag{2.4}$$

This Lorentz force is opposed by forces due to asymmetry and roughness of the copper surfaces of the device electrodes. These opposing forces will be bunched together as a 'frictional forces' F_f . Furthermore, as the glow rotates in the surrounding gas of the discharge, it experiences a drag force D given by:

$$D = \frac{1}{2} C\rho A\omega^2 \tag{2.5}$$

C is the drag coefficient, ρ is the ambient gas density, A is the cross sectional area of the glow, ω is the angular speed/frequency of the rotating glow discharge. Since it was observed through experiments that the beam rotates at a constant angular frequency, then the Lorentz force, the 'frictional force', and the drag force are in balance (equilibrium condition). Hence,

$$F_\theta - F_f = D \tag{2.6}$$

Thus, the velocity of rotation of the beam can be given as a function of magnetic field as

$$\omega = \sqrt{\frac{2(q_e v_{d_e} B_z + q_i v_{d_i} B_z - F_f)}{C\rho A}} \tag{2.7}$$

Equation (2.7) shows that the angular frequency of the glow depends on the applied magnetic field, drift velocity of the carriers (which depends on the mobility from (2.2),

the density of the ambient gas, and the cross sectional area of the beam (which depends on the distance between the pin anode and the ring cathode).

In addition to the physical factors given above, there is another factor which will limit the rotation of the beam. This is the time it takes for a gas discharge to form. This time can vary from a microsecond to a millisecond [2]. The rotation of the beam for one point to another can be considered as the switching off of the glow at one point on the cathode and its later switching on at the next point. The finite time it takes to form a self-sustaining glow discharge puts an additional upper limit on the maximum rotation frequency of the magnetic sensor.

2.9 A plasma-beam magnetic switch

The switch, shown in Fig. 2.16, is the magnetic analog of the electric switch of section 2.4. This switch was made by cutting a Y-shaped grove in a Polycarbonate slab. In this switch, the cathode was placed close to the grove junction that led to the two anodes. This was to make it easy for the beam to switch between the anodes on application of an actuation. Fig. 2.17 shows the change in the intensity of the plasma glow for different polarity of a magnetic field. Fig. 2.18 shows the measured plasma current between one of the legs of the relay for different magnetic polarities.

Like its electric analog, the plasma magnetic relay switch has a high leakage current (as you can visually tell) due to the asymmetry of the device. However, it was learned from the previous section that precisely fabricating a plasma device could significantly improve the performance of this type of device. Hence, this device, if precisely fabricated to be symmetric, can be used in practical high current switches and relays.

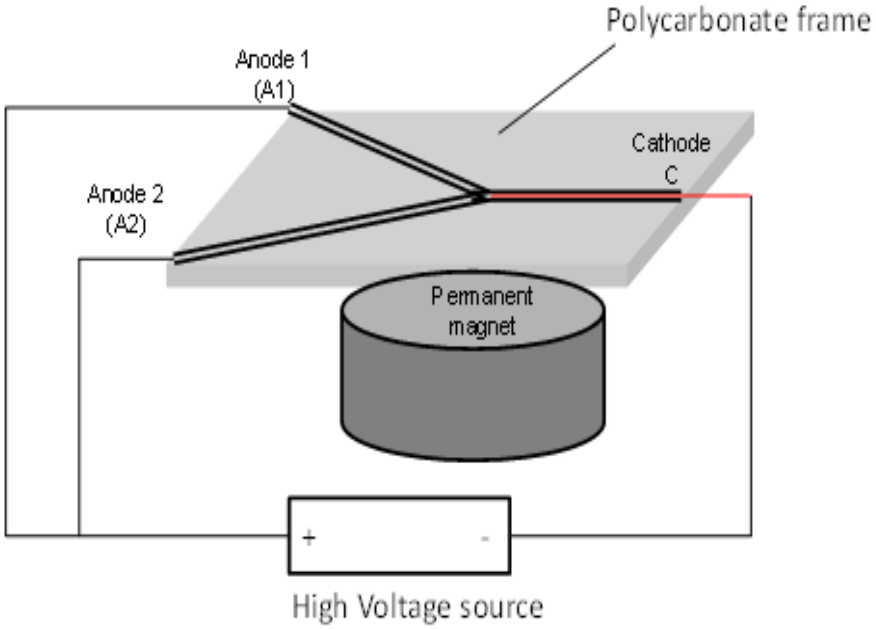

Fig. 2.16. Schematic of magnetically-actuated plasma switch. The magnet is placed close to the cathode for maximum deflection of the plasma switch.

(a) (b) (c)

Fig. 2.17. A plasma relay switch with magnetic actuation. (a) Device actuation with the North Pole of a 0.5T magnet (b) Device with no magnetic deflection (c) Actuation with the south pole of a 0.5T magnet.

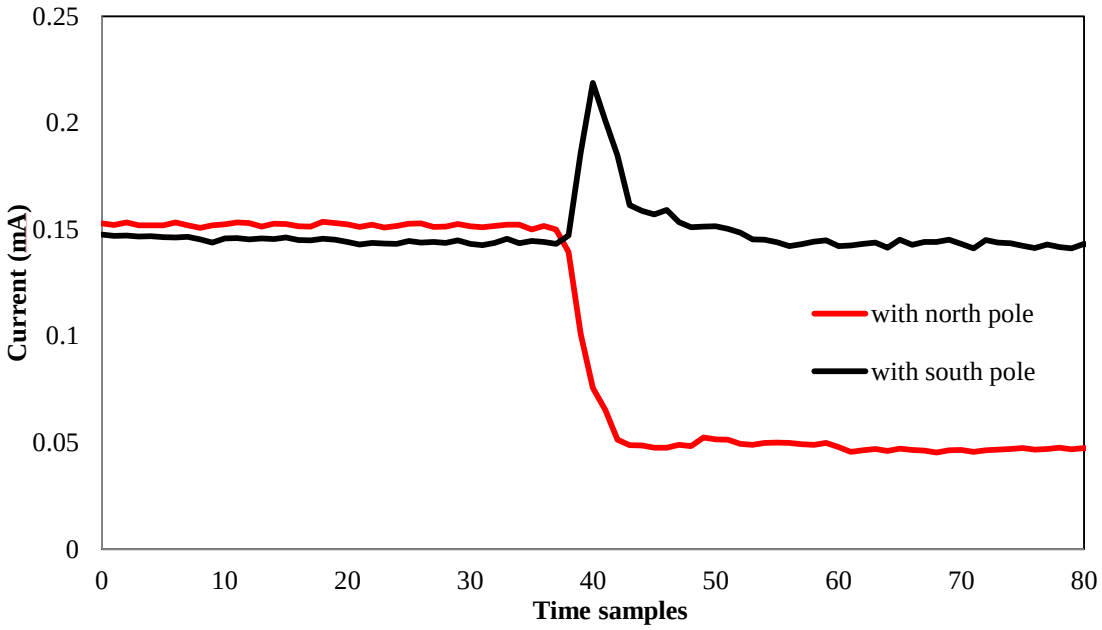

Fig. 2.18. Measured plasma current between anode A2 and cathode C for a 0.5 Tesla north and south pole magnets.

2.10 A plasma actuator (A 3D printed electrohydrodynamic pump)

The collision of the electrons and ions of a corona discharge with the air molecules is known to produce a sustained flow of air [8]. Hence, a 3D printer was used to create the electrodes design that will produce a corona discharge needed to blow air. This design consisted of two coaxial cones. The resulting electrohydrodynamic pumps are shown in Fig 2.19. The air flow rate obtained for these pumps for different electric fields are given in Fig. 2.20. More information about the design, characterization, and analysis of these pumps is given in [9].

2.11 Atmospheric-pressure plasma maze solver

This work also demonstrated the application of atmospheric-pressure plasma as an analog computer in solving shortest distance problems such as finding the solution to a

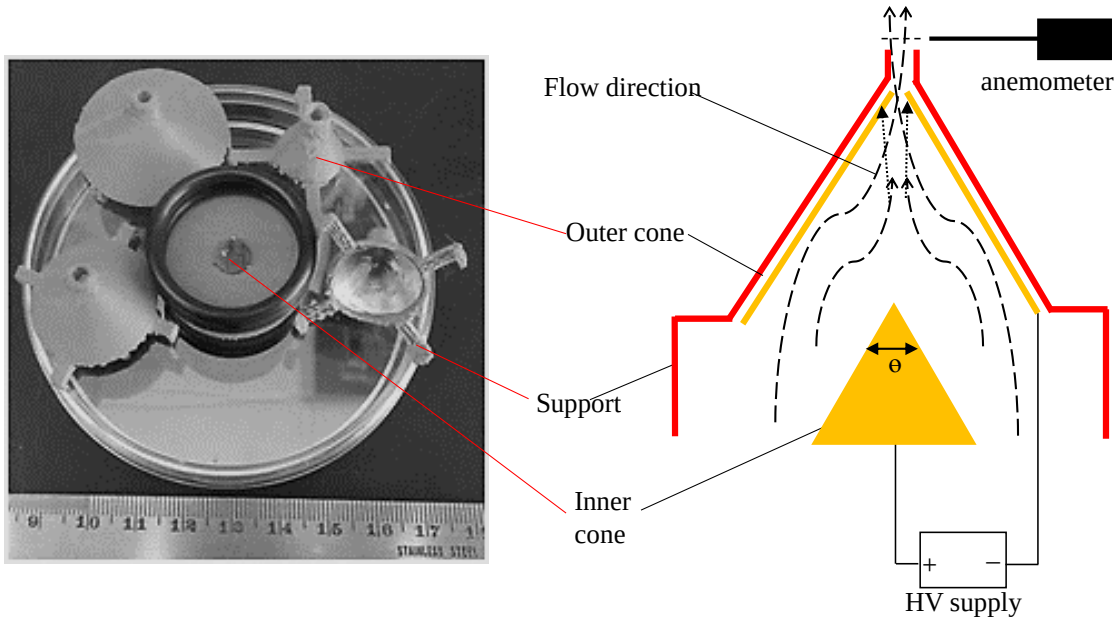

Fig. 2.19. 3D-printed electrohydrodynamic pumps. The left figure shows the pumps with one inner cone and 4 different outer cones of different conical angles. The right figure is a schematic of the pump assembly.

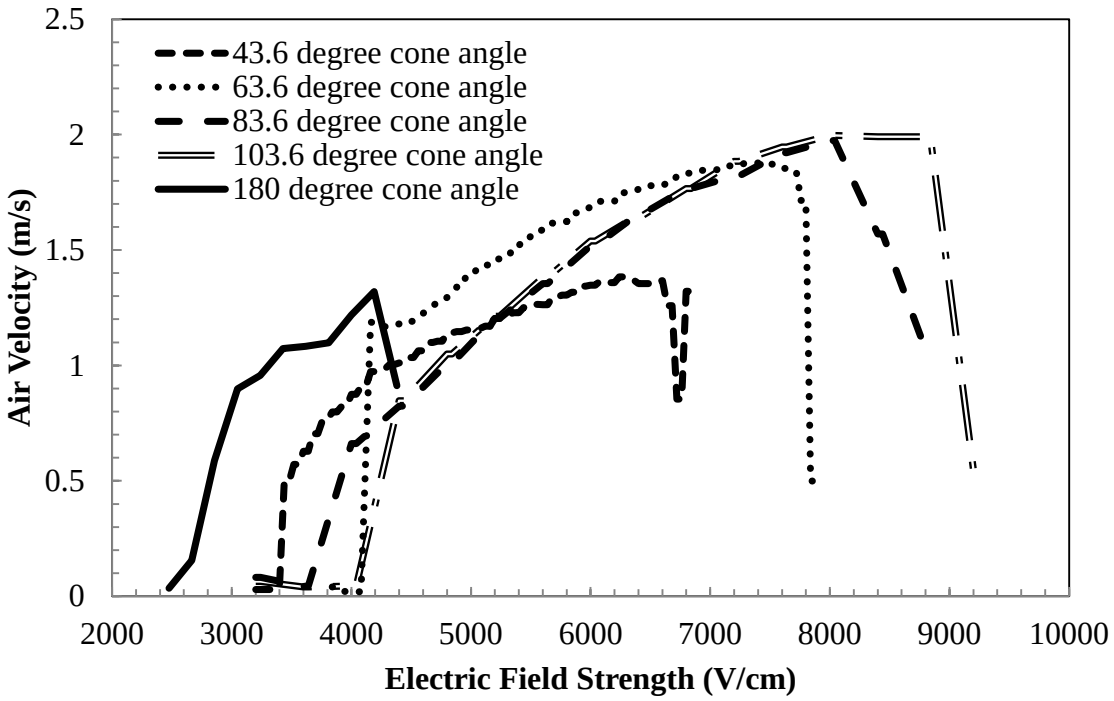

Fig. 2.20. Flow rate from corona discharge conical electrohydrodynamic pumps devices for different outer cone angles as a function of electric field strength.

maze problem. Earlier work for this application employed low-pressure (10-200 Torr) plasma [10]. The 6 by 6 maze shown in Fig. 2.21 was fabricated using a 40 W CO_2 laser cutter. Plasma electrodes were integrated at the entrance and the exit of the maze. The maze assembly was placed in a Plexiglas enclosure and helium gas was flowed into this enclosure. A high voltage (~ 8 kV) was applied between the maze electrodes. The plasma path almost instantaneously produced the solution of the maze as shown in Fig. 2.21.

2.12 Atmospheric DC plasma as source for soft x-rays

The electrons in the plasma are continuously being accelerated to high voltage by the DC source, and these electrons continuously lose their energy due to collision with ions and gas molecules. The energy lost by these electrons on collusion lies in the soft x-ray spectrum (5 – 10 kV).

The x-rays emitted by a DC plasma in atmospheric-pressure helium was characterized with a commercial Cadmium Telluride (CdTe) x-ray detector (Amptek X-123). The plasma x-ray spectrum is shown in Fig. 2.22; the inset in the figure shows the x-ray detector used in the measurement. The voltage for plasma generation for was ~ 4 kV. Although high density, low-pressure plasma focus is a well-known source for soft x-rays [11], these results shows that low-density, high-pressure plasma can be a good source for soft x-rays. This plasma x-ray source can be used in material identification systems similar to Energy-dispersive X-ray spectroscopy (EDAX) systems.

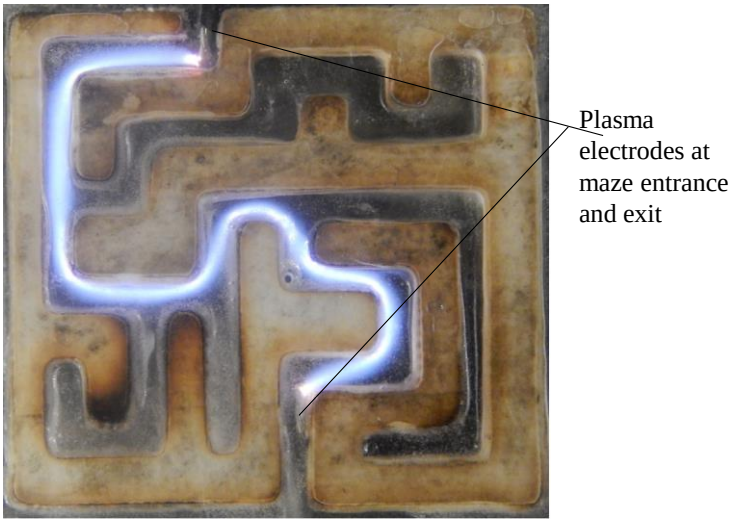

Fig. 2.21. Solution of a 6 by 6 maze by atmospheric pressure helium plasma.

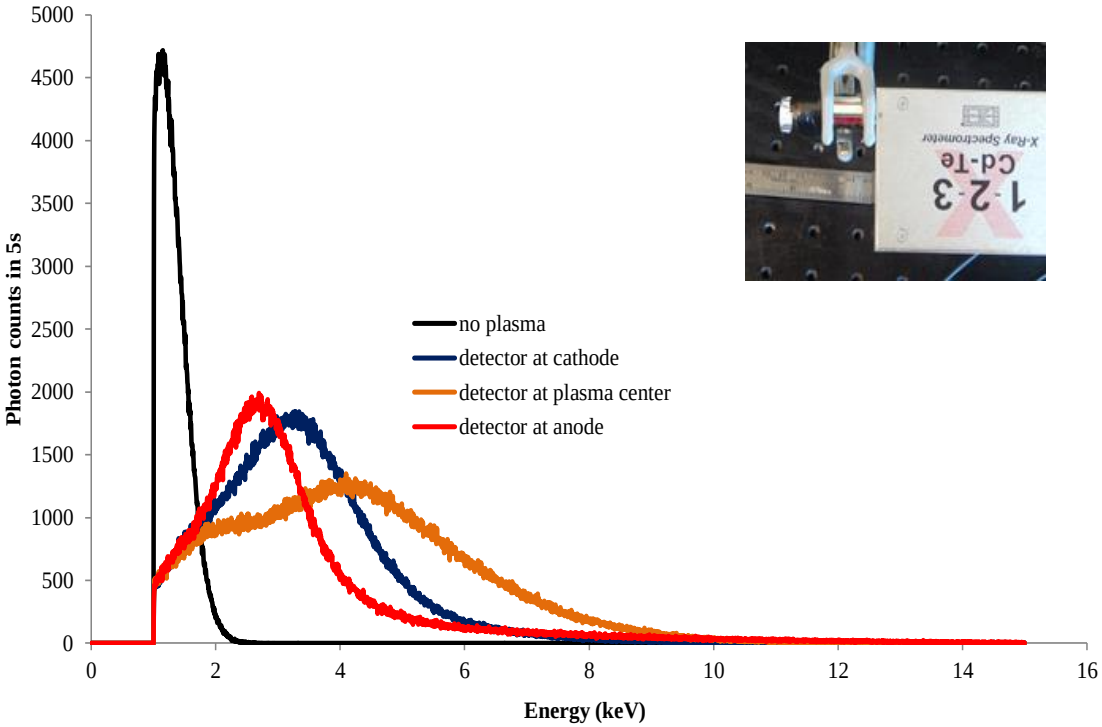

Fig. 2.22. X-ray spectrum for atmospheric pressure DC plasma in air with x-ray detector at different locations of the plasma. Inset shows the x-ray detector used for measurement.

2.13 An electron gun

The final study of charged particles of this chapter will be a study of electron beams. Thermionic emission is a common process by which electrons are produced [2]. Hence, in this study, thermionic electrons were produced in a vacuum chamber shown in Fig. 2.23 by electrically heating a tungsten filament. Inside a vacuum chamber, at a pressure of 40 mTorr, the thermionic electrons were extracted from the filament by applying a positive voltage to an annular ring anode. The thermionic electrons passed through a cylindrical focus electrode before reaching the anode. The focus voltage was negative with respect to the filament voltage. The particle tracing simulation model (with COMSOL) that illustrates the focusing action is given in Fig. 2.24. When no focusing potential was applied to the gun, most of the electrons spread transversely, due to mutual repulsion (space charge effect), and a lot of the electrons were intercepted by the annular ring (high intercepted current). However, when a focusing voltage was applied, most of the electrons were focused and they passed through the hole of the anode (low intercepted current). The result of the e-gun beam testing is given in Fig. 2.25 for two different acceleration voltages.

2.14 Chapter conclusions

In this chapter, an overview of the nature of plasma has been presented. Furthermore, some circuits that exploit the properties of plasma for switching, sensing, and actuation applications were also presented. Moreover, the design of an electron gun, a source for nonneutral plasma was also presented. Knowledge gained from these experiments are used in designing particle-wave interaction circuits in the next chapter and the traveling-wave-tube amplifier of Chapter 5.

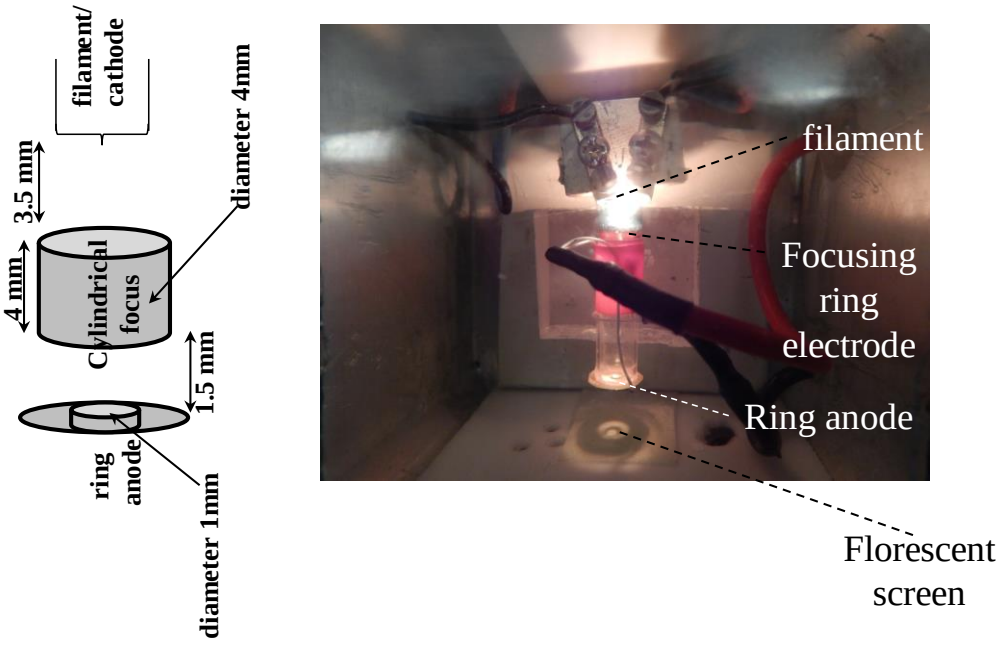

Fig. 2.23. An electron gun. (a) Schematic of the electron gun (b) Photograph of the electron gun.

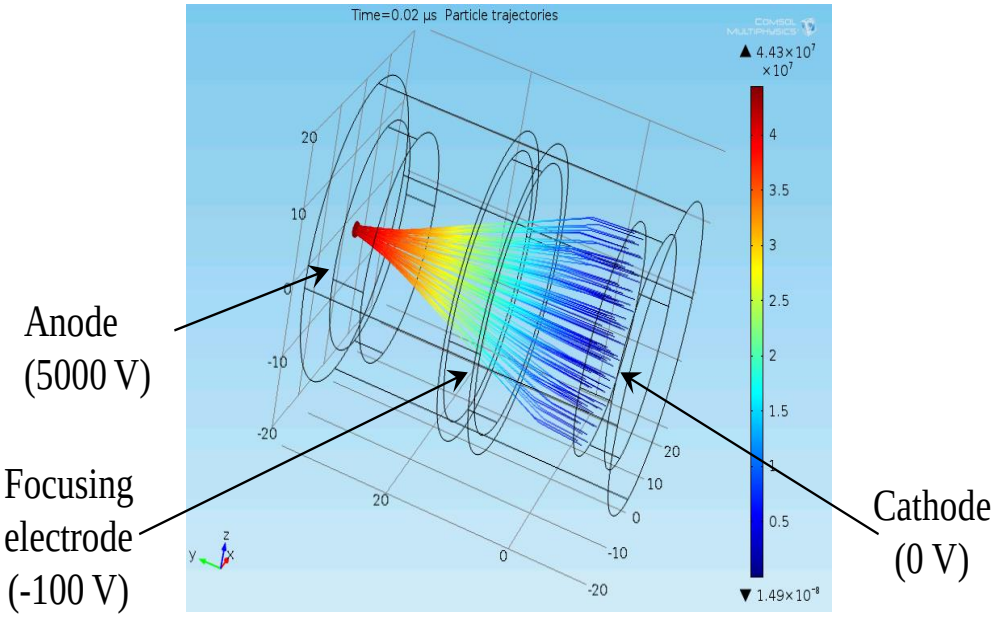

Fig. 2.24. Particle tracing simulation model that illustrates the focusing action of a focusing electrode on an electron beam in an electron gun.

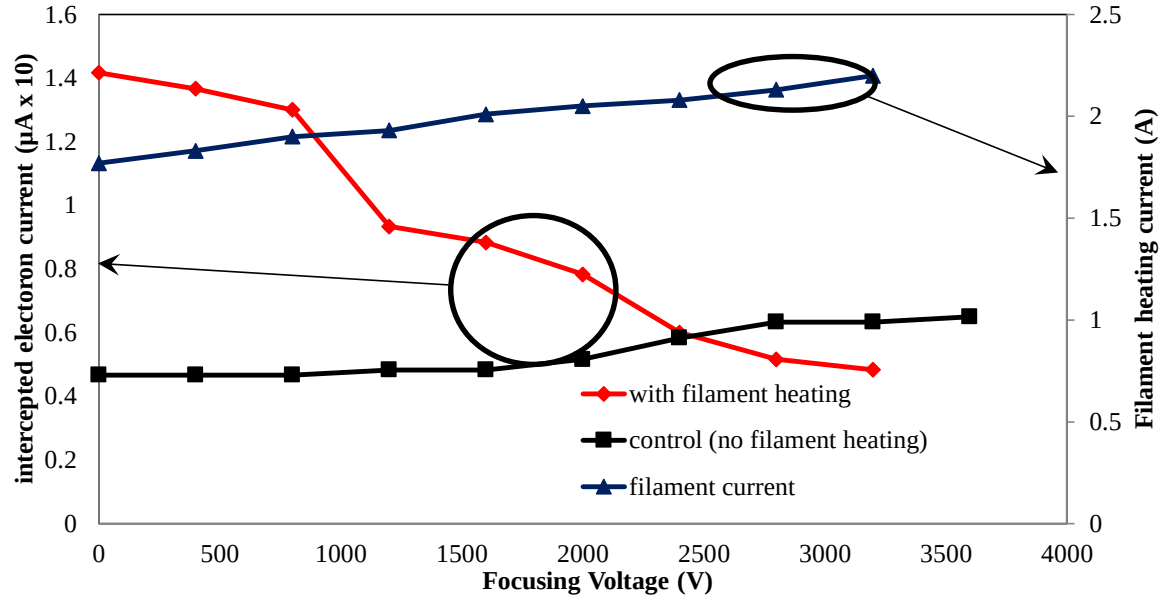

(a)

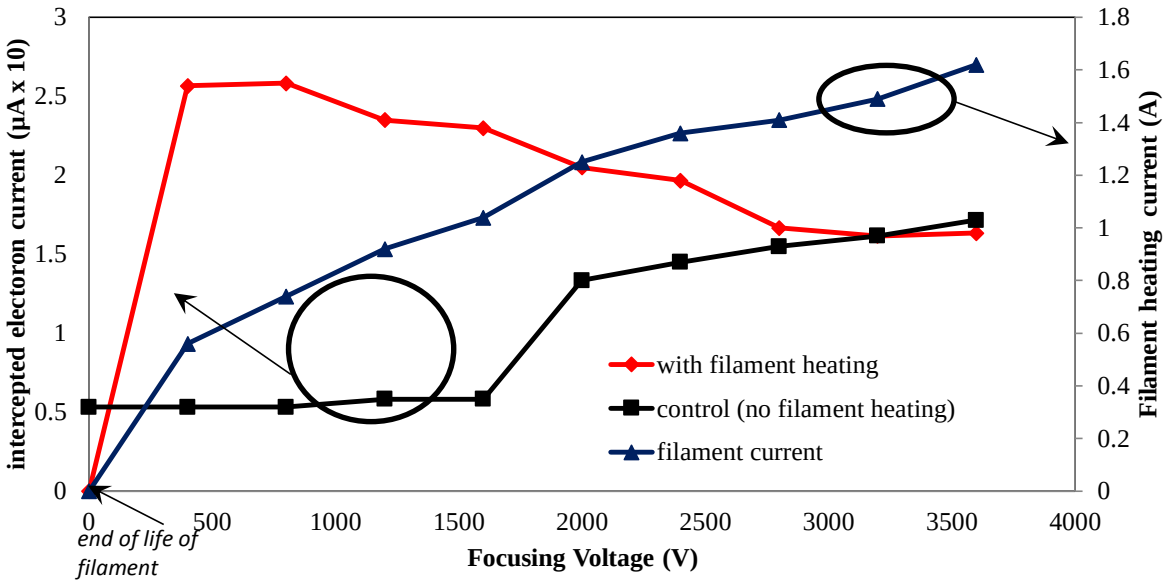

(b)

Fig 2.25. Intercepted current as a function of focusing voltage for the e-gun (a) Anode (acceleration voltage) of 2000 V (b) Anode voltage of 2400 V.

2.15 References

[1] F. F. Chen, *Introduction to plasma physics and controlled fusion volume 1: Plasma physics*, New York, NY: Plenum Press, 1985.

[2] Y. P. Raizer and J. E. Allen, *Gas discharge physics*, vol. 2. Berlin, Germany: Springer-Verlag, 1997.

[3] P. Pai and M. Tabib-Azar, "Micro-plasma field effect transistor operating with DC plasma," *IEEE Electron Device Letters*, vol. 35, no. 5, pp. 593-595, 2014.

[4] D. Staack, B. Farouk, A. Gutsol, and A. Fridman, "Characterization of a dc atmospheric pressure normal glow discharge," *Plasma Sources Science and Technology*, vol. 14, no. 4, p. 700, 2005.

[5] M. Cai, F. K. Chowdhury, and M. Tabib-Azar, "Micro-plasma field-effect transistors," in *IEEE Sensors 2012 Proceedings*, 2013, pp. 1-4.

[6] V. I. Kolobov, "Striations in rare gas plasmas," *Journal of Physics D: Applied Physics*, vol. 39, no. 24, p. R487, 2006.

[7] O. Fawole and M. Tabib-Azar, "A novel circular micro-plasma magnetic field sensor," in *2015 Transducers-2015 18th International Conference on Solid-State Sensors, Actuators and Microsystems (TRANSDUCERS)*, 2015, pp. 1957-1960.

[8] M. Goldman, A. Goldman, and R. S. Sigmond, "The corona discharge, its properties and specific uses," *Pure and Applied Chemistry*, vol. 57, no. 9, pp. 1353-1362, 1985.

[9] O. Fawole and M. Tabib-Azar, "A novel geometry for a corona wind electrohydrodynamic pump," in *IEEE Sensors 2014 Proceedings*, 2014, pp. 452-454.

[10] D. R. Reyes, M. M. Ghanem, G. M. Whitesides, and A. Manz, "Glow discharge in microfluidic chips for visible analog computing," *Lab on a Chip*, vol. 2, no. 2, pp. 113-116, 2002.

[11] J. W. Mather, "Formation of a high-density deuterium plasma focus," *Physics of Fluids (1958-1988)*, vol. 8, no. 2, pp. 366-377, 1965.

CHAPTER 3

CYLINDRICAL DIELECTRIC RESONATOR KLYSTRON AMPLIFIER

3.1 Introduction

In the previous chapter, the characteristic of plasmas and electrons, their generation techniques, and some circuits for manipulating plasma were presented. From the experiments with these circuits, it was concluded that the actuation that produce macroscopic (visible to the eyes) plasma response required high actuation electric fields or magnetic fields. Furthermore, it was inferred that the macroscopic response of plasma would be hampered by the inertia of the plasma. Hence, when the frequency (repetition frequency) of the actuating field was high, it became impossible to reliably measure the macroscopic response of the plasma.

Since the goal of this work is to develop a circuit where interaction between high frequency, small amplitude electromagnetic waves and a plasma or electron beam will lead to the amplification of the wave, it is necessary to design circuits, beams and experiments through which wave-beam interaction at a smaller time and length scale can be observed. The physics of small time/length scale interaction between particles and high-frequency electromagnetic waves is employed in vacuum electron tubes [1]. These electron tubes are designed such that their electron beams lose kinetic energy on microscopic interaction with an electromagnetic wave. The lost kinetic energy in the

electron will appear as electromagnetic energy in the wave (in accordance with the conservation of energy principle), and this will lead to the amplification of the electromagnetic wave.

The most basic electron tube amplifier is the grid-controlled tube whose basic structure is shown in Fig. 3.1. In this device, the time varying fields at the grid modulates the velocity of the electron current emitted from the cathode. This velocity modulation results in modulation of the electron beam current. This current, on being collected by the anode, results in an output current in the admittance Y such that the output ac power is amplified [1].

In the grid-controlled electron tube, the current flowing in the external circuit *i(t)* determines the gain obtainable from the grid-controlled tube, and this current is given by [1]:

$$i(t) = I_1 \ \frac{\sin\left(\frac{wT_0}{2}\right)}{\left(\frac{wT_0}{2}\right)} \sin w(t - \frac{T_0}{2}) \tag{3.1}$$

where I_1 is the electron DC beam current, ω is the frequency of the modulating signal, and T_0 is the electron transit time (the time it takes the electron to travel from grid B to C). The factor sin ($\omega T_0/2$)/($\omega T_0/2$), usually denoted by *M,* is the beam-coupling coefficient and ωT_0 is the electron beam transit angle θ. The plot of *M* as a function θ is shown in Fig. 3.2. Figure 3.2 shows that as the transit angle of the electron increases, the beam-coupling coefficient decreases, and this deteriorates the gain of the grid-controlled electron tube. The transit angle is a function of the separation distance between the grids B and C, and it is also as a function of frequency. A high frequency, high gain grid

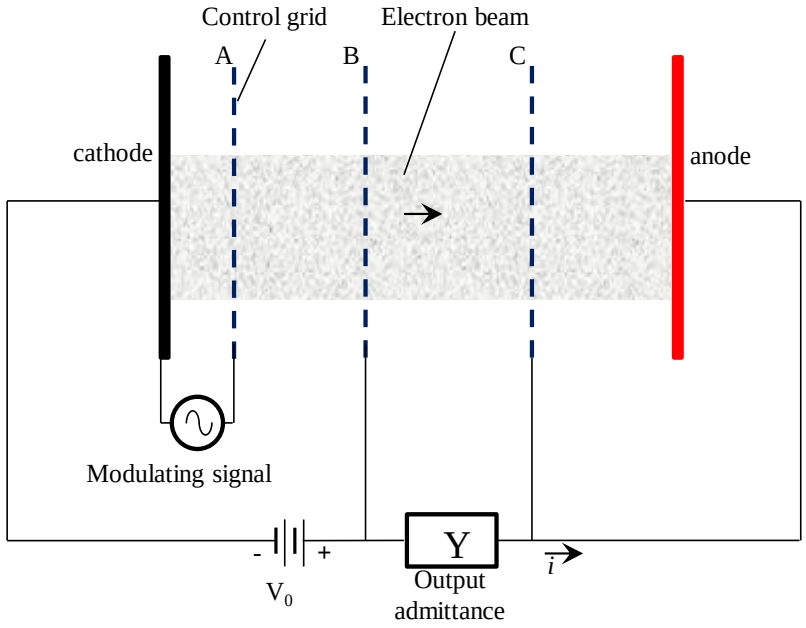

Fig. 3.1. Schematic of a grid-controlled electron beam tube.

amplifier will require very closely-spaced grids.

However, placing the grids too close together will introduce parasitic capacitances into the circuit, and this limits the applicability of this type of tube to low frequency operation.

Furthermore, other circuit factors such as lead inductances, stray capacitances, radiation losses, etc. limit the operating frequency of grid-controlled tubes to below 1 GHz operation.

In the late 1930s, the Varian brothers, invented the klystron ("a high frequency oscillator and amplifier") to overcome the high frequency limitations of the grid-control electron-tube amplifiers [2]. The basic schematic for the klystron is shown in Fig. 3.3. The basic klystron has two resonant high-frequency hollow metallic-wall cavities: the input and the output cavities. As in the grid-controlled tube, interaction between an electron beam and high frequency electric fields at a gap in the input cavity results in

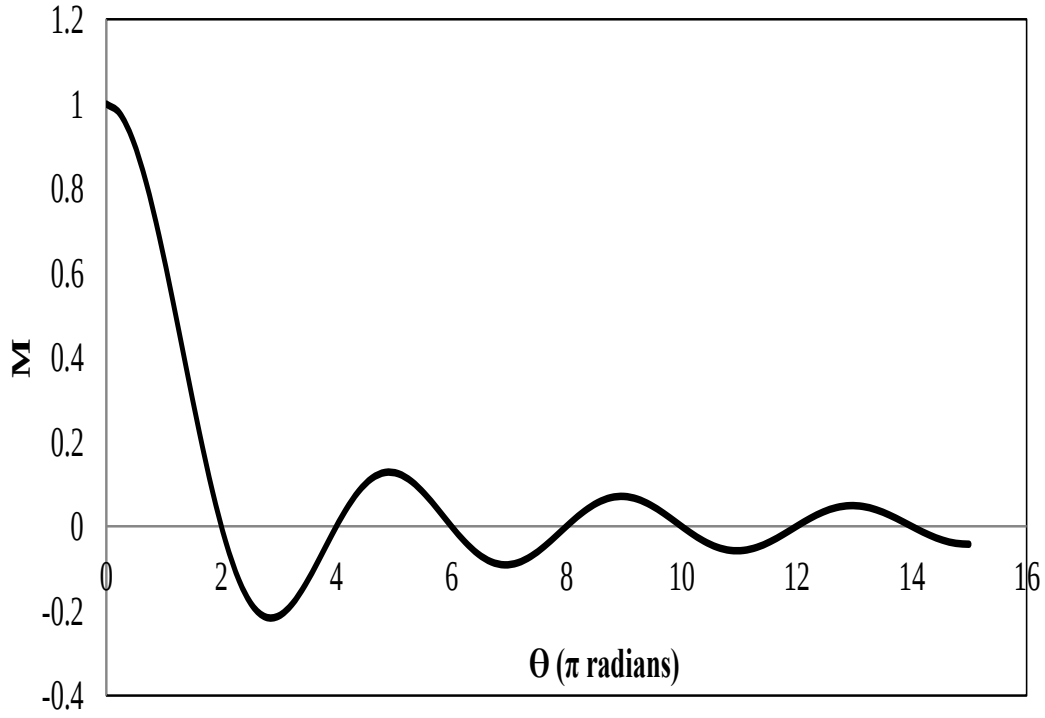

Fig. 3.2. Beam–coupling coefficient as a function of electron transit angle. Short transit time gives high coupling.

velocity modulation of the electron beam. The time-varying high-frequency electric fields impose an RF component on the DC velocity of the beam. The modulation of the beam leads to the 'bunching' of the electrons in the beam.

Bunching occurs when some of the electrons that enter the gap of the klystron cavity get decelerated because they enter the cavity gap at the moment when the gap oscillating electric field is rising, and some other electrons get accelerated because they enter the cavity gap at the moment when the gap oscillating electric field is falling. The overall effect of this is that the accelerated electrons travel at a velocity such that they overtake the slow moving electrons that are ahead of them in the beam. The velocity of modualation of the beam is described by (3.2) [1]:

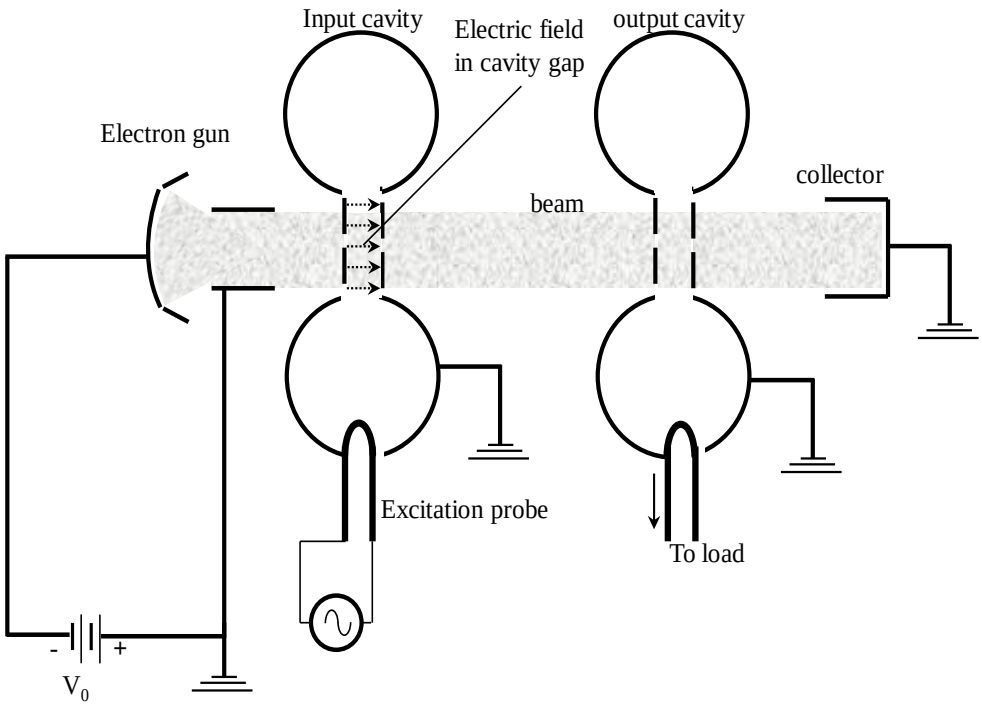

Fig. 3.3. The basic configuration for a two-cavity klystron amplifier. Klystron cavities are typically metallic wall resonators.

$$u(d) = u_0\left\{1 + \frac{MA}{2V_0}\sin(\omega t_0)\right\} \tag{3.2}$$

where *u(d)* is the velocity at the exit of the input cavity gap, u_0 is the dc velocity of the electron beam at the entrance of the input cavity gap, *M* is the beam-coupling coefficient, *A* is the voltage amplitude of the modulating electric field, V_0 is the DC beam voltage, and t_0 is the time at which the electron is at the center of the gap.

An RF current is later induced in the output klystron cavity by the bunched electron. The mathematical relation between the bunched electron current and the current induced in the output cavity of the Klystron is given in [1]. Since the induced current is independent of the load attached to the output of the Klystron, the Klystron can act as an RF amplifier.

A graphical way to illustrate bunching is by the use of the Applegate diagram which shows the trajectories of electrons on a distance-time plot as shown in Fig. 3.4. The slope of the straight lines in the Applegate diagram equals the velocity of the electron beam at the exit of the modulating gap.

In this chapter, a new design for a klystron is presented. This klystron design employs solid dielectric resonators as an interaction circuit for an electron beam. This design approach differs from the conventional klystron design that employs hollow metallic resonant cavities. In this klystron design, a dielectric resonator electric field distribution (resonant mode) suitable for interaction with an electron beam is the fundamental circularly-symmetric $TE_{10\delta}$ mode [3-5]. Hence, this chapter began by developing a low frequency (~7.5 GHz) prototype of a dielectric klystron.

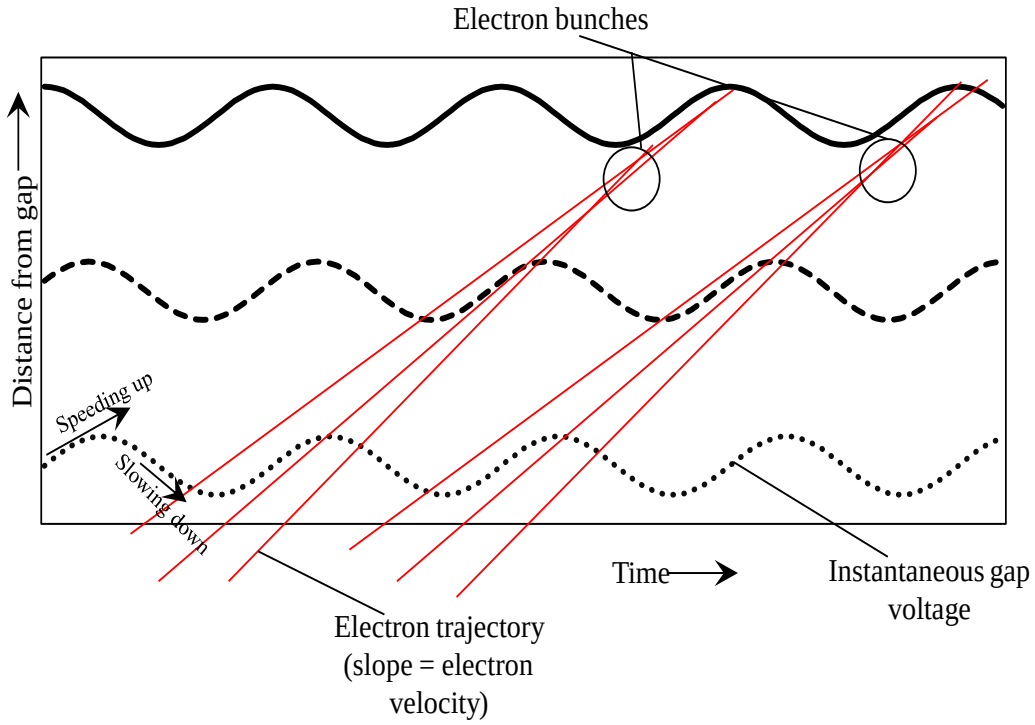

Fig. 3.4. Applegate diagram (electron distance-time plots) illustrating electron bunching. was developed to excite the $TE_{10\delta}$ mode in dielectric resonators.

The dielectric resonators employed in the dielectric klystron differ from the resonators employed in other RF circuits because the employed resonator material of the klystron resonators have a relatively low dielectric constant. This necessitated the development of a new method for exciting these low dielectric constant resonators. Furthermore, an experimental method was developed to map the fields in the excited resonator to confirm that the proposed excitation method truly excited the $TE_{10\delta}$ resonant mode. Next, it was demonstrated that the fields of these resonators are not too tightly confined within the material of the dielectric resonator, by demonstrating that the fields leaking out of the resonator could interact with an external plasma beam. Next, particle-in-cell simulation study of the amplification properties of the dielectric klystron was presented. Finally, in anticipation of the possible extension of the use of the dielectric klystron for very high frequency operation, a method for micromachining high frequency (terahertz) dielectric resonator and the micromachined resonators are also presented.

3.2 Low dielectric constant cylindrical resonators at gigahertz frequencies [6]

3.2.1 Introduction

As mentioned earlier, the resonant cavities of klystrons are generally metallic cavity resonators. However, in this work, the use of cylindrical dielectric resonators as alternative to metallic cavities was investigated. Some other research groups have also proposed dielectric-based electron tubes for high-bandwidth, high-gain amplifiers [7a]. Generally, dielectric resonators are not employed as resonant structures in klystrons and traveling wave tubes because the known excitation methods for dielectric resonators demand that the resonator must have a high dielectric constant ($\varepsilon_r > 20$). However, having

a high dielectric constant resonator means that most of the resonator electric fields will be confined within the material of the dielectric resonator. Such tightly confined fields cannot effectively interact with (modulate) an external particle beam. Therefore, a method to excite the fundamental $TE_{01\delta}$ resonant mode in low dielectric constant Cylindrical Dielectric Resonators (CDR) at microwave frequencies was developed in this work. Moreover, a method to map the electric fields of this mode to confirm that the right fields have been excited was also developed. As will be discussed later, the circularly symmetric electric field patterns of $TE_{01\delta}$ mode can modulate an external electron beam. [5, 7b].

The electromagnetic field distribution of the CDR $TE_{01\delta}$ mode is shown in Fig. 3.5a. The field patterns (electric and magnetic) are symmetric about the longitudinal axis of the CDR. Fig. 3.5b shows the variation of the magnitude of the electric field of the $TE_{01\delta}$ mode along the radial axis of an isolated CDR in the fundamental mode. The field variations in the radial direction are described theoretically by Bessel functions [3]. In a CDR of radius *a*, the magnitude of the electric field has a minimum value at the center of the CDR, a maximum value at 0.75*a* from the CDR's center. This field then decays in an exponential manner from this maximum value with increasing radial distance. In high-dielectric constant CDR, this outside field decays very rapidly, whereas in low dielectric constant CDR, this outside field decays gradually. Hence, a low dielectric constant resonator can be used as a basic unit of a beam-wave circuit.

Figure 3.5c shows a possible configuration for a klystron. This configuration employs CDRs in the $TE_{01\delta}$ mode. The electric fields at the input pair can modulate an electron beam and the beam can later excite an amplified signal at the output pair.

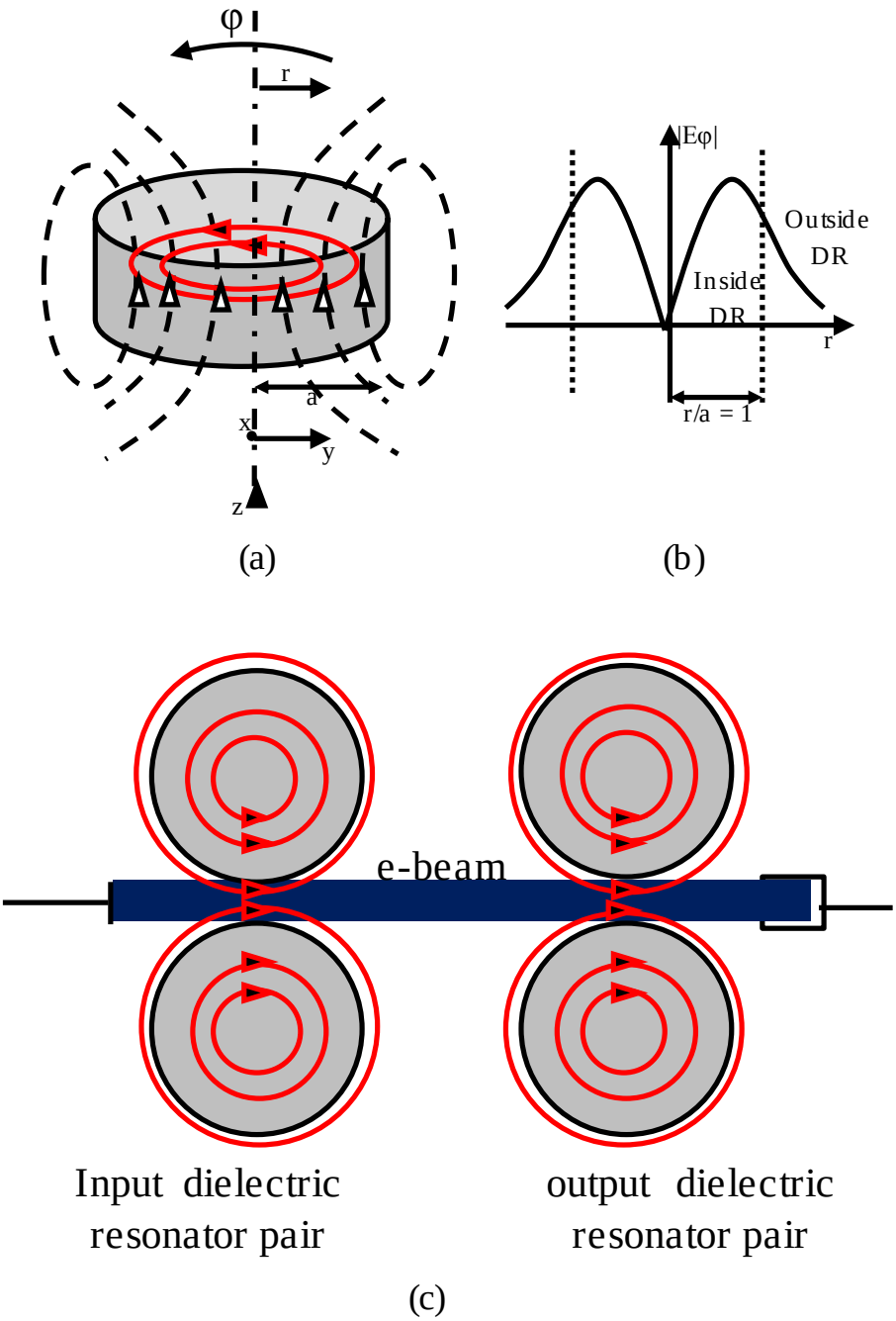

Fig. 3.5. Design of a dielectric klystron. (a) Electric field pattern (solid red lines), and the magnetic field pattern (dashed black lines) of the fundamental resonant mode ($TE_{01\delta}$) in an isolated dielectric resonator. (b) The variation of the magnitude of the radial electric field in the CDR as a function of radial distance. (c) Possible configuration (cross-sectional view) of a dielectric resonator klystron amplifier.

The basic principle for exciting the $TE_{01\delta}$ mode in a single CDR is using an excitation source that has either the same electric field distribution, the same magnetic field distribution, or both the same electric and magnetic field distribution as the $TE_{01\delta}$ mode. For example, the magnetic fields of a waveguide and of a microstrip line have similar H-field patterns as the $TE_{01\delta}$ mode. Hence, waveguide and microstrip lines excitations are often used to excite the fundamental mode in CDRs. However, waveguide-integrated CDRs are bulky and are difficult to fabricate, and microstrip line excitations are best suited for CDRs with very high dielectric constant (dielectric constant >20).

Here, the microstrip line excitation typical for high dielectric-constant CDR design was modified into a half-wavelength-long open-ended microstrip line. The electric fields at the coupling gap between the microstrip resonator and its microstrip line feed was used to excite the $TE_{01\delta}$ mode in a CDR. This excitation method is feasible because the electric field pattern at the coupling gap between the microstrip feed and microstrip resonator has the field pattern that is needed to support the electromagnetic $TE_{01\delta}$ in a CDR.

Furthermore, it was demonstrated that the $TE_{01\delta}$ mode excited in one CDR can be coupled to other CDRs in a resonator chain via evanescent field coupling. The authors in [8] used a similar method of evanescent field coupling via short-range electric fields to couple optical ring resonators into a chain.

The excitation methods developed in this chapter were validated with 3D electromagnetic simulations. More importantly, a new diagnostic tool, a ‘dielectric’ scanning near-field probe, was used to confirm that the $TE_{01\delta}$ fields were excited in the

CDRs. Different authors have developed electromagnetic scanning near-field probes of a similar type [9-16].

3.2.2 Method for exciting the $TE_{10\delta}$ mode in a single CDR

A single CDR was designed to be excited in the $TE_{01\delta}$ mode. The material for this CDR has a dielectric constant of 9.9. The height of the cylinder was 6.35 mm and its radius was 6.5 mm. The cylindrical resonator was excited by placing it over the coupling gap of a 50-ohm microstrip line resonator as shown in Fig. 3.6. The material used for the substrate of the microstrip lines has a dielectric constant of 3.55. The dimension of the substrate of the microstrip lines was 30 mm by 60 mm by 1.524 mm. The width of each microstrip line for 50-ohm impedance was 3.6 mm. The width of the coupling gap was 2 mm. The dielectric resonator was placed over the separation gap with its center offset from the common center line of by microstrip line by 4.95 mm. The inset in Fig. 3.6 shows the fabricated resonator.

The simulated and measured S-parameter results of the single CDR are shown in Fig. 3.7. The resonant frequency of this structure is the frequency at which the S_{11} and S_{21} are simultaneously small values (~ 7.8 GHz). This means that a considerable amount of RF power was transferred to the resonator at this frequency and that a considerable amount of power was stored in the resonator at this resonant frequency. The simulated vector electric field pattern of the CDR at resonance is shown in the inset of Fig. 3.7. This field pattern shows that the $TE_{01\delta}$ was excited in the resonator.

To confirm that $TE_{01\delta}$ fields were excited in the fabricated CDR , a near-field probe for measuring the tangential components of an electric field distribution was designed. This probe is a gap-coupled half-wavelength microstrip line resonator. Its

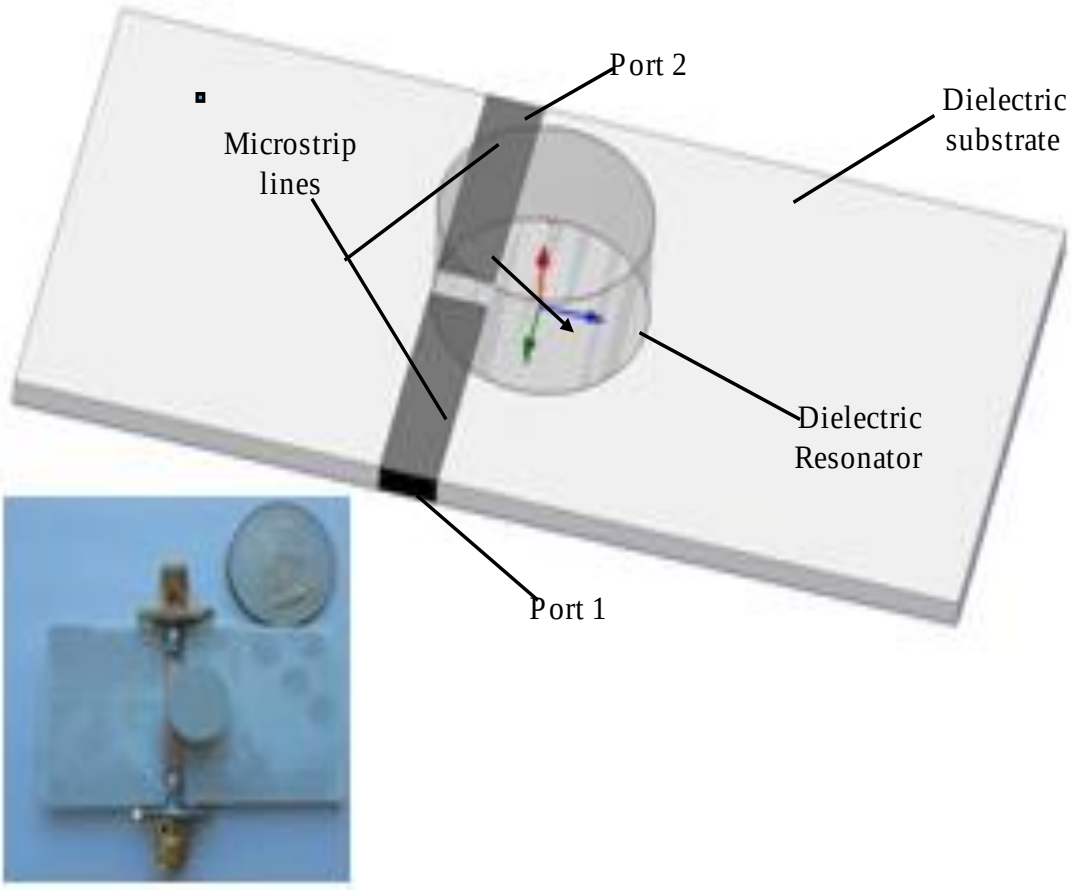

Fig. 3.6. Model of a single dielectric resonator. Inset shows photograph of the fabricated resonator.

structure is shown in Fig. 3.8. The simulated electric field distribution at the tip of the excited probe at 7.8 GHz is also shown in the figure. The simulated and measured S-parameters (reflection) of the probe are shown in Fig. 3.9. This probe was employed as a receiver in a phase sensitive detection system [17] of Fig. 3.10. When measuring tangential electric fields, this probe would record a high signal when the electric fields it detects at a point have the same orientation as its characteristic electric field, and a low

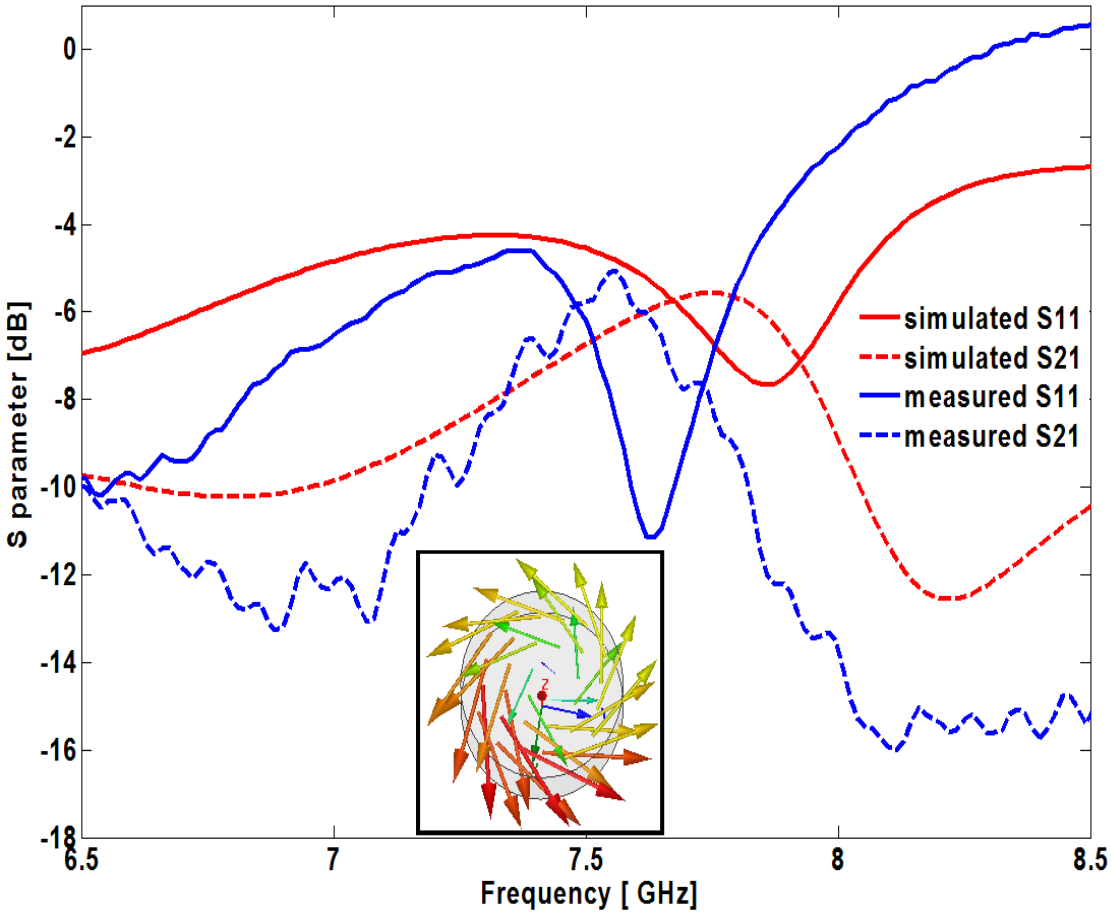

Fig. 3.7. Simulated and measured S-parameters of the single resonator. Inset is the simulated vector electric field at 7.8 GHz.

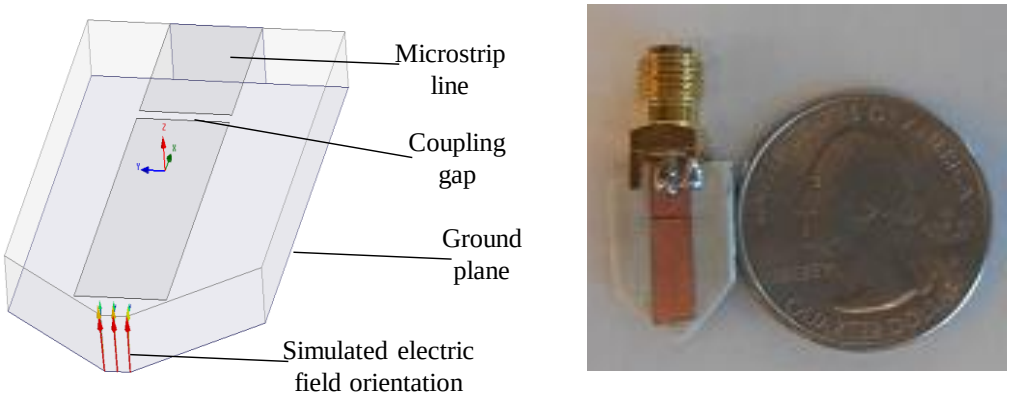

Fig. 3.8. Model of the near-field probe for tangential electric field measurement (left) and the fabricated probe (right).

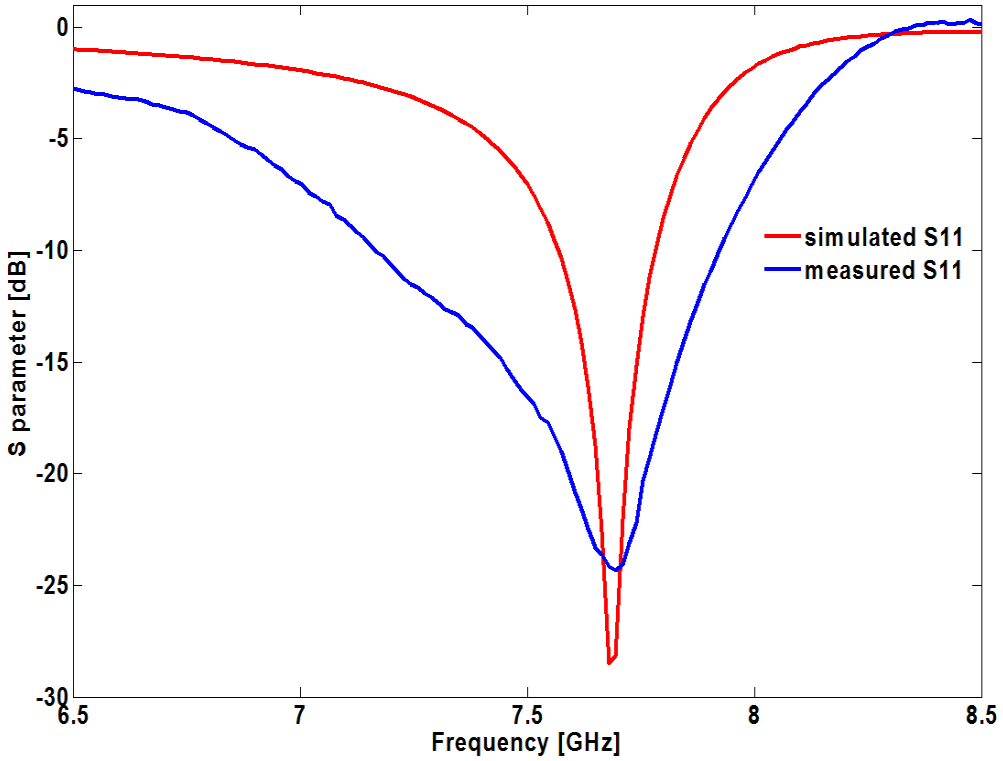

Fig. 3.9. Simulated and measured S_{11} (reflection) of the near-field probe.

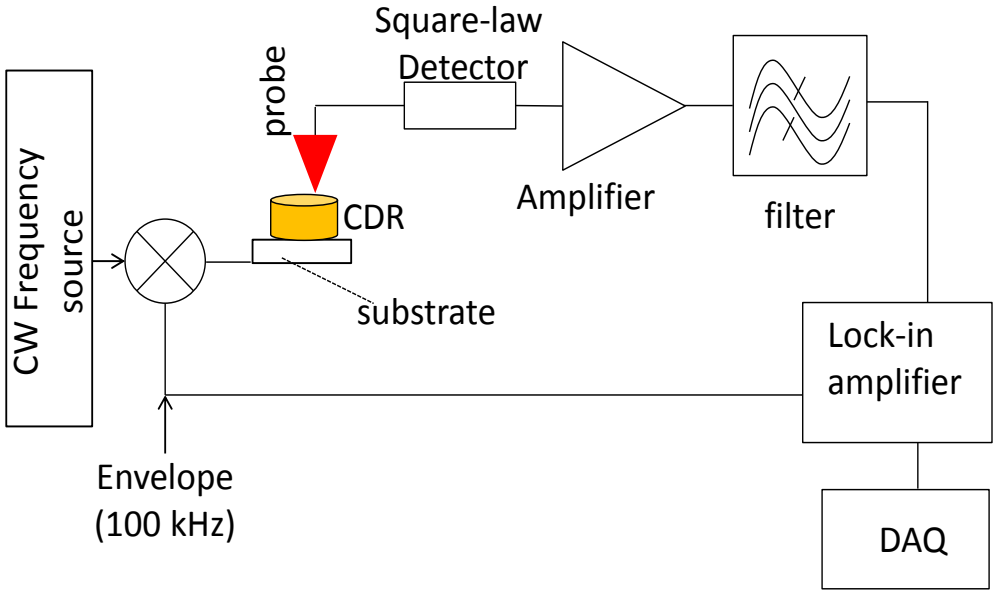

Fig. 3.10. Schematic of experimental setup to map the electric field pattern in a single CDR.

signal otherwise. Therefore, the probe could be oriented in a particular direction to measure the x-component of an electric field distribution, and then in an orthogonal direction to measure the y-component of an electric field.

In the setup of Fig. 3.10, the resonator was excited at 7.8 GHz with a continuous wave source, then the probe was raster-scanned over the CDR with a XY micropositioner stage. The field strength at each position of the probe was recorded with a data acquisition (DAQ) system. The measured components of the electric field pattern of the fabricated CDR and the simulated electric pattern are shown in Fig. 3.11.

In the pseudo-color plots of fields of Fig. 3.11, red (light) color indicates a high field and blue (dark) color indicates a low field. The absolute value of the fields strengths is not of critical importance in this experiment since only the pattern of the field is desired to be known. It is for this same reason that the spatial resolution of the probe was not investigated. If the spatial resolution of the probe were to be measured, the probe would be scanned over a sharp metallic tip, and the spread of the Gaussian-like plot of the field measured by the probe would give the spatial resolution of the probe.

3.2.3 Interaction of the fields of CDRs with an external plasma beam

Next, interaction of the electromagnetic electric fields in a low dielectric constant dielectric resonator with an external beam of particles will be investigated. The external beam of particle for this demonstration is a plasma beam. This interaction study with plasma beams can be further extended to electron beams.

It was observed from earlier experiments that plasma has a tendency to closely hug the walls of unexcited dielectric cylinders. This affinity of plasma for the walls of a dielectric cylinder is visible in Fig. 3.12. The physical affinity of the beam with the

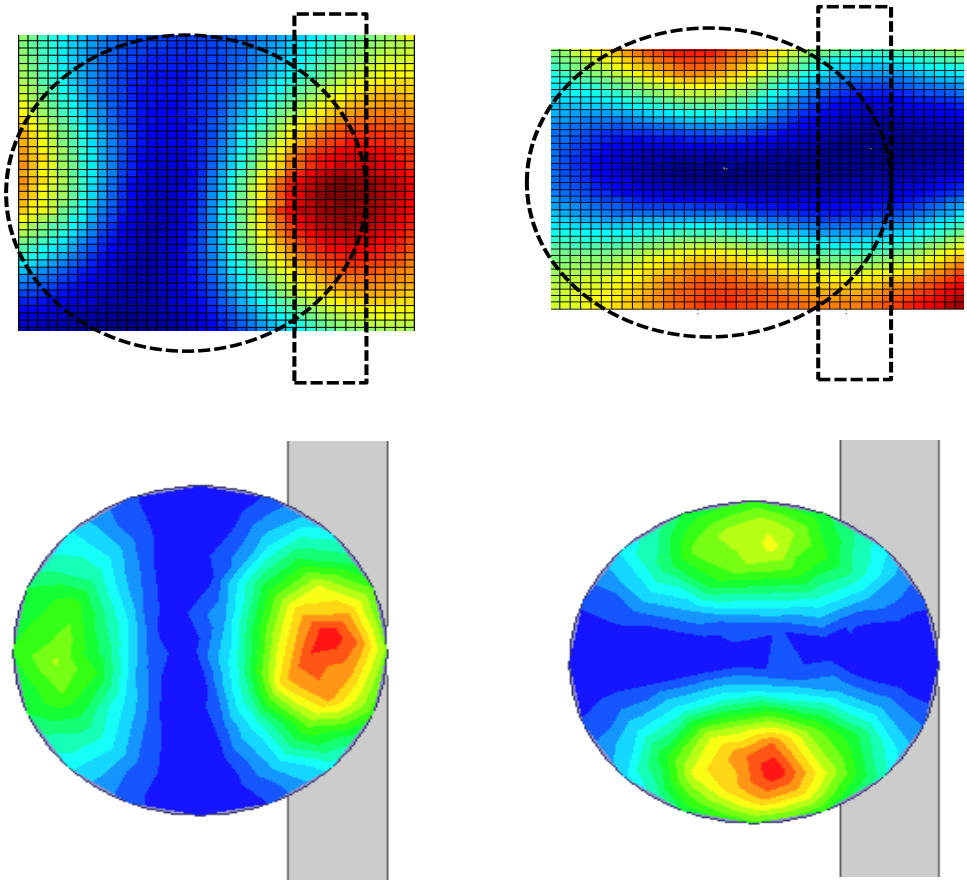

Fig. 3.11. Intensity plots of measured E_x^2 (top left), measured E_y^2 (top right), simulated E_x^2 (bottom left), simulated E_y^2 (bottom right). The phase sensitive detection method can measure only the square of the components of the fields.

dielectric walls will translate to stronger interaction between a plasma beam and electromagnetic fields of a CDR when the CDR is excited.

A two-dielectric resonator circuit shown in Fig. 3.13 was used to demonstrate interaction between a plasma beam and the low-dielectric constant CDR. The interaction between an electromagnetic field and a medium depends on the complex permittivity and permeability of the medium.The complex dielectric permittivity ε' of a medium is given by [18]:

$$\varepsilon' = \varepsilon + i4\pi\sigma/\omega \tag{3.3}$$

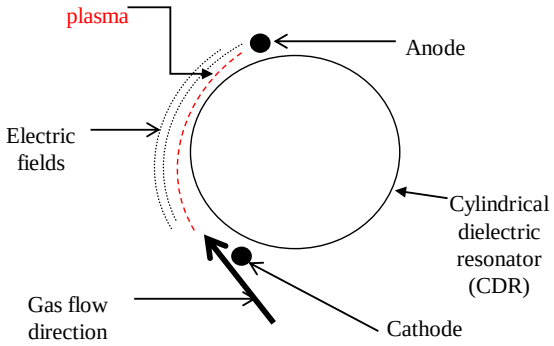

(a)

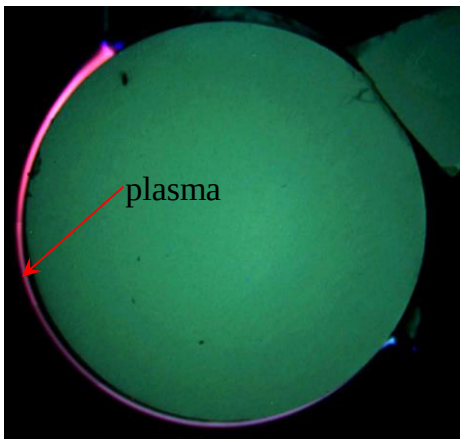

(b)

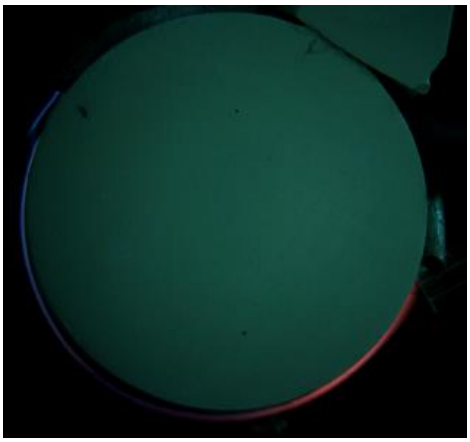

(c)

Fig. 3.12. Plasma interaction with a dielectric material. (a) Schematic of the experimental setup to show the tendency of plasma to closely hug the walls of a dielectric cylinder. (b) Photograph of the plasma hugging the dielectric cylinder when the seed gas flow is from the anode. (c) gas flow from cathode.

where ε is the real dielectric permittivity, σ is the conductivity of the medium and ω is the frequency of the electromagnetic wave in the medium. The real part of the permittivity of the plasma and the conductivity of plasma are given by [18]:

$$\varepsilon_\omega = 1 - \frac{4\pi e^2 n_e}{m(\omega^2 + v_m^2)} \tag{3.4}$$

$$\sigma_\omega = \frac{e^2 n_e v_m}{m(\omega^2 + v_m^2)} \tag{3.5}$$

where e is the electronic charge, m is the electronic mass, n_e is the number density of

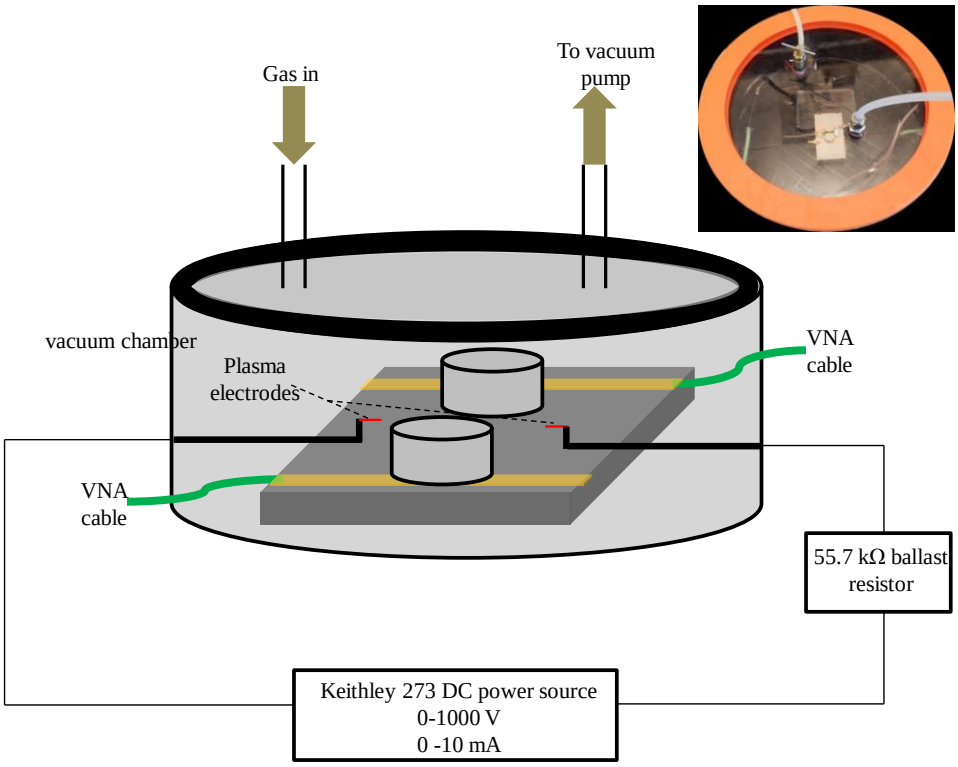

(a)

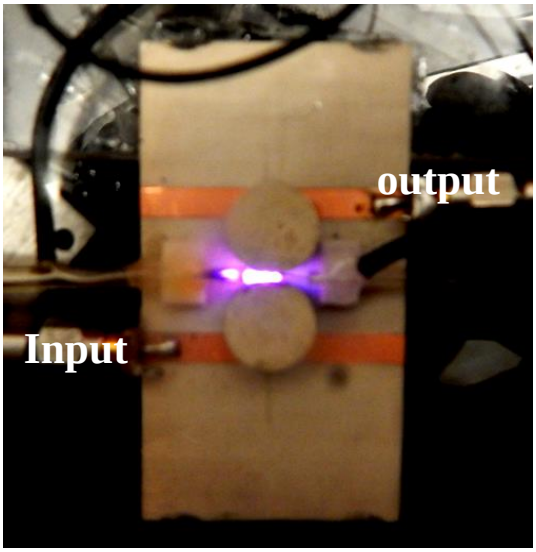

(b)

Fig. 3.13. Plasma interaction with the fields of a dielectric resonator. (a) Experimental setup to demonstrate interaction between plasma and the electromagnetic fields of CDR. Inset shows the photograph of the vacuum chamber of the experiment. (b) Two CDRs with a plasma beam between them.

electrons in the plasma, and ν_m is the effective collision frequency of momentum transfer.

The absorption coefficient of plasma is thus given as:

$$\mu_w = \frac{4\pi\sigma_w}{nc} \tag{3.6}$$

where n is the refractive index of the plasma given as $\sqrt{\varepsilon_\omega}$.

Therefore in the high frequency limit ($\omega >> \nu_m$), electromagnetic wave absorption is inversely proportional to frequency. Hence, higher frequency waves are less absorbed than lower frequency waves by plasma of fixed density n_e.

Furthermore, the critical density above which electromagnetic waves will propagate through plasma of density n_e without reflection is given by the plasma frequency ω_p which can be derived from (3.4) as the frequency at which $\varepsilon \geq 0$:

$$\omega_p = \sqrt{\frac{4\pi e^2 n_e}{m}} \tag{3.7}$$

This critical electron density $n_{e,cr}$ for an electromagnetic wave is given by:

$$n_{e,cr} = \frac{m\omega^2}{4\pi e^2} \tag{3.8}$$

To demonstrate the interaction between a plasma beam and electromagnetic waves (via attenuation or reflection of the wave by the plasma), a wave of low frequency and/or plasma of high conductivity/reflectivity (high collision frequency/electron density) must be employed.

In the upper end (8 GHz) of the frequency range of the CDR that was earlier

presented, the electron critical density from (3.8) corresponding to this frequency is ~7.9 x 10^{11} electrons/cm^3.

The relation between the current density j and electron density n_e is:

$$n_e = \frac{j}{e\mu_e E} \tag{3.9}$$

where μ_e is the electron mobility in the plasma and E is the electric field in the plasma. Hence, a high-density plasma can be obtained by designing the plasma circuit to be able to sustain a high discharge current. In [19], the authors estimated an n_e of ~ 1 x 10^{13} in an atmospheric pressure DC glow discharge of 10 mA current and length 0.5 mm. In addition, collusion frequency of the plasma (a function of plasma conductivity) can be tuned with the gas pressure of the seed plasma gas.

In the experimental setup for demonstrating interaction between the plasma and the fields in the low-dielectric constant CDR shown in Fig. 3.13, air plasma at 50 Torr was created over a length of 5 mm between the 0.5 mm of of 2 CDRs. In this experiment, the plasma current and applied voltage was 9 mA and 1000 V. Figure 3.14 shows the effect of the plasma on the electromagnetic reflection and transmission properties (S-parameters) of the CDR circuit.

Some other authors have used the interaction of plasma with electromagnetic waves to design plasma-tunable electromagnetic circuits [20-22].

3.2.4 Particle-in-cell simulation of the CDR klystron

Particle-in-cell (PIC) simulations were used to investigate the possibility of using the low-dielectric CDR in a klystron. The particle studio suite of Computer Simulation Technology (CST) software was used to model the interaction between an electron beam

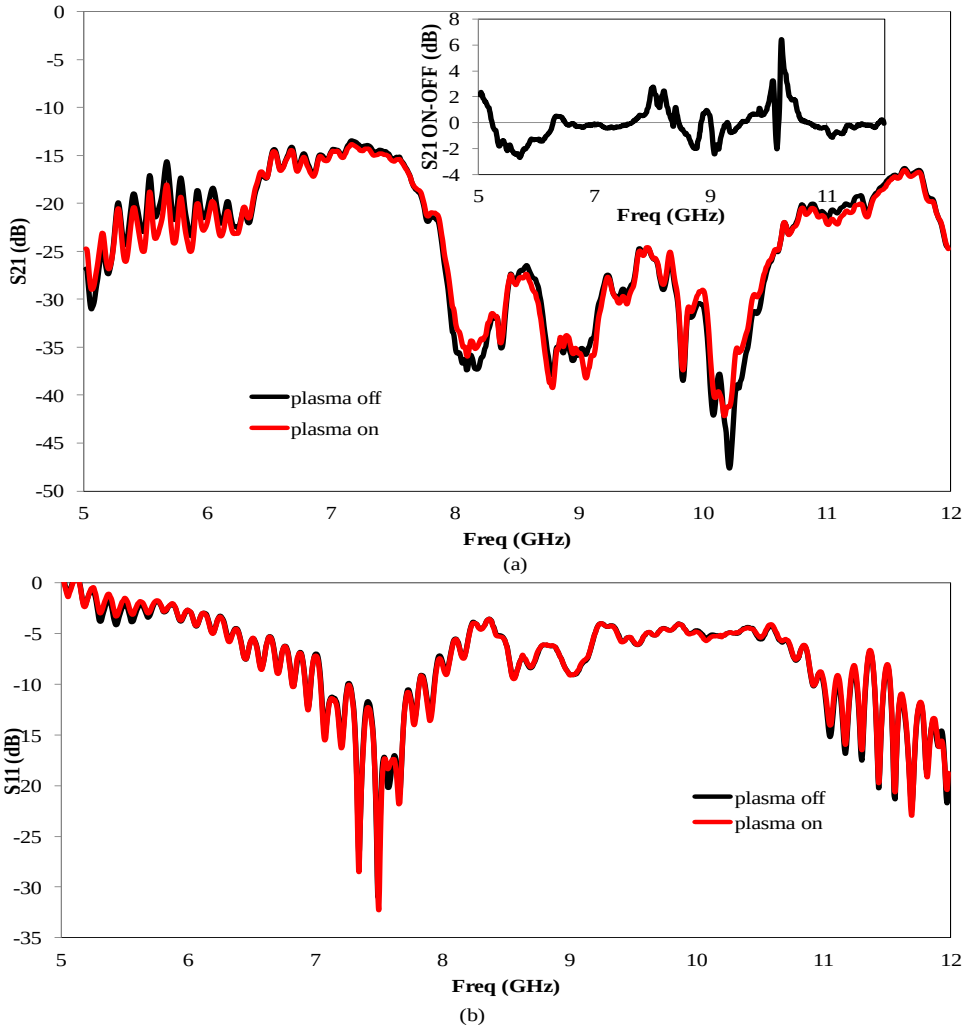

Fig. 3.14. Effect of the plasma on the S-parameters of a 2 CDR electromagnetic circuit. (a) Effect of plasma on the transmission between the two CDRs. Inset shows the difference in transmission between when the plasma is off and when it is on (b) Effect of plasma on the input impedance of the CDR circuit. The response time of the circuit to the plasma was almost instantaneous (< 200 ms response time). This indicates the circuit response was not thermally induced.

and the $TE_{01\delta}$ field of the CDR. The annotated simulation model is shown in Fig. 3.15.

The input ports, port 1 and port 2, of the CDR klystron were excited with identical time domain signals and an electron beam was injected along the beam path as shown in Fig. 3.15. Then the ratio of the Fourier-transformed output signal to the ratio of the Fourier-transformed input signal was computed as the amplification of the CDR. The results for the port 1 input - port 3 output (same result for the port 2 input-port 4 output because of the symmetry of the circuit) for different beam parameters are given in Fig. 3.16. Figure 3.17 shows the electric field distribution in the CDR at the frequency where the amplification peaked. From these field distributions, it can be deduced that the electric fields of the fundamental $TE_{01\delta}$ mode produced the amplification peak at 7.64 GHz (black dotted line) while the electric fields of the higher order $HEM_{12\delta}$ produced the amplification at 10.81 GHz.

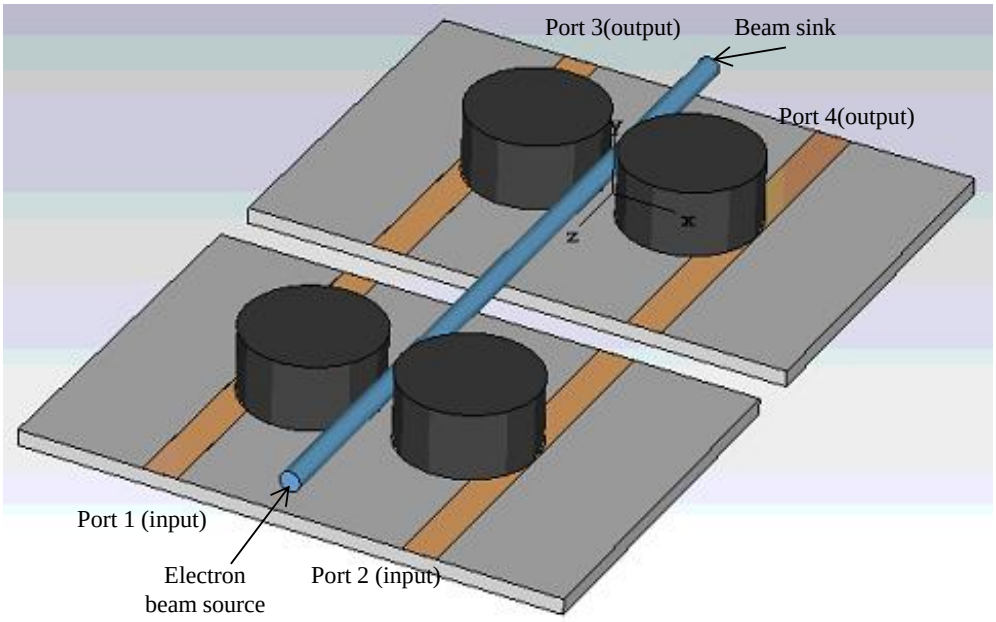

Fig. 3.15. Particle-In-Cell simulation model of the CDR klystron amplifier. The separation between input and output gap is 41 mm. This separation distance can be optimized to obtain higher klystron amplification.

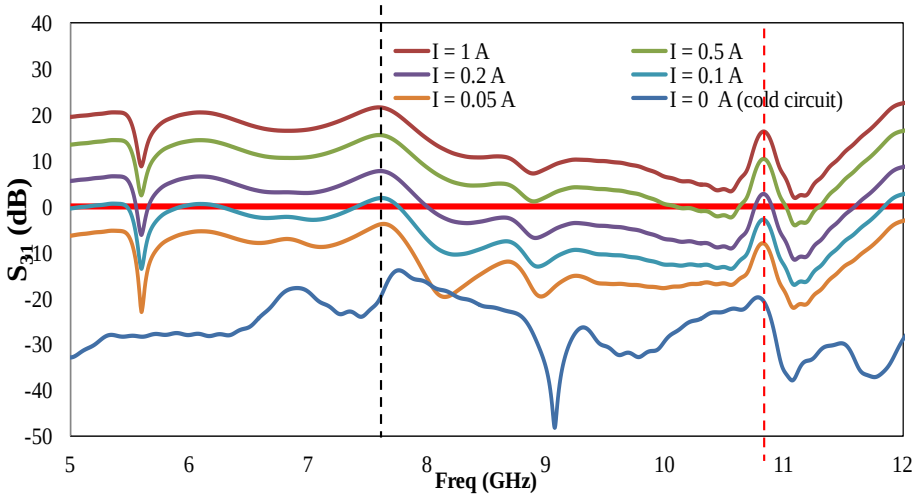

(a)

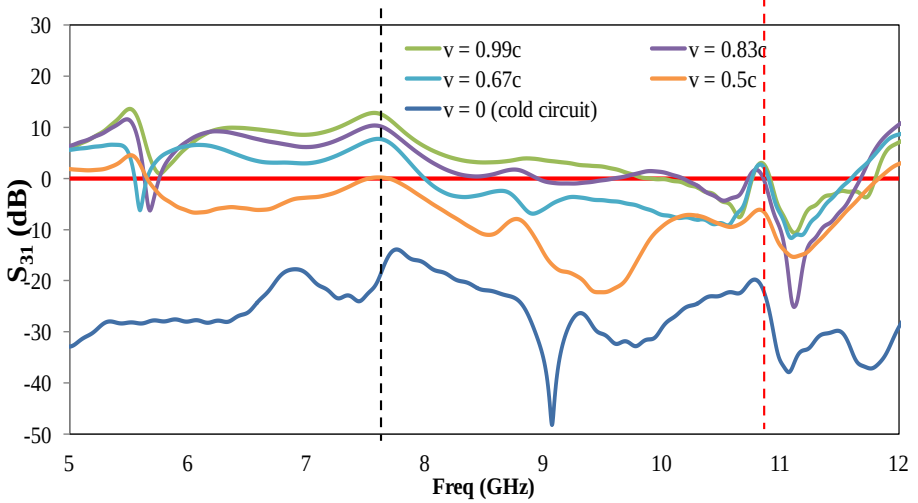

(b)

Fig. 3.16. Simulated amplification of the klystron amplifier as a function of electron beam parameters (a) amplification as function of electron beam current. Higher beam current produces higher gain (b) amplification as function of electron velocity relative to the speed of light *c*. Higher beam velocity produces higher gain.

3.3 Coupled CDR design and its field map

3.3.1 Coupled CDR design

The two-cavity klystron can be extend into a multicavity klystron by including multiple cavities in the klystron design. The multicavity has the advantage of higher gain and bandwidth than the two-cavity klystron. Therefore, a chain of coupled CDR was investigated for possible use in a multicavity klystron like configuration. The coupled

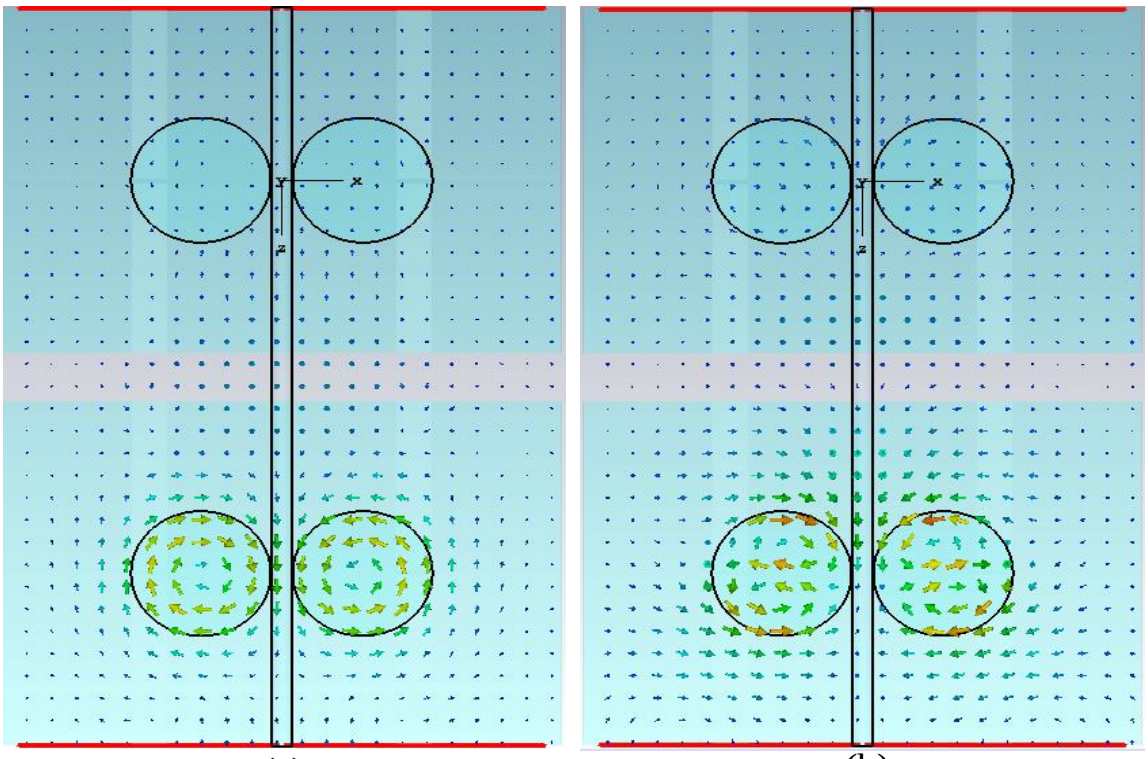

Fig 3.17. Distribution of the electric field in the equatorial plane of the CDR klystron (cold simulation) at the center frequencies where high amplification occurred (dotted lines) in Fig. 3.18 (a) fundamental $TE_{01\delta}$ fields at 7.64 GHz. (b) Higher order $HEM_{12\delta}$ fields at 10.81 GHz.

CDR chain was designed with ANSYS HFSS, a 3D full-wave electromagnetic solver. The schematic (for only 2 CDRs) of the truncated 6 CDR design is given in Fig. 3.18. In this design, the first CDR in the chain was excited by the electric field at the coupling gap of a microstrip resonator, the field in this first CDR was coupled to the next CDRs in the chain by evanescent field coupling, and so on. In this design, the substrate for the structure's microstrip lines is a material with dielectric constant of 3.55 and loss tangent of 0.0027. The microstrip feedline and the resonator are both 17 mm long and 3.3 mm wide, and the coupling gap has a size of 2 mm x 3.3 mm. The CDR chain consisted of 6 CDRs with no separation gap between them. Each CDR was cut out of a material with a

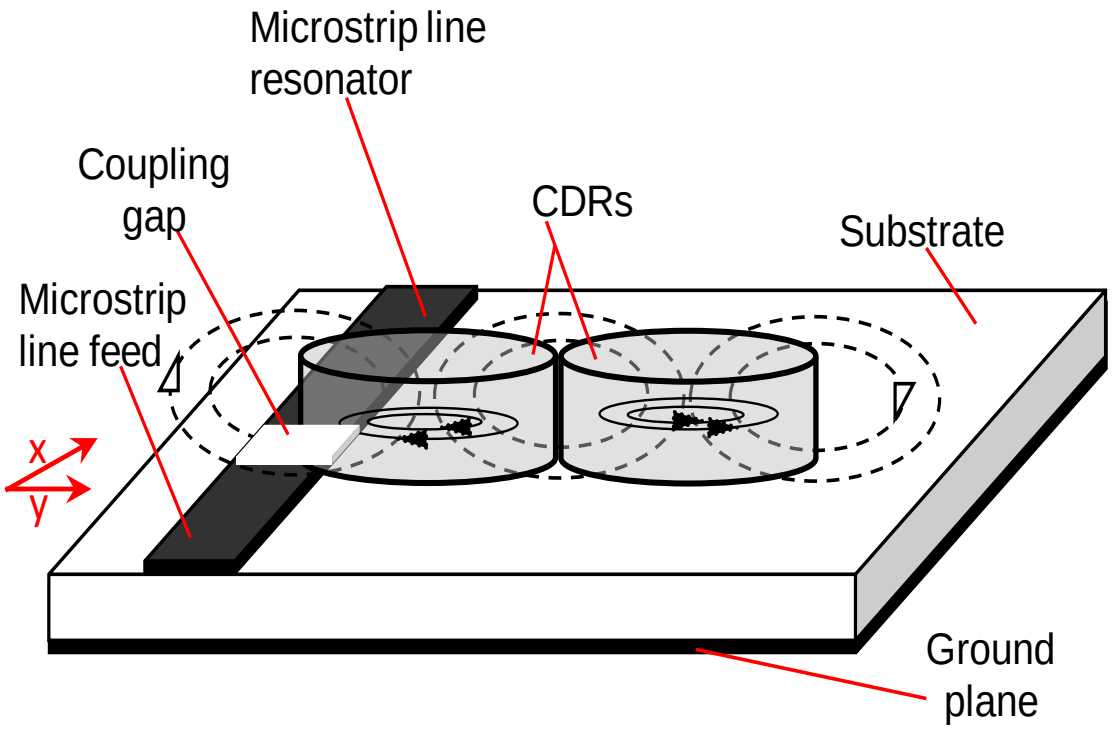

Fig. 3.18. Schematic of the method for exciting the $TE_{01\delta}$ mode in coupled CDRs with a microstrip line resonator. The electric and magnetic field lines at the coupling gap excites the first CDR, which then excites the next CDR via evanescent wave coupling.

dielectric constant of 9.9 and loss tangent of 0.0022. The radius and height of each CDR was 6.5 mm and 6.35 mm. The first and last CDRs in the chain were located at a y-offset distance of 4 mm from the center of the coupling gaps, and no x-offset. The size of the CDR substrate was 117 mm by 36 mm.

In Fig. 3.19, the simulated S-parameters of the coupled CDR (microwave reflection and transmission properties) are shown in Fig. 3.19a. The S-parameters are reciprocal. Fig. 3.19b shows the simulation model of the coupled CDR overlaid with the vector electric fields of the CDR at a representative frequency of 7.53 GHz. The field pattern shows that the modes of the CDRs are $TE_{01\delta}$ (the simulated magnetic field pattern have not been included in the figure, but they have the pattern of the $TE_{01\delta}$ mode). The

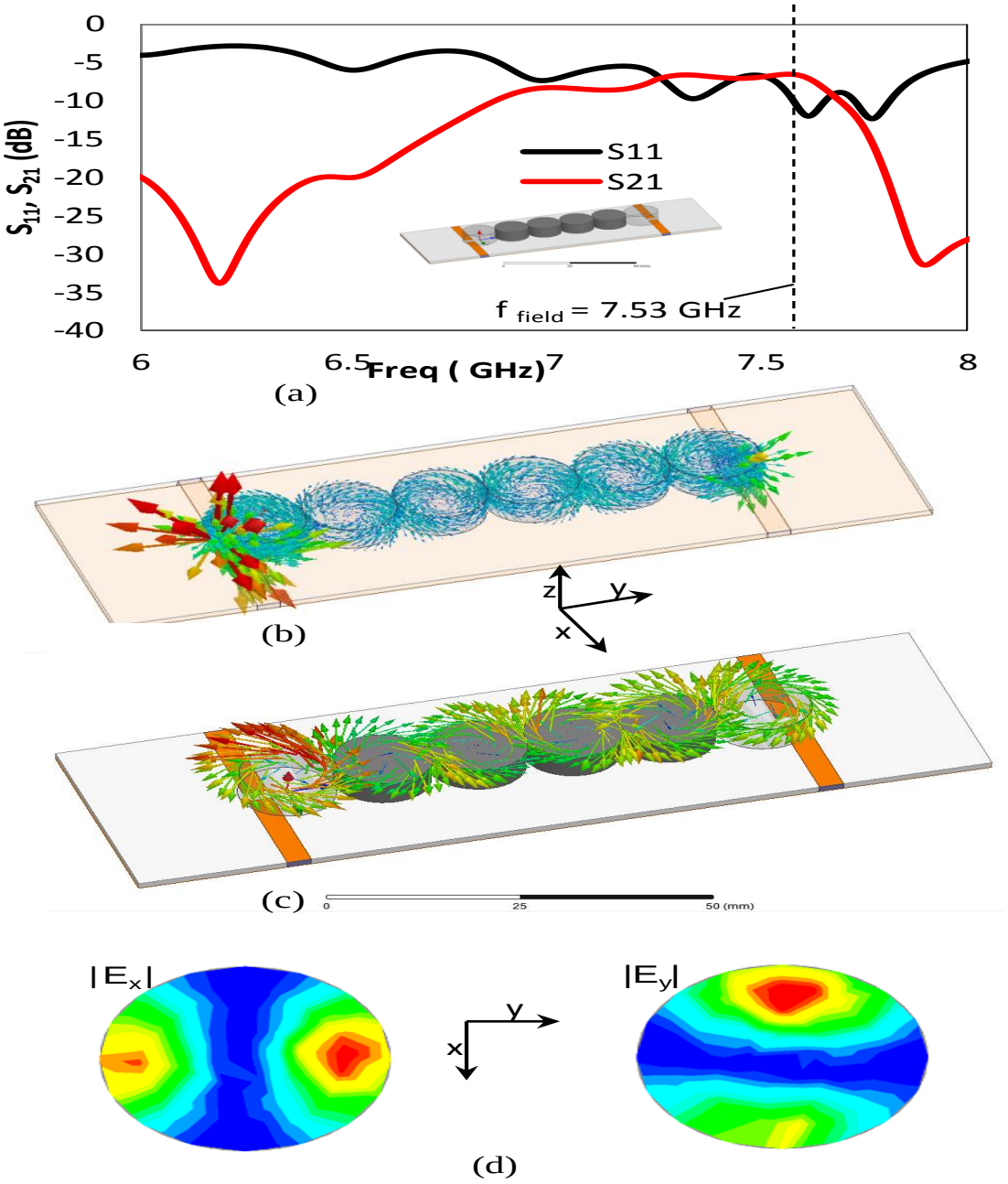

Fig. 3.19. Coupled CDRs (a) Simulated S-parameters showing the reflection (S_{11}) and transmission (S_{21}) spectra of the structure of 6 coupled CDRs that have been excited with a microstrip resonator. Inset is the model of the structure. The shown scale is 50 mm. (b) Simulated electric vector fields in the volume of the CDRs. The fields are at a representative frequency of 7.53 GHz. (c) Electric field vectors over the surfaces of the CDRs. Due to the symmetric nature of the coupled CDR structure, the field pattern is the same in any plane with the CDR that is perpendicular to longitudinal axis of the CDR. (d) simulated magnitude of the x component (left) and y component (right) of the electric field on top of one of the CDRs.

electric field pattern on the top surface of the CDRs is shown in Fig. 3.19c. For the symmetric $TE_{01\delta}$, the field pattern at the top surface of the CDR is the same as that at any plane perpendicular to the longitudinal axis of the CDR; hence the field pattern over the CDR can be measured to deduce the field pattern inside the CDR. The magnitudes of the x and y components of the electric field patern at the top surface of the CDR are shown in Fig. 3.19d.

3.3.2 Probe for mapping the electric field pattern of the $TE_{01\delta}$ mode in a CDR chain

The motivation for designing this probe is to map electric field patterns over a CDR in a chain, without perturbing the fields desired to be mapped. Hence, the probe whose exploded view is given in Fig. 3.20a of Fig. 3.20 was designed. This probe consisted of a stripline sandwiched between two grounded dielectric substrates. The copper trace of the stripline was 17 μm thick and ~2.5 mm maximum width. Furthermore, each dielectric substrate of the probe had a copper ground plane that is 17 μm thick. Each dielectric substrate of the probe was 0.76 mm thick with a dielectric constant of 3.66. The probe assembly was tapered into an apex. The probe will for three reasons have a negligible effect on the files that the probe will map: the probe has a tapered end, the metallic trace and ground are perpendicular to the fields to be mapped (to prevent the fields to be shortened out), and the bulk of the probe is mainly a dielectric material. This supposition was validated via simulation with HFSS. In order to use this probe to map arbitrary 2D vector fields, one needs to map one component of the vector field at a time (as in the probe discussed earlier). First, the probe has to be aligned with its ground planes perpendicular to the orientation of the first field component that is to be

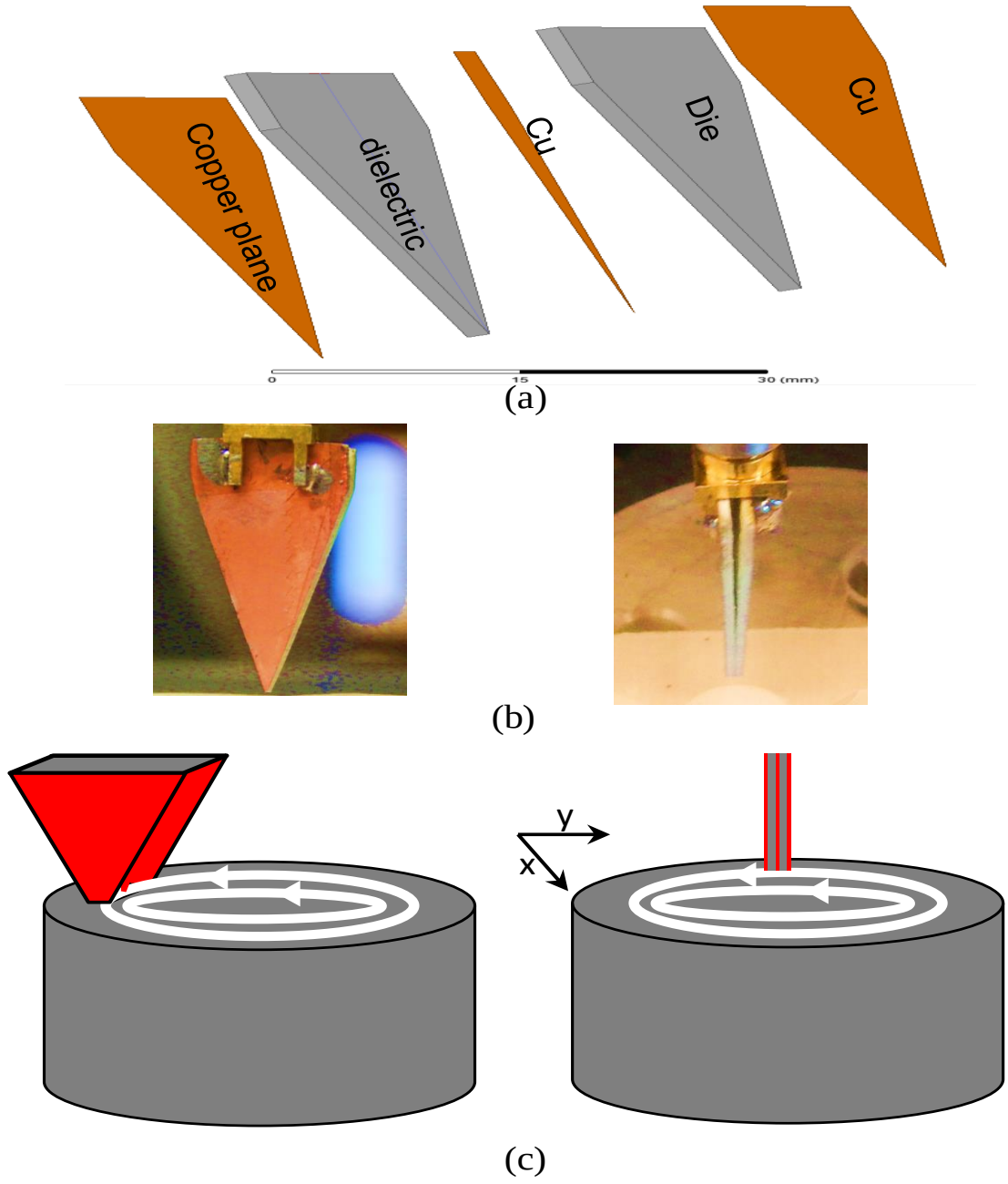

Fig. 3.20. A probe for mapping electric fields in a CDR. (a) Detailed construction of the 'dielectric' probe. Each copper layer is 17μm thick, and each dielectric layer is 0.76 mm thick. The middle Cu trace is 0.5 mm shorter and leaves a dielectric tip near the apex. (b) Front view (left) and side view (right) of the probe. (c) Probe orientations to measure x-component of the electric field in a CDR (left) and the y-component of the electric field (right).

mapped. Then the probe must be rotated by 90 degrees to map the second component (orthogonal component). These two components may then be postprocessed to obtain the 2D electric field map over a surface. This scheme is illustrated in Fig. 3.20c. The probe does not need to touch the surface of the DR to map its field patterns. There can be a small air gap between the probe and the CDR because the tangential electric fields will be continuous between the air-dielectric interface as dictated by boundary conditions for tangential electric fields.

3.3.3 Method for mapping the electric fields in CDRs

The coupled CDR design of subsection 3.3.1 was fabricated. Figure 3.21 shows the measured S-parameters of the fabricated coupled CDR (microwave reflection and transmission properties). The simulated result from Fig. 3.19 has also been included for comparison. The field pattern in the CDR was obtained at a representative frequency of 7.53 GHz within the passband of this structure. The schematic of the experimental setup to map the electric fields in the CDR is shown in Fig. 3.21b. The actual experimental setup is shown in Fig. 3.21c.

As shown in Fig 3.21b and Fig. 3.21c, the coupled CDR structure was attached to a computer-controlled two-axis micropositioner stage. With a Continuous Wave (CW) source at a frequency of 7.53 GHz and a power amplitude of 10 dBm, the input feed line of the coupled CDR was excited. The output feedline was terminated with a 50-ohm load. The probe was positioned at a standoff distance of 0.25 mm from the top plane of the CDR. The probe was connected to a VNA which served to measure the magnitude of the near field leaking out from the CDR at different positions over the top CDR at a single frequency. A LabVIEW program was used to synchronize the probe scan with the field

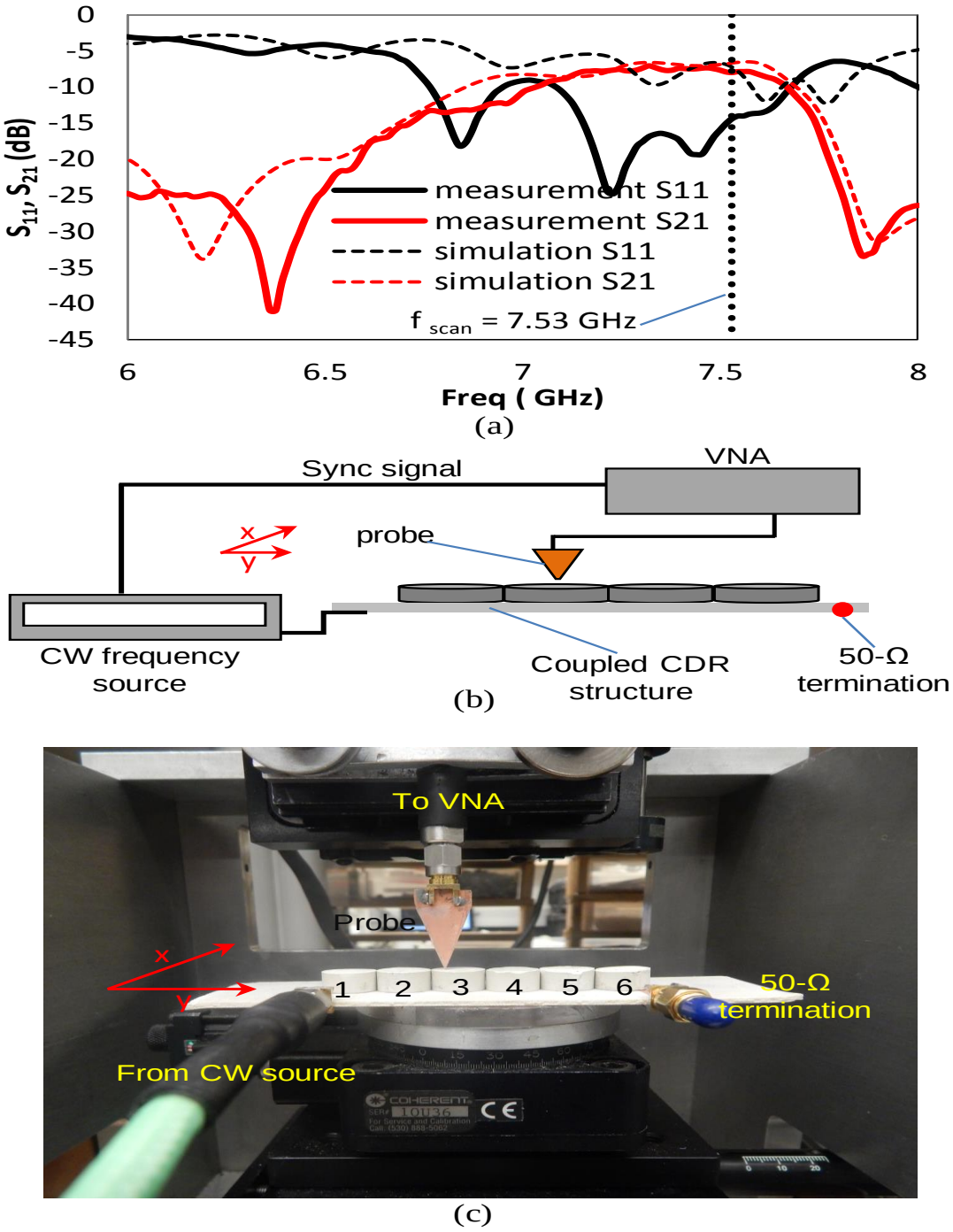

Fig. 3.21. Measured (in thick solid lines) and simulated (in thin dashed lines) S_{11} and S_{21} of the coupled CDR structure. (b) Schematic showing the setup to measure electric field pattern in a dielectric resonator. This schematic shows the case when we used the probe to measure $|E_x|$. We measured $|E_y|$ by rotating the probe by 90 degrees and repeating the 2D scan. Rotating the probe by 180 degrees would not change the measured field patterns since the probe has a symmetric design. (c) The fabricated coupled CDR chain and the setup to map its fields. Each CDR has been numbered for reference.

intensity captured by the VNA. The step size for the scans was 0.175 mm. The results of the field mapping are presented in the next subsection.

3.3.4 Mapped fields in coupled CDRs

The experimental 2D field patterns for CDR#3 (see Fig. 3.21a) are shown in Fig. 3.22. The field patterns are similar to the fields obtained in simulation (compare to Fig. 3.21d). As described earlier, each component of the electric fields was obtained by scanning the probe at two different but orthogonal orientations. Furthermore, a line scan for $|E_x|$ along the y-axis for CDRs #2 and #4 was measured. This line scan was obtained along the middle lines of the CDRs. These line scans are shown in Fig. 3.23. A similar line scan that was extracted from Fig. 3.22 (for CDR#3) has been included in this figure for comparison.

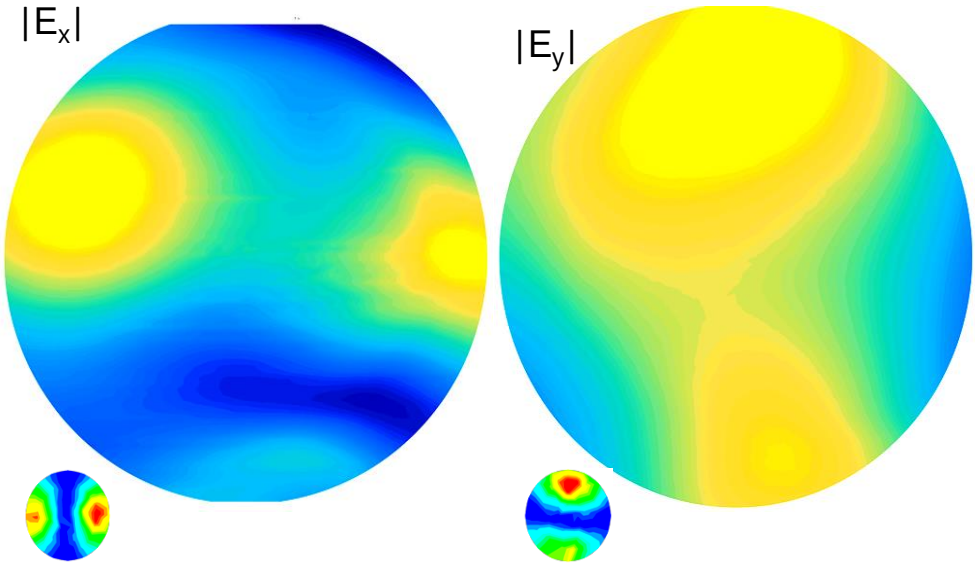

Fig. 3.22. Measured 2D electric field pattern |Ex| (left) and |Ey| (right) for CDR #3 (see Fig. 3.21c). The diameter of the CDR is 13 mm. The size of each pixel of the raw image is 0.175 mm x 0.175 mm. The simulated E-field pattern from Fig. 3.19d is shown in the lower left of each figure for quick reference.

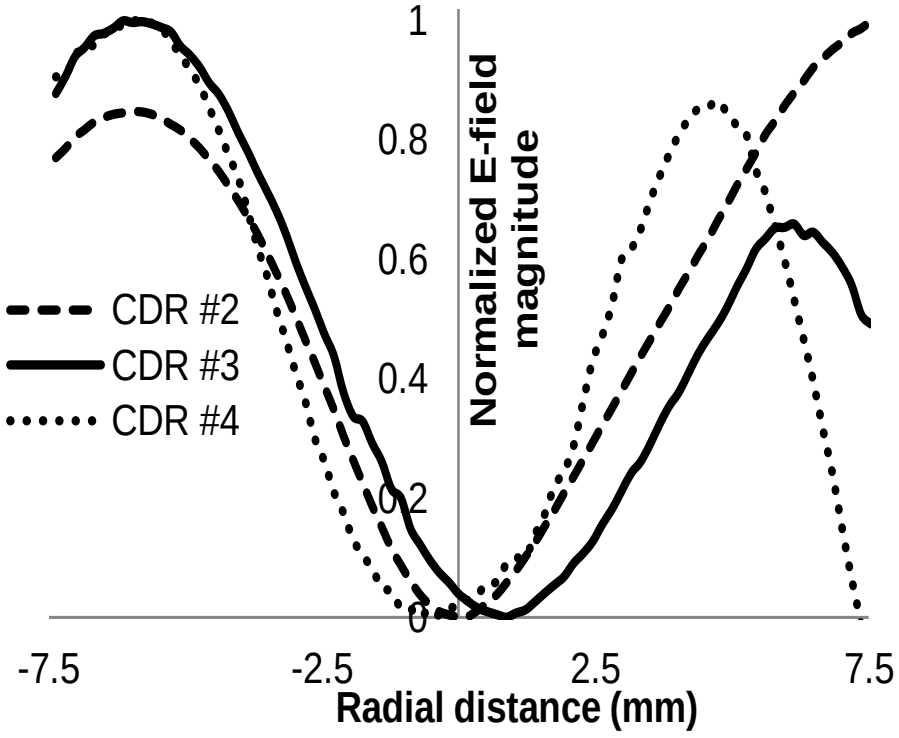

Fig. 3.23. Line scan results of measured $|E_x|$ along the center of CDR #2 and CDR #4. The measured $|E_x|$ along the center line of CDR #3 line that was extracted from Fig. 3.22 has been included for reference.

3.3.5 Coupled CDR chain in a 'multicavity' klystron configuration

Figure 3.24 shows the coupled CDR configured as a 'multicavity' klystron. In this figure, the interaction between atmospheric pressure helium plasma and the field in the resonator was investigated in a setup similar to that in Fig. 3.13. The gap between the two CDR chain is 1 mm, and the plasma voltage was 6.4 kV at a plasma current of ~ 1 mA. Figure 3.25 shows the change in S-parameters of the coupled CDR chains due to the effect of the plasma. The change in the transmission is not as significant as that in the setup of Fig. 3.13 because of the small plasma current in this case. This CDR chain can be further optimized for mode purity for greater interaction with plasma, and also with an electron beam.

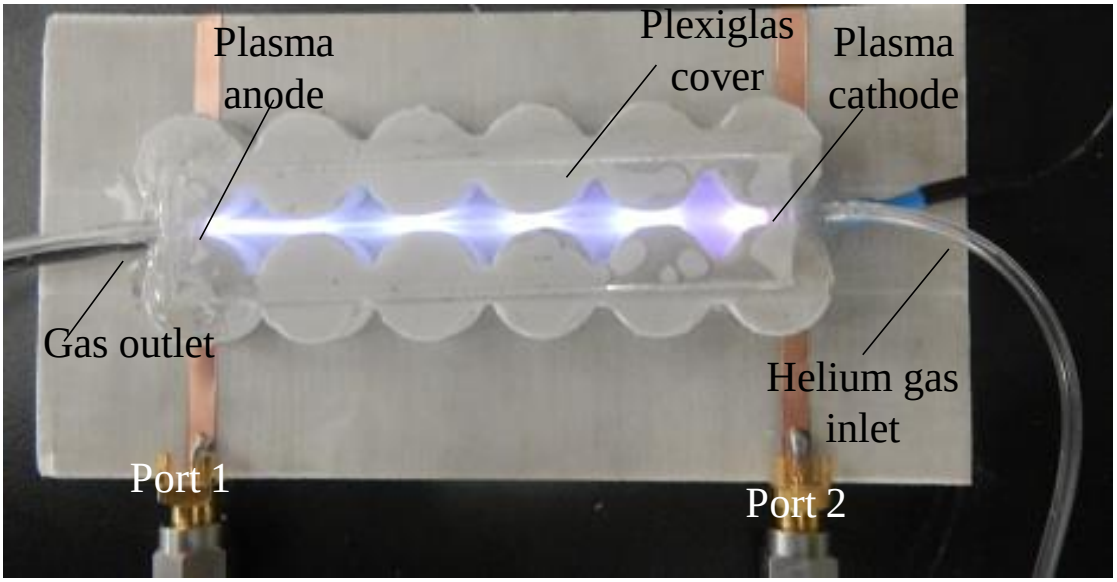

Fig. 3.24. A ‘multicavity’ coupled cylindrical dielectric resonator klystron.

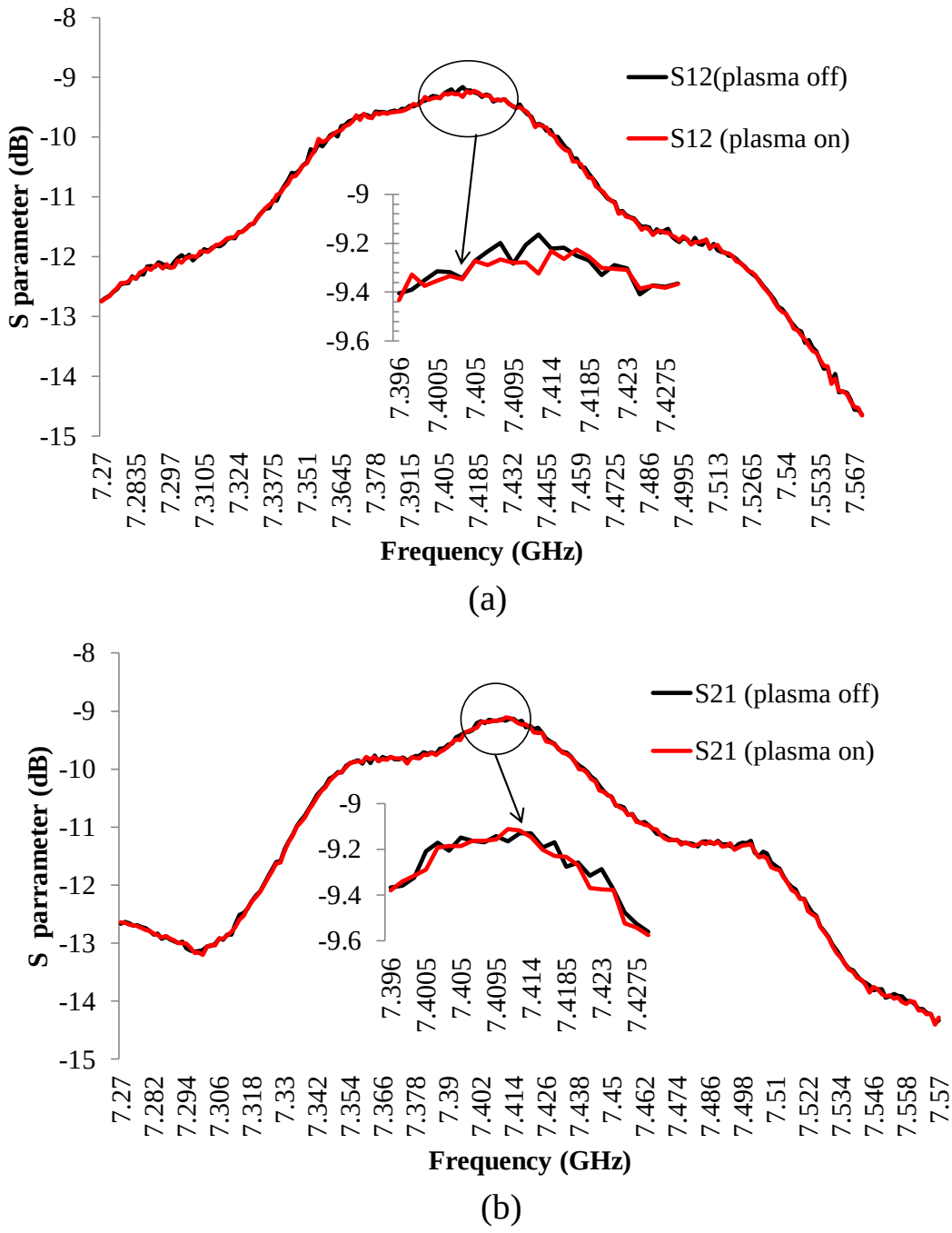

Fig. 3.25. Characterization of the coupled CDR chain structure. (a) Transmission from Port 2 to Port 1 of the coupled CDR chain structure (‘multicavity’ klystron) with and without plasma. Inset is a zoom on the peak of the curve showing slight change transmission (~0.15 dB) with plasma on. (b) Transmission from Port 1 to Port 2 of the coupled CDR chain with and without plasma. Inset is a zoom on the peak of the curve showing a slight change (~0.1 dB) in microwave transmission with plasma on.

3.4 Parylene terahertz resonators

Next, microfabrication processes were developed to fabricate dielectric resonators at terahertz frequency [22]. Parylene-C was used as the dielectric material for fabricating the terahertz CDR via chemical vapor deposition (CVD). Parylene-C has a dielectric constant of 2.62 at 1 THz and attenuation of 0.22 cm^{-1} at 1 THz [23, 24]. The terahertz loss of parylene-C was also measured independently. Figure 3.26 shows the loss measured in multiple layers of ~50 μm-thick parylene-C. The terahertz test system used to characterize these parylene-C layers will be described in the next chapter. Figure 3.27 and Fig. 3.28 show the scanning electron micrograph (SEM) images of the CVD-deposited parylene-C resonators. The CDRs in Fig. 3.27 have a diameter of 100 μm and height of 35 μm. The CDRs in Fig. 3.28 have a diameter of 500 μm and height of 40 μm.

3.5 Conclusions

This chapter has presented some studies on low dielectric constant cylindrical dielectric resonators. These resonators were proposed for use in klystron amplifiers. The mode configuration that was considered needed for klystron application of these dielectric resonators was investigated. Furthermore, interaction of the fields of these resonators with an external plasma beam was present. This interaction with plasma beam demonstrated the possibility of using these resonators with electron beams typical of klystron amplifier circuits.

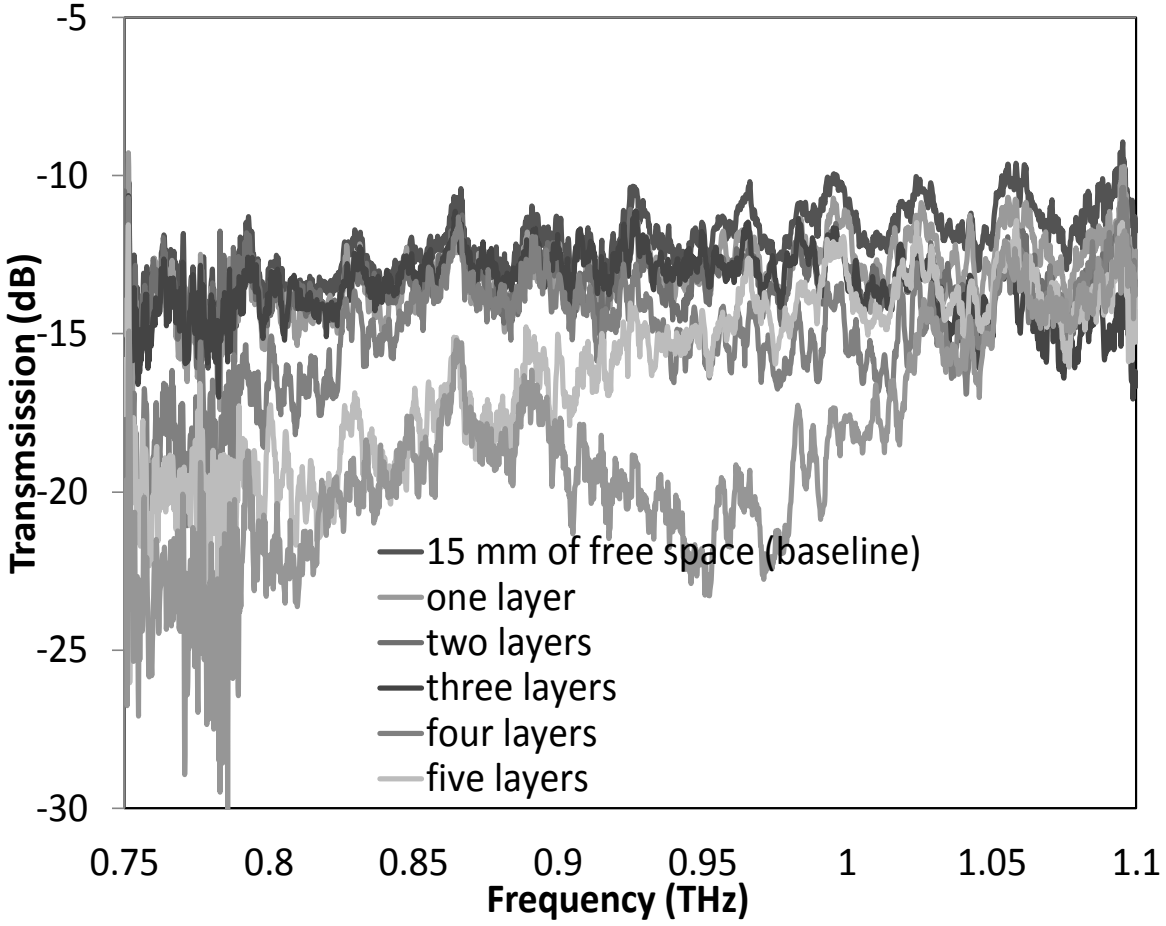

Fig. 3.26. Measured terahertz loss in multiple layers of parylene-C. Each parylene-C layer has a thickness of ~50 μm.

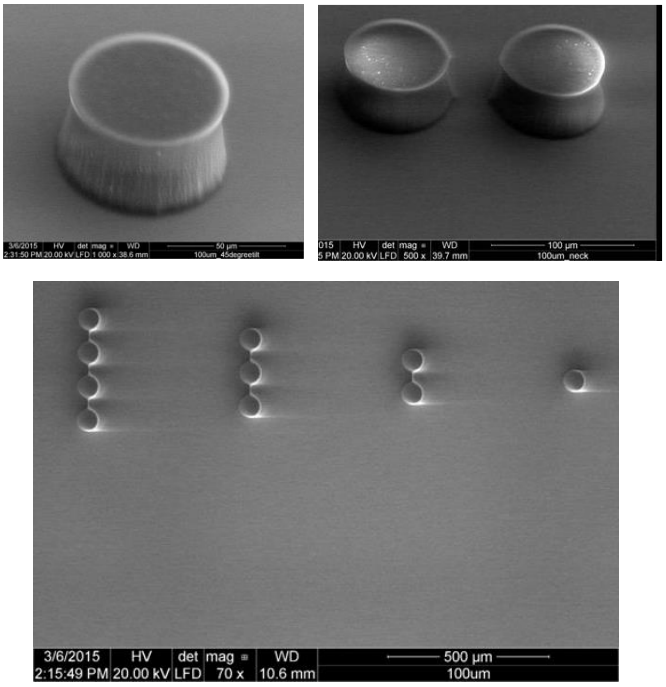

Fig. 3.27. CVD-deposited parylene-C CDRs. CDR diameter and height are 100 µm and 40 µm.

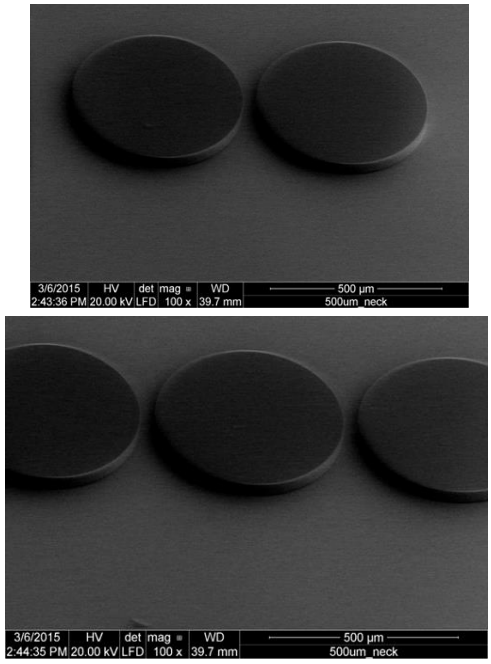

Fig. 3.28. CVD-deposited parylene-C CDRs. CDR diameter and height are 500 µm and 40 µm.

3.6 References

[1] J. W. Gewartowski and H. A. Watson, *Principles of electron tubes*, Princeton, NJ: D. Van Nostrand Company Inc., 1965.

[2] A. S. Gilmour, *Klystrons, traveling wave tubes, magnetrons, crossed-field amplifiers, and gyrotrons*, Norwood, MA: Artech House Inc., 2011.

[3] D. Kajfez and P. Guillon, *Dielectric resonators*, Norwood, MA: Artech House Inc., 1986, pp. 1-539.

[4] S. B. Cohn, "Microwave bandpass filters containing high-Q dielectric resonators," *Microwave Theory and Techniques, IEEE Transactions on*, vol. 16, no. 4, pp. 218-227, 1968.

[5] A. Karp, H.J. Shaw, and D.K. Winslow, "Circuit properties of microwave dielectric resonators," *Microwave Theory and Techniques, IEEE Transactions on*, vol. 16, no. 10, pp. 818-828, 1968.

[6] Some parts of this section were submitted for publication to the IEEE Sensors journal.

[7] (a) J. P. Calame, A. M. Cook, C. D. Joye, B. S. Albright, K. T. Nguyen, E. L. Wright, R. E. Myers, and L. Ludeking, "Dielectric and alternative-configuration-metal slow wave structures for W-Band traveling wave amplifiers," in *2014 IEEE 41st International Conference on Plasma Sciences (ICOPS) Held with 2014 IEEE International Conference on High-Power Particle Beams (BEAMS)*, 2014, p. 1.
(b)O. Fawole and M. Tabib-Azar, "A periodic dielectric resonator structure for terahertz wave amplification," in *Bulletin of the American Physical Society*, 2014, p. 1367.

[8] J. K. S. Poon, J. Scheuer, Y. Xu, and A. Yariv, "Designing coupled-resonator optical waveguide delay lines," *JOSA B*, vol. 21, no. 9, pp. 1665-1673, 2004.

[9] H. Bassen and G. S. Smith, "Electric field probes--A review," *Antennas and Propagation, IEEE Transactions on*, vol. 31, no. 5, pp. 710-718, 1983.

[10] Y. Gao and I. Wolff, "A new miniature magnetic field probe for measuring three-dimensional fields in planar high-frequency circuits," *Microwave Theory and Techniques, IEEE Transactions on*, vol. 44, no. 6, pp. 911-918, 1996.

[11] Y. Gao and I. Wolff, "Miniature electric near-field probes for measuring 3-D fields in planar microwave circuits," *Microwave Theory and Techniques, IEEE Transactions on*, vol. 46 no. 7, pp. 907-913, 1998.

[12] N. Dehghan, A. Porch, S. C. Cripps, and P. H. Aaen, "A novel high resolution E-

field microscope system with applications in HPA diagnostics," in *78th ARFTG Microwave Measurement Symposium*, 2011, pp. 1-3.

[13] A. Karbassi, C. A. Paulson, A. B. Kozyrev, M. Banerjee, Y. Wang, and D. W. van der Weide, "Quadraxial probe for high resolution near-field scanning rf/microwave microscopy," *Applied Physics Letters*, vol. 89, no. 15, p. 153113, 2006.

[14] S. K. Dutta, C. P. Vlahacos, D. E. Steinhauer, A. S. Thanawalla, B. J. Feenstra, F. C. Wellstood, Steven M. Anlage, and Harvey S. Newman, "Imaging microwave electric fields using a near-field scanning microwave microscope," *Applied Physics Letters*, vol. 74, no.1, pp. 156-158, 1999.

[15] R. Kantor and I. V. Shvets, "Measurement of electric-field intensities using scanning near-field microwave microscopy," *Microwave Theory and Techniques, IEEE Transactions on*, vol. 51, no. 11, pp. 2228-2234, 2003.

[16] B. Essakhi, D. Baudry, O. Maurice, A. Louis, L. Pichon, and B. Mazari, "Characterization of radiated emissions from power electronic devices: synthesis of an equivalent model from near-field measurement," *The European Physical Journal of Applied Physics*, vol. 38, no. 03, pp. 275-281, 2007.

[17] X. D. Xiang and C. Gao, "Quantitative complex electrical impedance microscopy by scanning evanescent microwave microscope," *Materials Characterization*, vol. 48, no. 2, pp. 117-125, 2002.

[18] Y. P. Raizer and J. E. Allen, *Gas discharge physics*, vol. 2, Berlin, Germany: Springer, 1997.

[19] D. Staack, B. Farouk, A. Gutsol, and A. Fridman, "Characterization of a dc atmospheric pressure normal glow discharge," *Plasma Sources Science and Technology*, vol. 14, no. 4, p. 700, 2005.

[20] F. Pizarro, R. Pascaud, O. Pascal, T. Callegari, and L. Liard, "Experimental study of RF/microplasma interaction using an inverted microstrip line," in *Antennas and Propagation (EuCAP), 2013 7th European Conference on*, 2013, pp. 1187-1190.

[21] A. Semnani and D. Peroulis, "Nano-plasma tunable evanescent-mode cavity resonators," in *2014 IEEE MTT-S International Microwave Symposium (IMS2014)*, 2014, pp. 1-3.

[22] O. Sakai and K. Tachibana, "Plasmas as metamaterials: a review," *Plasma Sources Science and Technology*, vol. 21, no. 1, p. 013001, 2012.

[23] Mr. Rugved Likhite fabricated these parylene devices.

[24] M. Ji, C. Musante, S. Yngvesson, A. J. Gatesman, and J. Waldman, "Study of

parylene as anti-reflection coating for silicon optics at THz frequencies," in *Eleventh Intern. Symp. Space THz Technology*, 2000, p. 407.

[25] Z. Jiang, M. Li, and X-C. Zhang, "Dielectric constant measurement of thin films by differential time-domain spectroscopy," *Applied Physics Letters*, vol. 76, no. 22, pp. 3221-3223, 2000.

CHAPTER 4

BIOLOGICAL SENSING APPLICATIONS OF TERAHERTZ WAVES

4.1 Introduction

The laws governing the propagation of time periodic electromagnetic waves are given by the universal and elegant Maxwell equations [1]:

$$\boldsymbol{\nabla}.\boldsymbol{D} = \rho \tag{4.1}$$

$$\boldsymbol{\nabla}.\boldsymbol{B} = 0 \tag{4.2}$$

$$\boldsymbol{\nabla} \times \boldsymbol{E} = -j\omega\boldsymbol{B} \tag{4.3}$$

$$\boldsymbol{\nabla} \times \boldsymbol{H} = \boldsymbol{J} + j\omega\boldsymbol{D} \tag{4.4}$$

where **D** is the electric flux density phasor with unit of coulomb/m^2, ρ is the volume charge density (coulomb/m^3), **B** is the magnetic flux density phasor (Weber/m^2), **E** is the electric field phasor (V/m), **H** is the magnetic field phasor (A/m) and **J** is the current density with unit of A/m^2). These equations are valid at any frequency ω in vacuum. The constitutive relationships between these phasors are given as:

$$\boldsymbol{J} = \sigma_\omega \boldsymbol{E} \tag{4.5}$$

$$\boldsymbol{D} = \varepsilon_0 \varepsilon_\omega \boldsymbol{E} \tag{4.6}$$

$$\boldsymbol{B} = \mu_0 \mu_\omega \boldsymbol{H} \tag{4.7}$$

The parameters σ_ω, ε_ω, and μ_ω are the conductivity, relative permittivity, and relative permeability of the propagating medium of the electromagnetic waves. ε_0, and μ_0 are the absolute permittivity and permeability of vacuum. In a nonvacuum medium, these parameters vary as a function of angular frequency ω. Hence, the manifestation of Maxwell's equations differs at different frequencies in the electromagnetic spectrum.

Furthermore, in addition to the frequency dispersion of ε_ω and μ_ω, the manifestation of Maxwell's equations is further complicated by vibrational and molecular resonant frequency of the material in which the electromagnetic wave is propagating. If the propagating wave has a frequency which coincides with the vibrational and molecular resonances of the medium, the material will strongly absorb the wave.

Resonant interaction of a material with an electromagnetic wave of a particular frequency can be used to precisely identify the material when the material is probed with an electromagnetic wave of the right frequency. One of the factors that attract researchers to terahertz research is that a lot of materials have vibrational resonances in the terahertz frequency range. Therefore, a lot of materials can be precisely identified by measuring their terahertz absorption spectrum. This technique is known as terahertz spectroscopy. For example, water vapor has well-known, well-defined absorption lines in the terahertz frequency band. This we confirmed with the experimental setup of Fig. 4.1. Details of the measurement system will be discussed later in this chapter. The terahertz transmission through the water vapor, recorded with the terahertz measurement system, is shown in Fig. 4.2. Table 4.1 summarizes the comparison of our measurement values with the values obtained from the Jet Propulsion Lab (JPL) database [2].

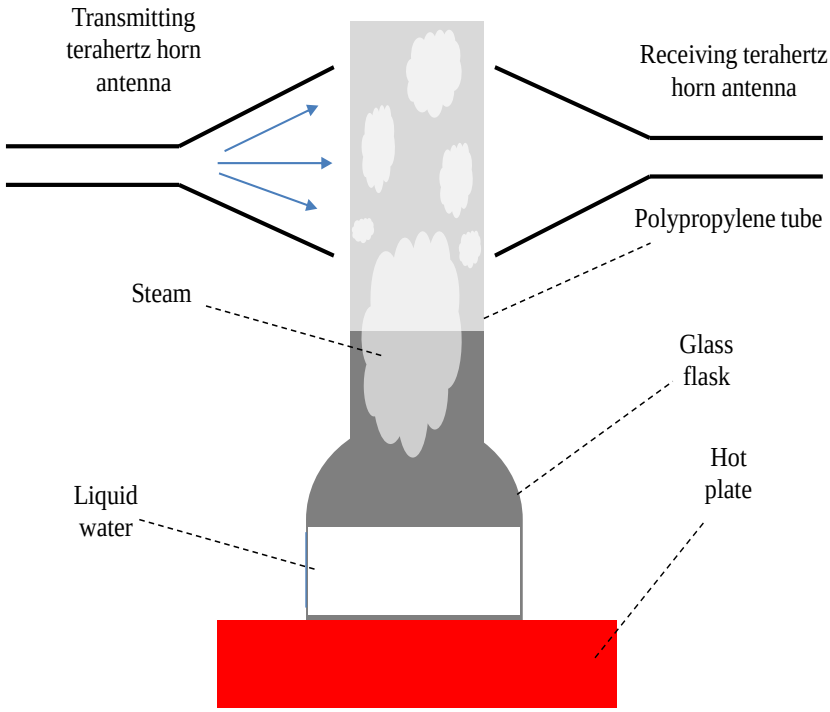

Fig. 4.1. Schematic of experimental setup for water vapor terahertz spectroscopy.

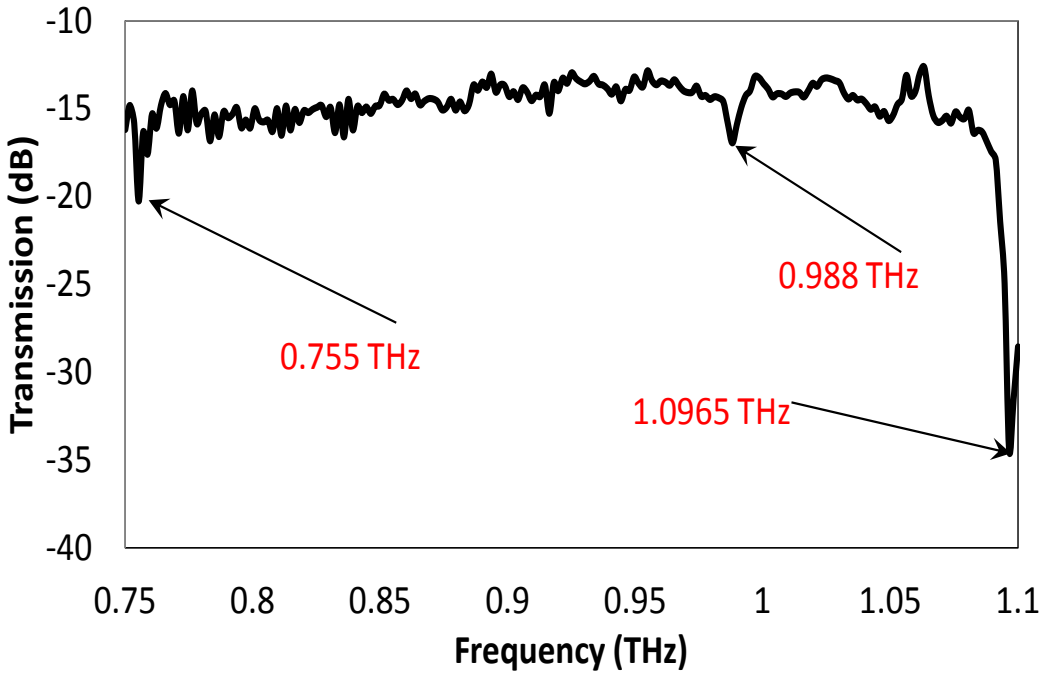

Fig. 4.2. Measured resonant absorption spectrum of water vapor between 0.75 and 1.1 THz.

Table 4.1. Comparison of measured and JPL database values of terahertz resonant absorption frequency and intensity of water vapor

Measured		**JPL database**	
Frequency	*Relative Intensity (dB)*	*Frequency*	*Intensity (Log_{10} nm^2 MHz)*
0.752	-3.32	0.7520331	-0.9985
0.988	0	0.9879268	-1.1374
1.097	-17.46	1.097365	-0.3222

The measured terahertz absorption frequencies of water vapor are close to what was expected, although the strength of the absorption different for well-known values probably due to the difference in temperature and pressure.

Another factor which drives terahertz research is that liquid water, which is a vital component of biological systems, strongly absorbs terahertz waves [3-6]. This absorption is over a wide terahertz frequency band. Hence, terahertz waves can be used to detect small amount of water in a nonaqueous medium. The ε_ω for water over a broad range of frequency is shown in Fig. 4.3 [7]. The imaginary part of ε_ω is a measure of the terahertz absorption of water.

Although terahertz waves are strongly absorbed by other polar liquids, the absorption by water is the strongest of all these polar liquids. [8].

In this chapter, some new biological sensing applications of terahertz waves will be presented. First, some terahertz scanning near-fields probes were developed, and these probes were used to image a number of biological samples. The near-field imaging at terahertz frequencies was then compared with imaging at other frequencies. Furthermore, the capabilities and limitations of using terahertz waves for the real-time noninvasive monitoring of the fermentation activities of yeast cells were presented.

As mentioned in the introductory chapter, one of factors that limited the

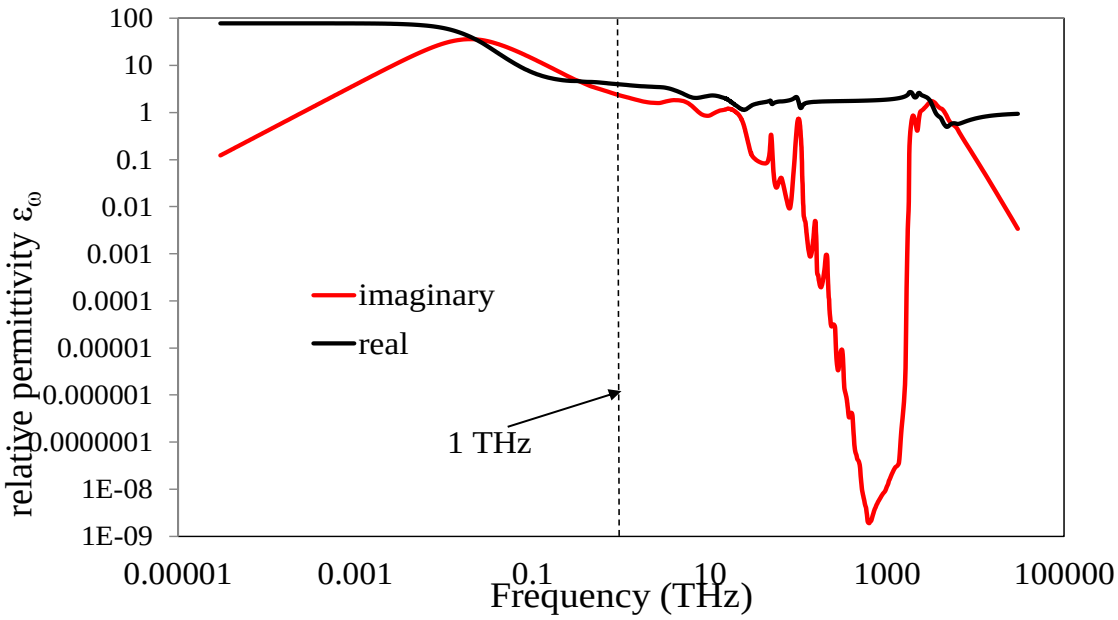

Fig. 4.3. Real and Imaginary ε_ω of water over a broad frequency band [7].

development of terahertz research is the inaccessibility of researchers to terahertz sources and detectors. Therefore, before delving into the aforementioned new applications of terahertz waves, a detailed description of the commercial turn-key terahertz source and detector used in the experiments of this chapter will be presented.

4.2 Overview of a terahertz test system

The terahertz test system used in this work is a vector network analyzer-based system. It is essentially a frequency multiplier/divider. Its general schematic is shown in Fig. 4.4 and a photograph of the system is shown in Fig. 4.5. This terahertz vector network analyzer (T-VNA) presents to its users an operational interface that is similar to that of a traditional vector analyzer. Like the traditional VNA, the T-VNA performs a frequency sweep of excitation signals on a device under test, and it measures the response of the device at each frequency point of the swept excitation [9]. The T-VNA consist of a

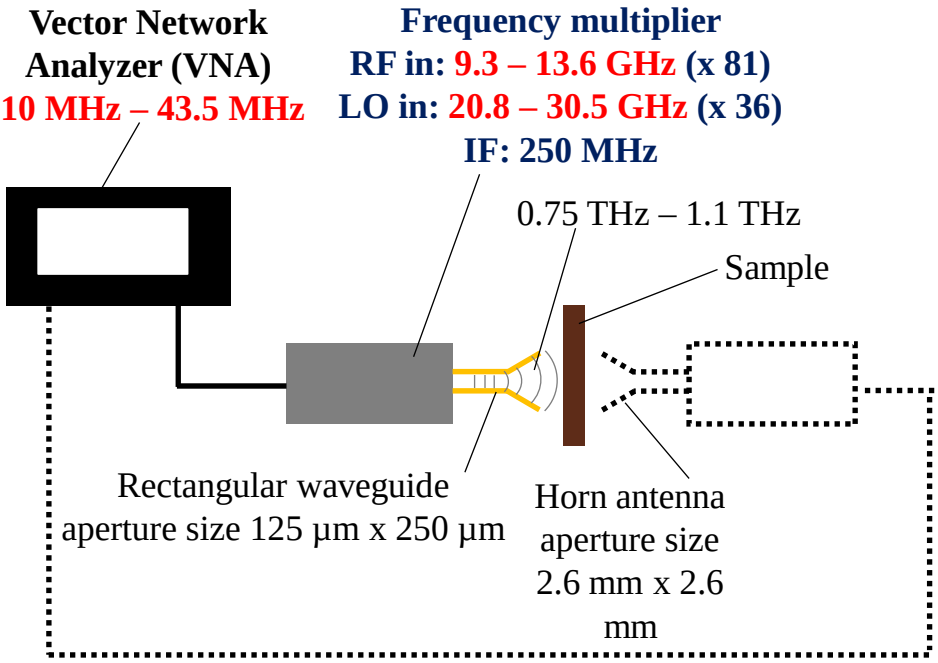

Fig. 4.4. Schematic of the terahertz vector network analyzer (T-VNA).

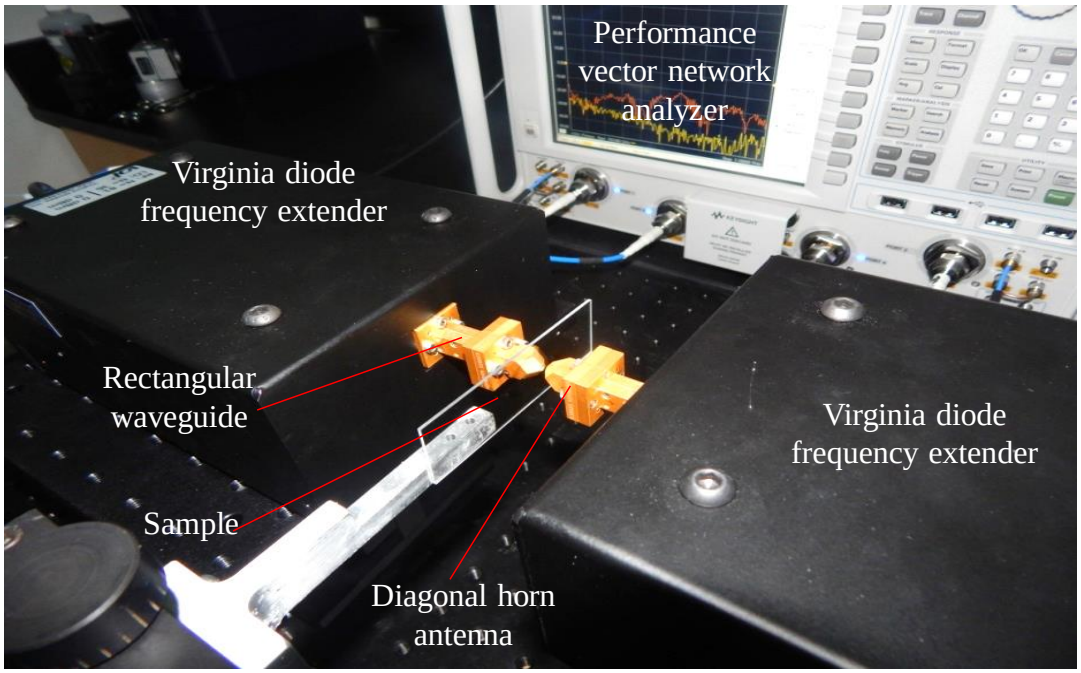

Fig 4.5: Photograph of the T-VNA.

traditional intermediate-bandwidth VNA (~ 0 – 50 GHz). Two frequency extender (VNAX) peripherals of the T-VNA make it possible to multiply the output signal of the traditional VNA to terahertz frequencies (0.75 – 1.1 THz), and also divide the signal from the VNAX into frequencies that can be processed by the traditional VNA. The block diagram of the VNAX is shown in Fig. 4.6 [10].

As shown in Fig. 4.4 and Fig. 4.5, the output of the T-VNA is a WR 1.0 rectangular waveguide. The diagonal horn antenna shown attached to the T-VNA output is optional, and it is used as an effective transition for matching from the metallic waveguide output of the T-VNA to free space [11]. The dimension of the T-VNA rectangular waveguide input/output aperture is 125 μm x 250 μm. The diagonal horn

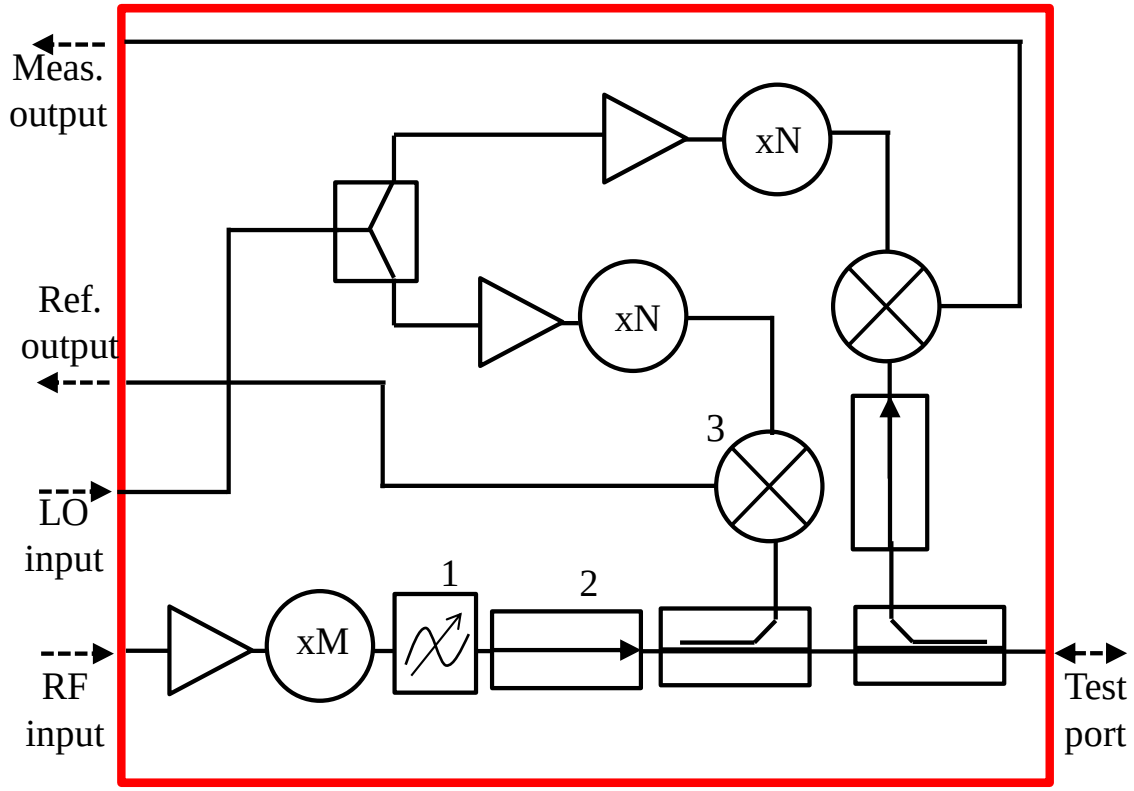

Fig. 4.6. Functional block diagram of a THz VNA frequency extender (VNAX).

antenna has an input aperture size of 125 μm x 250 μm, a taper angle of 2.9 degrees, an output aperture diameter of 1.6 mm and a horn length of 16 mm. The T-VNA is calibrated with a Short-Open-Load-Thru calibration algorithm with waveguide-based calibration standards. Some important performance specifications of the T-VNA are given in Table 4.2 [12].

4.3 Terahertz imaging of biological samples with scanning near-field probes

4.3.1 An introduction to terahertz near-field imaging

Near-field imaging methods are used to overcome the spatial resolution limits of the conventional far-field imaging techniques which are limited by the Abbe diffraction limit [13-15]. The Abbe diffraction limit limits the imaging resolution that can be obtained from an electromagnetic wave of wavelength λ to a minimum of 0.5 λ.

The basic concept of near-field imaging is to generate near fields between samples and sharp tips or at subwavelength apertures. The apertures can be formed in metallic plates and the tips can be sharp metallic or dielectric tips with subwavelength apexes. In all these cases, the role of the aperture/tip is to confine the electromagnetic waves to subwavelength regions. The electromagnetic fields of a near-field probe are

Table 4.2. Performance specifications of the T-VNA

Frequency Band (GHz)	**750-1100**
Dynamic Range (dB)	60
Magnitude Stability (±dB)	1
Phase Stability (±deg)	15
Test Port Power (dBm)	-35

highly nonuniform and result in fairly high spatial resolution images. The contrast of the image is produced by the convolution of these nonuniform fields and the nonuniformities in the electromagnetic properties of the sample. Samples that are opaque at visible frequencies, but transparent at terahertz frequencies, are of particular interest in terahertz near-field imaging. To image a sample with near fields, a detection system is used to measure the amount of interaction between the probe's near fields and each sample point.

Near-field imaging systems operate either in a reflection mode or in a transmission mode. In reflection-mode near-field imaging, the probe is scanned over a sample, and probe-sample interaction manifests itself as a change in the probe impedance that, in turn, results in a change in the resonant frequency and quality factor of the probe. These changes are recorded to obtain a map of the sample's electromagnetic properties as well as its topography. Transmission-mode near-field imaging is only possible in thin and transparent samples and provides similar information as the reflection mode, as well as the sample's thickness variations.

Near-field imaging at microwave and optical frequencies have been developed and carried out during the past 3 decades [14, 15], and some authors have demonstrated the applicability of microwave and optical near-field imaging for biological applications [16, 17]. Recent developments in terahertz science and technology and the easier accessibility to terahertz sources and detectors have motivated the extension of near-field imaging techniques to the terahertz (0.1 – 10 THz) regime [18 - 20]. As mentioned earlier, many bond and free molecules have vibration and resonant absorption bands in the terahertz frequency range (for example DNA macromolecules have some of their vibrational resonances in the terahertz frequency range [21]). Samples that contain these

molecules may be imaged in high resolution with terahertz near-field probes. Furthermore, as mentioned earlier terahertz waves are strongly absorbed by water over a wide bandwidth. Water is a major component and product of bio tissues and exists in different forms in biological systems along with CO_2 and complexes containing C, N, and S. Resonant interaction of terahertz waves with these complexes may be useful in obtaining terahertz images that show metabolism and other processes in biological systems.

Many other research groups have reported near-field probe designs and imaging techniques at terahertz frequencies. Here, in our work, we used our T-VNA measurement system to develop and characterize three different near-field probes (a metallic-tip probe and two dielectric-tip probes). A similar technique has been used for near-field imaging at microwave frequencies [22, 23]. With our T-VNA terahertz near-field imaging system, we obtained the images of different biological samples with metallic, Teflon, and quartz (dielectric) probes. We excited these probes with the diagonal horn antenna of the T-VNA. The imaging resolution of the metallic probe was 445 μm at 0.8375 THz (λ_{free} ~375 μm), while the Teflon probe had a resolution of 230 μm at 1.0422 THz ((λ_{free} ~288 μm), and the quartz probe had resolution of 75 μm at 0.8024 – 0.8424 THz (λ_{free} ~364 μm). With these probes we imaged a slice of mouse brain, a dwarf umbrella tree leaflet section, and a boxelder bug wing section.

The two configurations used in the near-field imaging system of this chapter are shown in Fig. 4.7. Fig. 4.7a illustrates the reflection mode configuration, and Fig. 4.7b illustrates the transmission-mode configuration. Figure 4.8 shows the photograph of a

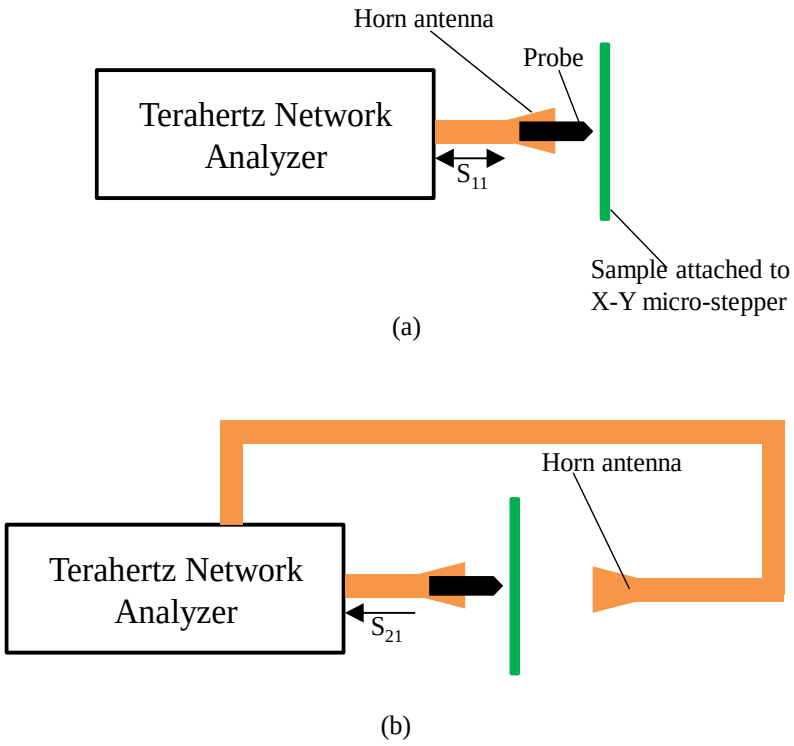

Fig. 4.7. Configurations of our near-field imaging system (a) reflection mode (b) transmission mode.

reflection-mode configuration. The design of these probes, their characterizations, and applications in biological imaging will now be discussed.

4.3.2 A metallic terahertz near-field probe

4.3.2.1 Probe design

Figure 4.9 shows the schematic of the metallic probe. To enable efficient coupling of the metal tip to the rectangular waveguide, a transition region composed of a Teflon region was employed. The Teflon jacket has an inner diameter of 0.66 mm and a wall thickness of 0.30 mm. The base of the metallic tip has a diameter of 0.66 mm and it terminates at a ~100 μm apex. Fig. 4.9a shows other dimensions (longitudinal dimensions) of the probe. Metal wires are reported as terahertz waveguides in the past

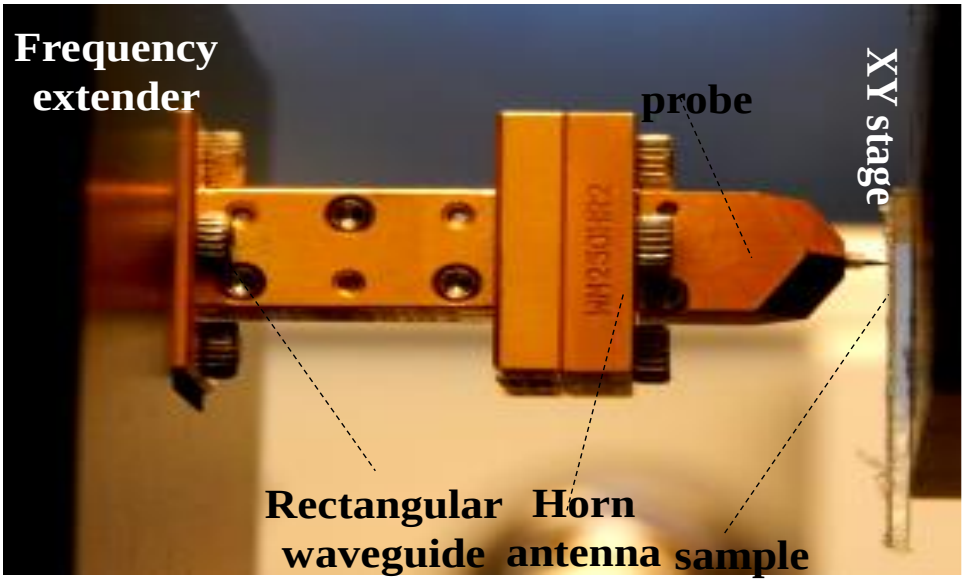

Fig. 4.8. Photograph of the configuration of a probe excited with a diagonal horn antenna.

[24]. The horn antenna aperture produces transverse fields that give rise to longitudinal oscillatory motion of charges in the metallic probe. The Teflon jacket is instrumental in enabling the transverse fields to excite longitudinal motion of charges in the tip as can be seen in Fig. 4.9. The longitudinal fields near the tip strongly interact with the nearby sample. A 3D terahertz full-wave electromagnetic simulation model (with ANSYS HFSS) of this probe is shown in Figs. 4.9b and 4.9c. These figures illustrate the conversion of transverse mode electric fields at the T-VNA waveguide to longitudinal fields at metal tip. Interaction between the fields and a nearby sample changes the probe's impedance and resonant frequency that is measured as a change in S_{11}.

4.3.2.2 Metallic probe characterization

The S_{11} spectrum of the metallic probe in the frequency range of 0.75 – 1.1 THz (the bandwidth of the T-VNA) is shown in Fig 4.10a of Fig. 4.10. The spectrum has

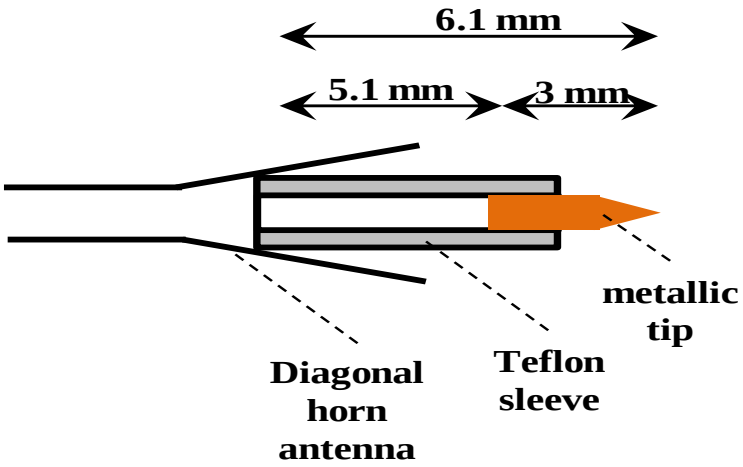

(a)

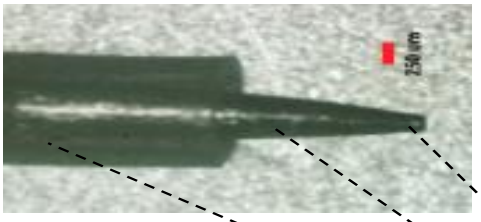

(b)

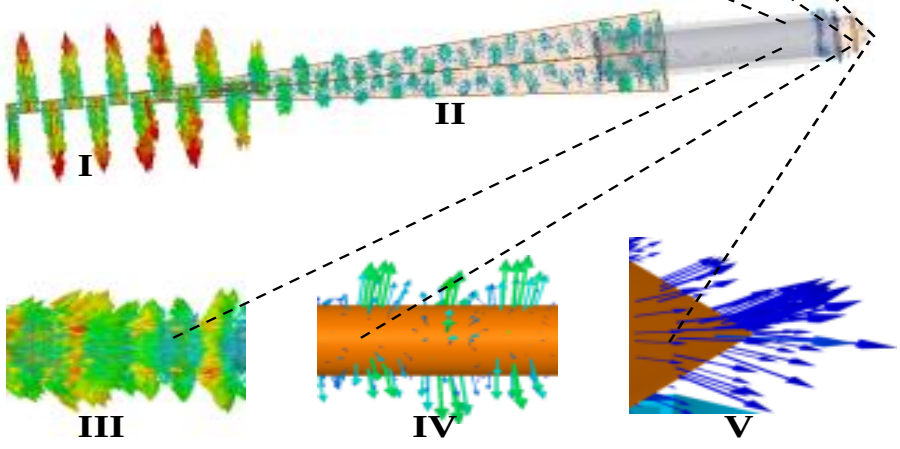

(c)

Fig. 4.9. A metallic probe. (a) A terahertz near-field imaging setup with a metallic probe (b) 3D electromagnetic simulation model of the probe showing the conversion of the transverse mode electric vectors at the extender waveguide and horn antenna (I and II) to radial modes in the Teflon sleeve and at the base of the metallic tip (III and IV) and finally to longitudinal modes at the metallic tip (V). (c) Photograph of the end of the metallic probe. The scale (red line) is 250 μm.

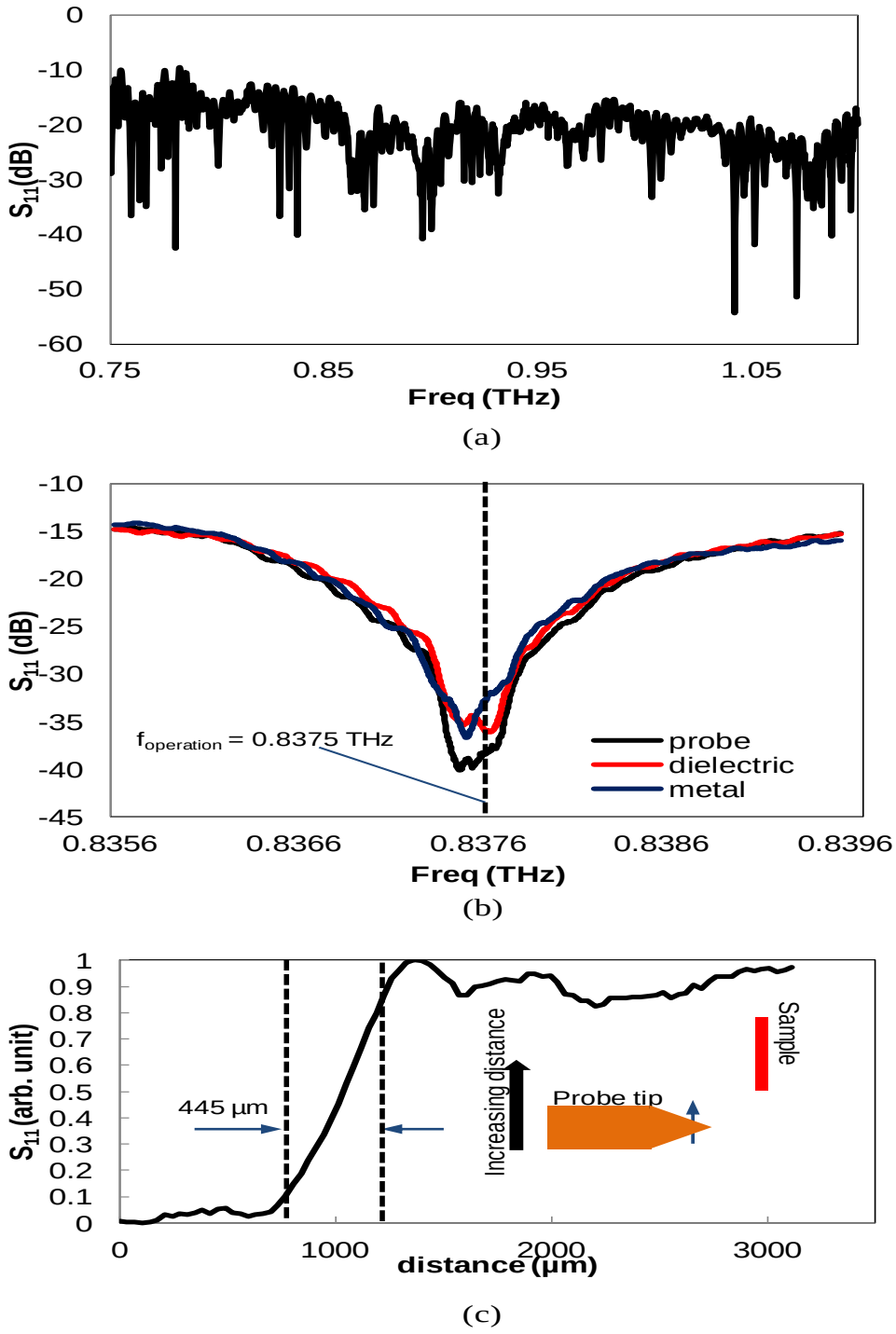

Fig. 4.10. Characterization of the metallic probe. (a) Broadband S_{11} spectrum of the metallic probe showing the multiple resonances. (b) The narrowband S_{11} spectra of the metallic probe for different samples: free space (air), a thin (100 µm) dielectric (εr~2) sample, and a copper sample. The dotted vertical line shows the operation frequency where S_{11} change was maximum. (c) Edge response of the metallic probe at the probe's operating frequency. The spatial resolution of this probe was 445 µm.

many resonances due to multiple reflections of the terahertz waves (from the T-VNA waveguide input/output aperture) at the walls of the horn, the walls of the Teflon sleeves and at the surfaces of the metallic tip. The resonances that changed the most due to the effect of the sample are due to reflections from the probe tip to the T-VNA output/output aperture [25]. Hence, a copper sample and a dielectric sample were placed in front of the probe. The change in S_{11} was largest between 0.8356 to 0.8395 THz, and within this narrow range, $f_{operation} \sim 0.8375$ THz was selected as the operating frequency of the probe (Fig. 4.10b) [17]. The operation frequency is affected by the resonant characteristics of the probe and the dispersion in the sample. To optimize the probe sensitivity, the resonant properties of the probe should be matched with the dispersion characteristics of the sample.

The interaction between the sample and the probe usually shifts the probe's resonant frequency to lower values and it may increase its insertion losses. With the metallic probe, the best operation frequency of the probe was experimentally determined by running the probe in air, over a dielectric, and over a metallic sample and searching for a frequency range where the reflection coefficient change is maximum. Next, the probe's edge response was measured by scanning the probe over the edge of a metallic sample at a stand-off distance of ~50 μm and in steps of 17.5 μm. A LabVIEW program was used to synchronize the probe scan with the S_{11} data capture from the T-VNA at each step. The schematic for this process and the measured edge response are shown in Fig. 4.10c. The spatial resolution (decay length) of this probe was 445 μm (the 10% - 90 % rise distance) as shown in the figure.

4.3.2.3 Terahertz image of a mouse brain slice

Next, the metallic probe was scanned over a slice of mouse brain [26]. Mouse brain imaging with terahertz waves is of importance because it can be extended for use as a clinical tool in human brain surgery. In [27], the authors used a 250 μm spatial resolution near-field imaging system to clearly identify tumors in the brain of a mouse. Furthermore, the authors in [28] and [29] used a terahertz imaging system to diagnose Alzheimer's disease in mice and human brains, respectively. The setup for the mouse brain terahertz imaging is similar to that shown in Fig. 4.8. The standoff distance between the brain slice and the probe tip was ~50 μm, and the scan step size was 35 μm. A step size smaller than the spatial resolution of the probe was used in the scan to improve the quality of the image. The optical and terahertz image of the mouse brain slice are shown in Fig. 4.11. In the obtained terahertz image, the different regions of the mouse brain can be distinguished due to the different terahertz reflectivity of the constituent materials of the brain slice sections.

4.3.3 A Teflon probe

4.3.3.1 Probe design

As mentioned in the previous section, it is hard to efficiently couple terahertz waves into a metallic probe. Poor coupling will affect the quality of the image that can be obtained from a metallic probe (except when an elaborate excitation and detection mechanism is used with the probe in the imaging system). Hence, an alternative to the metallic probe, a dielectric probe made out of Teflon (polytetrafluoroethylene), was investigated. Teflon is a suitable material for use as a probe tip for terahertz near-field imaging because Teflon has very low dielectric constant and loss at terahertz frequencies

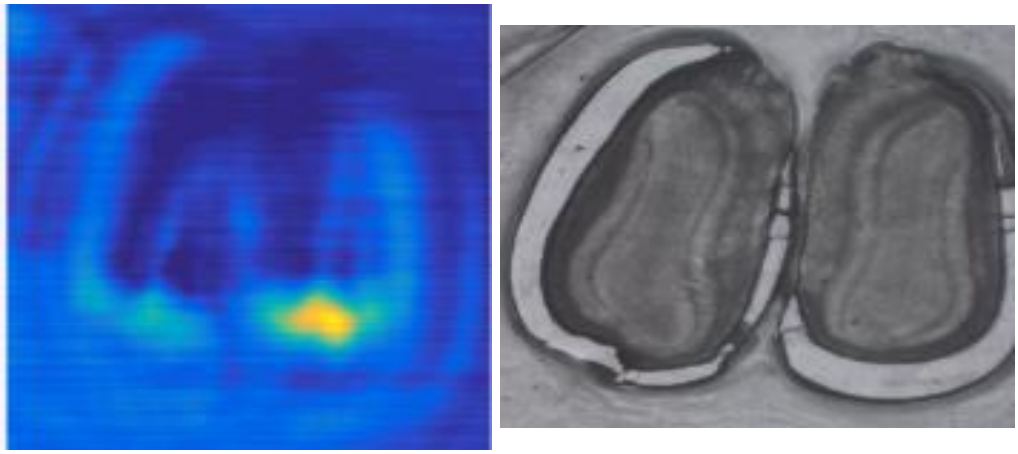

(a) (b)

Fig. 4.11. Mouse brain images. (a) Terahertz image of mouse brain slice (size 5.6 mm x 5.6 mm : 160 pixels x 160 pixels). The image was obtained at 0.8375 THz. (b) Optical image of the brain slice.

[30]. The schematic of the horn-coupled Teflon probe and an image of the tip of the Teflon probe are shown in Fig. 4.12a and Fig. 4.12b. To form the Teflon probe, one end of a Teflon rod was tapered by mechanically polishing the end. The terahertz electromagnetic simulation model (with ANSYS HFSS) of the Teflon probe is shown in Fig. 4.12c. From the terahertz simulation model, it is seen that the Teflon probe effectively guides the terahertz waves from the horn to the Teflon apex for interaction with a sample. However, the electric fields are not tightly confined within the probe. In addition, the orientations of these fields are mainly transverse to the probe's axis.

4.3.3.2 Probe characterization

The change in the S_{11} spectrum of the Teflon probe for metal and dielectric samples in the frequency range of 0.75 – 1.1 THz was measured. The S_{11} showed the largest change between 1.036 – 1.045 THz as shown in Fig. 4.13a of Fig. 4.13. 1.0422 THz was chosen as the operating frequency of the probe. The experimental setup for

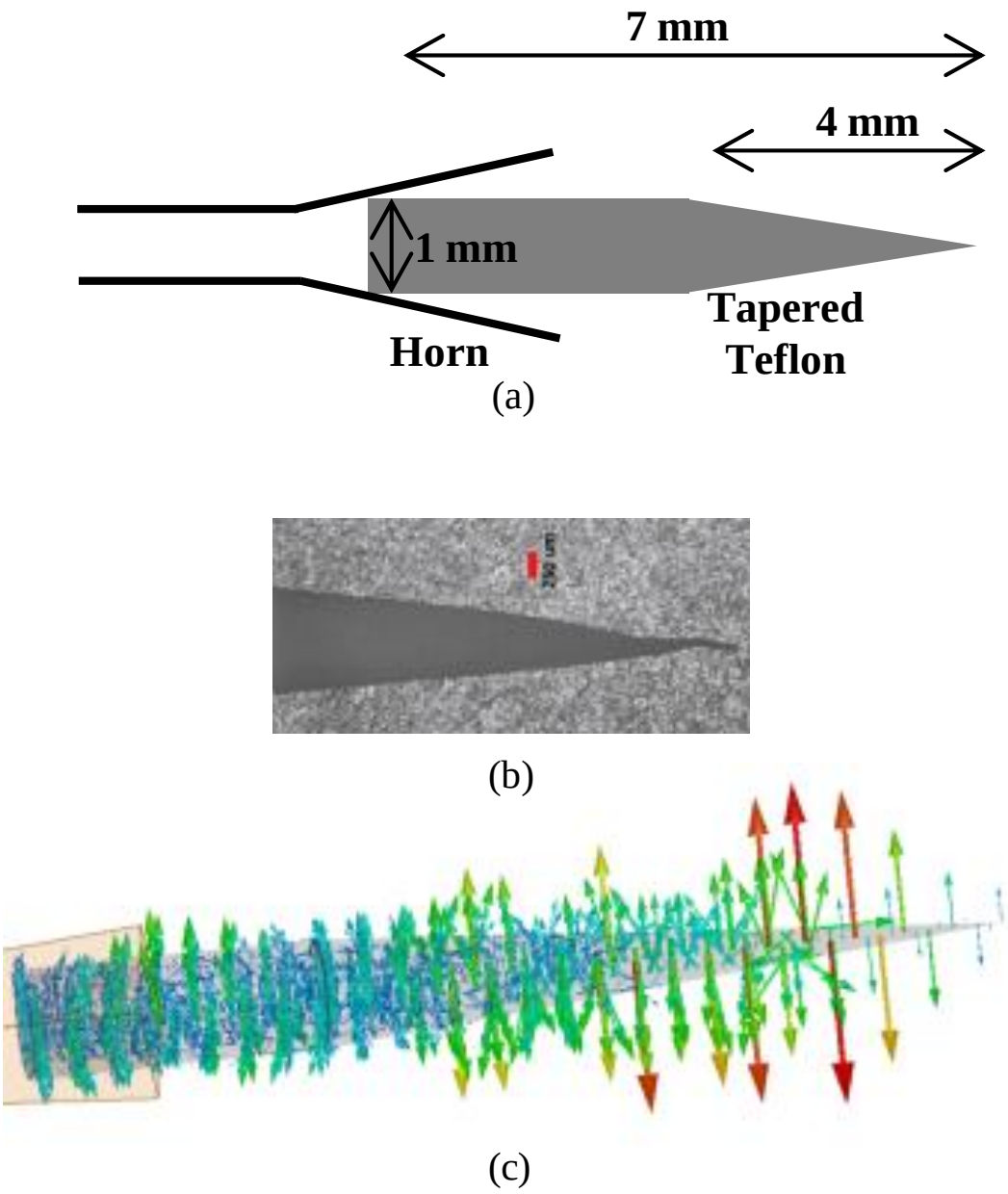

Fig. 4.12. A Teflon probe. (a) Schematic of the horn-coupled Teflon probe. (b) 3D electromagnetic simulation model of the Teflon probe showing the fields at the probe tip. (c) Image of the Teflon probe. The scale (red line) scale is 250 μm.

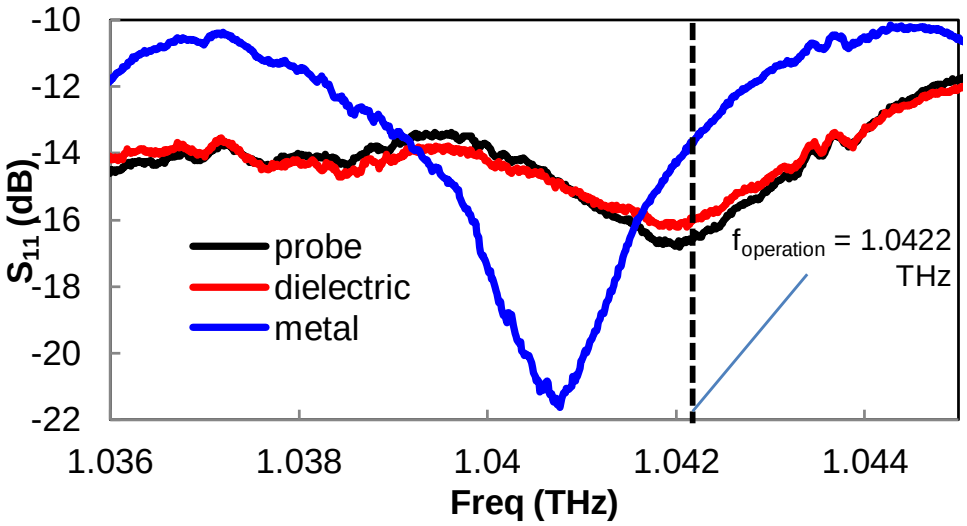

(a)

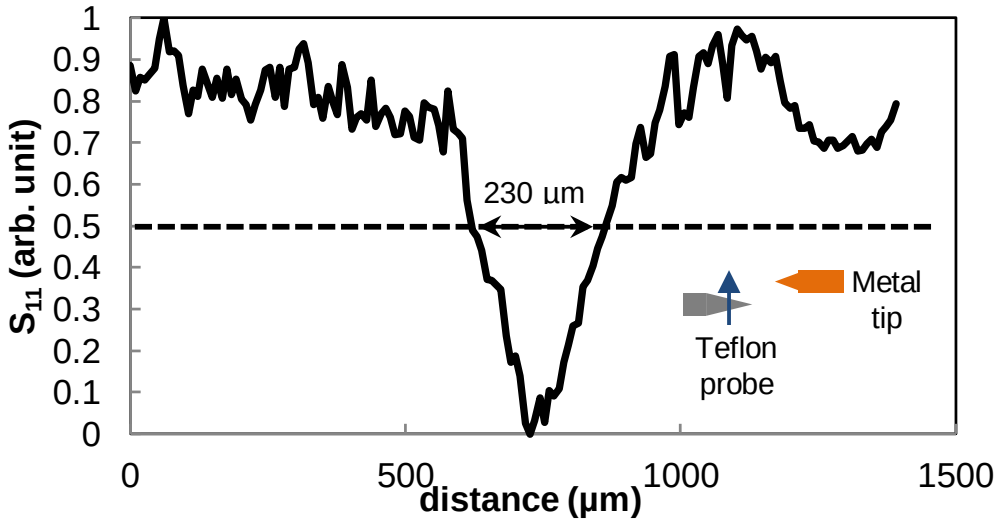

(b)

Fig. 4.13. Teflon probe characterization. (a) The reflection spectra of the metallic probe in free space (air), over a 100 µm thick dielectric (εr~2), a copper sample (metal). (b) The point spread function of the Teflon probe at the probe's operating frequency. The spatial resolution of this probe is 230 µm.

determining the spatial resolution of the Teflon probe is the same as before. However, instead of scanning the probe over a metallic edge, the probe was scanned over a sharp metallic tip to obtain the probe's point spread function (inset in Fig. 4.13b). From the point spread function, the estimated spatial resolution (full-width-at-half-maximum) of the Teflon probe was 230 μm.

4.3.3.3 Terahertz image of the leaflet of a dwarf umbrella tree

The plant leaf/leaflet is a common sample to image with terahertz waves [31, 32] because its veins appear as sharply-defined features in a terahertz image. The veins of the leaf have higher water content relative to the other parts of the leaf, and terahertz waves are strongly absorbed by water making the veins appear as high-contrast features in the leaf's image. With the Teflon probe, we obtained the terahertz image of the leaflet of the *Schefflera arboricola* (the dwarf umbrella tree), a common house plant. The *S. arobricola* has 7-9 leaflets on each petiole. Each leaflet of this plant has a tough and smooth surface with 5-6 pairs of primary lateral veins [33]. The Teflon probe was used to image a section of dorsal (sunlight facing part) of a *S. arboricola* leaflet. This section contains a primary lateral vein and a secondary lateral vein. The standoff distance between the surface of the plant leaf and the probe tip was ~50 μm, and the lateral step size we used to obtain this image was 35 μm. The optical image and the terahertz image of the plant leaflet are shown in Fig. 4.14. It should be noted that the vein features seen in the terahertz image result from both the topography (since the vein region is depressed relative to the other parts of the leaf) and the high water content of the leaf vein.

After mechanically sharpening the Teflon tip, it became less rigid making it susceptible to mechanical drifts and bending. Moreover, as shown above, the Teflon tip

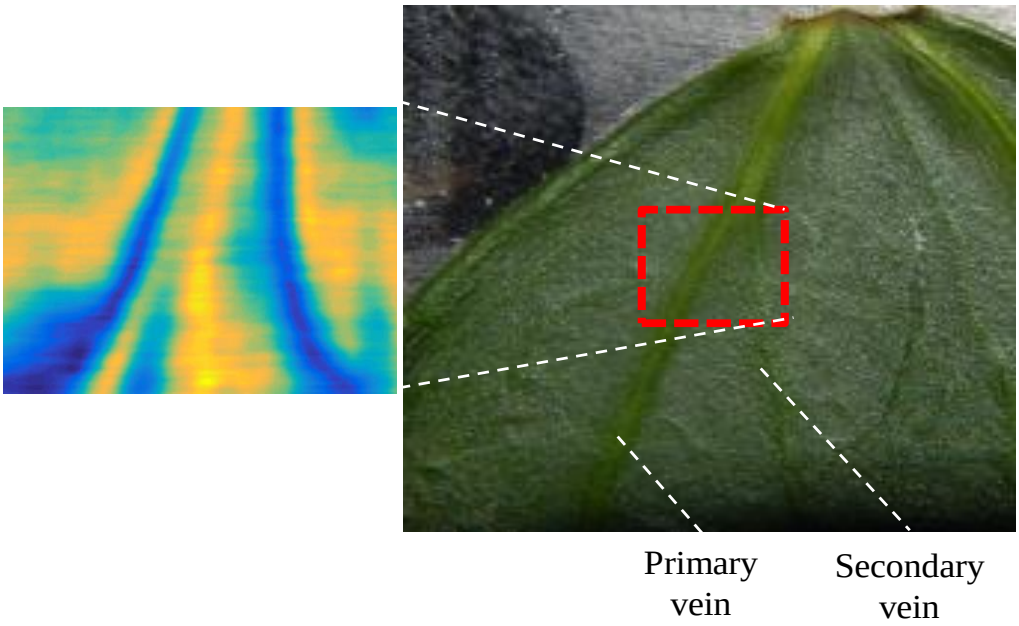

Fig. 4.14. Leaflet images. Left: Terahertz image of a section of the *S. arboricola* leaflet (5.25 mm width 2.80 mm height: 150 pixels by 80 pixels). We obtained the image at 1.0422 THz, at the dotted line mark in Fig. 4.14a. Right: Optical image of the leaflet section.

did not tightly confine the terahertz waves. Therefore, it is necessary to find a better tip material with more robust mechanical properties and larger permittivity than Teflon at 1 THz. A material with these desirable properties is quartz. A quartz probe will be discussed next.

4.3.4 A metalized quartz probe

4.3.4.1 Probe design

Teflon, quartz has very low dielectric losses at terahertz frequencies [34] making it easy to couple terahertz waves effectively unto it. Unlike Teflon, quartz stays rigid after sharpening. Although the terahertz dielectric constant of quartz is about twice that of Teflon, it was still necessary to improve its field confinement using a metallic coating. Metallization improves the confinement of fields in dielectric probes as discussed in [25]

but it can potentially increase probe losses. The quartz probe shown in Fig. 4.15 consisted of a 0.6 mm thick, 1.22 mm wide, and 5.2 mm long ST quartz material. The probe was cut from a quartz wafer and after mechanical polishing it was mildly etched in buffered hydrofluoric acid for a few minutes. The probe was inserted into the horn antenna and was covered with a copper tape with a small hole that exposed a very small area ~50 μm^2 at the end of the quartz tip. The metallic coating confined the electromagnetic fields near the apex of the probe. The schematic, the 3D terahertz full-wave electromagnetic simulation model (with ANSYS HFSS), and the image of the quartz tip probe are shown in Fig. 4.15b and 4.15c.

4.3.4.2 Probe characterization

The S_{11} of the quartz probe did not change appreciably when the probe was used to probe metal and dielectric samples. This irresponsiveness was due to the attenuation of terahertz by the metallization. Hence, to characterize this probe type, an identical probe was designed and the terahertz transmission (S_{21}) between two probes were measured. Fig. 4.16a shows the reverse and forward transmission spectra (S_{12} and S_{21}) between the two identical quartz probes over 0.8024 – 0.8424 THz. This narrow frequency range was chosen because the change in S_{21} and S_{21} were largest. The transmission point spread function (Fig. 4.16b) of the quartz probes was obtained by scanning the two quartz probes relative to each other laterally and recording the frequency-averaged transmission at each lateral position of the scan. The spatial resolution of each quartz probe was extracted to be 75 μm.

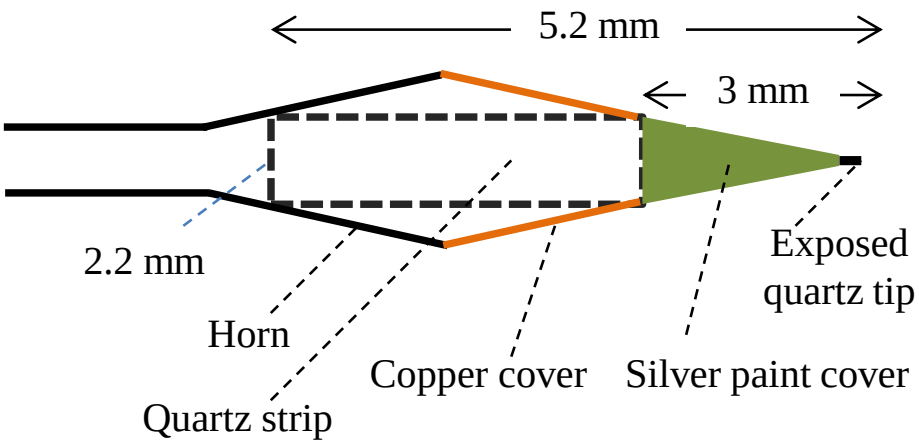

(a)

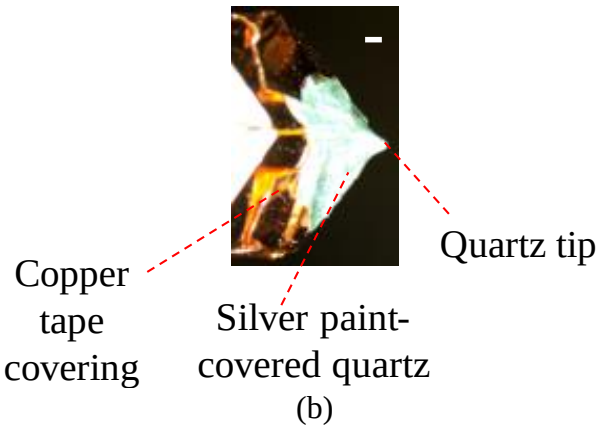

(b)

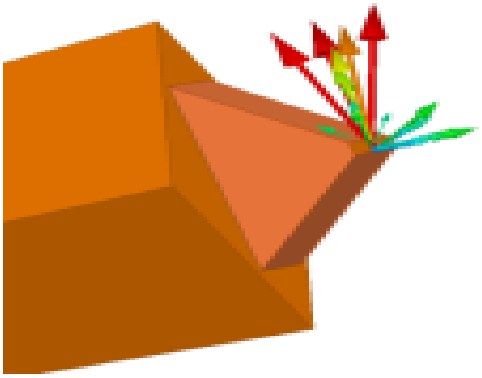

(c)

Fig. 4.15. The quartz probe. (a) Schematic of the quartz probe. (b) The 3D electromagnetic simulation model of the quartz probe showing the orientation of the electric fields at the un-metalized quartz tip. (c) Image of the quartz probe. Scale is 250 μm (white line).

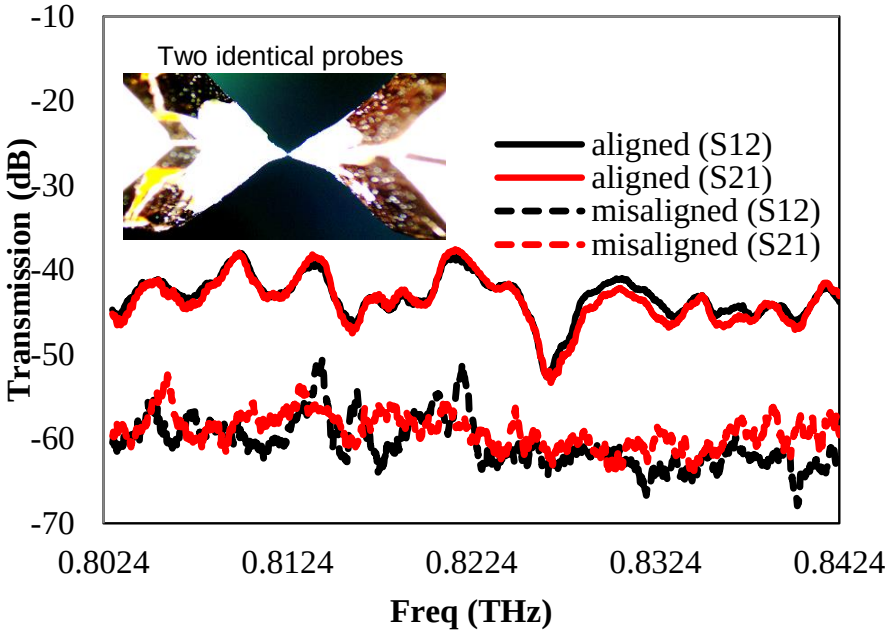

(a)

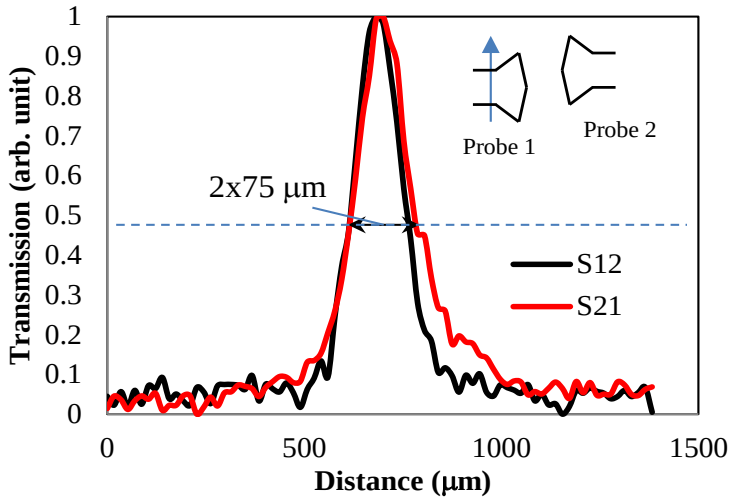

(b)

Fig. 4.16. Quartz probe characterization. (a) The transmission spectra (forward and reverse) of two quartz probes for the setup where we aligned the two probes with a gap of ~ 50 um between them (as shown in the inset) and when we misaligned the probes (not shown). These spectra are in the frequency band within 0.75 – 1.1 THz where the transmission between the two probes is maximum. (b) The point spread function of the quartz probe at probe's operating frequency band. The inset illustrates the scanning technique to obtain the response. The spatial resolution of each probe was 75 μm.

4.3.4.3 Terahertz image of the wing of a boxelder bug

The terahertz imaging system was set up to obtain the image of a section of the wing of the boxelder bug (*Boisea trivittatatus*) as shown in Fig. 4.17. Like the plant leaf, the bug wing has well-defined features, its veins. These features make the bug wing an interesting sample for demonstrating the capabilities of terahertz near-field imaging techniques [35]. Furthermore, infrared spectroscopic imaging of bug wings (dragon dragonfly, damselfly and cicada wing) has provided some unique insight into the biochemical composition of the probed wings. Such insights could be used to discover the origin of the strength of bug wings, which could help in designing novel high-strength materials [36]. In addition, some bug wings showed interesting behaviors when illuminated by visible light (e.g., iridescence), and it is of interest to see if such phenomena occur at terahertz frequencies.

The boxelder bug is a plant bug. Boxelder bugs are hard to come by during the summer, but they can be a pest during the winter. Fall is the time these bugs come out of their hiding in large numbers in a bid to find homes for themselves for the cold winter.

Like most plant bugs, the front wing of the boxelder bug consists of a basal hardened portion (corium), and an apical membranous portion (membrane) [37]. These two portions have different optical transmissions, with the corium being more opaque.

The transition from corium to the membrane of the boxelder bug was investigated with terahertz near-field imaging. In the setup, the back of the bug's wing was illuminated with a terahertz beam from a horn antenna, and the quartz probe was used to measure the near-field transmission through the bug's wing. The schematic for this setup is shown in Fig. 4.18. The bug wing was placed on a two-axis micropositioner,

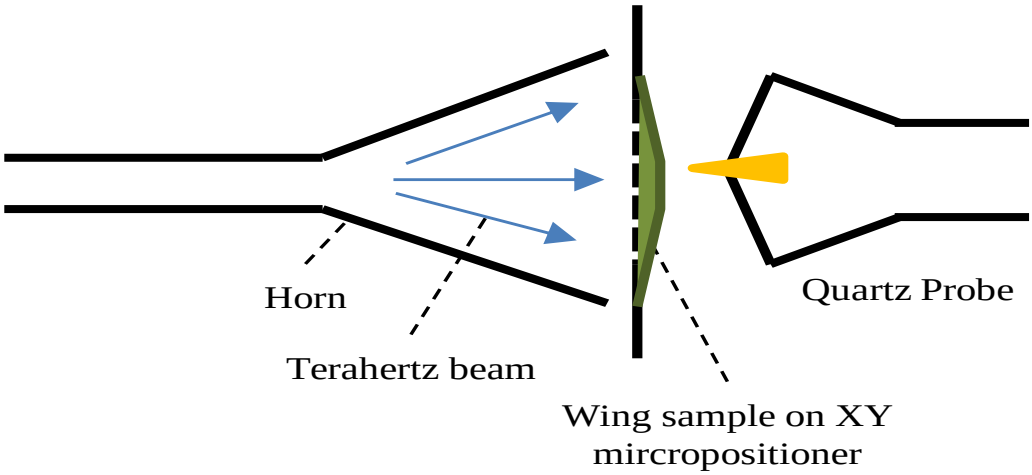

Fig. 4.17. Setup for obtaining the terahertz image of the bug wing mounted on the two-axis micropositioner. The horn antenna back illuminates the bug wing, and the quartz probe picks up the terahertz transmission though the wing at an array of locations on the wing.

and the wing was scanned relative to the fixed illuminating horn antenna and the fixed pick-up probe. There was no standoff between the back of the bug wing and the horn antenna, and the standoff distance between the probe and the front part of the bug was ~50 μm. The scan step size in this setup was 17.5 μm. Fig. 4.18 shows the optical and terahertz images. In the terahertz image blue (dark) indicates low terahertz transmission, yellow (light) indicates high terahertz transmission through the bug wing. To capture the image in Fig. 4.18c, the bug wing was back-illuminated with white light, and the picture of the dorsal side was taken under a 2x magnification optical microscope.

It is remarkable that some sections of the bug wing that showed high transmission to visible light do not show high transmission to terahertz waves. These features are worth further investigation.

Table 4.3 summarizes the three probes, their pros and cons, and their application to imaging different samples that we discussed in this chapter.

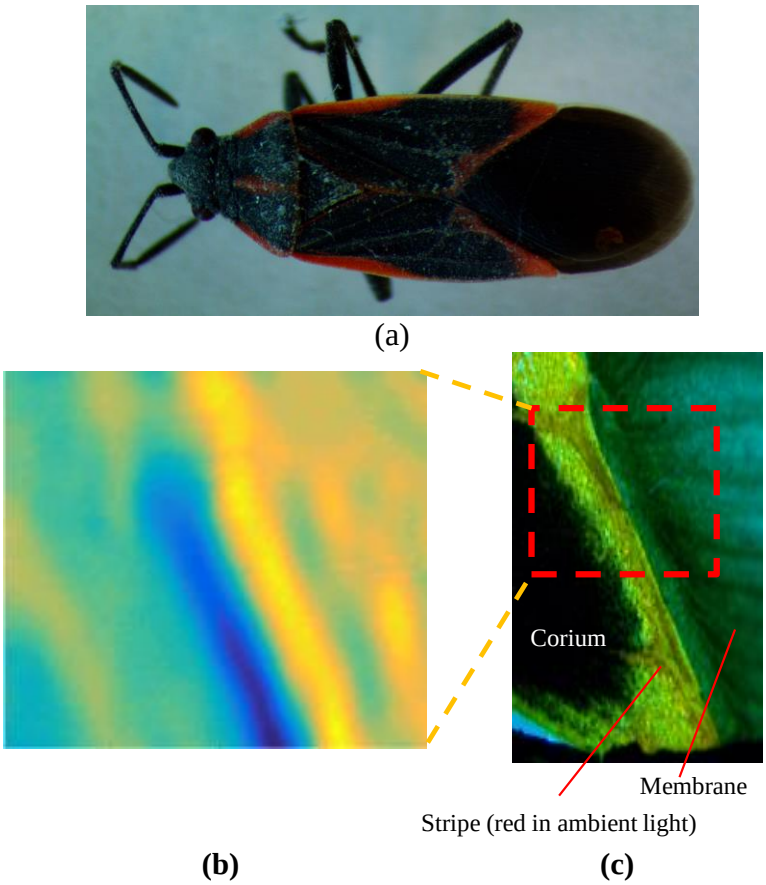

Fig. 4.18. Bug wing images. (a) An adult boxelder bug. (b) Terahertz image of a boxelder bug wing section. The size of the image is 1.2 mm x 1.2 mm (70 pixels by 70 pixels). The light spots are the region with high terahertz transmission; the dark spots are regions with low terahertz transmission. (c) The back-illuminated optical image of the bug wing. The dark part with low light transmission is the corium and the light part is the membrane.

4.4 Yeast fermentation monitoring with terahertz waves

4.4.1 Overview of fermentation and quality control with terahertz waves

As mentioned in the introduction section of this chapter, one of the properties of terahertz waves is that they are strongly absorbed by polar substances like water, ethanol, and sugar. Therefore, some authors have used terahertz waves in applications that involved quantifying polar substances in a solution [6,38,39]. Furthermore, some other authors have demonstrated interesting applications of terahertz waves such as in food

Table 4.3. Summary of near-field terahertz probes

Probe	Resolution (μm)	Resolution (λ)	Advantages	Disadvantages	Application
Metallic	445	1.44λ	Mechanically stable and sharp	Poor coupling to T-VNA	Mouse brain slice
Teflon	230	λ/1.3	Mechanically soft and low loss	Low resolution	Plant leaflet section
Quartz metallized	75	λ/4	Low loss and high resolution	Low signal	Bug wing section

inspection and quality control [40]. However, earlier reports delineating utilization of terahertz waves for quality control have only demonstrated the application of terahertz waves to identify defects in finished products [40]. What has not been shown is terahertz wave's capability to monitor real-time production process for immediate quality control at the production plant.

Fermentation (the conversion of carbohydrates to ethanol, carbon dioxide, lactic acid, glycerol, etc. by yeasts and certain bacteria) is an important production process that can benefit from real-time monitoring. Fermentation has been used in food production processes for thousands of years. Moreover, over the past 15 years, there has been renewed interest in fermentation for the efficient production of bioethanol, a cleaner, more reliable, and renewable alternative to fossil fuels. Controlling and maximizing ethanol yield from the fermentation process requires a real-time (online) method to monitor fermentation without contaminating the fermentation broth. High Performance Liquid Chromatography (HPLC) is a common chemical method used in the analysis of the chemical compositions of the fermentation broth. However, this method is invasive

and cannot be adapted to produce results in real-time. Therefore, a number of authors have used waves in different parts of the electromagnetic spectrum to detect various levels of solutes in the fermentation broth to monitor fermentation progression in real-time. Table 4.4 summarizes the results from some of these authors.

However, there are no reports on the use of waves in the terahertz band for fermentation monitoring, although terahertz waves have been previously used to noninvasively determine the period of yeast activation in sugar/artificial sweetener mixtures [46]. Here, the ability of terahertz waves to reliably detect trace amounts of the sugar and ethanol in water was demonstrated. A similar quantification of sugar and ethanol concentration with terahertz was reported in [39]. Then, for the first time it was demonstrated that terahertz waves are suitable to monitor fermentation in a noninvasive and real-time fashion. Finally, the intrinsic sensitivity of terahertz waves to variations in ethanol concentration in water was compared to the intrinsic sensitivity of electromagnetic waves of other frequencies for ethanol monitoring. It was concluded that microwaves are better suited for ethanol quantification/fermentation. However, an earlier work that used microwave for this purpose did not result in a sensitive measurement system [42].

4.4.2 Ethanol and sugar concentrations quantification with terahertz waves

The experimental setup (Fig. 4.19) for ethanol and sugar quantification consisted of the terahertz VNA that was described in the beginning of this chapter.

To improve the sensitivity of the terahertz system, a Short-Open-Load calibration of the terahertz VNA was performed, with the calibration reference plane at the aperture of the horn antenna. A sample holder (a polypropylene tube) was placed at a stand-off

Table 4.4. Summary of electromagnetic fermentation monitoring at different frequency bands

Frequency range	**Monitored components**	**Not invasive ?**	**Sensitivity of measurement system**	**Reference**
0.3–10 MHz (radio frequency)	beta-dispersion parameters of yeast cells	No		[41]
0.2 – 20 GHz (microwave)	Dielectric constant of fermentation broth	No	4% ethanol by volume, 10g/L sugar	[42]
0.75 – 1.1 THz (far infrared)	Dielectric constant of fermentation broth	Yes	0.3% ethanol ,1.5% sugar by weight	This work
12 – 120 THz (mid infrared)	Optical cell density, glucose, ethanol	No	0.546 optical density, 1.386 g/L of glucose, 0.985 g/L ethanol	[43]
130 – 270 THz (near infrared)	glucose, ethanol, glycerol	Yes and No	9 g/l glucose, 2.4 g/l ethanol, and 1 g/l glycerol	[44]
270 – 430 THz (Short-wavelength near infrared)	Water, ethanol, yeast	Yes	0.27 % by weight ethanol (prediction error)	[45]

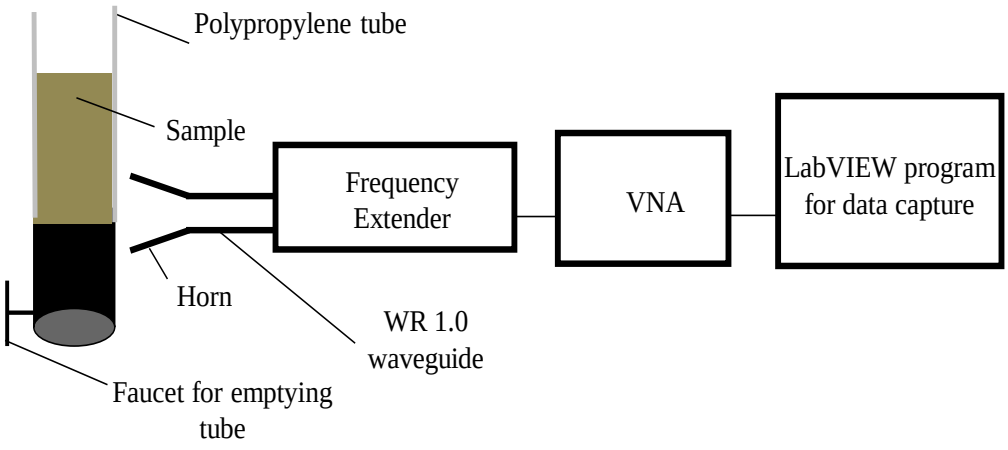

Fig. 4.19. Schematic of setup to measure terahertz reflection properties of sugar and ethanol solutions, and of a fermentation broth.

distance of 0.15 mm from the horn aperture, at normal incidence. The sample holder had a diameter of 15 mm, and a wall thickness of 0.6 mm.

Sugar solutions of various concentrations were prepared by dissolving pure granulated sugar in deionized water, and then the terahertz reflections of these solutions were measured. Ethanol solutions were obtained from laboratory-grade ethanol in a similar manner, and terahertz reflections for different ethanol concentrations were measured.

The terahertz reflection for different concentrations of sugar and ethanol are shown in Fig. 4.20 and Fig. 4.21, respectively. It was observed that due to the Fabry-Pérot effects at the wall of the sample holder, the ethanol and sugar mixtures are selective to terahertz frequencies (a surface plasmon resonance-like effect). It was observed that the highest terahertz reflection sensitivity to ethanol and sugar concentration variation was in the frequency range of 0.913 - 1.023 THz and 0.858 - 0.935 THz, respectively. This difference in frequency range of sensitivity could allow the separation of the terahertz response of ethanol and sugar in an aqueous solution in which both solutes are

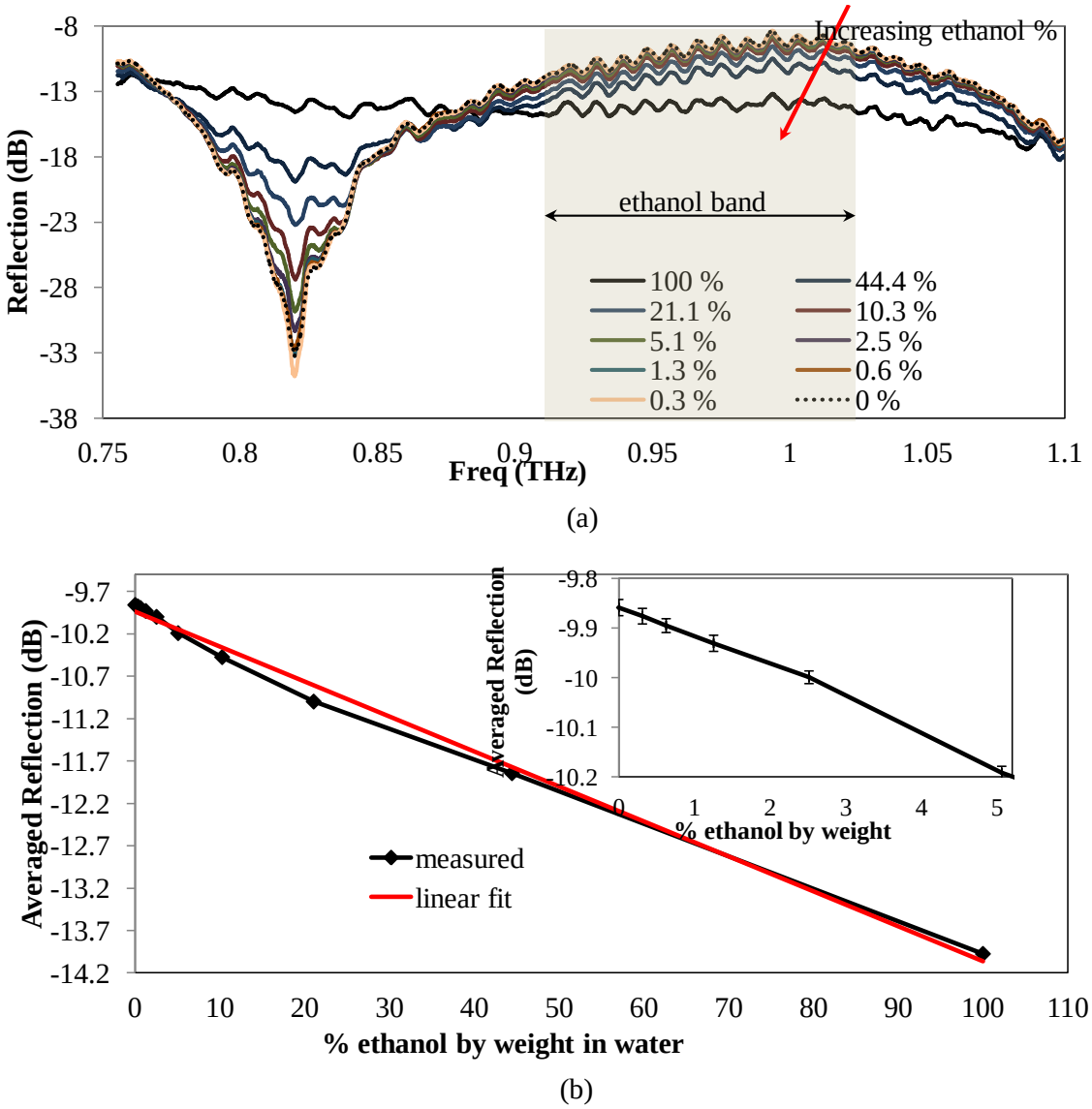

Fig. 4.20. Terahertz reflection spectra for different ethanol concentrations (% by weight in water). (a) Reflection spectra from 0.75 – 1.1 THz. (b) Frequency-averaged reflection in the frequency range of highest ethanol sensitivity (0.913 – 1.023 THz). Inset is a zoom-in on the smaller ethanol concentration range.

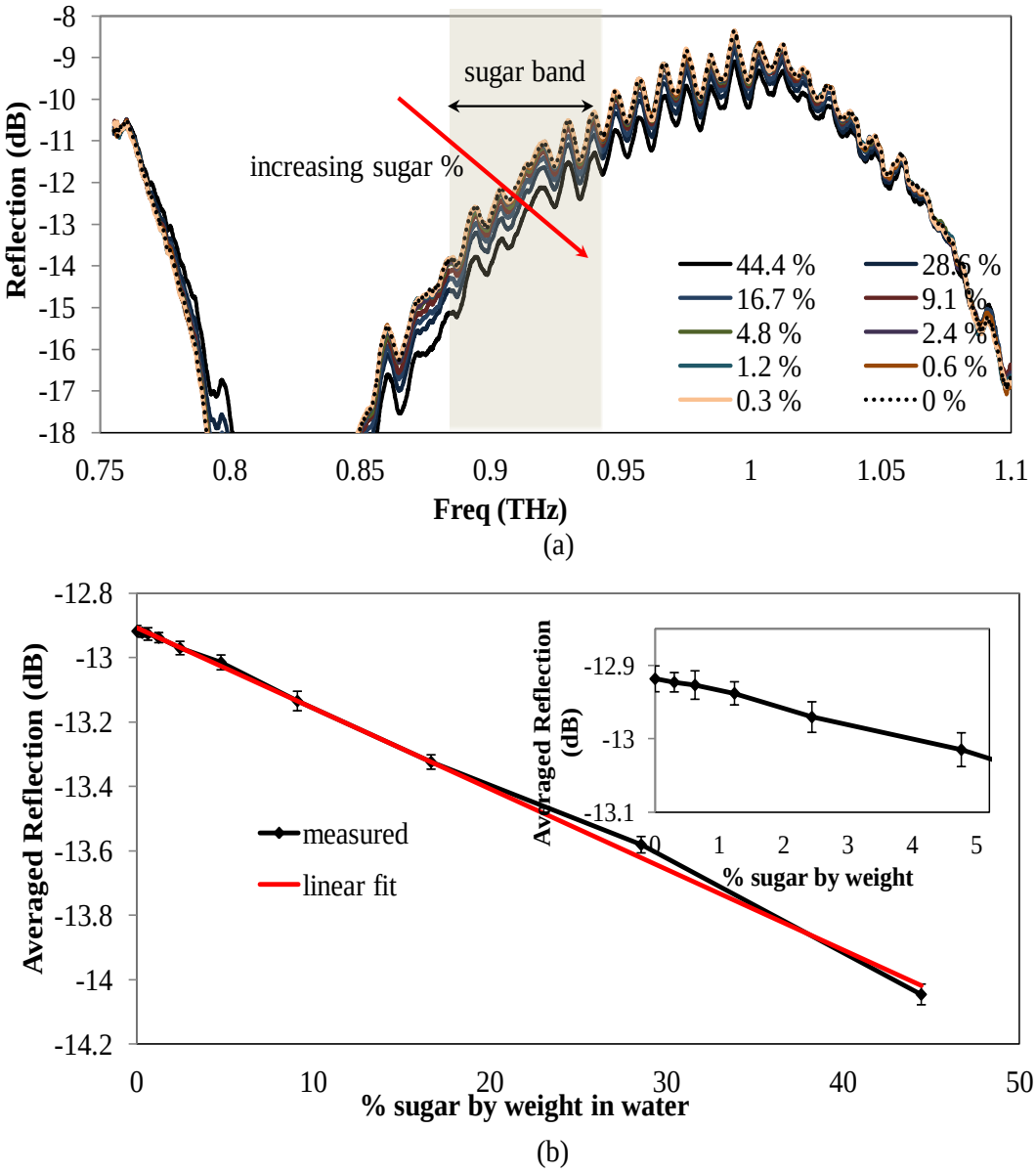

Fig. 4.21. Terahertz reflection spectra for different sugar concentration (% by weight) in water. (a) Reflection spectra from 0.75 – 1.1 THz. (b) Frequency-averaged reflection in the frequency range of highest sugar sensitivity (0.858 – 0.935 THz). Inset is a zoom-in on the smaller sugar concentration range.

present. Fig. 4.20b and Fig. 4.21b show the frequency-averaged reflection for different ethanol and sugar concentration in water, respectively. The error bars are standard errors for four consecutive measurements. The slopes of the linearly-fitted curves in Fig. 4.20b and Fig. 4.21b, for the averaged ethanol and sugar reflection in their respective frequency bands of highest sensitivity are -0.0412 dB/% and -0.0250 dB/%, respectively.

4.4.3 Real-time monitoring of yeast fermentation

Next, a fermentation broth was prepared by dissolving 4 grams of pure granulated sugar and 2 grams of Fleischmann's active dry yeast in 20 ml of deionized water at 24 °C. A control broth was also prepared by dissolving 2 grams of yeast in 20 ml of deionized water at 24 °C. A syringe needle was used to extract samples from these preparations. The syringe needle (of inner diameter 0.16 mm) also doubled as a filter that prevented the extraction of large yeast particles into the sample broths. The time evolution of the terahertz reflection of these broths was measured using the setup of Fig. 4.19.

The control broth was first monitored, and then the fermentation broth. Figure 4.22 shows the broths at different times into the monitoring. It was observed that the yeast started forming sediments (flocs) [47] 17.5 hours after the preparation of both fermentation and control broths. These sedimentation activities were also observed in terahertz reflection measurements as will be discussed later.

The frequency-averaged reflection plots over time for the fermentation and control broth are given in Fig. 4.23a for the frequency band of highest ethanol sensitivity (0.913-1.023 THz, see Fig. 4.20), and in Fig. 4.23b in the frequency band of highest sugar sensitivity (0.858-0.935 THz, see Fig. 4.21).

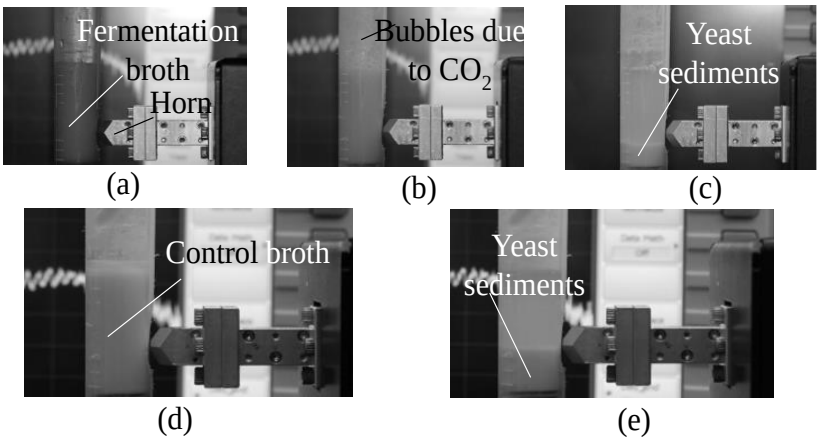

Fig. 4.22. Photographs of fermentation monitoring stages. (a) Fermentation broth at 0 hours. (b) Fermentation broth at 1 hour. (c) Fermentation broth at 30 hours. (d) Control broth at 0 hour. (e) Control broth at 20.2 hours.

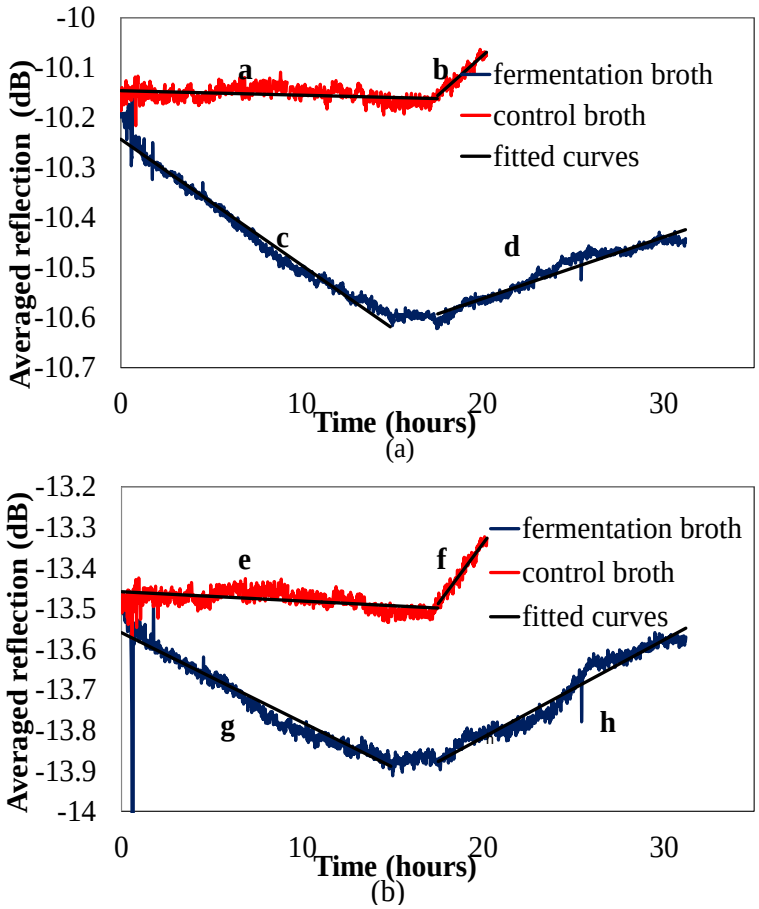

Fig. 4.23. Monitoring fermentation in the frequency band of highest (a) ethanol sensitivity. (b) sugar sensitivity. The different slopes observed for the curves are indicated by alphabetic characters.

In Fig. 4.23, the frequency-averaged terahertz reflection of the fermentation and control broth were plotted every minute for a period of 30 hours and 20.2 hours, respectively. It was observed that from time 0 to 17.5 hours, the terahertz reflection of the fermentation broth decreased with time due to the production of ethanol that was accompanied by the production of carbon dioxide (CO_2). The depletion of sugar due to fermentation would have less effect on terahertz reflection than the production of ethanol since the measurement setup is more sensitive to ethanol than to sugar.

The terahertz reflection of the control broth from 0 hour to 17.5 hours showed no remarkable change. However, beyond 17.5 hours, the terahertz reflection of both the control and the fermentation broth increased due to the effect of yeast sedimentation. This is reasonable since dispersed yeast would lower the overall dielectric constant of a solution, and hence reduce the terahertz reflection. Therefore, when the yeast formed sediments, the terahertz reflection would increase.

However, the continuous production of ethanol due to fermentation would mitigate the increase in terahertz reflection. This could be seen in the greater rate of increase in terahertz reflection in the control broth when compared to the fermentation broth. Furthermore, after 17.5 hours, the slope of the monitored reflection is lower in the ethanol band than in the sugar band, showing that the ethanol band is more sensitive to ethanol than to sugar. Table 4.5 is a summary of the slopes of the curves we fitted to the measured reflection curves (see Fig. 4.23).

Table 4.5. Slope of each of the fitted curves in Fig. 4.23

	Ethanol band		**Sugar band**	
	Control	**Fermentation**	**Control**	**Fermentation**
First slope (dB/hr)	-0.0009 (a)	-0.0252 (c)	-0.0023 (e)	-0.0221 (g)
Second slope (dB/hr)	0.0321 (b)	0.0123 (d)	0.0598 (f)	0.0240 (h)

4.4.4 Intrinsic limitation of terahertz waves for detecting ethanol concentration in water

The frequency dispersion of the complex relative permittivity ε*(f) of a mixture of ethanol and water mixture is given by the triple term Debye relaxation model [54]:

$$\varepsilon^*(f) = \varepsilon_\infty + \frac{\Delta\varepsilon_1}{1 + i2\pi f\tau_1} + \frac{\Delta\varepsilon_2}{1 + i2\pi f\tau_2} + \frac{\Delta\varepsilon_3}{1 + i2\pi f\tau_3} \quad (4.8)$$

f is the frequency, ε_∞ is the high-frequency relative permittivity of the mixture, $\Delta\varepsilon_i = \varepsilon_i - \varepsilon_\infty$ are the dielectric increments (the difference between the low-frequency relative permittivities of the mixture and the high-frequency relative permittivity), $\Delta\tau i$ are the relaxation times of the mixture. Hence, using (4.8) and the model parameter values prescribed in [48] for (4.8), we have plotted in Fig. 4.24 the magnitude of the relative permittivities of ethanol in water for different molar percentages of ethanol across 4 orders of frequency magnitude (0.1 GHz to 1 THz). Furthermore, since the reflection coefficient, ρ, of a plane wave incident from air into a mixture of ethanol and water is given by (4.9).

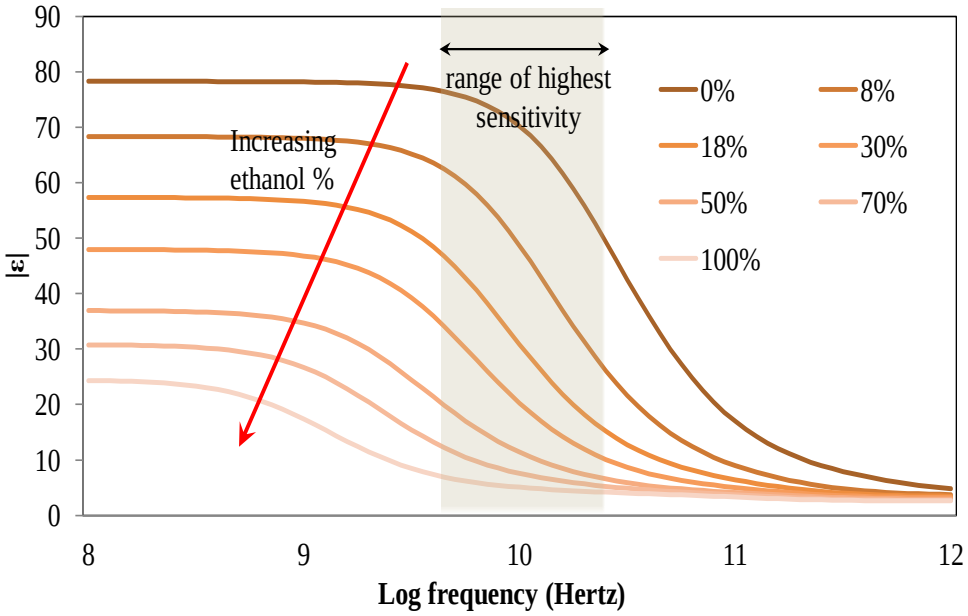

Fig. 4.24. Magnitude of the relative dielectric constant of ethanol-water mixtures for different molar concentrations of ethanol.

$$\rho = \frac{\eta_2 - \eta_1}{\eta_2 + \eta_1}, \qquad \eta_i = \sqrt{\mu_i / \varepsilon_i} \tag{4.9}$$

where η_1 and η_2 are the wave impedance of the air and water-ethanol mixture, respectively, μ and ε are the permeability and permittivity of a dielectric media.

Therefore, (4.8) and Fig.4.24 suggest that the frequency range that will show the highest reflection changes for changes in ethanol concentration is between 0.5 and 20 GHz. Hence, assuming that the effect of sugar and yeast in the fermentation broth can be ignored, the frequency range intrinsically suited for fermentation monitoring is between 0.5 and 20 GHz.

4.5 Conclusions

This chapter has demonstrated some applications of terahertz waves in biosensing. Terahertz waves are suitable for biosensing principally because water (polar substances in general), an essential component of biological system, is strongly absorbed by terahertz waves.

4.6 References

[1] S. Ramo, J. R. Whinnery, and T. V. Duzer, *Fields and waves in communication electronics*, New York, NY: John Wiley & Sons, 2008.

[2] Jet Propulsion Laboratory Catalog. [Online]. Available: http://spec.jpl.nasa.gov/

[3] Y. Lee, *Principles of terahertz science and technology*, vol. 170, New York, NY: Springer Science & Business Media, 2009.

[4] P. H. Siegel, "Terahertz technology," *IEEE Transactions on Microwave Theory and Techniques*, vol. 50, no. 3, pp. 910-928, 2002.

[5] M. Tonouchi, "Cutting-edge terahertz technology," *Nature Photonics*, vol. 1, no. 2, pp. 97-105, 2007.

[6] R. Cunnell, T. Luce, J. H. P. Collins, R. Rungsawang, J. R. Freeman, H.E. Beere, D. A. Ritchie, L. F. Gladden, M. L. Johns, and J. A. Zeitler, "Quantification of emulsified water content in crude oil using a terahertz quantum cascade laser," *2009 34th International Conference on Infrared, Millimeter, and Terahertz Waves*, 2009, pp. 1-2.

[7] D. J. Segelstein, "The complex refractive index of water," PhD dissertation, Dept. of Physics, University of Missouri, Kansas City, MS, 1981. [Online]. Available: http://www.philiplaven.com/p20.html

[8] K. Peiponen, A. Zeitler, and M. Kuwata-Gonokami, *Terahertz spectroscopy and imaging*, vol. 171, New York, NY: Springer, 2012.

[9] D. M. Pozar, *Microwave engineering*, New York, NY: John Wiley & Sons, 2009.

[10] J. L. Hesler, Y. Duan, B. Foley, and T. W. Crowe, "THz vector network analyzer measurements and calibration," in *21st Intl. Symp. on Space Terahertz Technology, Oxford, UK*, 2010, pp. 23-25.

[11] F. Johansson and N. D. Whyborn, "The diagonal horn as a sub-millimeter wave antenna," *Microwave Theory and Techniques, IEEE Transactions on,* vol. 40, no. 5, pp. 795-800, 1992.

[12] Virginia Diodes Vector Network Analyzer Extender Data Sheet. [Online]. Available: http://vadiodes.com/

[13] *A form of this section was published in IEEE Sensors journal.*

[14] E. Betzig and J. K. Trautman, "Near-field optics: microscopy, spectroscopy, and surface modification beyond the diffraction limit," *Science,* vol. 257, no. 5067, pp. 189-195, 1992.

[15] S. M. Anlage, V. V. Talanov, and A. R. Schwartz, "Principles of near-field microwave microscopy," in *Scanning probe microscopy*, New York, NY: Springer, 2007, pp. 215-253.

[16] F. De Lange, A. Cambi, R. Huijbens, B. de Bakker, W. Rensen, M. Garcia-Parajo, N. van Hulst, and C. G. Figdor, "Cell biology beyond the diffraction limit: near-field scanning optical microscopy," *Journal of Cell Science,* vol. 114, no. 23, pp. 4153-4160, 2001.

[17] M, Tabib-Azar, J. L. Katz, and S. R. LeClair, "Evanescent microwaves: a novel super-resolution noncontact nondestructive imaging technique for biological applications," *Instrumentation and Measurement, IEEE Transactions on,* vol. 48, no. 6, pp. 1111-1116, 1999.

[18] J. L Adam, "Review of near-field terahertz measurement methods and their applications," *Journal of Infrared, Millimeter, and Terahertz Waves,* vol. 32, no. 8-9, pp. 976-1019, 2011.

[19] M. A. Seo, A. J. L. Adam, J. H. Kang, J. W. Lee, S. C. Jeoung, Q. Han Park, P. C. M. Planken, and D. S. Kim, "Fourier-transform terahertz near-field imaging of one-dimensional slit arrays: mapping of electric-field-, magnetic-field-, and Poynting vectors," *Optics Express,* vol. 15, no. 19, pp. 11781-11789, 2007.

[20] Y. Kawano and K. Ishibashi, "An on-chip near-field terahertz probe and detector," *Nature Photonics,* vol. 2, no. 10, pp. 618-621, 2008.

[21] B. M. Fischer, M. Walther, and P. Uhd Jepsen, "Far-infrared vibrational modes of DNA components studied by terahertz time-domain spectroscopy," *Physics in Medicine and Biology,* vol. 47, no. 21, p. 3807, 2002.

[22] Y. Gao and I. Wolff, "A new miniature magnetic field probe for measuring three-dimensional fields in planar high-frequency circuits," *Microwave Theory and Techniques, IEEE Transactions on,* vol. 44, no. 6, pp. 911-918, 1996.

[23] O. Fawole and M. Tabib-Azar, "A new method for mapping fields in coupled cylindrical dielectric resonators," in *IEEE Sensors 2015 Proceedings*, 2015, pp. 1-4.

[24] K. Wang and D. M. Mittleman, "Metal wires for terahertz wave guiding," *Nature*, vol. 432, no. 7015, pp. 376-379, 2004.

[25] N. Klein, P. Lahl, U. Poppe, F. Kadlec, and P. Kužel, "A metal-dielectric antenna for terahertz near-field imaging," *Journal of Applied Physics*, vol. 98, no. 1, p. 014910, 2005.

[26] Mouse brain slices provided by Prof. Matt Wachowiak of the Department of Neurobiology and Anatomy, University of Utah.

[27] S. J. Oh, S. Kim, Y. B. Ji, K. Jeong, Y. Park, J. Yang, D. W. Park, S. K. Noh, S. G. Kang, Y. M. Huh, and J. H. Son, "Study of freshly excised brain tissues using terahertz imaging," *Biomedical Optics Express*, vol. 5, no. 8, p. 2837, 2014.

[28] L. Shi, P. Shumyatsky, A. Rodríguez-Contreras, and R. Alfano, "Terahertz spectroscopy of brain tissue from a mouse model of Alzheimer's," *Journal of Biomedical Optics*, vol. 21, no. 1, p. 15014, 2016.

[29] W. G. Yeo, O. Gurel, N. K. Nahar, C. L. Hitchcock, N. L. Lehman, S. Park, and K. Sertel, "THz imaging of Alzheimer's disease: Spectroscopic differentiation between normal and diseased tissues," in *2014 39th International Conference on Infrared, Millimeter, and Terahertz waves (IRMMW-THz)*, 2014, pp. 1-2.

[30] Y. Jin, G. Kim, and S. Jeon, "Terahertz dielectric properties of polymers," *Journal of the Korean Physical Society*, vol. 49, no. 2, pp. 513-517, 2006.

[31] U. Schade, K. Holldack, P. Kuske, G. Wüstefeld, and H-W. Hübers, "THz near-field imaging employing synchrotron radiation," *Applied Physics Letters*, vol. 84, no. 8, pp. 1422-1424, 2004.

[32] A. O. Bitzer and M. Walther, "Terahertz near-field microscopy with subwavelength spatial resolution based on photoconductive antennas," *Applied Optics*, vol. 49, no. 19, pp. E1-E6, 2010.

[33] T. S. Huang, *Flora of Taiwan: Angiosperms-Monocotyledons (Alismataceae-Triuridaceae)*, vol. 3, T.S. Huang, ed. Taipei, Taiwan: Editorial Committee of the Flora of Taiwan, 2000, p. 1002. [online]. Available: http://tai2.ntu.edu.tw/ebook/ebookpage.php?book=Fl.%20Taiwan%202nd%20edit.&volume=3&list=4253

[34] D. Grischkowsky, S. Keiding, M. Van Exter, and C. Fattinger, "Far-infrared time-domain spectroscopy with terahertz beams of dielectrics and

semiconductors," *JOSA B*, vol. 7, no. 10, pp. 2006-2015, 1990.

[35] L. Rong, T. Latychevskaia, D. Wang, X. Zhou, H. Huang, Z. Li, and Y. Wang, "Terahertz in-line digital holography of dragonfly hindwing: amplitude and phase reconstruction at enhanced resolution by extrapolation," *Optics Express*, vol. 22, no.14, pp. 17236-17245, 2014.

[36] M. J. Tobin, L. Puskar, S. H. Nguyen, J. Hasan, H. K. Webb, C. J. Hirschmugl, M. J. Nasse, G. Gervinskas, S. Juodkazis, G. S. Watson, and J. A. Watson, "Fourier transform infrared spectroscopy and imaging of dragonfly, damselfly and cicada wing membranes," *Spectroscopy Europe*, vol. 27, no. 4, pp. 15-18, 2015.

[37] R. H. Arnett Jr., *American insects: a handbook of the insects of America north of Mexico*, 2nd ed., Boca Raton, FL: CRC Press, 2000, pp. 241-258.

[38] Result in this section was presented at International Microwave Symposium (IMS) 2016, and some parts of this result will appear in the IMS proceedings.

[39] P. U. Jepsen, U. Møller, and H. Merbold, "Investigation of aqueous alcohol and sugar solutions with reflection terahertz time-domain spectroscopy," *Optics Express*, vol. 15, no. 22, pp. 14717-14737, 2007.

[40] A. Gowen, C. O'Sullivan, and C. P. O'Donnell, "Terahertz time domain spectroscopy and imaging: emerging techniques for food process monitoring and quality control," *Trends in Food Science & Technology*, vol. 25, no. 1, pp. 40-46, 2012.

[41] P. Tibayrenc, L. Preziosi-Belloy, and C. Ghommidh, "On-line monitoring of dielectrical properties of yeast cells during a stress-model alcoholic fermentation," *Process Biochemistry*, vol. 46, no. 1, pp. 193-201, 2011.

[42] R. Olmi, V. V. Meriakri, A. Ignesti, S. Priori, and C. Riminesi, "Monitoring alcoholic fermentation by microwave dielectric spectroscopy," *Journal of Microwave Power and Electromagnetic Energy*, vol. 41, no. 3, pp. 37-49, 2007.

[43] V. L. Ennis, J. Irudayaraj, and A. Demirci, "An online approach to monitor ethanol fermentation using FTIR spectroscopy," *Biotechnology Progress*, vol. 23, no. 2, pp. 494-500, 2007.

[44] B. Liebmann, A. Friedl, and K. Varmuza, "Applicability of near-infrared spectroscopy for process monitoring in bioethanol production," *Biochemical Engineering Journal*, vol. 52, no. 2, pp. 187-193, 2010.

[45] G. Cavinato, D. M. Mayes, Z. Ge, and J. B. Callis, "Noninvasive method for monitoring ethanol in fermentation processes using fiber-optic near-infrared spectroscopy," *Analytical Chemistry*, vol. 62, no. 12, pp. 1977-1982, 1990.

[46] O. Fawole, K. Sinha, and M. Tabib-Azar, "Monitoring yeast activation with sugar and zero-calorie sweetener using terahertz waves," in *IEEE Sensors 2015 Proceedings*, 2015, pp. 1-4.

[47] V. Vidgren and J. Londesborough, "125th anniversary review: yeast flocculation and sedimentation in brewing," *Journal of the Institute of Brewing*, vol. 117, no. 4, pp. 475-487, 2011.

[48] T. Sato and R. Buchner, "Dielectric relaxation processes in ethanol/water mixtures," *The Journal of Physical Chemistry A*, vol. 108, no. 23, pp. 5007-5015, 2004.

CHAPTER 5

TERAHERTZ MEANDERING WAVEGUIDE TRAVELING WAVE AMPLIFIERS

5.1 Introduction

In the introduction chapter of this work, it was mentioned that solid-state amplifiers have low power handling capabilities. Although these circuits can be easily designed for low frequency, high power operations, it is challenging to make these circuits operate at high power and high frequency/speed. On the other hand, waveguide-based distributed circuits such as traveling wave tube amplifiers (TWTs) circuits can be easily scaled into higher frequency by simply scaling the characteristic dimension of the waveguide. However, the main challenge with scaling waveguide-based devices to higher frequency is finding a fabrication method that can be used to fabricate these waveguide-based circuits with the desirable dimensional tolerance and surface finish. Fortunately, processes for fabricating microelectromechanical systems (MEMS) can be easily adapted to fabricating miniature waveguide-based traveling wave amplifier circuits with the desired tolerances and smoothness.

One waveguide-based traveling wave amplifier circuit design that is particularly suited for MEMS fabrication is the meandering waveguide (also known as the folded waveguide or the serpentine waveguide). This meandering waveguide design, in addition to its ease of fabrication with MEMS process, has a decent operating bandwidth and gain.

A number of authors have studied, via computer simulations, the suitability of the meandering waveguide for TWT amplifier applications for frequencies between 0.1 THz to 0.2 THz [1-3]. Furthermore, the Northrop Grumman Electronic Systems (NGES) has practically demonstrated high gain (~ 30 dB gain) meandering waveguide TWT amplifiers at frequencies between from 0.2 THz to 0.850 GHz [4-7]. This chapter presents a meandering waveguide TWT amplifier that operates at around 0.9 THz.

In the beginning part of this chapter, a description of the amplification of electromagnetic waves through particle-wave interaction in traveling wave tube is presented. The meandering waveguide is fundamentally a backward wave amplifier. This means the direction of power flow in the meandering amplifier is opposite the direction of the wave velocity of the traveling wave. Hence, the output of the amplifier when operated in the fundamental backward wave mode is at the cathode (electron source) rather than at the collector (the electron sink). However, the problem with backward wave traveling wave amplifier is their narrow bandwidth and their tendency to become unstable (by acting as an oscillator rather than an amplifier). Hence, in the meandering waveguide amplifier presented here, the amplifier will be configured to operate at a high order mode forward wave mode.

The general equations that describe this amplification of a forward traveling wave amplifier are given in Appendix A. Next, this chapter presents theoretical basis of the meandering waveguide as an interaction circuit suitable for THz wave amplification. Next, the microfabrication processes used to fabricate the meandering waveguide terahertz circuits whose operating frequency is centered at 0.9 THz are presented. Finally, the results of the cold tests and hot tests (active characterization with electron beam) on

the meandering waveguides are presented.

5.2 Description of high frequency wave amplification by traveling wave tube

Like the klystron amplifier, traveling wave tubes (TWTs) are suited for the amplification of high frequency signals without the effect of parasitic impedances that limit the operation frequency of grid-controlled electron tube amplifiers. In a TWT amplifier, continuous interaction of an electron beam with the slow wave circuit produces amplification of the wave. This is unlike the amplification mechanism of the klystron amplifier described in Chapter 3. In the klystron, interaction at discrete positions in the electromagnetic circuit leads to wave amplification. The amplification by continuous interaction in TWTs leads to higher gain over a wider frequency bandwidth in TWTs.

The general schematic of a traveling wave tube amplifier is shown in Fig. 5.1, and the photograph of a commercial TWT amplifier, the Varian VTC-6361H1 400 W C-band helix traveling wave amplifier with operating frequency between 5.85 GHz and 6.425 GHz, is shown in Fig. 5.2. A traveling-wave-tube amplifier basically consists of DC electrodes for creating an electron beam along the length of the TWT vacuum tube, a magnetic field for focusing the electron beam (to reduce the divergence of the beam due to mutual repulsion of the beam electrons), and an electromagnetic circuit that can provide good interaction between the electron beam and an electromagnetic wave. The TWT is designed such that interaction between the electron beam and the waves results in the amplification of the wave. One of the conditions that produce the type of wave-beam interaction that leads to amplification is that the electron beam and the electromagnetic wave to be amplified have to have the same (or almost the same) velocity.

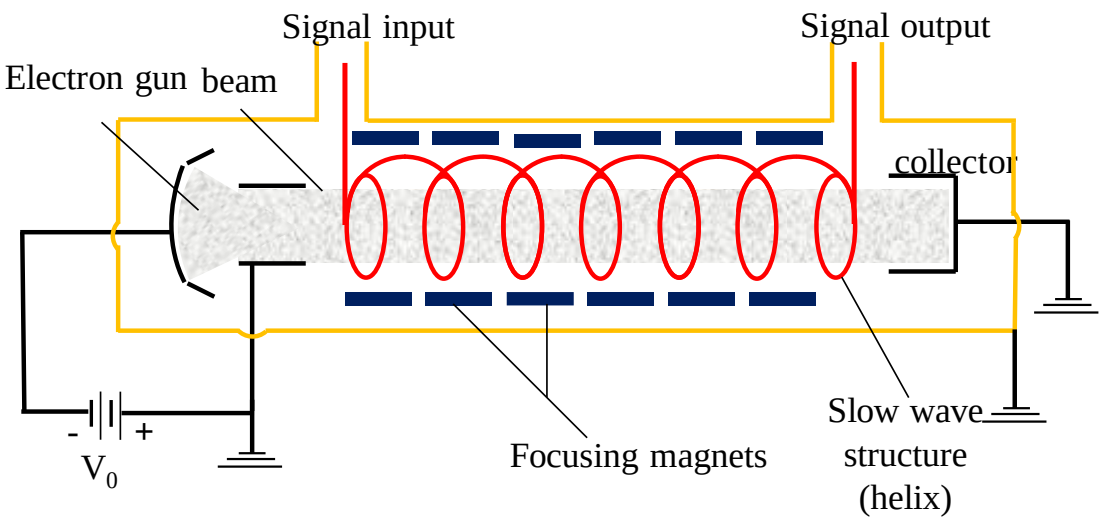

Fig. 5.1. Schematic of a traveling wave tube amplifier.

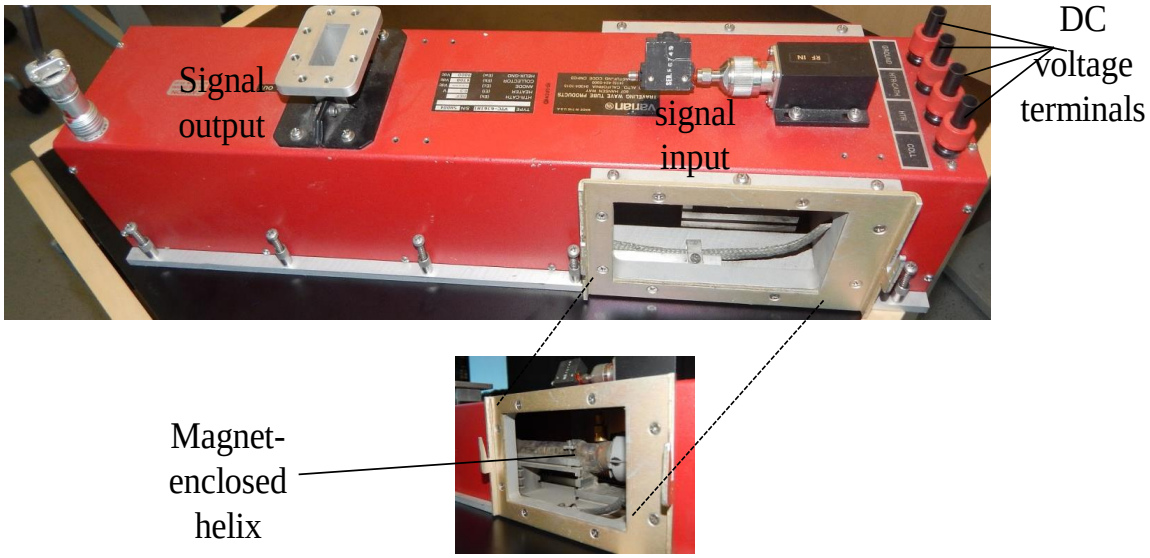

Fig. 5.2. Photograph of a helix slow wave traveling wave tube amplifier.

In free space and inside unloaded waveguides, electromagnetic waves propagate at the speed of light and above the speed of light, respectively. However, a very high voltage is required to accelerate an electron beam to a velocity close to the velocity of light. Hence, it is necessary to design an electromagnetic structure in such a way that an electromagnetic wave propagating through it presents a low effective velocity to an electron. This effective velocity has to be lower than the speed of light. Furthermore, this effective velocity must be the velocity (or close to the velocity) of the electrons. Such an electromagnetic structure is called a slow wave structure, and it is used extensively in TWTs.

In a TWT, the slow wave structure is designed such that the phase velocity of the electromagnetic wave that interacts with the electron is a little bit higher than the phase velocity of the electrons. The reason for this and the description of the wave-electron interaction process is illustrated in Fig. 5.3 [8]. The electrons are modeled as discs which are represented by lines in the figure. The axial electric field of the slow wave structure exerts a force to the left on the electron discs A, B, C, D, and E and to the right on the electron discs G, H, I , J and K, and this force causes electron bunches to start forming around disc L.

As mentioned earlier, the TWT is operated such that the electron velocity is higher than the phase velocity of the wave. Hence, the bunch centered around disc L will drift into the retarding field on the slow wave structure. If the wave is retarding the electrons, then the electrons will have to transfer their energy to the wave in the slow wave structure for the system to obey the law of conservation of energy. Hence, the slow wave is amplified by the transfer of energy to it by the electron beam.

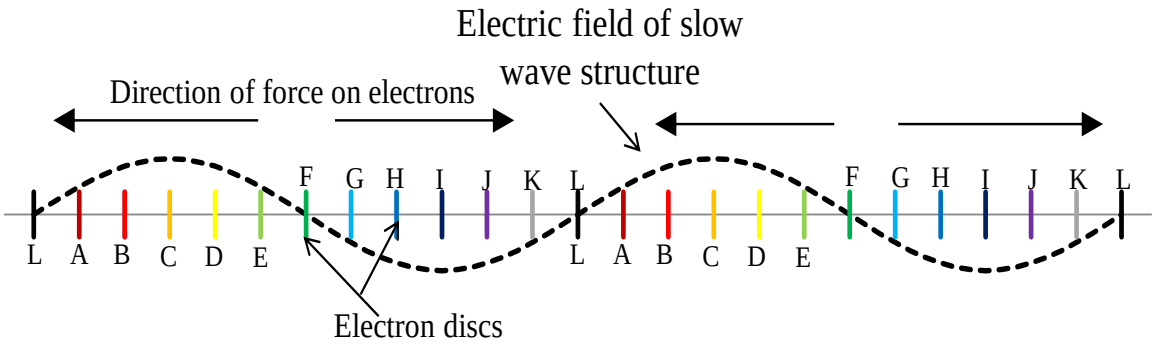

Fig. 5.3. Illustration of amplification of a slow wave via synchronous beam-wave interaction.

5.3 The meandering waveguide as a slow wave traveling-wave tube structure

5.3.1 Description

The 3D structure of a meandering waveguide is shown in Fig. 5.4a. The meandering waveguide is formed by folding a TE_{01} waveguide in a periodic manner. Hence, the electric fields in the meandering waveguide are between the two broad sides of the meandering waveguide as shown in Fig. 5.4a. For operation in the frequency span of 0.6 to 1.2 THz (center 0.9 THz), the design dimension of the meandering waveguide for a TE_{10} mode operation is 250 μm x 125 μm. When used in an electron tube, a channel for the electron beam has to be created in the meandering waveguide. The cross section of a meandering waveguide with a beam tunnel is shown in Fig. 5.4b of a cross section of a meandering waveguide. The slow wave properties of the meandering waveguide depend on the length of the fold of the meander. The explanation for this is that a longer fold means the wave velocity along the axis of the meander (where the wave-beam interaction occurs) is slower than the velocity along the path of the meander. The factor by which the wave is slowed down depends on the ratio of the length of the fold to the axial separation of the beam crossing. The slow wave properties of a slow wave structure

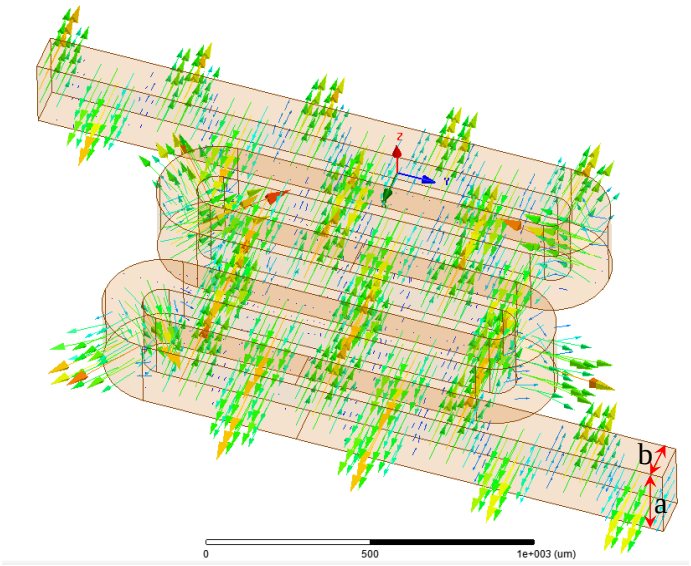

(a)

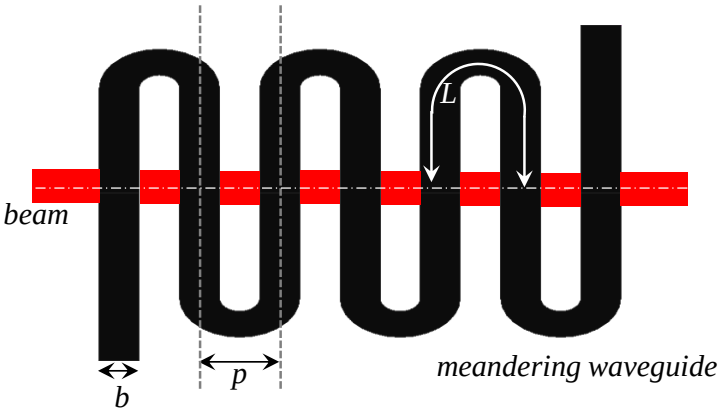

(b)

Fig. 5.4. The meandering waveguide (a) 3D model of the meandering waveguide showing the orientation of its electric field vectors for TE_{10} mode operation (b) Basic structure of the meandering waveguide from its cross-sectional view.

are described by its dispersion relation. The dispersion relation of a meandering waveguide is given in the next section.

The spatial periodicity of the geometry of a slow wave structure requires that the solution of the wave equation to be an infinite sum of electric fields (from Fourier transform of periodic functions). Each of these electric field solutions has its own propagation constant and phase velocity, and each of these electric field solutions is called a space harmonic.

5.3.2 Spatial harmonics in periodic structures and dispersion relation of a meandering waveguide

Periodic slow wave structures are designed such that most of the excitation power goes to the space harmonic that will be interacting with the electron beam in a slow wave structure.

The dispersion relation of a meandering waveguide can be estimated for the geometry of a folded waveguide [9] shown in Fig. 5.5. From geometrical consideration, an electron traveling through a beam tunnel in the folded/meandering waveguide sees a wave traveling with phase velocity:

$$v = \frac{p}{b+p}c \tag{5.1}$$

with $2\pi/\lambda_g = \omega/v$ and $2\pi/\lambda = \omega/c$ where λ_g is the waveguide wavelength, ω is the angular frequency and c is the velocity of propagation of a wave in free space. Hence, (5.1) can be written as:

$$\lambda_g = \lambda \frac{p}{b+p} \tag{5.2}$$

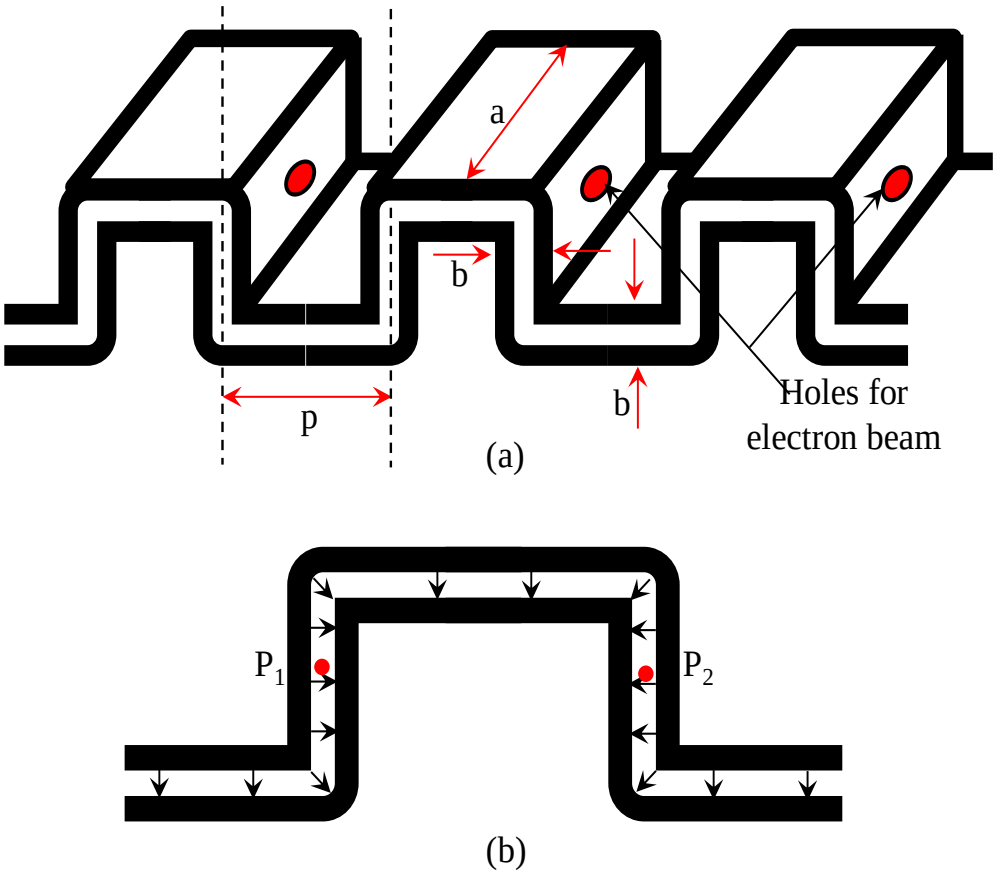

Fig. 5.5. A folded waveguide slow wave structure. (a) Schematic of a folded (meandering) waveguide. (b) illustration of the 180-degree phase reversal experienced by an electron in a folded waveguide. This phase reversal is what makes the meandering waveguide a fundamental backward wave structure.

The phase constant of this wave is:

$$\beta_{01} = \frac{\omega}{v} = \frac{\omega}{c}\frac{b+p}{p} = k\frac{b+p}{p} \tag{5.3}$$

A phase shift of 180 degrees occurs at each crossing of the electron with the waveguide as shown in the inset of Fig. 5.5b, as illustrated for positions P_1 and P_2. Hence, the fundamental phase constant is:

$$\beta_0 = \beta_{01} + \pi \tag{5.4}$$

The phase constant of all the phase harmonics are given by:

$$\beta_n L = \beta_0 L + 2n\pi = \beta_{01} L + (2n+1)\pi \tag{5.5}$$

The picture of a dispersion relation curve (plot of the phase constant versus frequency) for the meandering waveguide is shown in Fig. 5.6 [9]. The dispersion relation of the first three space harmonics is shown.

The analysis of the folded waveguide shown in Fig. 5.5 can be extended to that of the meandering waveguide of Fig. 5.4 with little or no modification [10]. The extension of this folded waveguide analysis to a meandering waveguide will be done next.

5.3.3 Phase velocity equation of a meandering waveguide

The analysis of a meandering waveguide to obtain its phase velocity is given in [10]. The phase velocity of the nth space harmonic, $v_{p,n}$, in a meandering waveguide structure is given by the equation:

$$v_{p,n} = \frac{\omega}{\Delta\varphi_{z,n}/p} \tag{5.6}$$

where ω is the angular frequency of the slow wave, $\Delta\varphi$ is the change in the phase of the slow wave's electric field between subsequent beam crossings, and p is the distance between subsequent beam crossings as illustrated in Fig. 5.5b. $v_{p,n}$ is the velocity at which an electron beam has to travel in order to be in sync with a slow wave so as to interact with the wave.

The denominator in (5.6) is the effective axial wave number of the nth space harmonic $\beta_{z,n}$ given as:

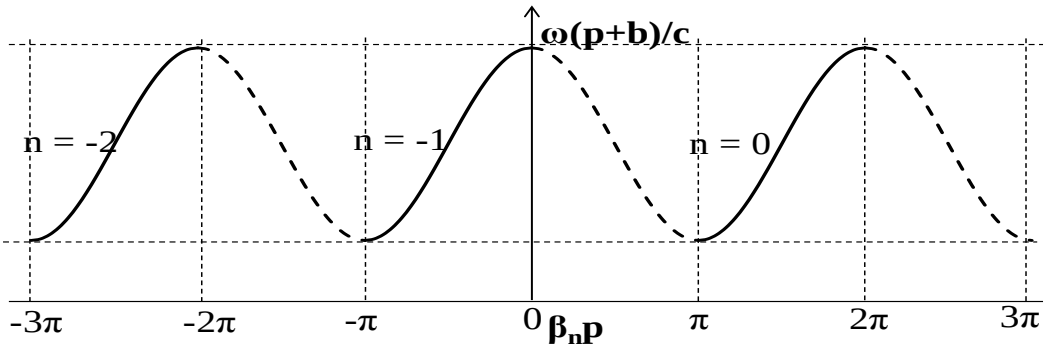

Fig. 5.6. Picture of the dispersion relation of the folded waveguide.

$$\beta_{z,n} = \frac{\Delta\varphi_{z,n}}{p} \tag{5.7}$$

For a meandering waveguide, the phase shift of the nth spatial harmonic is given by:

$$\Delta\varphi_{z,n} = \left[\left(\frac{\omega}{v_{z,wave}}\right)p + \pi\right] + 2\pi n \tag{5.8}$$

where $v_{z,wave}$ is the axial phase velocity of the wave in the meandering waveguide. From the geometrical consideration of Fig. 5.4, $v_{z,wave}$ is given as:

$$v_{z,wave} = \frac{p}{L}\, v_{straight\ waveguide} \tag{5.9}$$

where $v_{\text{straight waveguide}}$ is given as:

$$v_{straight\ waveguide} = \frac{c}{\sqrt{1 - \left(\frac{\omega_{co}}{\omega}\right)^2}} \tag{5.10}$$

where c is the speed of light in free space, and ω_{co} is the cutoff frequency of the straight waveguide with the same transverse dimension as the meandering waveguide. For the fundamental TE_{01} waveguide mode, ω_{co} is given as $\pi c/a$.

Substituting into (5.8–5.10) in (5.6) one obtains the axial phase velocity seen by the electrons as:

$$v_{p,n} = \frac{p}{L} \frac{c}{\sqrt{1 + \left(\frac{w_{co}}{w}\right)^2 + \frac{\pi c}{wL} + \frac{2\pi mc}{wL}}} \tag{5.11}$$

The plot of the phase velocity (normalized to the speed of light in free space) as a function of frequency in a meandering waveguide for the second space harmonic (n = 0), which is a forward wave, of the fundamental waveguide mode (TE_{10}) is shown in Fig. 5.7.

As annotated in Fig. 5.4a, the terahertz meandering waveguide was designed with b = 125 μm and a = 250 μm, and as annotated in Fig. 5.4b, the meandering wave guide has p = 250 μm, and L = 785.4 μm (length of a bend) + 2 x 500 μm (half length of the straight section of the meander). Figure 5.7 shows that the meander with these

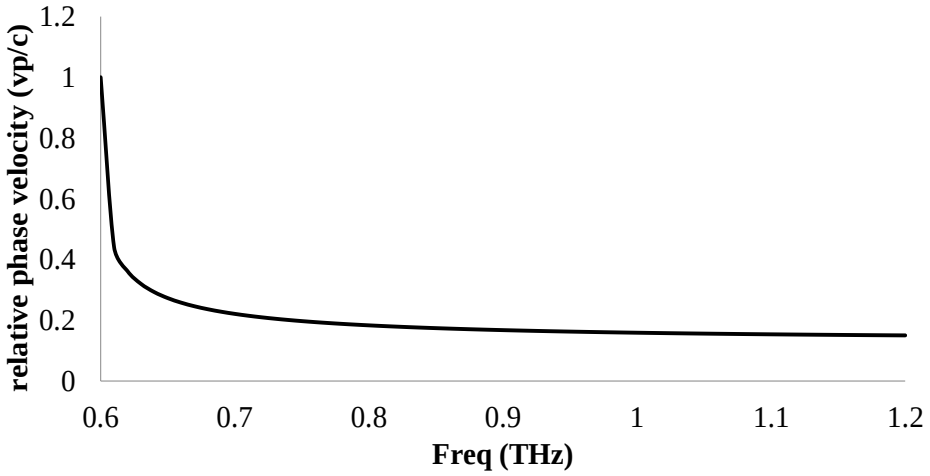

Fig. 5.7. Analytic phase velocity of a second space harmonic wave in a TE_{01} meandering waveguide with axial period of 250 μm and a meander whose half physical length is 1785.4 um.

dimensions can reduce the effective axial phase velocity of a propagating wave to about one fifth the speed of light in free space ($0.2c$) at 0.9 THz. Different authors have compared the result of phase velocity obtained via numerical simulations with the analytic equation of (65), and these authors have found close agreement between these two results [1,2,10].

5.3.4 Interaction impedance equation

In Appendix A, the general form of the interaction impedance is given by (A. 26) and the gain of a traveling wave tube is given by (A.59) which depends on the small-signal gain parameter *C*. *C* is a function of the interaction impedance K_n. For a meandering waveguide, the on-axis interaction impedance of the nth space harmonic K_n of the slow wave structure is given analytically by [10]:

$$K_{axis,n} = K_{wg,10} \frac{1}{\left(\beta_{z,n} p\right)^2} \left[\frac{\sin\left(\frac{\beta_{z,n} b}{2}\right)}{\frac{\beta_{z,n} b}{2}} \right]^2 \frac{1}{I_0^2(\kappa_{cm} r_b)} \tag{5.12}$$

where $K_{wg,10}$ is the waveguide impedance of the TE_{01} waveguide mode and it is given as:

$$K_{wg,10} = \frac{2b}{a} \frac{\eta_0}{\sqrt{1 - \frac{w_{co}^2}{w^2}}} \tag{5.13}$$

where κ_{cm} is given by:

$$\kappa_{cm}^2 = \beta_{z,n}^2 - \left(\frac{w}{c}\right)^2 \tag{5.14}$$

where r_b is the beam radius, and η_0 is the characteristic impedance of free space which is

equal to 377 Ω. The analytic interaction impedance of the second spatial harmonic of our meandering waveguide is given in Fig. 5.8.

Different authors have compared the result of interaction impedance obtained via numerical simulations with the analytic equation of (5.12), and these authors have found close agreement between these two results [1,2,10].

5.4 Microfabrication process of meandering waveguide TWT at terahertz frequencies: design considerations

Micromachining techniques used in Microelectromechanical Systems (MEMS) technology are proving to be cost-effective methods to batch-produce waveguide-based terahertz circuits [11]–[14]. However, there are a number of challenges associated with the fabrication of terahertz circuits with MEMS technology. In [15a], some of the challenges associated with microfabricated waveguide-based devices were discussed. In the following discussion, the challenges peculiar to TWT meandering waveguides fabrication, and how these challenges can be overcome in a meandering waveguide

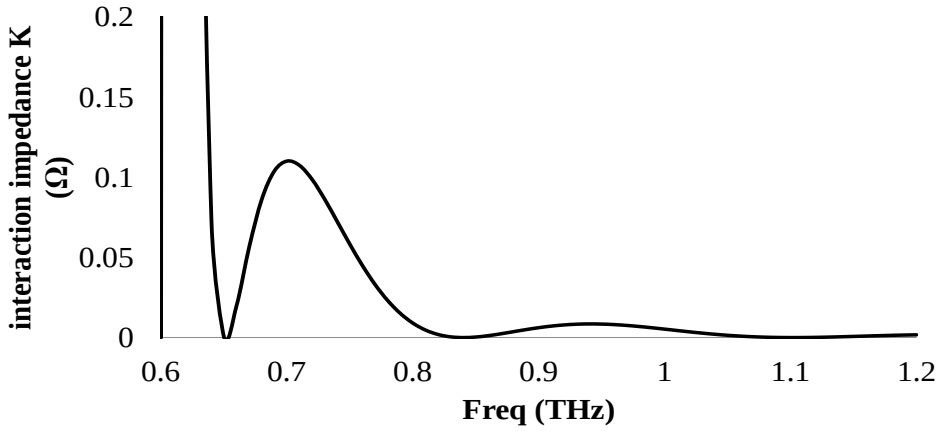

Fig. 5.8. Analytic interaction impedance of a TE_{01} meandering waveguide with axial period of 250 μm and half meander length of 1785.4 μm.

TWT circuit will be discussed.

As mentioned earlier, a 250 μm x 125 μm rectangular waveguide will operate in the TE_{01} mode at a center frequency of 0.9 THz, and this waveguide can be folded into a meander to operate as a slow wave structure in a traveling wave tube. The meandering waveguide is well-suited for fabrication via microfabrication techniques. Deep Reactive Ion Etching (DRIE), a MEMS fabrication process, can be used to pattern the meander on one silicon substrate, and gold can then be sputtered on the patterned wafer to form the metallic waveguide walls. The metalized meander grooves can then be covered with another gold-coated silicon wafer to complete the structure of the meander.

One of the major challenges of designing waveguides at terahertz frequencies is designing waveguide walls such that the surface roughness of the walls is less than the skin depth at terahertz frequency [14]. To achieve wall smoothness the DRIE sidewalls will be chemically polished using isotropic wet etching. Attenuation through terahertz waveguides can be further reduced if the metallic waveguide is coated with a thin dielectric [15b]. Hence, aluminum dioxide and Praylene-C will be deposited on the waveguide walls via Atomic Layer Deposition (ALD) and Chemical Vapor Deposition (CVD) to improve their terahertz transmission.

The terahertz test system that will be used to test the meandering waveguide devices has WR 1.0 waveguide aperture with a flange. The best coupling of the meander to the test waveguide requires the integration of 3-dimension WR 1.0 flanges to the test devices. However, DRIE is a lithographic method that can only produce 2.5 –dimensional structures. The coupling of the fabricated meandering waveguide to the test system will be improved by integrating a transition region with the meandering waveguide. This

transition will be butt-coupled to the test system's waveguide aperture.

The beam-wave interaction impedance equation assumes a circular electron beam. The beam tunnel will be designed to have a rectangular cross section suitable to the DRIE meander. Transition regions (as in the meander input/output) will be attached to the ends of the beam tunnel to ease the coupling of an electron beam from the outside into the beam tunnel. In [1], the authors employed wave-particle simulation models to investigate the effect of replacing the usual circular beam tunnel of a TWT with a square beam on the performance of a TWT amplifier. The effect is tolerable. The design for the mask of the terahertz meandering waveguide, with the above mentioned design consideration taken into account, is shown in Fig. 5.9.

5.5 Microfabrication process of the meandering waveguide TWT [16]

Figure 5.10 shows a simplified one-mask fabrication process for the meandering waveguide devices. A two-substrate process was used to fabricate these devices. The meandering waveguide is first etched on the first silicon wafer substrate (10a – 10d). A second patterned substrate was used as a cover for the etched substrate.

Two-period, three-period, four-period, and 21-period meanders were batch

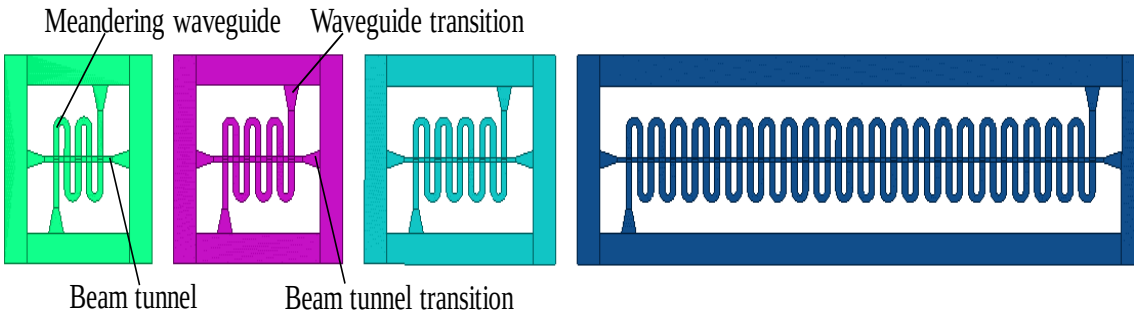

Fig. 5.9. Design pattern for the mask of the meandering waveguide for different meander periods.

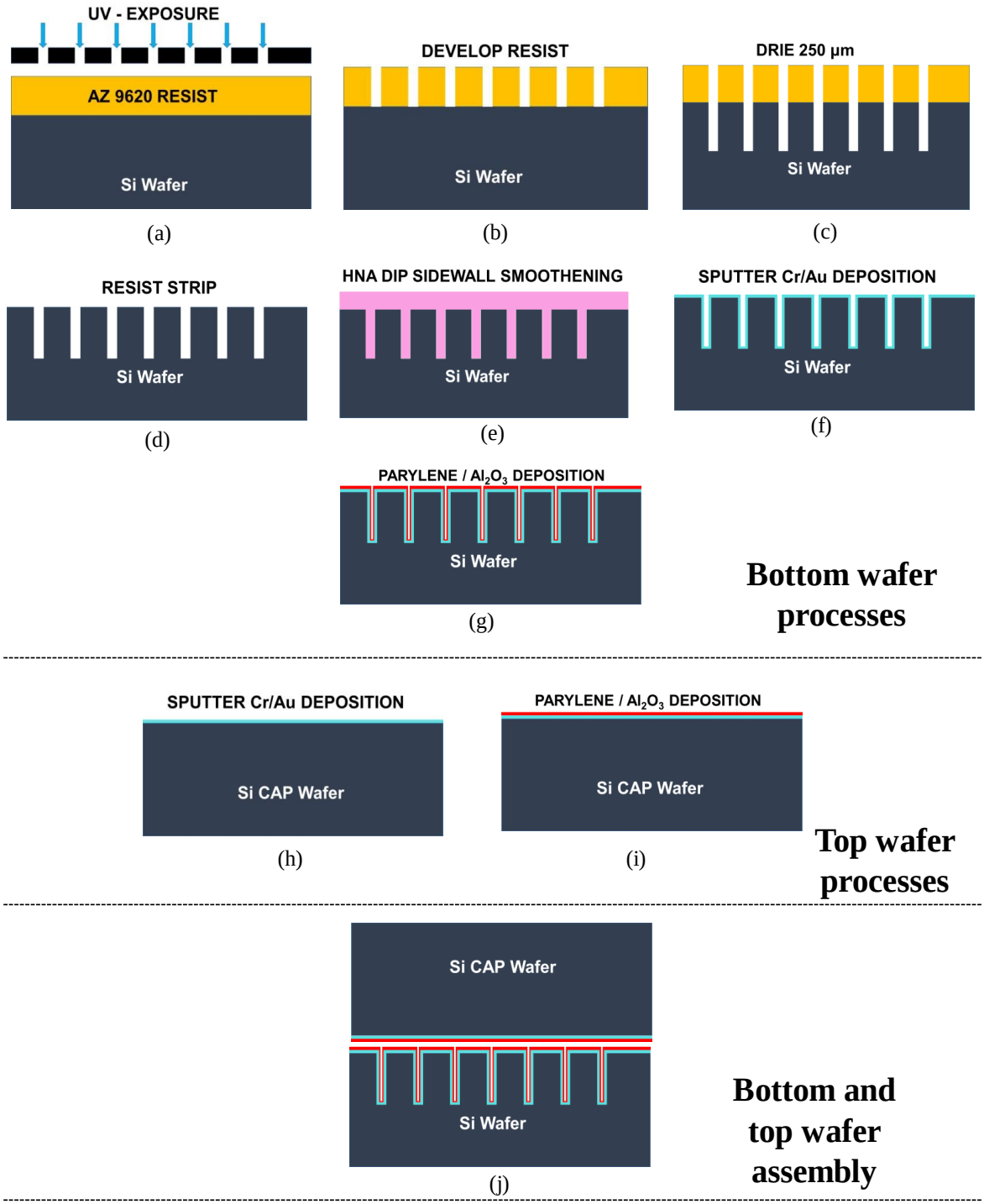

Fig. 5.10. Microfabrication steps of the meandering waveguide.

patterned on the same wafer. Conventional lithography and Deep Reactive Ion Etching (DRIE) were used to etch the patterns of the meandering waveguide 250μm deep into the silicon wafer.

Since one of our major goals for the structure of the meandering waveguide is to obtain very smooth waveguide walls, a liquid silicon etch (HNA) was used to smooth the silicon walls of the meander before metallization (10e). The HNA solution consisted of HF, nitric acid, acetic acid in the ratio 1:8:1. The patterned silicon wafer was dipped in HNA for 15 seconds and then immediately rinsed with deionized water, and the wafer was spin dried. Next (Fig. 5.10f), 150 nm-thick gold was sputtered on the patterned wafer. A 50 nm-thick layer of sputtered chromium was used as an adhesion layer for the sputtering process. To further reduce the terahertz loss of the meandering waveguide, a 50 nm thin layer of aluminum dioxide or 20 um-thick parylene-C was deposited on the metalized waveguide walls through Atomic layer deposition (ALD) process or Chemical Vapor Deposition (CVD), respectively (Fig. 5.10g).

Next, the second substrate which is the top cover of the meandering waveguide was processed. A 150 nm-thick layer of gold on a 50 nm-thick adhesive layer of chromium was sputtered on a silicon substrate. Next, 50 nm-thick ALD aluminum dioxide or 20 um Parylene-C was deposited on the metalized wafer (Fig. 5.10i). After device singulation of both substrates by dicing, the meander and cap were then mechanically clamped in preparation for testing (Fig. 5.10j). Fig. 5.11 shows the SEM image of one of the meandering waveguide devices after DRIE.

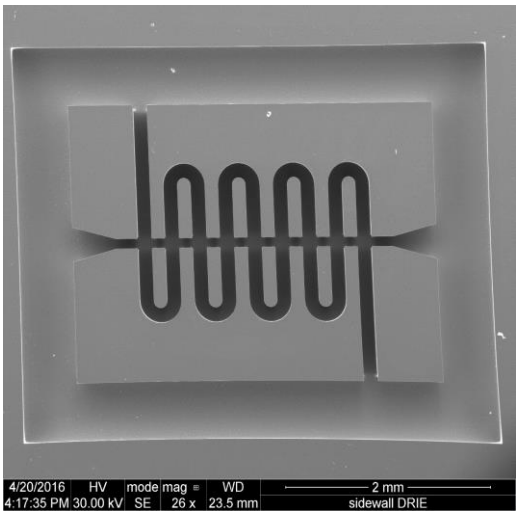

Fig. 5.11. SEM of the DRIE-patterned 4-period meander on a silicon wafer (the meander in this device does not have an input/output transition).

5.6 Cold testing of the different periods and coating materials of the meandering waveguide

The RF characteristic (S-parameters) of the microfabricated meandering waveguide was measured without an electron beam in its beam tunnel (cold test). The terahertz S-parameters (terahertz reflections at the input/output aperture of the meandering waveguide and the terahertz transmissions from one aperture to the other) were measured with the terahertz vector network analyzer (T-VNA) described in Chapter 4. As stated in Chapter 4, the T-VNA has a rectangular waveguide input/output with aperture size of 250 μm x 125 μm. In addition, it was mentioned earlier that the meandering waveguide devices have an input/output transition that will make it quick and easy to butt-couple the meandering waveguide to the ports of the T-VNA. The taper of the transition of the meandering waveguides is only in the E-plane of the waveguide, and the taper angle of the transition is 20 degrees over a length of 400 um. Hence, the

input/output port of the meandering waveguide has an aperture size of 339.4 um x 250 um. The schematic of our characterization setup is shown in Fig. 5.12.

As discussed earlier, meandering waveguides with different periods (2-period, 3-period, 4-period, and 21-period) and different dielectric coatings of the metalized walls (uncoated, aluminum dioxide-coated, parylene-coated) were fabricated. Figure 5.13 shows the comparison of the S-parameter of three different periods of the aluminum-dioxide coated meandering waveguides. The transmission spectrum (S_{12}) of Fig. 5.13a clearly shows the length dependent attenuation of the meandering periods, the transmission through the waveguide decreases with an increase in number of waveguide periods.

Furthermore, in anticipation of the hot testing of the meandering waveguide where a vacuum environment will be needed to create an electron beam, the waveguide aperture of the meandering waveguide was plugged with a conical Teflon plug. This plug

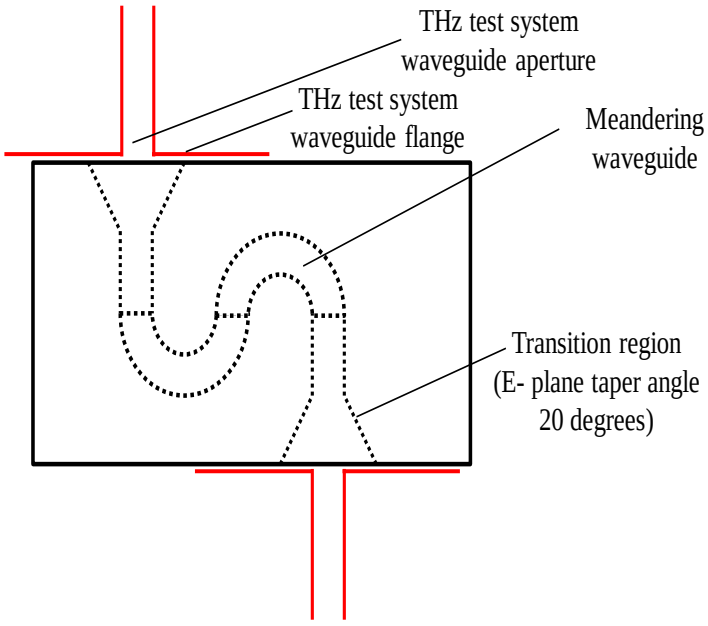

Fig. 5.12. Schematic of setup for testing meandering waveguides.

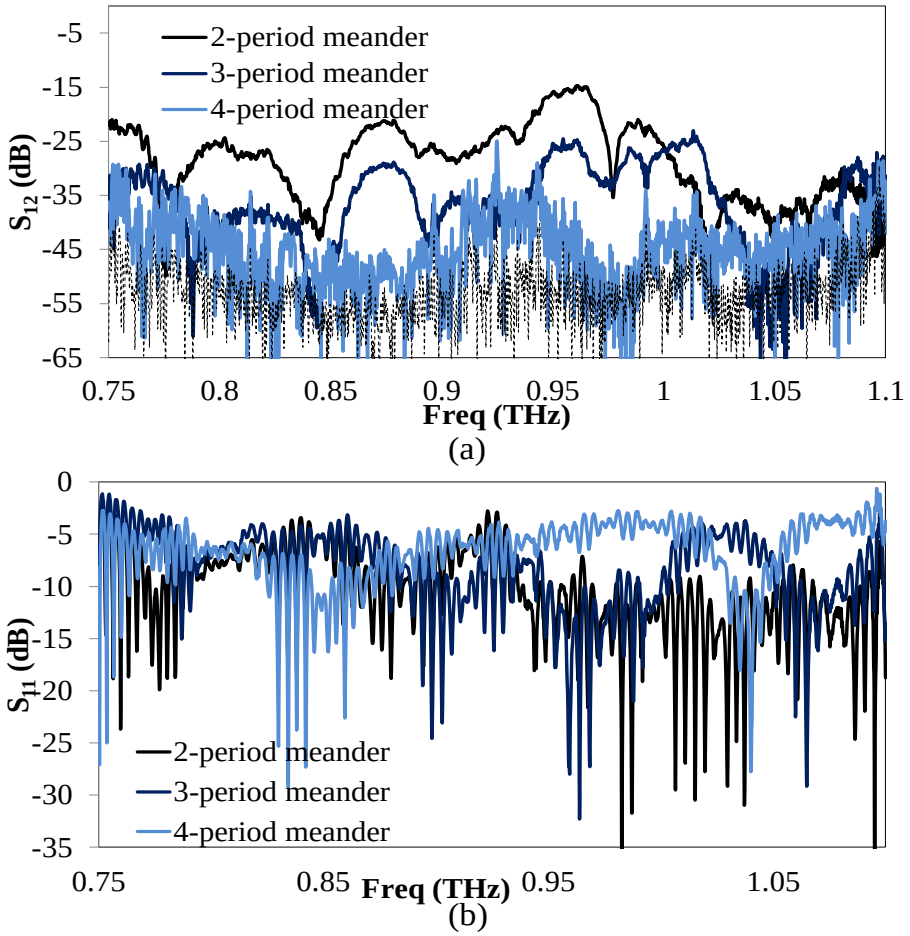

Fig. 5.13. Comparison of the S-parameters of the different periods of the aluminum dioxide-coated meandering waveguides. (a) S_{12} (transmission). (b) S_{11} (reflection).

prevents air or other gases from getting into the hot-test setup thorough the meander waveguide input. The plugging process is illustrated in Fig. 5.14. The Teflon plug, shown in Fig. 5.14e, has a length of 700 μm, a base diameter of 350 μm, and a taper angle of 10 degrees. Fig. 5.15 shows the S-parameters of the different variation of the 2-period meandering waveguide: uncoated, parylene coated, aluminum dioxide coated, and Teflon-plugged aluminum dioxide coated.

From the S_{12} data of Fig. 5.15 of the 2-period meander, it can be seen that the thin (50 nm-thick) aluminum dioxide coating improves the transmission through the

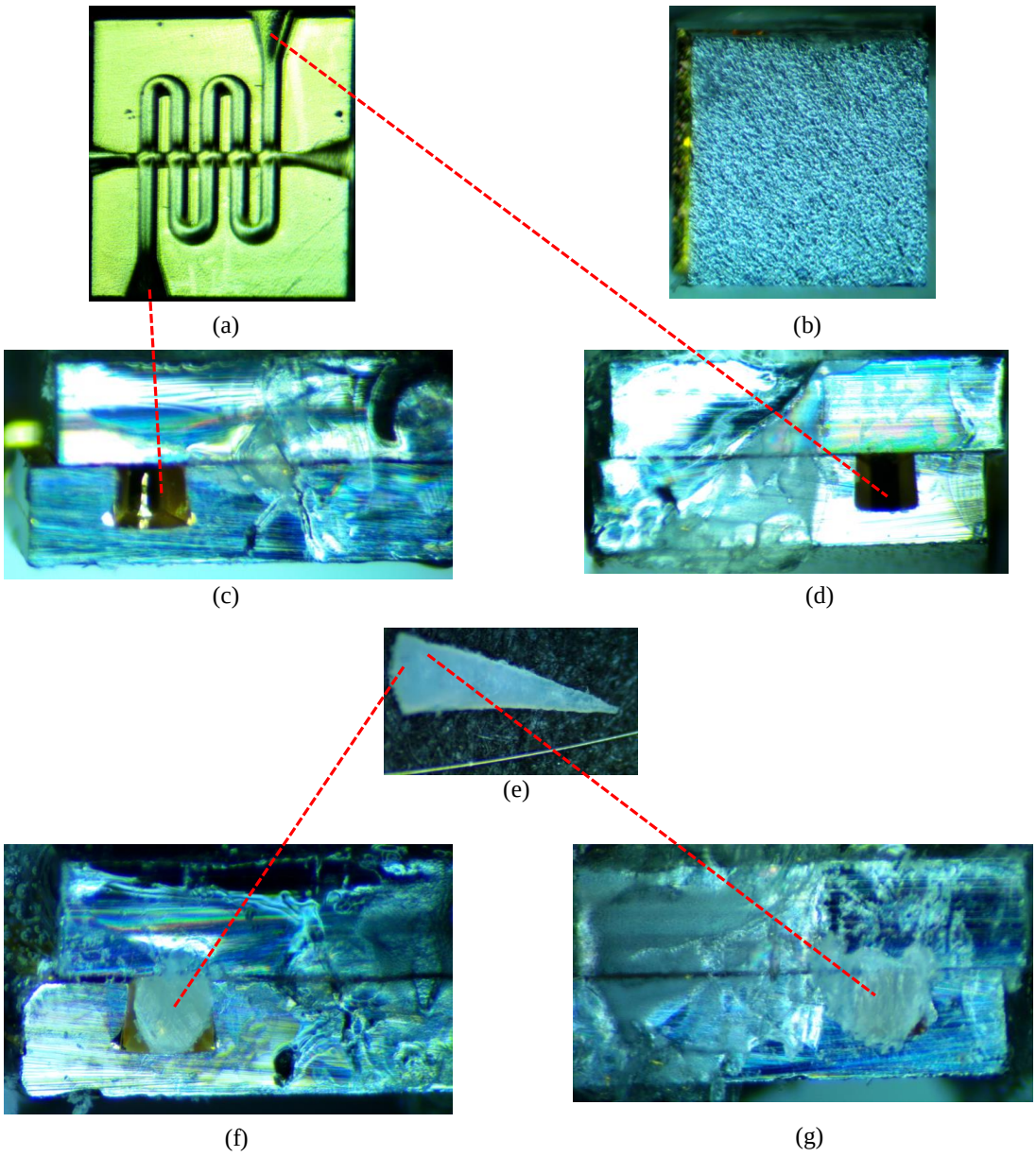

Fig. 5.14. Steps for cold testing a Teflon-plugged meandering waveguide. Teflon plugging is one of the steps necessary to create a vacuum environment necessary for the hot testing of the meander with an electron beam. (a) Cross-sectional view of the top (b) top view (c, d) end views (e) Teflon plug (f, g) end views with Teflon plug.

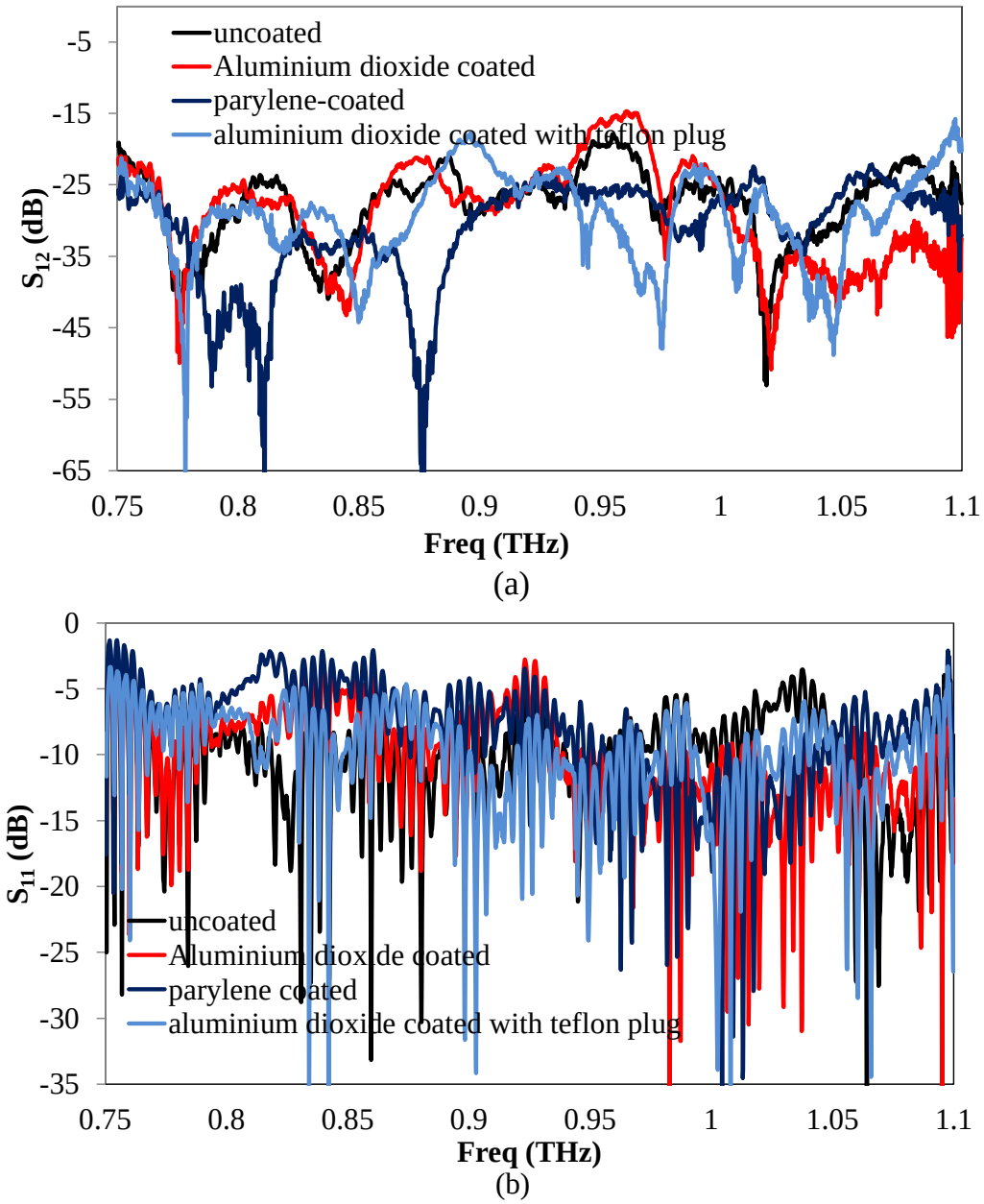

Fig. 5.15. S-parameters of the different variations of the 2-period meander. (a) S_{12} (transmission) (b) S_{11} (reflection) data.

meandering waveguide (compared to the uncoated meander) and improves the transmission through the meander at some frequency ranges.

Figure 5.16 is a 3-period meander version of Fig. 5.14. In this figure, it is observed that the same trend occur in the 2-period meander and the 3-period meander. In both, the aluminum dioxide coating improves the transmission, parylene coating deteriorates the transmission, and the Teflon plug of the aluminum dioxide coated meander improves the transmission at certain frequency ranges.

5.7 Terahertz simulation of the meandering waveguide

A low-loss meandering waveguide should have negligible transmission resonance dips and peaks above its cutoff frequency. In order to determine what contributed to the resonance dips and peaks that were observed in the characterized meandering waveguide, the meandering waveguide was simulated in steps with the HFSS, a 3D electromagnetic solver. First, the effect of the transitions on the S-parameters of the meandering waveguide was investigated. Fig. 5.17 shows the model of meandering waveguide with no transitions and a meandering waveguide with transitions. Fig. 5.18 is a comparison of the S-parameters of these waveguides. From the transmission spectrum of Fig. 5.18a and Fig. 5.18b, the resonances that the 20-degree E-plane taper of 400 μm height will introduce in the transmission and reflection spectra can be seen. The explanation for this is that the transition aperture has a different size from the standard aperture size of the WR 1.0 waveguide (250 um x 125 um) of the test system. Hence, the mismatch in the characteristic impedances of excitation port and the meandering waveguide aperture results in the standing waves seen in the S-parameter spectra.

Next, the effect of integrating a beam tunnel with the meandering

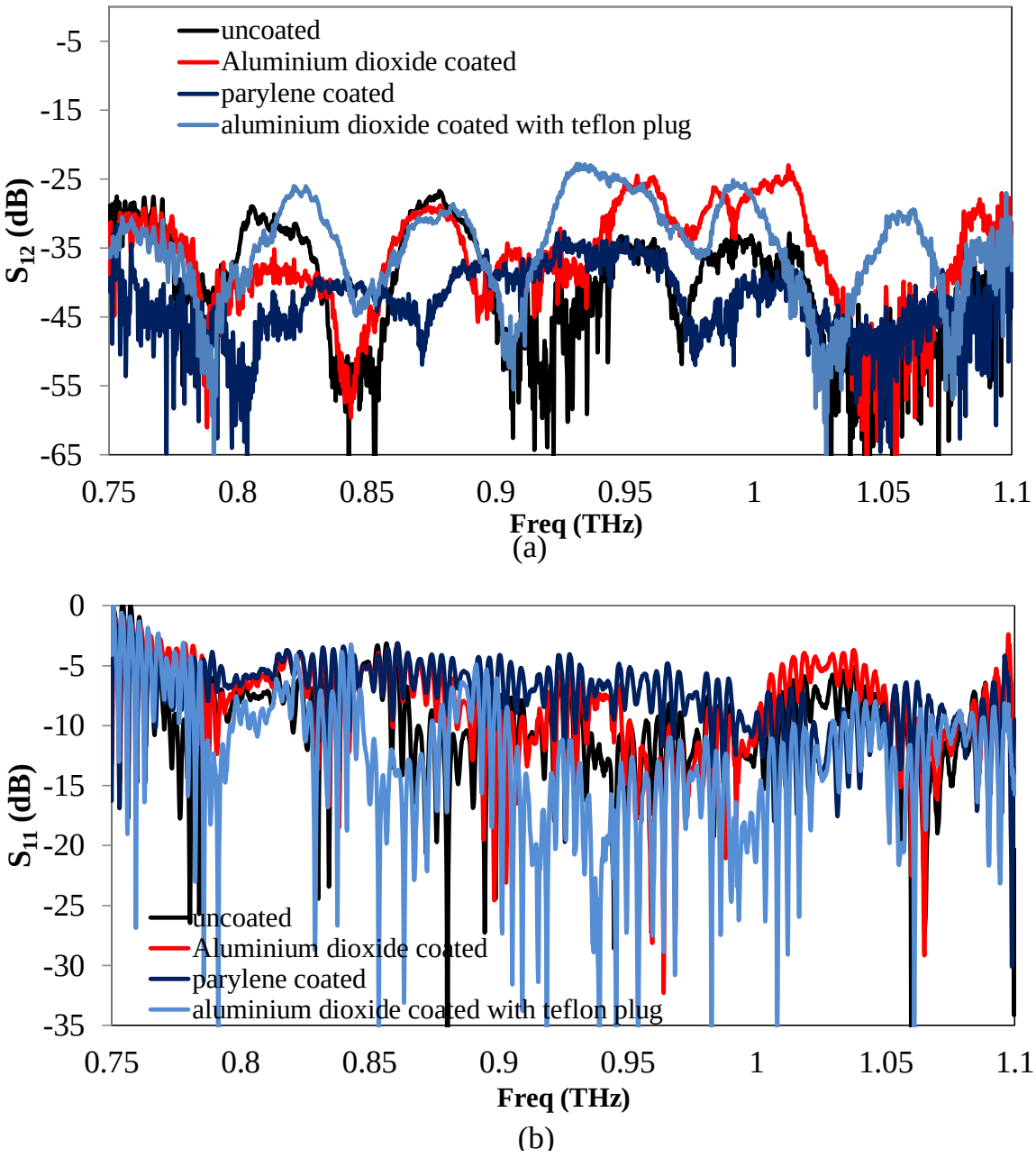

Fig. 5.16. Comparison of the different variations of the 3-period meander (a) S_{12} (transmission) (b) S_{11} (reflection) data.

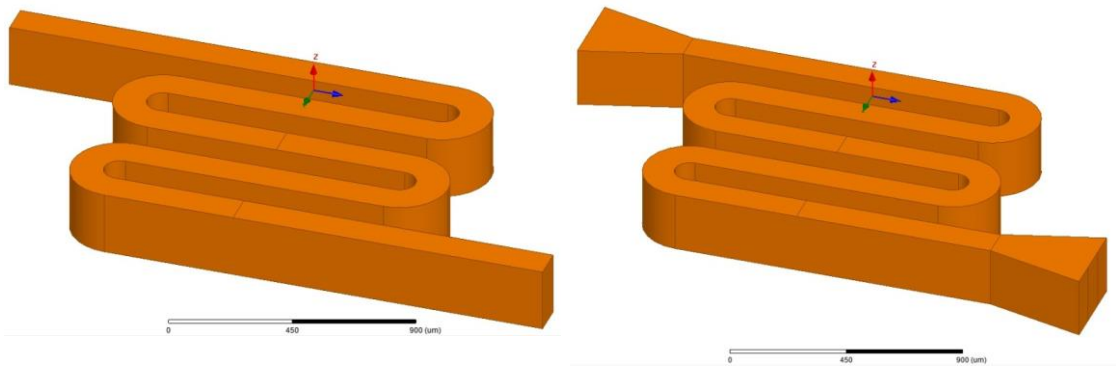

(a) (b)

Fig. 5.17. Model of 2-period meandering waveguide (a) without input/output transition. (b) with input/output transition.

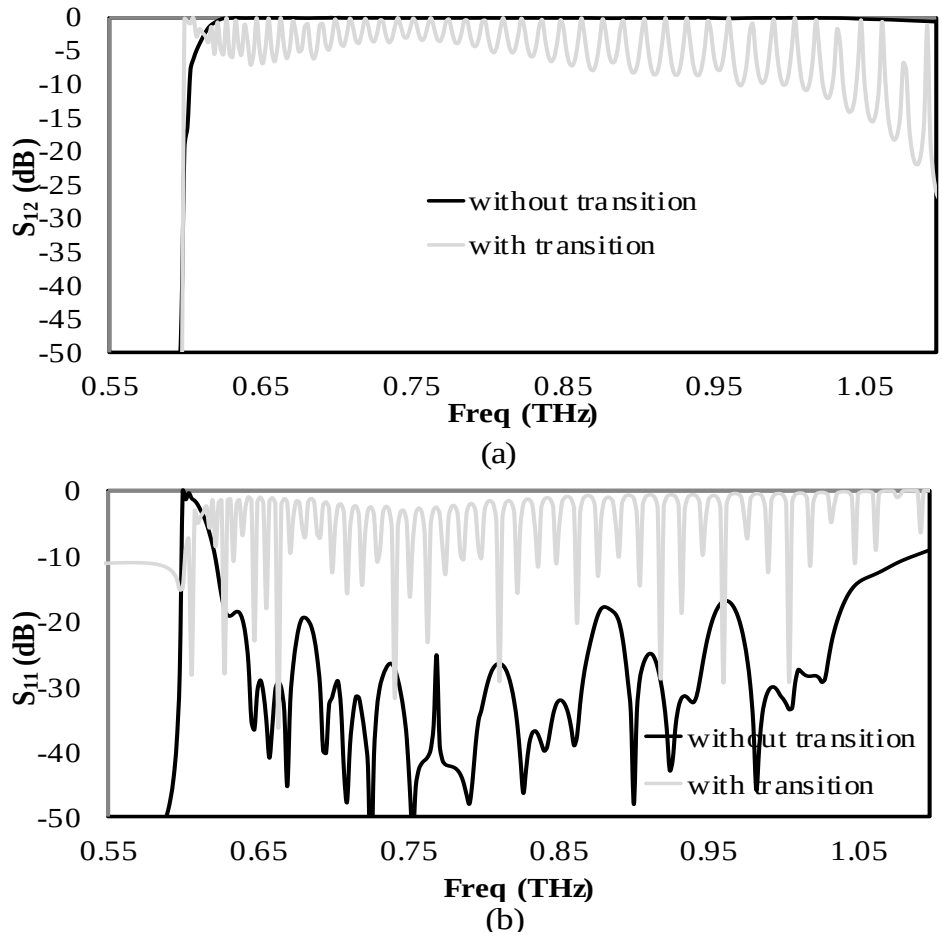

Fig. 5.18. Comparison of the S-parameters of a meandering waveguide with no transition and a meandering waveguide with transition. (a) S_{12} spectrum (b) S_{11} spectrum.

waveguide on the S-parameters of the waveguide will be investigated.

The simulation model is shown in Fig. 5.19. A parametric sweep of the thickness of the beam tunnel from 25 μm to 250 μm was performed while keeping the width of the beam fixed at 80 μm.

Fig. 5.20 shows the transmission through the meander for different beam thicknesses. From Fig. 5.20, it can be seen that increasing the beam thickness increases the depth of the resonances observed in the S_{12} spectrum. This is because the beam tunnel introduces discontinuities in the meandering waveguide, and these discontinuities modify the characteristic impedance of the waveguide, leading to mismatches that manifest as standing waves in the transmission spectrum.

In Fig. 5.21 and 5.22, the measured S_{12} of the 2-period and the 3-period meander (from Fig. 5.16a and Fig. 5.17a) were compared with their respective simulated S_{12}. The beam tunnel width and beam tunnel thickness for the simulated model is 80 μm and 250 μm (same for the fabricated devices).

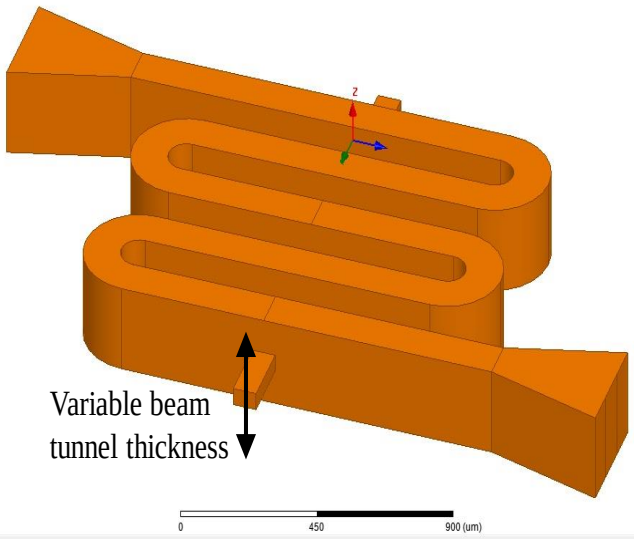

Fig. 5.19. Model of the 2-period meander with its beam tunnel.

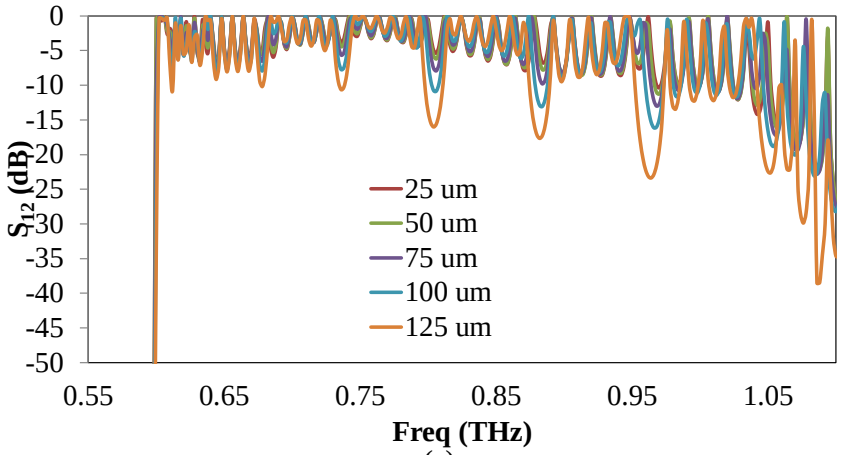

(a)

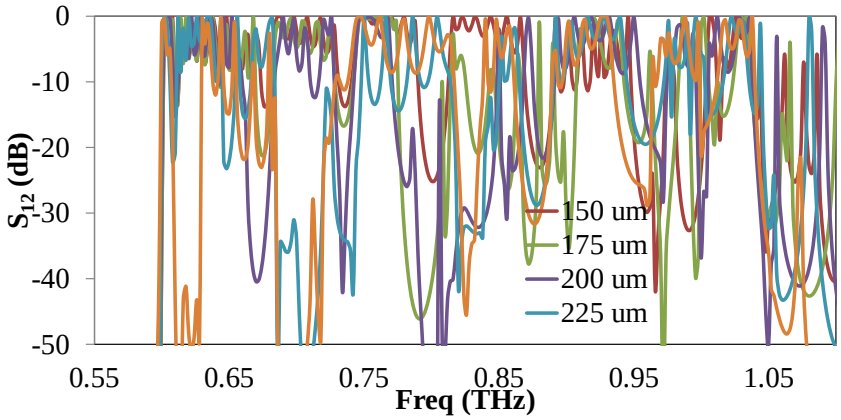

(b)

Fig. 5.20. Effect of beam tunnel of various thicknesses on the S_{12} spectrum of the 2-period meander (a) beam thickness 25 µm – 125 µm (b) beam thickness 150 µm – 125 µm.

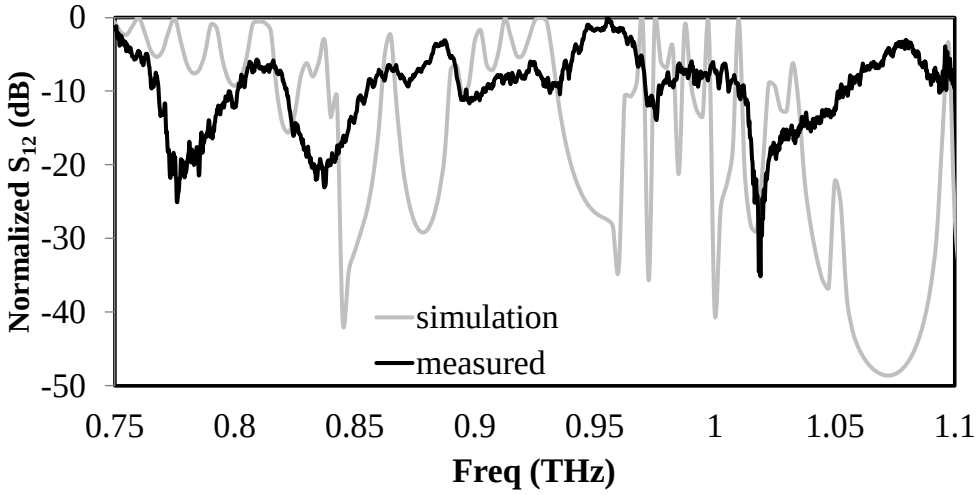

Fig. 5.21. Comparison of simulated and measured S_{12} of the 2-period meander.

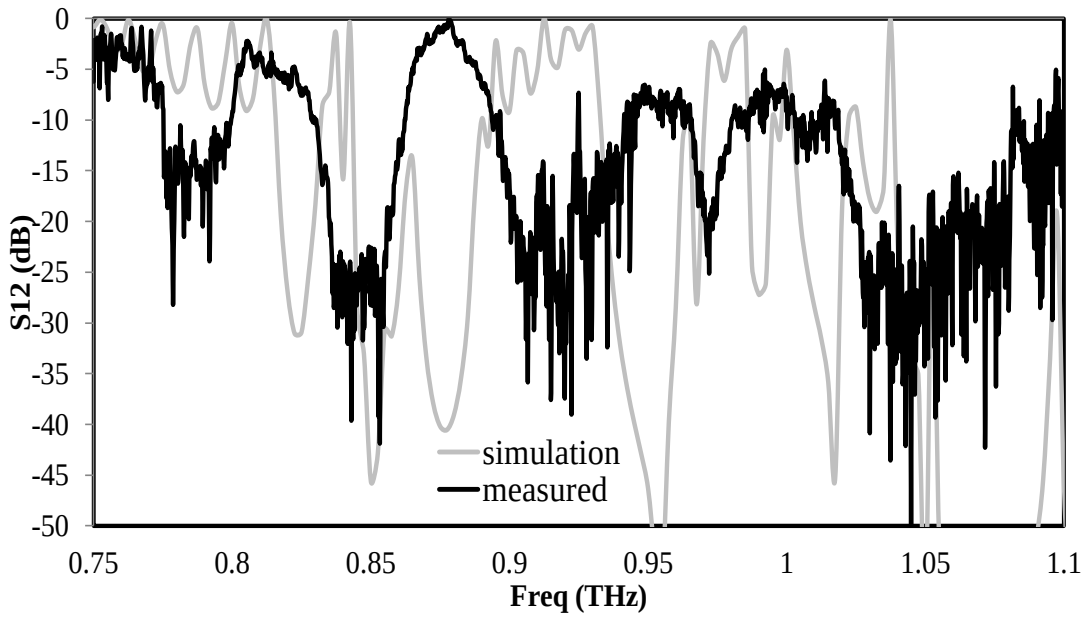

Fig. 5.22. Comparison of simulated and measured S_{12} of the 3-period meander.

5.8 Particle-in-cell simulation of the meandering waveguide TWT

Next, particle-in-cell (PIC) simulations (with CST particle studio) of the 2-period and a 3-period meandering waveguide structures were performed. In the simulation model, a beam of electrons was injected through the structures as shown in the schematic of Fig. 5.23. The fabricated meandering waveguide was modeled in a simple form in the PIC simulation model by eliminating the transitions and replacing the rectangular cross section beam tunnel with a circular beam tunnel. A parametric sweep was performed on the electron beam velocity and electron current to find the beam parameters that will produce the largest amplification. Fig. 5.24 shows the amplification of the terahertz wave through the meanders for a beam with electron velocity of 8.2×10^7 ($0.27c$) and beam current of 2A. The amplification maximum amplification for the 2-period meander and the 3-period meander is 4 dB and 5 dB, respectively. The focusing magnetic field in this model was 0.5 Tesla.

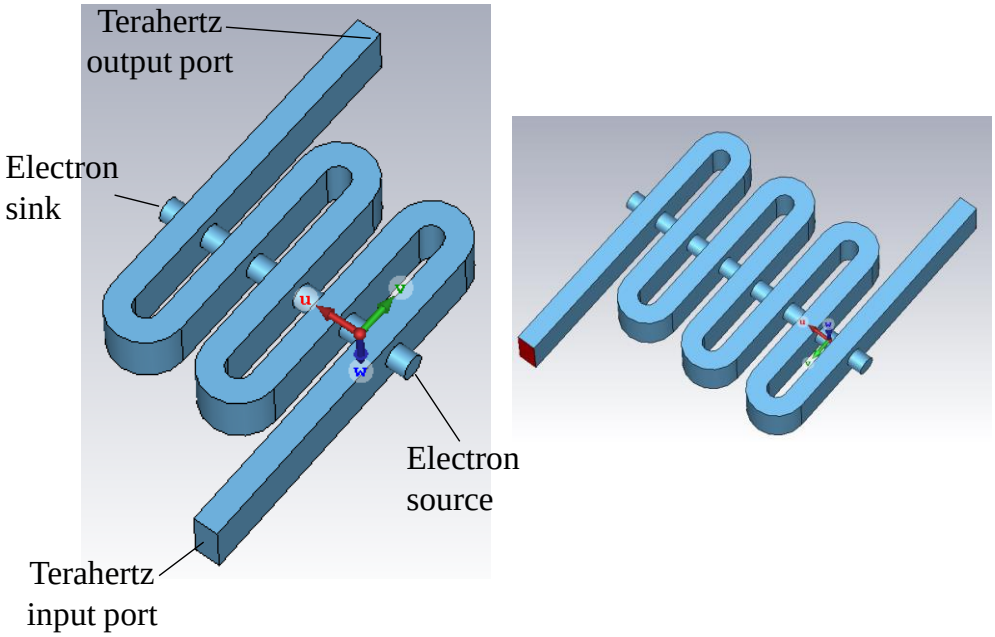

Fig. 5.23. Particle-in-cell model of a 2-period (left) and 3-period (right) meandering waveguide.

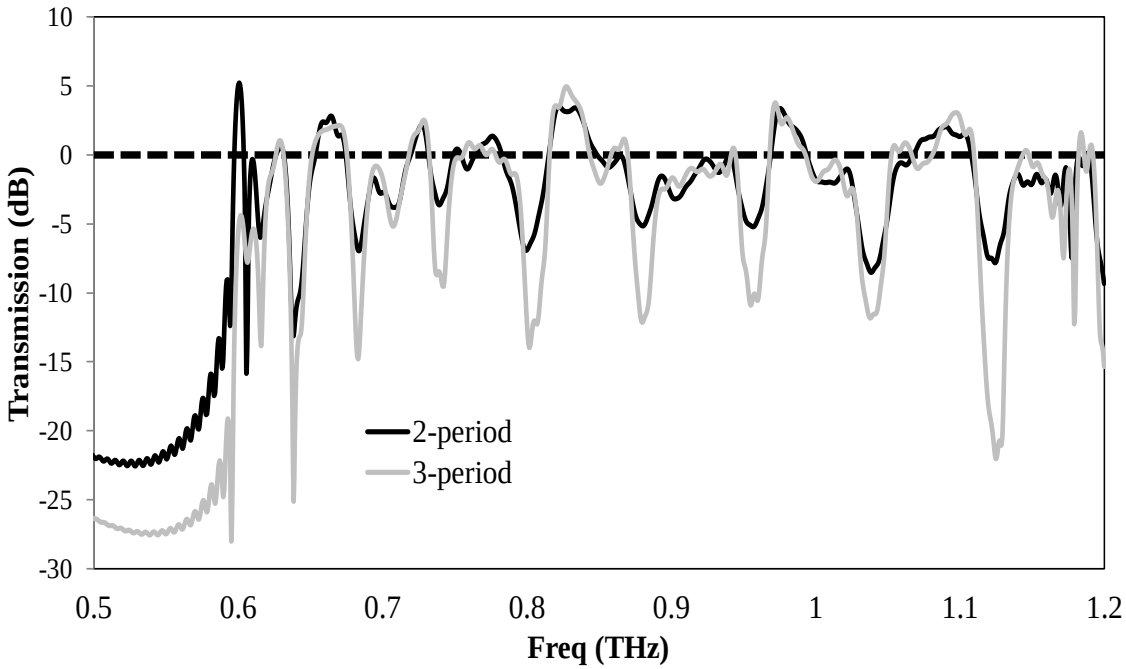

Fig. 5.24. Simulated THz amplification by a lossless 2-period and 3-period meandering waveguide.

5.9 Hot test measurement

The steps to prepare the meandering waveguide for hot testing are shown in Fig. 5.25. The integrated beam tunnel in the fabricated meandering waveguide was extended with glass capillary tubes. A seal was created between the beam tunnel and the capillary tube with epoxy. As mentioned earlier, the input and output apertures of the meandering waveguide were sealed with a Teflon plug in anticipation of the vacuum environment in which the hot test will be performed. The schematic of the hot test setup is shown in Fig. 5.26. With a rotary pump, a low pressure (vacuum) of ~ 18 mTorr was created in the test device and its adjoining capillary tubes. A thermionic emitter (a hot tungsten filament) was heated to boil off electrons from the emitter from one side of the meandering waveguide, the electrons emitted were then accelerated with a high voltage, and then collected at the electrode at the other side of the meandering waveguide after the electrons have passed through the beam tunnel. The electron gun configuration for this hot test is similar to the configuration presented in section 2.12. Here in this setup, the filament voltage was 2V, and the filament current was 1A. The acceleration voltage (relative to the filament) was fixed at 4.88 kV. The waveguide flange of the terahertz test system was covered with a thin Kapton tape to prevent electric sparks from jumping from the electric circuit device electron gun device to the waveguide flange of the test system. Fig. 5.27 is a photograph of the hot test setup. Fig. 5.28 shows the result of the hot test for different collector voltages. The maximum amplification of the 2-period meander from this hot test was ~12 dB at 0.91275 THz for a collector voltage 4.8 kV over a bandwidth of 1 GHz at TWT terahertz transmittance of -45 dB.

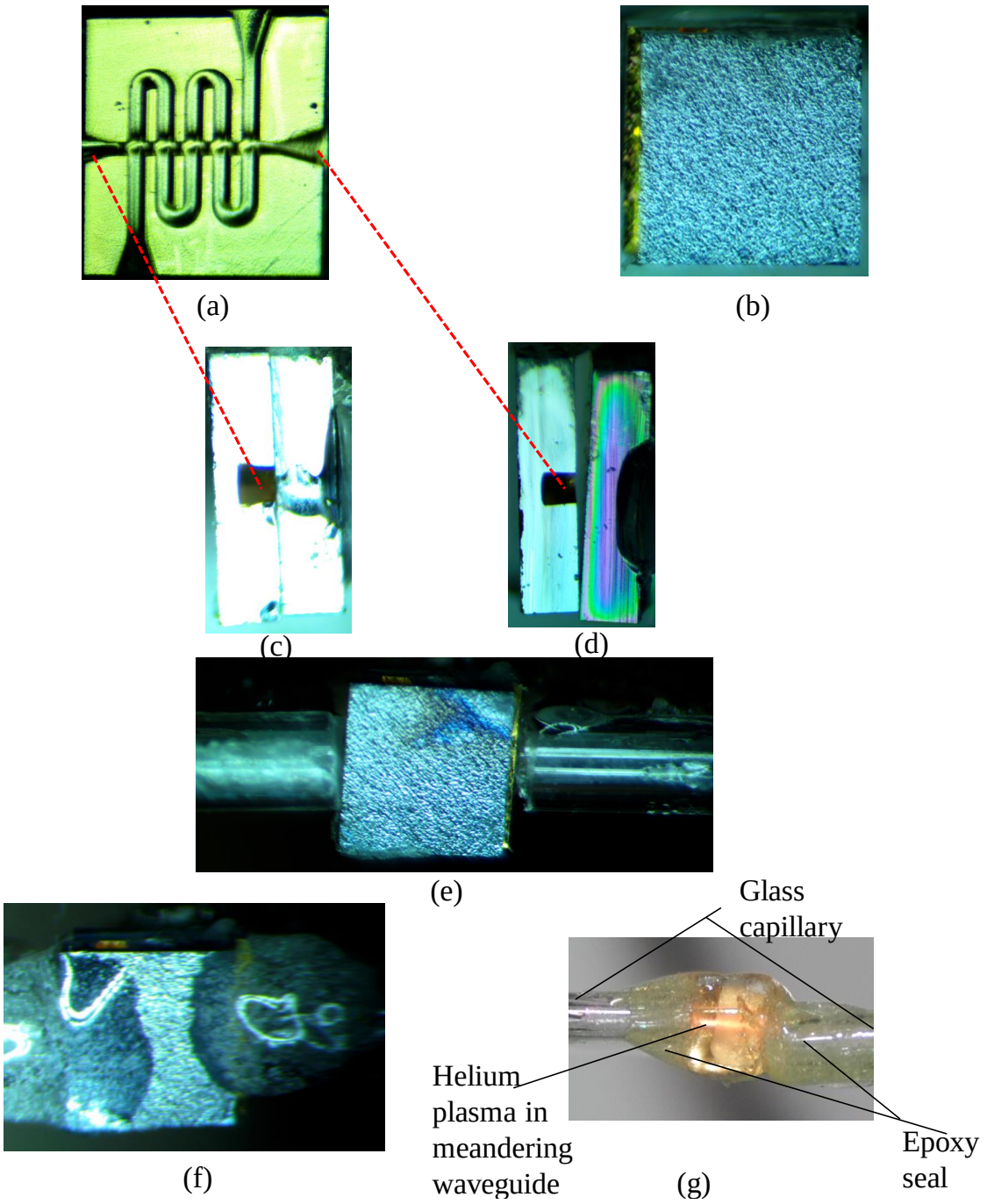

Fig. 5.25. Illustration of the steps to prepare the meandering waveguide for hot test. (a) Cross-sectional view of device top (b) top view (c, d) side views (e) capillary tubes coupled to the ends of the beam tunnel (f) vacuum-tight epoxy connection to the beam tunnel of the meandering waveguide (g) Pre-hot test to check the clearance of the 80 μm width beam tunnel with the creation of a helium plasma in the tunnel. The meander was covered with a transparent glass slab in order to be able to see the beam.

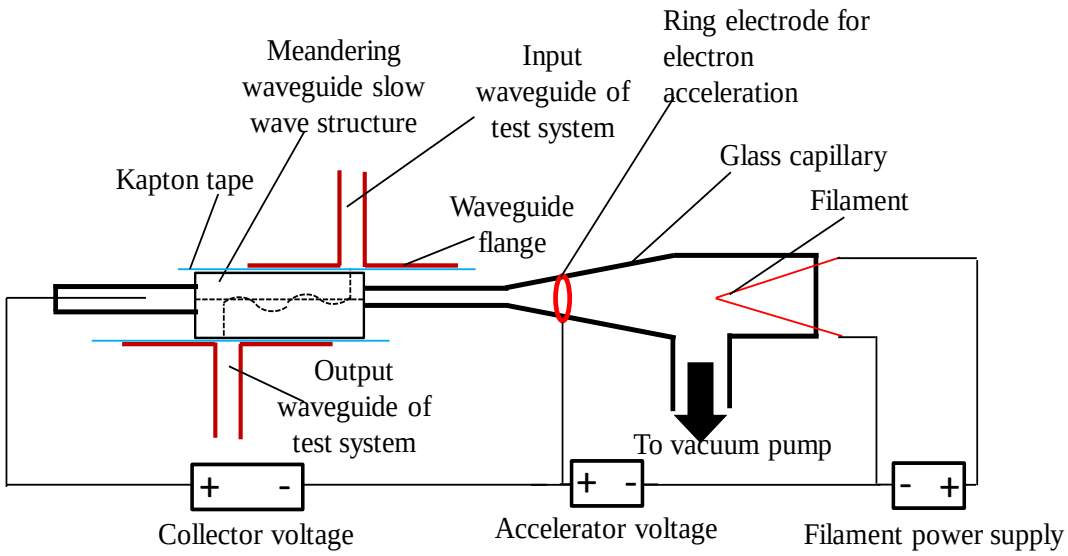

Fig. 5.26. Schematic for the hot test setup.

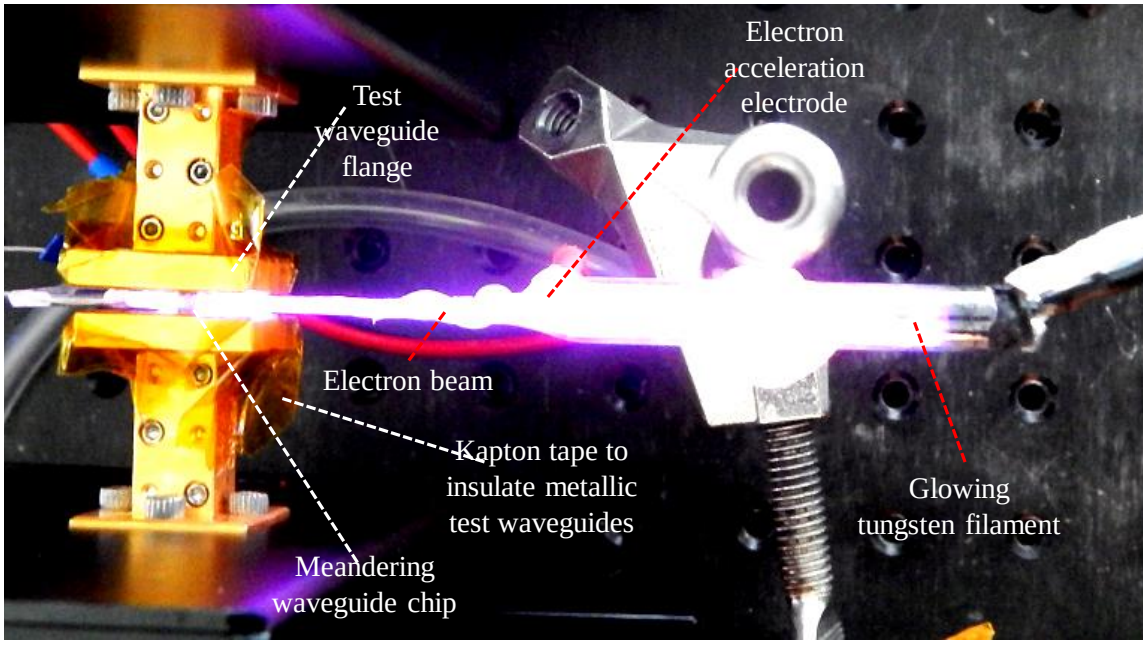

Fig. 5.27. Photograph of the experimental setup of the hot test setup.

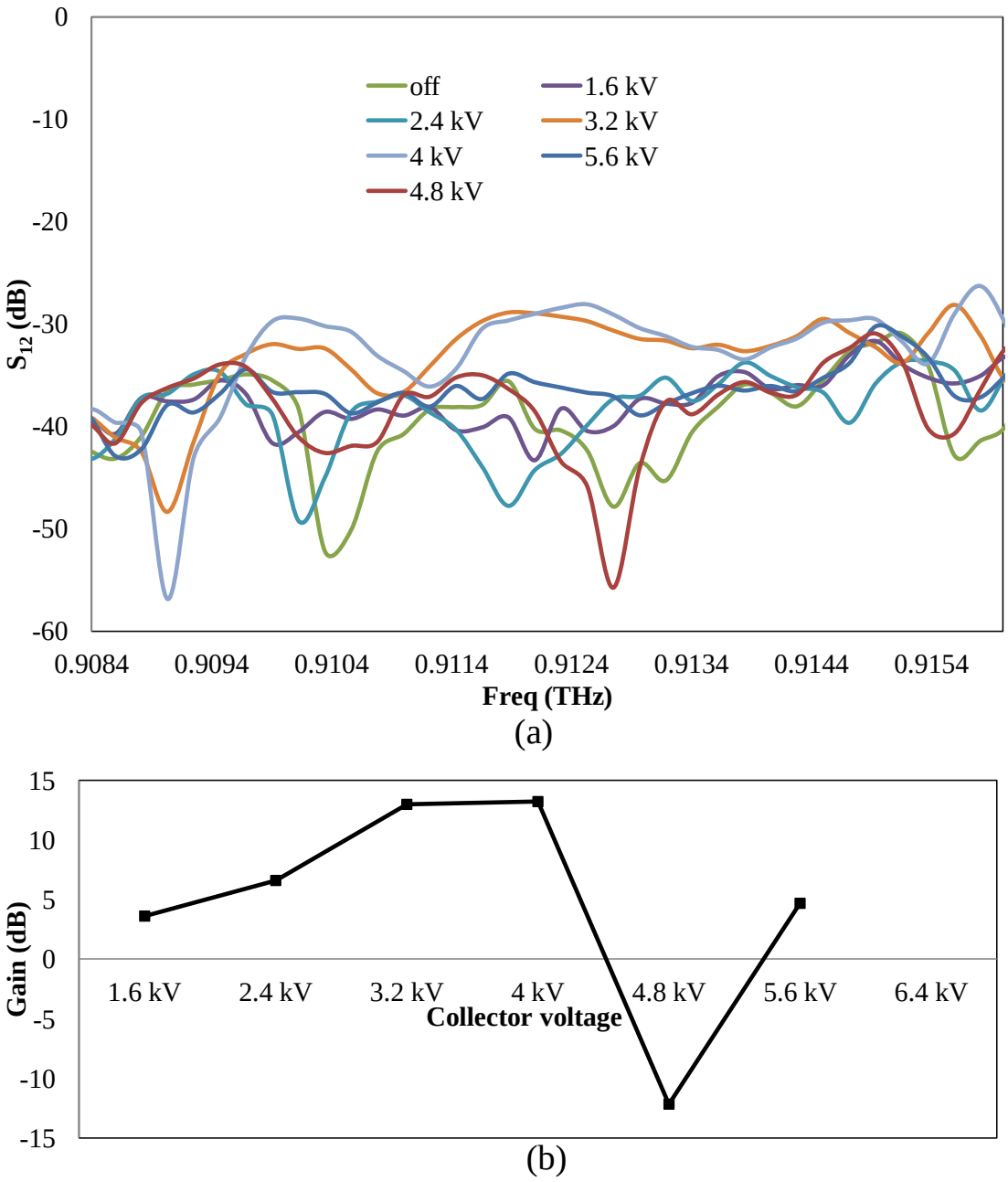

Fig. 5.28. Amplification of the terahertz waves in the 2-period meandering waveguide slow wave structure by an electron beam (a) S_{12} spectra for different collector voltage over the frequency range of highest gain (b) gain as function of collector voltage at 0.91275THz.

5.10 Conclusions

This chapter has extended previous work on the meandering waveguide for terahertz wave amplification by extending the operating frequency of the meandering waveguide to ~ 1THz. Although the meandering waveguide is fundamentally a backward wave structure, this meandering waveguide has been used as a forward wave amplifier to avoid the problems of low bandwidth and instability that characterized backward wave amplifiers. Design factors and fabrication methods for the ~ 1 THz meandering waveguide amplifier were presented. Simulation studies were performed to gain insight into the cold and hot characteristics of the meandering waveguide amplifier. The electron gun used in the amplifier design consisted of a V shaped thermionic tungsten filament in a tube at a pressure of ~18 mTorr. This 'high' pressure in the tube is a source of ion in the amplifier beam, in addition to the thermionic electrons. These ions will reduce the interaction between the thermionic electrons and the electromagnetic wave. However, these ions will produce the desirable effect of focusing the thermionic electrons. This reduces the divergence of the electrons away from the axis of the beam tunnel. The gain of the design presented can be improved by increasing the electron beam current, while keeping the beam divergence to a minimum with a magnetic field. Furthermore, developing a longer but lower loss interaction circuit can produce an amplifier with higher gain.

5.11 References

[1] R. Zheng, P. Ohlckers, and X. Chen, "Particle-in-cell simulation and optimization for a 220-GHz folded-waveguide traveling-wave tube," *IEEE Transactions on Electron Devices*, vol. 58, no. 7, pp. 2164-2171, 2011.

[2] W. Liu, C. Zhao, K. Li, Y. Wang, and Z. Yang, "Two-section folded-waveguide

slow-wave structure for terahertz extended interaction oscillator," *IEEE Transactions on Electron Devices*, vol. 61, no. 3, pp. 902-908, 2014.

[3] Y. Hou, J. Xu, S. Wang, Z. Lu, Y. Wei, and Y. Gong, "Study of high efficiency novel folded waveguide traveling-wave tube with sheet electron beam," *Progress in Electromagnetics Research*, vol. 141, pp. 431-441, 2013.

[4] K. E. Kreischer, J. C. Tucek, M. A. Basten, and D. A. Gallagher, "220 GHz power amplifier testing at Northrop Grumman," in *Vacuum Electronics Conference (IVEC), 2013 IEEE 14th international*, 2013, pp. 1-4.

[5] J. C. Tucek, M. A. Basten, D. A. Gallagher, K. E. Kreischer, Ri. Lai, V. Radisic, K. Leong, and R. Mihailovich, "A 100 mW, 0.670 THz power module," in *Vacuum Electronics Conference (IVEC), 2012 IEEE 13th International*, 2012, pp. 31-32.

[6] J. C. Tucek, M. A. Basten, D. A. Gallagher, and K. E. Kreischer, "Testing of a 0.850 THz vacuum electronic power amplifier," in *Vacuum Electronics Conference (IVEC), 2013 IEEE 14th International*, 2013, pp. 1-2.

[7] J. C. Tucek, D. A. Gallagher, K. E. Kreischer, and R. Mihailovich, "A compact, high power, 0.65 THz source," in *Vacuum Electronics Conference (IVEC), 2008 IEEE 9th International*, 2008, pp. 16-17.

[8] J. W. Gewartowski and H. A. Watson, *Principles of electron tubes*, Princeton, NY: D. Van Nostrand Company Inc., 1965.

[9] R. G. E. Hutter, *Beam and wave electronics in microwave tubes*, Boston, MA: Technical Pub., 1965.

[10] J. H. Booske, M. C. Converse, C. L. Kory, C. T. Chevalier, D. A. Gallagher, K. E. Kreischer, V. O. Heinen, and S. Bhattacharjee, "Accurate parametric modeling of folded waveguide circuits for millimeter-wave traveling wave tubes," *IEEE Transactions on Electron Devices*, vol. 52, no. 5, pp. 685-694, 2005.

[11] V. M. Lubecke, K. Mizuno., and G. M. Rebeiz, "Micromachining for terahertz applications," *Microwave Theory and Techniques, IEEE Transactions on*, vol. 46, no. 11, pp. 1821-1831, 1998.

[12] T. J. Reck, C. Jung-Kubiak., J. Gill, and G. Chattopadhyay, "Measurement of silicon micromachined waveguide components at 500–750 GHz," *Terahertz Science and Technology, IEEE Transactions on*, vol. 4, no.1, pp. 33-38, 2014.

[13] P. A. George., C. Manolatou, F. Rana, A. L. Bingham, and D.R. Grischkowsky, "Integrated waveguide-coupled terahertz microcavity resonators," *Applied Physics Letters*, vol. 91, no. 19,191122, 2007.

[14] Y. M. Shin, L. R Barnett, D. Gamzina, N. C. Luhmann Jr., M. Field, and R. Borwick, "Terahertz vacuum electronic circuits fabricated by UV lithographic molding and deep reactive ion etching," *Applied Physics Letters*, vol. 95, no. 18, p. 181505, 2009.

[15] (a)O. Fawole and M. Tabib-Azar, "Multimode rectangular cavity terahertz resonators," in *Wireless Symposium (IWS), 2016 IEEE MTT-S International,* 2016 pp. 1-4.
(b)B. Bowden, J. A. Harrington, and O. Mitrofanov, "Low-loss modes in hollow metallic terahertz waveguides with dielectric coatings," *Applied Physics Letters*, vol. 93, no. 18, p. 181104, 2008.

[16] Mr Shashank S. Pandey fabricated these meandering waveguide devices.

[17] S. Arslanagić, T. V. Hansen, N. A. Mortensen, A. H. Gregersen, O. Sigmund, R. W. Ziolkowski, and O. Breinbjerg, "A review of the scattering-parameter extraction method with clarification of ambiguity issues in relation to metamaterial homogenization," *IEEE Antennas and Propagation Magazine*, vol. 55, no. 2, pp. 91-106, 2013.

CHAPTER 6

CONCLUSIONS

The research work presented in this dissertation consisted of design, fabrication and characterization of waveguide-based terahertz amplifier circuits that used the plasma/electron beams as their energy sources. The dissertation started with a study of plasma, its generation, its modes of operation, its interaction with magnetic fields, its interaction with electric fields, and its interaction with its constituent gases. This initial study led to the development of a) a novel electrically-actuated plasma switch, b) a novel magnetically-actuated switch, c) a novel rotating plasma magnetic sensor, d) a new electrode geometry for an electrohydrodynamic pump, e) a plasma soft x-ray source, and f) an electron gun. The electrically-actuated switch operated in atmospheric pressure gas and it required 3.7 kV for actuation. The magnetically-actuated switch operated in an atmospheric pressure gas and it required 0.5 T for actuation. The actuation field of these two switches can be drastically reduced by scaling the device dimension and employing microfabrication techniques. The minimum field required to deflect the plasma beam in the rotating plasma magnetic sensor rotate was 40 mT. This device was sensitive to very small magnetic fields because of its symmetric design. The corona wind electrohydrodynamic pump developed in this work was fabricated with a 3D printer. The 3D printer allowed for the rapid prototyping of different variations of its coaxial conical electrodes. The maximum air flow velocity from the corona wind pump was 2 m/s. The

plasma x-ray source produced soft x-rays with a mean energy of ~4 keV. The electron gun produced a maximum of ~20 μA from a tungsten thermionic emitter with a heating current of 1.5 A and an acceleration voltage of 2.4 kV.

Furthermore, this dissertation proposed coupled dielectric resonators as interaction structures in traveling wave amplifiers and electron tubes. Towards this end, gigahertz prototypes of the resonators at ~ 7 GHz were designed. A method for exciting the fundamental modes in these resonators was developed. In addition, a near-field probing method for imaging the fields in these resonators was also developed. The interaction of charge carriers in a plasma beam (9 mA current) at 50 Torr with the fields in this prototype dielectric resonators was demonstrated. Then a particle-in-cell simulation was performed to demonstrate that the dielectric resonator can interact with an electron beam to produce amplification of electromagnetic waves. Finally, chemical vapor deposition was use to fabricate terahertz prototypes of these resonators.

The biosensing application demonstrated in this dissertation was a near-field probing system for obtaining the terahertz near-field images of biological samples. A number of near-field probes were designed, developed, characterized and were then employed in this imaging system. The spatial resolution of these probes ranged from 445 μm to 75 μm. The biological samples that were imaged consisted of a mouse brain slice, a leaflet of an umbrella plant, and a section of the wing of a box elder bug. The terahertz near-field images were obtained by measuring the terahertz reflection/transmission of the near-field probe at discrete points over these samples. The terahertz near-field images provided a unique perspective into the structure of these samples. Furthermore, this research demonstrated that terahertz waves can be used to reliably detect a minimum

concentration of sugar and ethanol of 0.3% ethanol and 1.5% sugar by weight, respectively, in water. This capability of terahertz waves was used to monitor in real time and noninvasively the ethanol production by the yeast cells.

Finally, this research presented a meandering waveguide slow wave structure as an interaction circuit for amplification of terahertz waves. The meandering waveguides were fabricated with deep reactive ion etching of silicon that were subsequently coated with 100 nm gold and a thin layer of a high quality dielectric Al_2O_3 or a 20 μm-thick layer of parylene. Different meandering waveguide geometries were fabricated and tested. The two period meandering waveguide devices covered with a 50 nm aluminum dioxide layer showed the smallest attenuation of terahertz waves. These devices were then hot tested with an electron beam current of ~20 μA and beam were acceleration voltage of 4.8 kV. This circuit yielded an amplification of 12 dB of a -55 dBm, 0.91 Terahertz signal over a 1 GHz bandwidth.

APPENDIX A

THEORETICAL DESCRIPTION OF A TRAVELING WAVE TUBE AMPLIFIER

A.1 Introduction

Here, we present the equations that govern the operation of the TWT operating in the forward wave mode [1]. First, we derive the equation for determining the radio frequency (RF) current induced in an electron beam due to the RF electric field on the slow wave structure (the electronic equation). Next, we present the equation that relates the electric field induced in a slow wave circuit as a result of a modulated electron beam (the circuit equation). Finally, we present the cumulative interaction equation for induced current due to the slow wave RF field, and the induced RF field due to a modulated RF current. This will be obtained by simultaneously solving the electronic equation and the circuit equation. We will derive the amplification of the TWT from the cumulative interaction equation.

In the analysis that follows, we will assume small signal operation, and that the RF qualities are sinusoidal, and are of the form:

$$U = Re[ue^{jwt-\Gamma z}] \tag{A.1}$$

where u is a phasor quantity with no time or position z dependence. Hence

$$\frac{\partial U}{\partial t} = Re\left[jwue^{jwt-\Gamma z}\right] \tag{A.2}$$

and

$$\frac{\partial U}{\partial z} = Re\left[-\Gamma ue^{jwt-\Gamma z}\right] \tag{A.3}$$

Since all RF qualities are of the form (A.1), we may omit the exponential factor in equations where these qualities occur.

A.2 Electronic equation

The total instantaneous (DC and RF pertubation) beam velocity, convection current, and charge density are written as:

$$u_{tot} = u_0 + u \tag{A.4}$$

$$I_{tot} = -I_0 + i \tag{A.5}$$

$$\rho_{tot} = -\rho_0 + \rho \tag{A.6}$$

The convention current density as:

$$J_{tot} = -J_0 + J \tag{A.7}$$

However:

$$J_{tot} = \rho_{tot} u_{tot} \tag{A.8}$$

Or:

$$-J_0 + J = -\rho_0 u_0 + u_0 \rho - \rho_0 u + \rho u \tag{A.9}$$

We shall assume that all RF terms are small relative to the DC terms, hence product of two or more RF terms will be ignored. Since $J_0 = \rho_0 u_0$, then:

$$J = u_0\rho - \rho_0 u \tag{A.10}$$

Therefore:

$$i = (u_0\rho - \rho_0 u)S \tag{A.11}$$

where *S* is the cross section of the electron beam.

The equation of continuity is:

$$\nabla . J = -\frac{\partial \rho}{\partial t} \tag{A.12}$$

which in phasor form is:

$$-\Gamma i = -jw\rho S \tag{A.13}$$

Combining (A.11) and (A.13), we obtain:

$$u = -\frac{jw - u_0\Gamma}{jw\rho_0 S} i \tag{A.14}$$

Equation (A.14) relates the electron beam RF velocity to the electron beam RF current.

The acceleration of an electron is given by:

$$\frac{dU}{dt} = -\frac{e}{m} E_{zT} \tag{A.15}$$

where E_{zt} is the total instantaneous RF electric field seen by the electrons. Since the

velocity of an electron is a function of both position and time, then the total derivative in (A.15) is the sum of two partial derivatives:

$$\frac{dU}{dt} = \frac{\partial U}{\partial t} + \frac{\partial U}{\partial z}\frac{\partial z}{\partial t} \tag{A.16}$$

For small signal levels, $\partial z/\partial t$ is approximately given by the DC beam velocity. Hence:

$$\frac{dU}{dt} = \frac{\partial U}{\partial t} + u_0\frac{\partial U}{\partial z} \tag{A.17}$$

In phasor form (A.15) becomes:

$$(jw - u_0\Gamma)u = -\frac{e}{m}E_{zT}$$

$$= -\frac{e}{m}(E_{zn} + E_{zsc}) \tag{A.18}$$

because E_{zT} is the sum of the electric field of the synchronous space harmonic (E_{zn}) and the electric field of the electron beam space charge (E_{zsc}).

The electric field due to the electron beam space charge can be obtained by solving Poisson's equation. Assuming a one-dimensional beam with infinite cross section, Poisson's equation becomes:

$$-\Gamma E_{zsc} = \frac{\rho}{\varepsilon_0} \tag{A.19}$$

Using (A.13), we obtain:

$$E_{zsc} = j\frac{i}{w\varepsilon_0 S} \tag{A.20}$$

However, for a finite beam, the electric field is reduced by a space-reduction factor R^2. Hence:

$$E_{zsc} = jR^2 \frac{i}{w\varepsilon_0 S} \tag{A.21}$$

However, the plasma frequency (natural frequency of oscillation of an electron cloud when perturbed) is given by:

$$w_p^2 = \frac{e\rho_0}{m\varepsilon_0} \tag{A.22}$$

And the reduced plasma frequency due to finite beam size is:

$$w_q = Rw_p \tag{A.23}$$

Using (A.22) and (A.23) in (A.21), we obtain:

$$E_{zsc} = j\frac{mw_q^2}{e\rho_0 Sw} i \tag{A.24}$$

Finally, (A.14), (A.18), and (A.24) can be combined to eliminate E_{zsc} and u to yield:

$$i = \frac{j\beta_e I_0 E_{zn}}{2V_0\left[(\Gamma - j\beta_e)^2 + \frac{{w_q}^2}{u_0^2}\right]} \tag{A.25}$$

(A.25) is the electronic equation and it gives RF current induced in a DC electron beam by an space harmonic E_{zn}.

A.3 Circuit equation

The circuit equation gives the current induced in a slow wave circuit due to a RF electron beam current. We begin the derivation of the circuit equation by defining a parameter called the beam interaction impedance K_n of the nth space harmonic as:

$$K_n = \frac{\int |E_{zn}|^2 dS}{2\beta_n^2 PS} \tag{A.26}$$

From (25), we can define the instantaneous power flow along the slow wave structure as:

$$p = \frac{E_{zn}^2}{\beta_n^2 K_n} \tag{A.27}$$

where E_{zn} is the instantaneous value of the space harmonic electric field averaged over the beam cross section. Hence:

$$dp = \frac{2E_{zn} dE_{zn}}{\beta_n^2 K_n} \tag{A.28}$$

where $|E_{zn}|$ is the amplitude of the axial electric field on the nth space harmonic, βn is the phase constant of the nth space harmonic, P is the average circuit power flow, S is the cross section area of the beam.

Next, we divide the beam up into short segments of length dz as shown in Fig. A.1. In the figure, E_{zn+} and E_{zn-} are the instantaneous values of the n^{th} space harmonic propagating to the left and right, respectively. The current induced by the beam causes these the left and the right propagating space harmonics to change by $dEzn+$ and $dEzn-$ respectively. But due to symmetry,

$$dE_{zn+} = dE_{zn-} \tag{A.29}$$

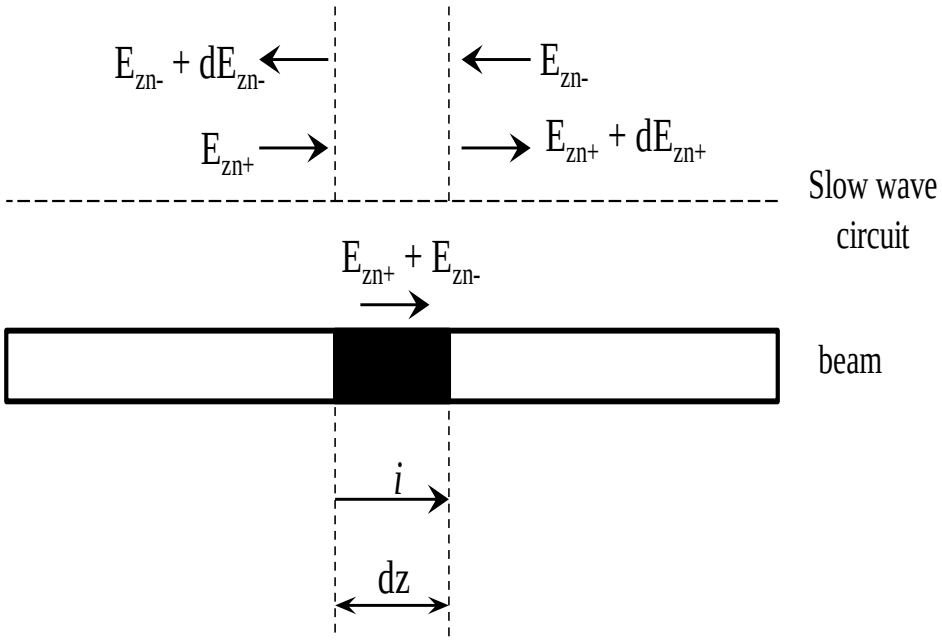

Fig. A.1. Schematic illustrating the induction of differential forward and backward propagating electric fields on a circuit by a differential length of RF current.

Since the change in instantaneous power is given by (A.28), therefore, the total instantaneous power is given by:

$$dp = dp_+ + dp_-$$

$$= \frac{2}{\beta_n^2 K_n}[E_{zn-}dE_{zn-} + E_{zn+}dE_{zn+}]$$

$$= \frac{2}{\beta_n^2 K_n}[E_{zn-} + E_{zn+}]dE_{zn-}$$

$$= \frac{2}{\beta_n^2 K_n}[E_{zn-} + E_{zn+}]dE_{zn+} \qquad (A.30)$$

where we have made use of (A.29).

From Maxwell's equation, the incremental instantaneous power flow into the

circuit from the length *dz* of the electron beam can be written as:

$$dp = -iE_z dz \tag{A.31}$$

where *i* is the instantaneous value of the convention current, and *Ez* is the total electric field resulting from the wave on the slow wave circuit. Hence from (A.31):

$$dp = -i(E_{zn-} + E_{zn+})dz \tag{A.32}$$

Combining (A.30) and (A.32) we obtain:

$$dE_{zn-} = dE_{zn+} = -\frac{1}{2}\beta_n^2 K_n i dz \tag{A.33}$$

(A.33) in phasor notation is:

$$dE_{zn-} = dE_{zn+} = -\frac{1}{2}\beta_n^2 K_n i dz \tag{A.34}$$

We have thus obtained the increment waves propagating away from a region of a differential length of current that induces the wave.

Let $\Gamma_0 = \alpha + j\beta_n$ be the complex propagation of the nth space harmonic wave. We can write the total space harmonic field at an arbitrary point ($z = a$) as the sum of three contributions:

$$E_{zn}(a) = E_{zn}(0)e^{-\Gamma_0 a} - \frac{1}{2}\beta_n^2 K_n \int_0^a i e^{-\Gamma_0(a-z)}\, dz$$

$$-\frac{1}{2}\beta_n^2 K_n \int_a^l i e^{-\Gamma_0(z-a)}\, dz \tag{A.35}$$

where *l* is the total length of the circuit.

Changing the variable in the definite integrals of (A.35) from *dz* to *dτ*, and replacing *a* with *z*, an arbitrary point, and after two successive differentiations of (35), we obtain:

$$\Gamma^2 E_{zn} = \Gamma_0^2 E_{zn}(0) e^{-\Gamma_0 z} - \frac{1}{2}\Gamma_0^2 \beta_n^2 K_n \int_0^z i e^{-\Gamma_0 (z-\tau)}\, d\tau - \frac{1}{2}\Gamma_0^2 \beta_n^2 K_n \int_z^l i e^{\Gamma_0 (z-\tau)}\, d\tau + \Gamma_0 \beta_n^2 K_n i \qquad (A.36)$$

Combining (A.36) with (A.35) (now with the variable *a* replaced by *z* and *dz* replaced with *dτ*), we obtain:

$$E_{zn} = \frac{\Gamma_0 \beta_n^2 K_n i}{\Gamma^2 - \Gamma_0^2} \qquad (A.37)$$

(A.37) is the circuit equation which relates the field E_{zn} generated in the slow wave circuit by the RF electron current *i*.

A.4 Electronic-circuit interaction equation

We can now simultaneously solve the electronic equation and circuit equation, and this combination will reveal that only certain values of spatial propagation constant Γ are allowed in a TWT. Solving for *Ezn/i* in both (A.25), the electronic equation and (A.37), the circuit equation, and equating the results, we obtain:

$$(\Gamma^2 - \Gamma_0^2)\left[(\Gamma - j\beta_e)^2 + \frac{w_q^2}{u_0^2}\right] = \frac{j\beta_e \beta_n^2 \Gamma_0 K_n I_0}{2V_0} \qquad (A.38)$$

Now we define a small signal-gain parameter *C* given by:

$$C^3 \equiv \frac{K_n I_0}{4V_0} \tag{A.39}$$

C is a small dimensionless parameter with typical values ranging from 0.01 and 0.1.

Next we define a space-charge parameter *QC* as:

$$QC \equiv \frac{w_q^2}{4C^2 w^2} \tag{A.40}$$

Since βe and βn are approximately equal for synchronous interaction, and since Γ must have similar imaginary part, we will now define parameters *b*,*d* and δ by the equations:

$$\Gamma_0 \equiv j\beta_e(1 + Cb - jCd) \tag{A.41}$$

and

$$\Gamma \equiv j\beta_e(1 + jC\delta) \tag{A.42}$$

Since $\Gamma_0 = \alpha + j\beta_n$ then b and d are real numbers given by:

$$b = \frac{\beta_n - \beta_e}{\beta_e} = \frac{u_0 - v_{pn}}{v_{pn}C} \tag{A.43}$$

$$d = \frac{\alpha}{\beta_e C} \tag{A.44a}$$

b is a measure of the amount of synchronism between the electrons and the space harmonic of the slow wave structure. *d* is a function of the attenuation of the slow wave structure.

Substituting (A.39) – (A.42) into (A.38) and solving, using the fact the *C* is small, we obtain:

$$\delta^2 = \frac{1}{(-b + jd + j\delta)} - 4QC \qquad (A.44b)$$

where we used the approximation

$$\frac{\Gamma_0 \beta_n^2}{j\beta_e^3} \cong 1 \qquad (A.45)$$

Solution of (A.44) will yield three different roots for δ. Hence, there are 3 possible solutions for the propagation constant Γ of the circuit-beam coupled system. Now we find the Γ in a TWT for a simple case where:

$$b = d = QC = 0$$

(44) becomes:

$$\delta^3 = -j \qquad (A.46)$$

with solutions:

$$\delta_1 = \frac{\sqrt{3}}{2} - j\frac{1}{2}, \delta_2 = -\frac{\sqrt{3}}{2} - j\frac{1}{2}, \delta_3 = j \qquad (A.47)$$

The corresponding values of Γ are:

$$\Gamma_1 = -\frac{\sqrt{3}}{2}\beta_e C + j\beta_e\left(1 + \frac{C}{2}\right) \quad (growing\ wave)$$

$$\Gamma_2 = \frac{\sqrt{3}}{2}\beta_e C + j\beta_e\left(1 + \frac{C}{2}\right) \quad (decaying\ wave)$$

and

$$\Gamma_3 = j\beta_e(1 - C) \ \ (constant\ wave) \tag{A.48}$$

since the fields vary as:

$$e^{jwt - \Gamma z}$$

Γ_1 corresponds to a growing traveling wave, Γ_2 corresponds to a decaying traveling wave, and Γ_3 corresponds to a constant amplitude traveling wave.

Before ending our discussion in this regard, we now find the phase velocity of the growing wave from the propagation constant Γ_1

$$v_{p1} = \frac{w}{\beta_e(1 + {}^{1}/_{2}\, C)} = \frac{u_0}{1 + {}^{1}/_{2}\, C} \tag{A.49}$$

Hence, the phase velocity of the growing wave is less than the velocity u_0 of the electron beam. This is always true regardless of the values of *b*, *d*, and *QC*. Hence, to obtain amplification through synchronous interaction, the electron drift velocity must be greater than the wave velocity as postulated in the previous section on the description of TWT amplification.

A.5 Gain of a traveling wave tube amplifier

The gain of a TWT amplifier of length *l* can be written as:

$$gain = 20 \log \left| \frac{E_{zn}(l)}{E\_zn(0)} \right| \ dB \tag{A.50}$$

For practical TWT, the gain may be derived from the growing wave alone:

$$gain = 20\log\left|\frac{E_{zn1}e^{-\Gamma_1 l}}{E\_zn(0)}\right| \; dB \tag{A.51}$$

Since:

$$|e^{-\Gamma_1 l}| = e^{\beta_e C x_1 l} \tag{A.52}$$

where x_1 is the real part of Γ_1.

Equation (A.51) now becomes:

$$gain = A_1 + \; 20\beta_e C x_1 l \; loge + A_2 \tag{A.52}$$

where A_1 is the initial loss factor given as:

$$A_1 = 20\log\left|\frac{E_{zT1}}{E_{zn}(0)}\right| dB \tag{A.53}$$

and E_{zT1} is the total electric field given by the summation of the nth harmonic space wave and the space charge electric field ($E_{zT1} = E_{zn1} + E_{zsc1}$).

The relationship between E_{zT1} and δ and $E_{zn}(0)$ (the space harmonic at the input of the TWT) is:

$$\frac{E_{zT1}}{E_{zn}(0)} = \frac{\delta_1^2}{(\delta_1 - \delta_1)(\delta_1 - \delta_3)} \tag{A.54}$$

Also, from (A.52), A_2 is the space charge loss factor defined as:

$$A_2 = 20\log\left|\frac{E_{zn1}}{E_{zT1}}\right| \; dB \tag{A.55}$$

which can be written as

$$A_2 = 20 \log \left| \frac{\delta_1^2 + 4QC}{\delta_1^2} \right| dB \tag{A.56}$$

Also, we can define a parameter *B* as:

$$B = (40\pi \log e)\, x_1 = 54.6\, x_1 \tag{A.57}$$

And *N*, the electronic wavelength of the circuit, as:

$$N = \frac{\beta_e l}{2\pi} \tag{A.58}$$

Hence, the gain of the TWT amplifier can be written as:

$$gain_{dB} = A_1 + A_2 + BCN \tag{A.59}$$

A.6 Reference

[1] J. W. Gewartowski and H. A. Watson, *Principles of electron tubes*, Princeton, NJ: D. Van Nostrand Company Inc., 1965.

APPENDIX B

DIELECTRIC CIRCUITS FOR PLASMA-TERAHERTZ WAVE INTERACTION

B.1 Introduction

In this work, some dielectric circuits were designed for studying the interaction between plasma and terahertz waves. These circuits are presented here. Dielectric circuits, with the proper selection of dielectric material, can be designed to have low insertion loss such that the terahertz waves for plasma interaction do not get lost as a result of circuit material absorption. Some dielectric materials investigated for the circuit design are Teflon, quartz, and fused quartz. These materials were employed in waveguide-like circuits. Different circuit geometries were investigated with these materials: viz slab, pipe, slotted pipe, meandering slab, thin fiber, parallel-plate, etc. These circuits are briefly presented in Figs. B.1 - B.10.

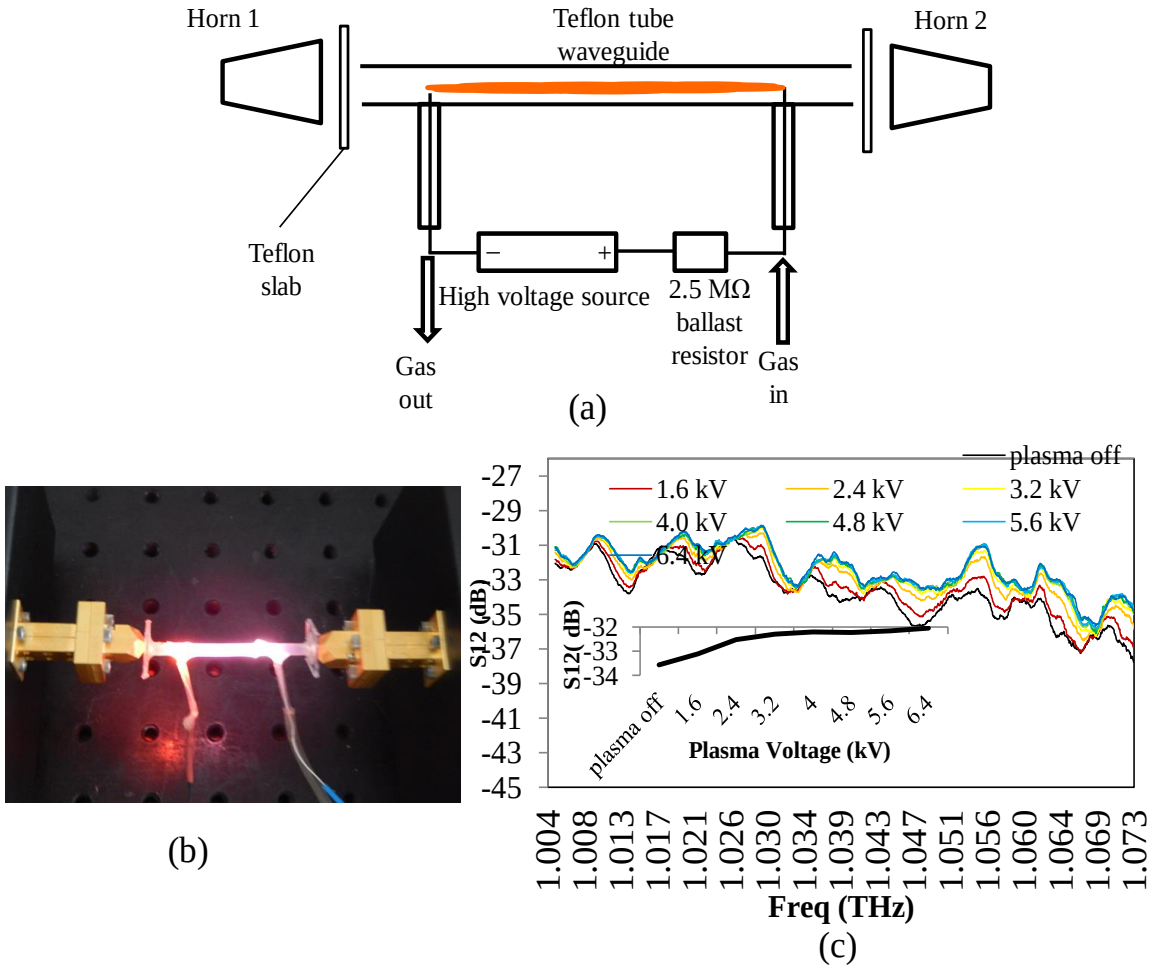

Fig. B.1. A Teflon tube interaction circuit. (a) Schematic of experimental setup showing the Teflon tube guiding terahertz between two diagonal horn antennas. The plasma was ignited with the tube with a high voltage source, and the ballast resistor in the circuit serves to prevent sparks in the plasma discharge. The terahertz-transparent polystyrene screen protects the terahertz measurement system in case of a spark. (b) The experimental setup showing the ignited neon discharge (c) Change in terahertz transmission from horn 2 to 1 through plasma-Teflon tube circuit as a function of plasma voltage. Inset shows the frequency-averaged transmission from 1.033 THz to 1.040 THz.

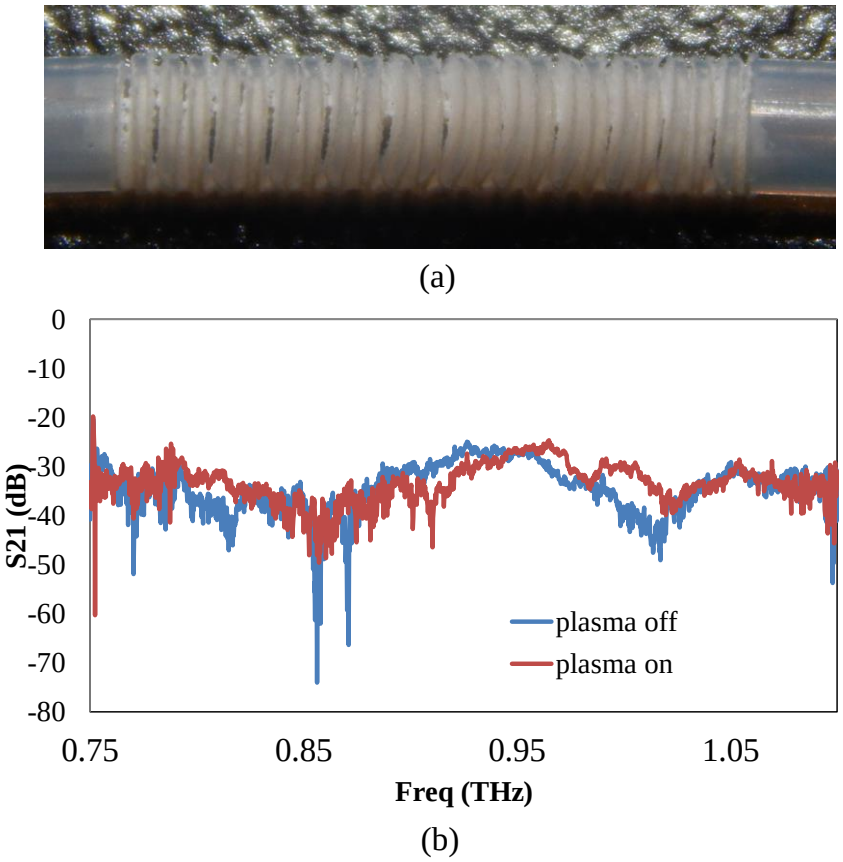

Fig. B.2. A corrugated Teflon tube interaction circuit. (a) Photograph of the corrugated Teflon tube (diameter ~0.3 mm). Corrugations were ~50 μm wide (b) Effect of atmospheric plasma on the interaction with wave in corrugated Teflon.

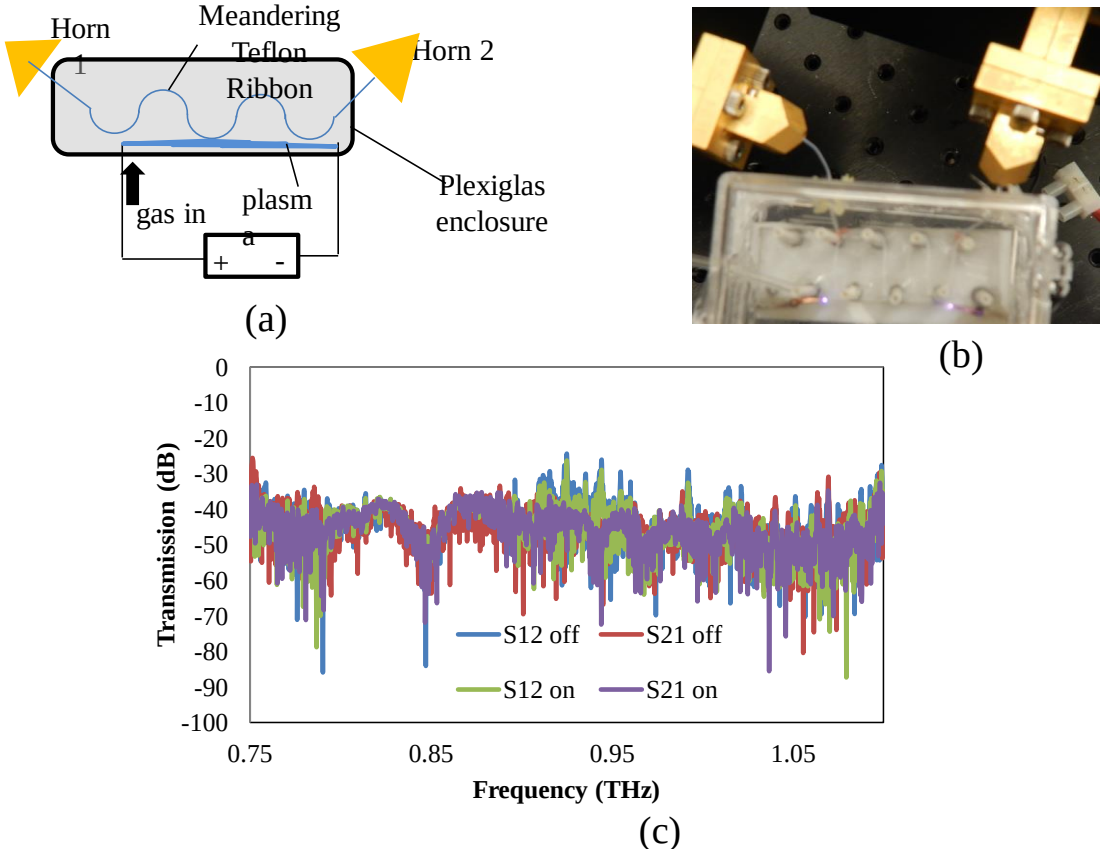

Fig. B.3. Meandering Teflon ribbon interaction circuit. (a) schematic of the meandering Teflon ribbon interaction circuit. (b) picture of the interaction circuit. (b) effect of atmospheric pressure plasma on transmission through the circuit.

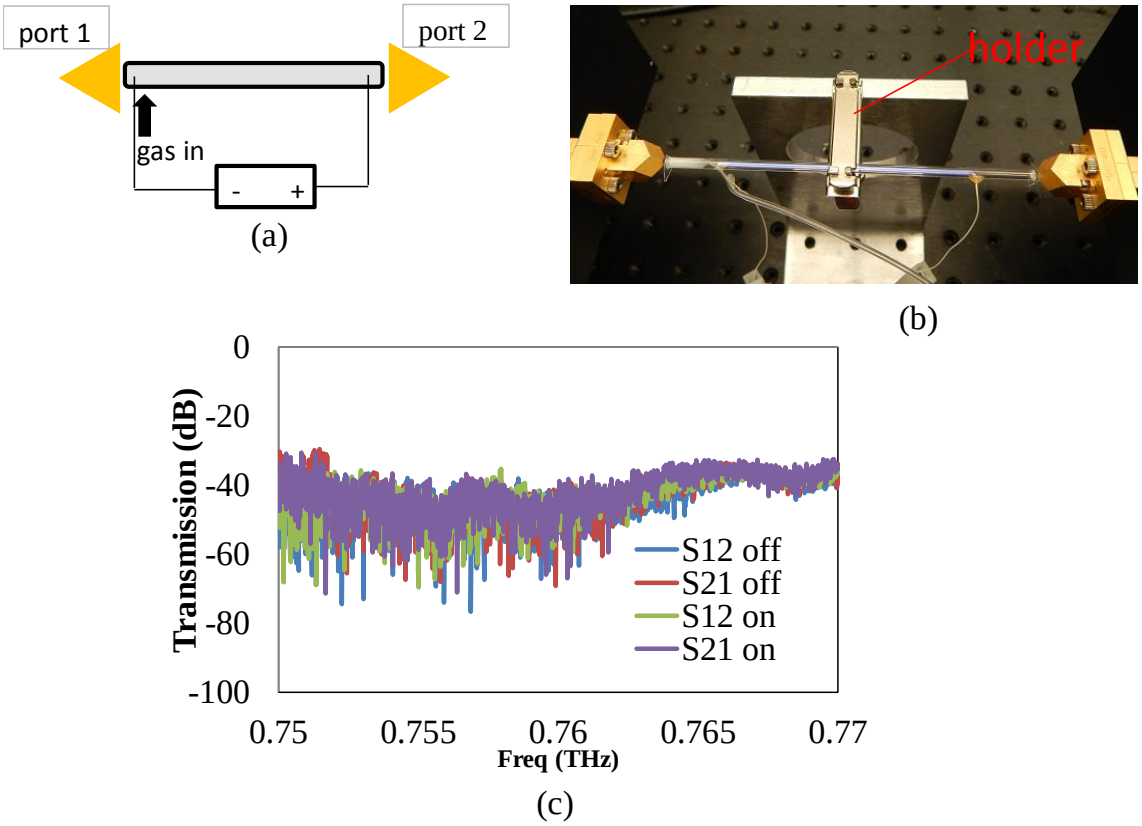

Fig. B.4. Quartz tube interaction circuit. (a) schematic of quartz tube interaction circuit. (b) photograph of quartz tube circuit under test. (c) effect of atmospheric pressure plasma on transmission through the circuit (S_{12} and S_{21} for plasma on and off).

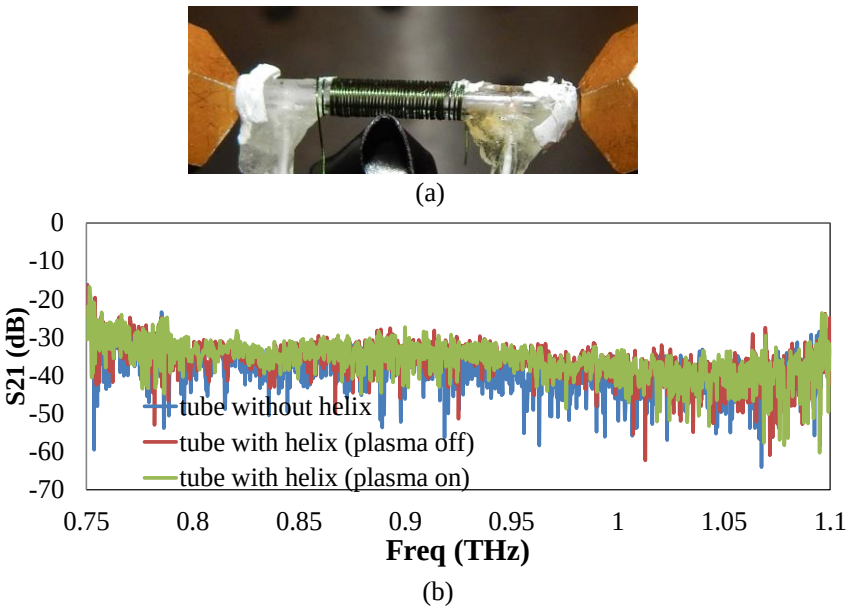

Fig. B.5. Helix-enclosed Teflon tube interaction circuit. (a) picture of the helix-enclosed Teflon tube interaction circuit under test. (b) effect of atmospheric plasma on transmission through interaction circuit.

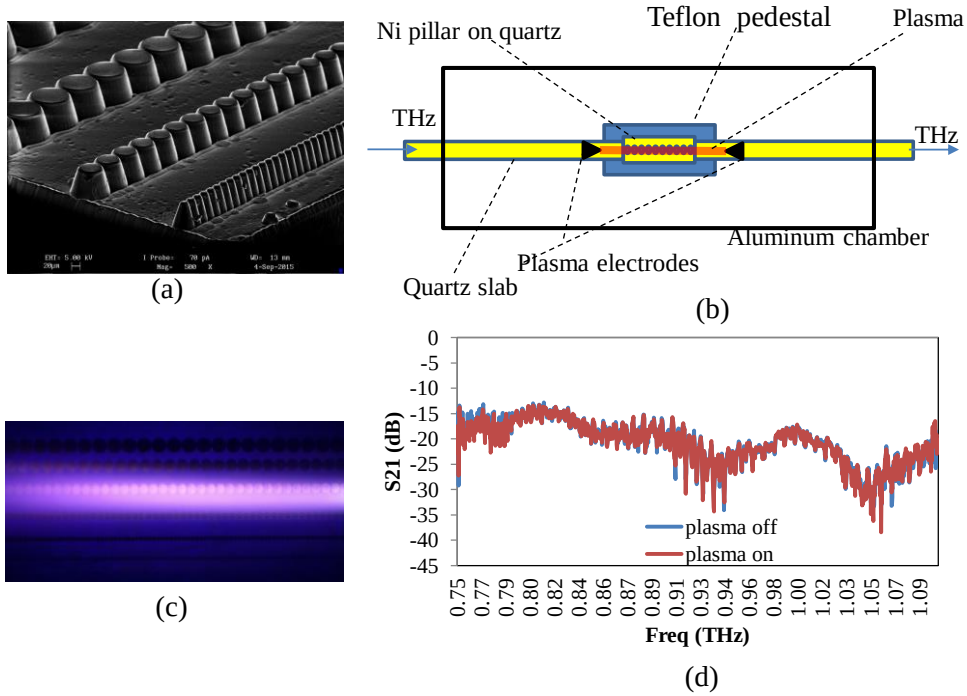

Fig. B.6. Nickel-on-quartz interaction circuit. (a) scanning electron micrograph of the microfabricated nickel pillar on quartz substrate device (b) schematic of experimental setup for testing the device (c) photograph of device under test (d) effect of low pressure plasma on transmission through interaction circuit device.

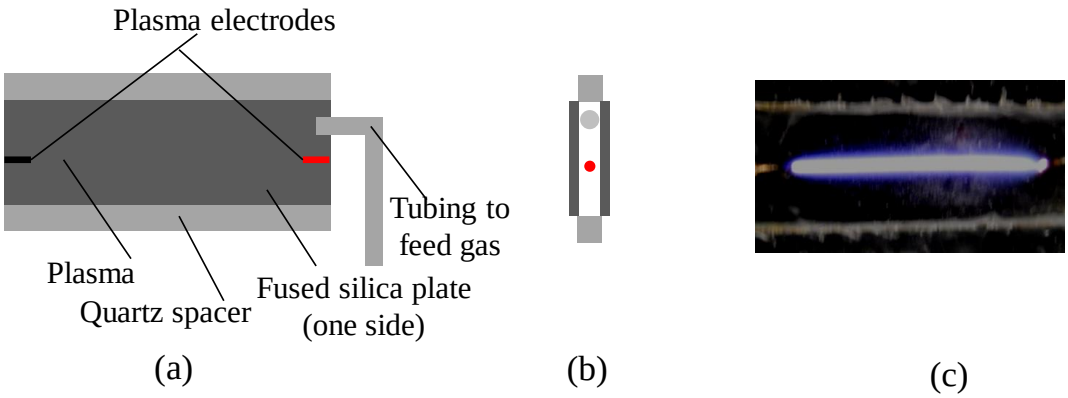

Fig. B.7. Parallel-plate fused silica interaction circuit. (a) schematic of front view (b) schematic of side view (c) picture of plasma dielectric device.

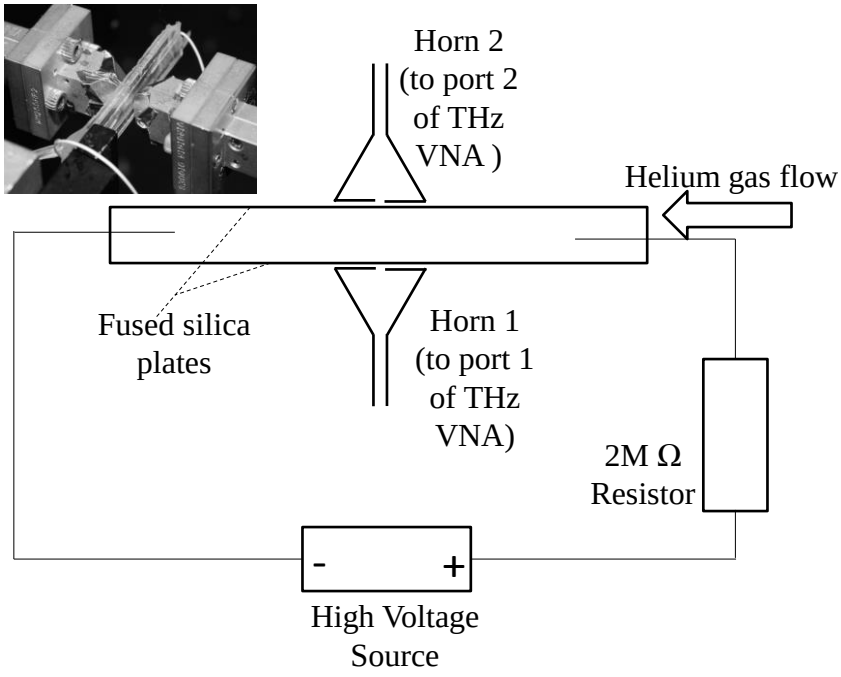

Fig. B.8. Schematic of experimental setup of the parallel-plate fused silica circuit. Inset shows photograph of experimental setup.

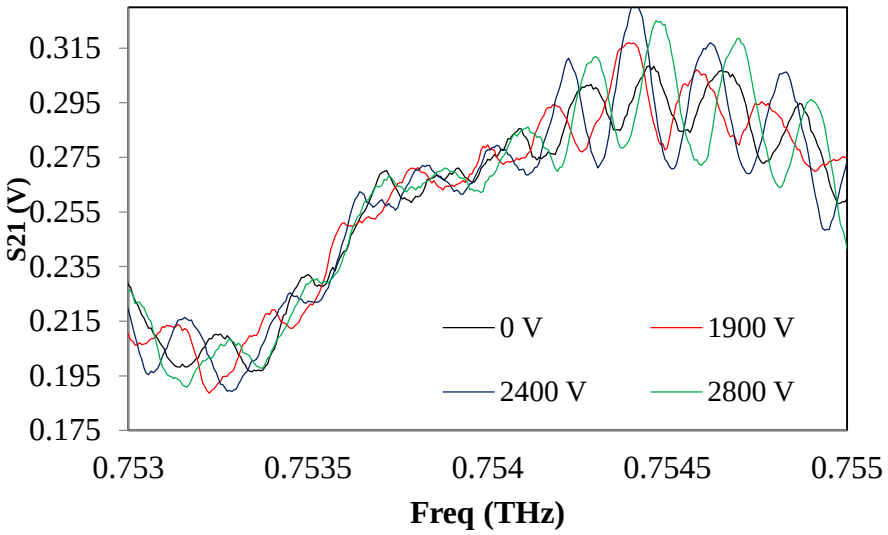

Fig. B.9. Change in transmission through the parallel-plate fused silica circuit for different plasma voltages.

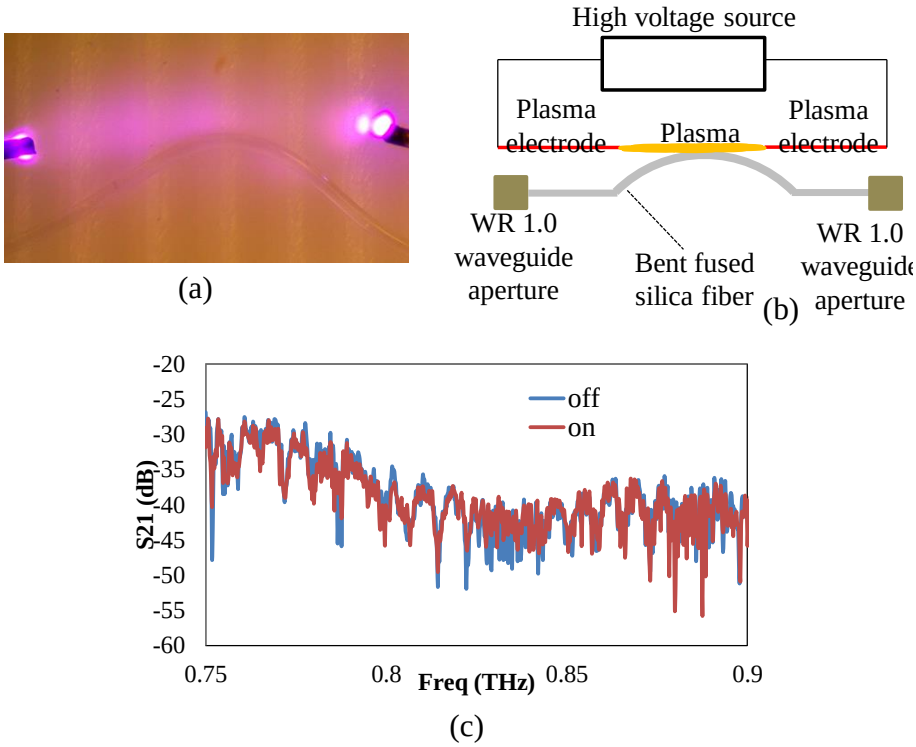

Fig. B.10. Bent silica fiber interaction circuit. (a) photograph of the bent silica fiber (~150 μm diameter) with atmospheric pressure plasma beam. (b) schematic of the interaction experiment setup. (c) transmission through the fiber on interaction with plasma.

B. 2 Caveats on measured plasma-terahertz interaction in dielectric circuits

The S-parameter results presented in the earlier sections were not obtained at the instant the plasmas were created (due to the long measurement time of the terahertz vector network analyzer). Therefore, in addition to plasma-wave interaction, some other effects contributed to the interaction (terahertz transmission) results presented above. These other effects include thermal effects. This is because the high temperature of the circuits will manifest in the terahertz transmission. This effect is more pronounced in Teflon-based circuits because Teflon has a high thermal expansion coefficient. Thermal effects are less pronounced in quartz, and fused silica has a very low thermal expansion coefficient. Thermal effects can also lead to microphonics in the interaction circuits. A solution to this problem is measuring the response of the circuit at a high data acquisition speed (the measurement time of the results presented is >= 300 milliseconds). Furthermore, the dielectric materials can be thermally stabilized or thermally compensated to eliminate thermal effects.